## 84<sup>th</sup> ARFTG Microwave Measurement Conference



# The New Frontiers for Microwave Measurements

December 4<sup>th</sup>-5<sup>th</sup> 2014 St. Julien Hotel Boulder, Colorado



IEEE Catalog Number: CFP14ARG-USB ISBN: 978-1-4799-7084-1



Copyright and Reprint Permission: Abstracting is permitted with credit to the source. Libraries are permitted to photocopy beyond the limit of U.S. copyright law for private use of patrons those articles in this volume that carry a code at the bottom of the first page, provided the per-copy fee indicated in the code is paid through Copyright Clearance Center, 222 Rosewood Drive, Danvers, MA 01923. For reprint or republication permission, email to IEEE Copyrights Manager at pubs-permissions@ieee.org. All rights reserved. Copyright ©2014 by IEEE.

### 84<sup>th</sup> ARFTG Conference Organizers

General Chairs Ron Ginley
Technical Program Chairs Mitch Wallis

## 84<sup>th</sup> ARFTG Technical Program Committee

Peter Aaen, University of Surrey James Randa, NIST

Dave Blackham, Keysight Technologies J. Apolinar Reynoso-Hernandez,

Gayle Collins, MaXentric Technologies CICESE

Dazhen Gu, NIST

Nick Ridler, NPL

Leonard Hayden, TriQuint

Patrick Roblin, The Ohio State

Semiconductor University

Karel Hoffmann, Czech Technical Dominique Schreurs, KU Leuven

University in Prague Ken Wong, Keysight Technologies

John Wood, Maxim Integrated Products

### The 2014 ARFTG Executive Committee (ExCom)

President Mohamed Sayed, MMS

Vice President Jon Martens, Anritsu

Secretary **Dominique Schreurs**, K.U.Leuven

Treasurer and Standards Ronald Ginley, NIST

Nonlinear Network Analyzers and Publicity

Jean-Pierre Teyssier, Keysight Technologies

Electronic Communications Mitch Wallis, NIST

Education and Workshops Patrick Roblin, Ohio State University

Publications David Blackham, Keysight Technologies

Sponsorship Joe Gering, RFMD

Technical Coordination and Planning

John Wood, Maxim Integrated Products

Membership and Standards Ken Wong, Keysight Technologies

Exhibits Rusty Myers, Maury Microwave

Technical Coordination and Planning Nick Ridler, NPL

Electronic Publicity Peter Aaen, University of Surrey

MTT-S Liaison and Awards Leonard Hayden, TriQuint Semiconductor

#### **Ex-Officio**

Executive Secretary John Cable

#### **Session A: Remote Sensing and Noise Measurements**

Session Chair: Mohamed Sayed, MMS

## **CubeSat-based Radiometer Systems from Millimeter-wave to Terahertz: Enabling Frequent Global Observations of the Earth's Atmosphere**

S. C. Reising, Colorado State University, Fort Collins, Colorado, United States

## Comparison of Noise-Parameter Measurement Strategies: Simulation Results for Amplifiers

J. Randa, NIST, Boulder, Colorado, United States

## On-wafer Differential Noise Figure Measurement without Couplers on a Vector Network Analyzer

Y. Andee<sup>1,2</sup>, A. Siligaris<sup>1,2</sup>, F. Graux<sup>3</sup>, F. Danneville<sup>4</sup>, <sup>1</sup>Univ. Grenoble Alpes, Grenoble, France, <sup>2</sup>CEA, Grenoble, France, <sup>3</sup>Rohde&Schwarz France, Meudon-la-Foret, France, <sup>4</sup>IEMN, Villeneuve d'Ascq, France

#### **Session B: mm-Wave and THz Measurements**

Session Chair: Jon Martens, Anritsu

## Novel Flexible Dielectric Waveguide for Millimeter and Sub-Millimeter Frequencies – Design and Characterization

H. Nickel, J. Zovo, Spinner GmbH, Feldkirchen-Westerham, Germany

## **Evaluating the Effect of Using Precision Alignment Dowels on Connection Repeatability of Waveguide Devices at Frequencies from 750 GHz to 1.1 THz**

N. Ridler<sup>1</sup>, R. Clarke<sup>2</sup>, <sup>1</sup>National Physical Laboratory, Teddington, United Kingdom, <sup>2</sup>University of Leeds, Leeds, United Kingdom

## **Accuracy and Repeatability of Automated Non-Contact Probes for On-wafer Characterization**

C. Caglayan, G. C. Trichopoulos, K. Sertel, ElectroScience Laboratory, Columbus, United States

#### Session C: Measurements for Communications Technology and Nonlinear Applications

Session Chair: Dave Blackham, Keysight

#### Free-Field Measurements of Integrated Wireless Devices in Reverberation Chambers

K. Remley, NIST, Boulder, United States

#### On High Frequency / mm-Wave IMD Measurements with Small Tone Spacing

J. Martens, Anritsu, Morgan Hill, United States

#### A Test Set-up for the Analysis of Multi-Tone Intermodulation in Microwave Devices

J. Teyssier<sup>1</sup>, J. Sombrin<sup>2</sup>, R. Quéré<sup>1</sup>, S. Laurent<sup>1</sup>, G. Francis<sup>3</sup>, <sup>1</sup>XLIM-cnrs, Brive la Gaillarde, France, <sup>2</sup>XLIM-Labex, Limoges, France, <sup>3</sup>CNES, Toulouse, France

#### **Session D: On-wafer measurements**

Session Chair: Peter Aaen, University of Surrey

#### Via-Adjusted Microstrip Launch for Sub-Terahertz Wafer Probing

K. Jung, J. Ebner, Cascade Microtech Inc., Beaverton, United States

#### Adaptive Estimation of Complex Calibration Residual Errors of Wafer-Level S-Parameters Measurement System

A. A. Savin<sup>1</sup>, V. G. Guba<sup>2</sup>, A. Rumiantsev<sup>3</sup>, B. D. Maxson<sup>4</sup>, S. Schubert<sup>5</sup>, U. Arz<sup>5</sup>, <sup>1</sup>Tomsk State University of Control Systems and Radioelectronics, Tomsk, Russian Federation, <sup>2</sup>NPK Tair, Tomsk, Russian Federation, <sup>3</sup>MPI Corporation, Chu-Pei City, Taiwan, <sup>4</sup>Copper Mountain Technologies, Indianapolis, United States, <sup>5</sup>Physikalisch-Technische Bundesanstalt (PTB), Braunschweig, Germany

#### LZZM: An Extension of the Theory LZZ Calibration Technique

M. A. Pulido-Gaytan<sup>1</sup>, J. A. Reynoso-Hernandez<sup>1</sup>, A. Zarate-de Landa<sup>1</sup>, J. R. Loo-Yau<sup>2</sup>, M. C. Maya-Sanchez<sup>1</sup>, Cicese, Ensenada, Mexico, <sup>2</sup>Cinvestav, Guadalajara, Mexico

#### **Session E: Materials Characterization**

Session Chair: Jon Martens, Anritsu

## Noncontact Conductivity and Dielectric Measurement for High Throughput Roll-to-Roll Nanomanufacturing

N. Orloff, NIST, Boulder, United States

### Study of Reflection Effect at Fixture Interfaces on Permittivity Measurements using the Transmission/Reflection Method

Y. Kato, M. Horibe, National Institute of Advanced Industrial Science and Technology, Tsukuba, Japan

## Free-space Reconstruction of the Electrical Properties of Carbon Nanotube Composites in the Q-band

A. M. Hassan, J. Obrzut, E. J. Garboczi, National Institute of Standards and Technology, Gaithersburg, United States

#### **Session F: Calibration and Verification**

Session Chair: Nick Ridler, NPL

#### **A Calibration Procedure for Electronic Calibration Units**

J. Stenarson<sup>1</sup>, C. Eiø<sup>2</sup>, K. Yhland<sup>1</sup>, <sup>1</sup>SP Technical Research Institute of Sweden, Boras, Sweden, <sup>2</sup>NPL National Physical Laboratory, Teddington, Middlesex, United Kingdom

## Offset-Shorts Vector-Network-Analyzer Calibration with Simultaneous Modeling of Calibration Standards

A. Lewandowski<sup>1</sup>, W. Wiatr<sup>1</sup>, P. Barmuta<sup>2</sup>, <sup>1</sup>Warsaw University of Technology, Warsaw, Poland, <sup>2</sup>KU Leuven, Leuven, Belgium

#### **Two-Port Calibration Insensitive to Flange Misalignment**

A. Arsenovic<sup>1</sup>, R. M. Weikle<sup>2</sup>, J. Hesler<sup>1</sup>, <sup>1</sup>Virginia Diodes, Charlottesville, United States, <sup>2</sup>University of Virginia, Charlottesville, United States

#### Residual Error Analysis of a Calibrated Vector Network Analyzer

F. A. Mubarak, VSL, Delft, Netherlands

#### **Interactive Forum**

Session Chair: Mitch Wallis, NIST

#### Evaluation and Validation of a National WR-15 (50 to 75 GHz) Power Measurement System

X. Cui<sup>1</sup>, Y. Meng<sup>2</sup>, Y. Shan<sup>2</sup>, W. Yuan<sup>1</sup>, C. Ma<sup>1</sup>, Y. Li<sup>1</sup>, <sup>1</sup>National Institute of Metrology, Beijing, China, <sup>2</sup>National Metrology Centre, Singapore

## A Near-Field Scanning Microwave Microscope for Measurement of the Permittivity and Loss of High-Loss Materials

A. P. Gregory<sup>1</sup>, J. F. Blackburn<sup>1</sup>, K. Lees<sup>1</sup>, R. N. Clarke<sup>1</sup>, T. E. Hodgetts<sup>2</sup>, S. M. Hanham<sup>3</sup>, N. Klein<sup>3</sup>, <sup>1</sup>National Physical Laboratory, Teddington, United Kingdom, <sup>2</sup>Consultant on behalf of the National Physical Laboratory, Teddington, United Kingdom, <sup>3</sup>Imperial College, London, United Kingdom

## Measurement Uncertainty in Waveguide VNA Calibrated by Offset Short Calibration with Oversized Waveguide Aperture at Sub-millimeter Wave Frequency

M. Horibe, R. Kishikawa, AIST, Tsukuba, Japan

## **Broadband Dielectric Spectroscopy Calibration Using Calibration Liquids with Unknown Permittivity**

S. Liu<sup>1</sup>, I. Ocket<sup>2,1</sup>, P. Barmuta<sup>3,1</sup>, T. Markovic<sup>1</sup>, A. Lewandowski<sup>3</sup>, D. Schreurs<sup>1</sup>, B. Nauwelaers<sup>1</sup>, <sup>1</sup>University of Leuven, Heverlee, Belgium, <sup>2</sup>Interuniversity Microelectronics Center, Heverlee, Belgium, <sup>3</sup>Warsaw University of Technology, Warsaw, Poland

#### Progress Towards a NIST Microwave Brightness Standard for Remote Sensing

D. Houtz, D. K. Walker, D. Gu, National Institute of Standards and Technology, Boulder, United States

## Development of an Automated Unintended Radiated Emission (URE) Radio Frequency (RF) Measurement System

J. E. Friedel<sup>1</sup>, A. P. Burr<sup>1</sup>, V. V. Nguyen<sup>2</sup>, <sup>1</sup>Naval Surface Warfare Center Indian Head Explosive Ordnance Disposal Technology Division, Indian Head, United States, <sup>2</sup>Naval Surface Warfare Center Indian Head Explosive Ordnance Disposal Technology Division, Indian Head, United States

## Comparison of Noise-Parameter Measurement Strategies: Simulation Results for Amplifiers\*

James Randa

RF Technology Division

National Institute of Standards and Technology (NIST)

Boulder, CO 80303

Abstract — A previously developed simulator for noise-parameter measurements has been used in an extensive investigation and comparison of different measurement strategies for measuring the noise parameters of low-noise amplifiers (LNAs). This paper summarizes the methodology and reports the salient results of that investigation. The simulator is based on a Monte Carlo program for noise-parameter uncertainties and enables us to compare the uncertainties (both type A and type B) obtained with a given set of input terminations. We focus on results that do not depend (or depend only weakly) on details of the device under test (DUT). One noteworthy result is the marked improvement in the noise-parameter measurement uncertainties when a matched, cold (i.e., well below ambient noise temperature) source is included in the set of input terminations.

Index Terms — Amplifier noise measurement, amplifier noise parameters, noise-parameter measurement, measurement uncertainty, Monte Carlo simulation.

#### I. INTRODUCTION

Several years ago, a simulator for noise-parameter measurements was developed [1], based on a Monte Carlo program for noise-parameter uncertainties [2]. Some minor improvements have been made to that simulator, and it has now been used in a rather extensive investigation and comparison of different strategies for measuring the noise parameters of low-noise amplifiers (LNAs). This paper summarizes the methodology and reports the salient results of that investigation. We focus on results that do not depend (or depend only weakly) on details of the device under test (DUT).

There is commercial instrumentation that enables the user to perform routine amplifier noise-parameter measurements, but it is still of interest to consider how such measurements might be improved, or what strategies might be employed for difficult special cases. Some of the results might be anticipated based on common intuition, but even in such cases it is still useful to have a quantitative confirmation and an estimate of the size of the expected effect. In this paper, we compare different measurement strategies on the basis of the uncertainties obtained with the given strategy (or set of input states) and on the basis of the frequency of occurrence of

unphysical measurement results or sets of measurements that do not admit a good fit to the simulated measurement data.

From the early days of noise-parameter measurements, there has been work on choosing the set of input terminations; see, e.g., [3] - [5] or the summary in [6]. The present investigation assumes that the specific properties of the DUT are not known, although its general characteristics may be. We do not attempt to find the optimum pattern of impedances for the input terminations for a given amplifier. Instead, we try to find general features of the input set that work well for a range of amplifiers. We also consider variations in the measurement strategy, such as inclusion of additional non-ambient inputs or inclusion of a reverse measurement.

In our simulations, we start with a basic measurement strategy, with a small set of input states, and consider a number of possible improvements. Some of the improvements are modifications of the input states, adding or substituting additional states, and some involve modifications of the basic measurement set. Of course, the results depend on details of the amplifier being measured. In order to identify general features that are likely to be true for most DUTs, we have performed all the simulations on three different amplifiers, with very different properties.

In the next section we provide a short overview of the simulator, including the input uncertainties and the recent modification. We also give the properties of the amplifiers and input terminations that we consider in this work. Section III presents the simulations performed and the results obtained, and Section IV contains a summary and conclusions.

#### II. METHODOLOGY

#### A. The Simulator

The simulator assumes measurements of the form pictured in Figure 1, which also shows relevant conventions regarding notation. The DUT is characterized by its scattering parameters ( $S_{ij}$ ) and its noise parameters. A series of input terminations with known noise temperatures ( $T_{1,i}$ ) and reflection coefficients ( $T_{1,i}$ ) is connected to the input of the DUT, and the output noise temperature ( $T_{2,i}$ ) or noise power is

\*

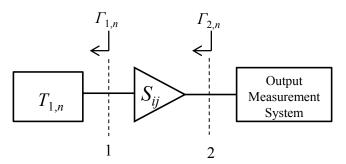


Fig. 1 Configuration for forward measurements.

measured for each. An equation can be written for the output noise temperature (or noise power) as a function of the four noise parameters and the gain, and the noise parameters and gain can then be determined by fitting to the set of equations for the output for each different input termination. There are many different, equivalent forms for the equations [6]; we perform the analysis and computations in terms of noise-wave parameters, but we will present and discuss the results in terms of the usual IEEE noise parameters.

For a given measurement strategy and set of input terminations, the simulation program generates  $N_S$  sets of simulated measurements. All results reported in this paper were obtained with  $N_S = 20,000$ . Each set includes all input noise temperatures and reflection coefficients, the amplifier Sparameters, the output noise temperatures, and the output reflection coefficients  $\Gamma_{2,n}$ . (The output reflection coefficients can instead be computed from input reflection coefficients and S-parameters; see subsection III.E below.) Each simulated measurement set is analyzed in the same manner as a real set of measurements would be analyzed, with a least-squares fit to the set of equations for the output noise temperature in terms of the noise parameters (and the measured quantities). The fit results in values for each noise parameter (and the gain), as well as a type A uncertainty for each of these quantities, which is obtained from the statistics of the fit. The type B uncertainty is computed in the usual Monte Carlo manner, taking the root mean square error (RMSE) of the sample of  $N_S$  values,

$$u_B(y) = RMSE(y) = \sqrt{Var(y) + (\bar{y} - y_{true})^2}, \quad (1)$$

where y is any of the noise parameters, and Var(y) is the variance of the sample of simulated results for y. The fact that the mean  $(\bar{y})$  is not necessarily equal to the "true" value is due to the presence of various nonlinearities. In order to obtain a representative value of the type A uncertainty for the particular measurement strategy that we are considering, we take the root mean square of the  $N_S$  values for the type A uncertainty in that noise parameter.

Some quality checks (goodness of fit, physical and mathematical consistency of results) are applied to each set of simulated measurement results, as would be done for real results [6]. A measurement set that fails one or more of these

tests is considered a "bad" set and is discarded (as is usually the case for real measurements), and it is not included in the computation of uncertainties. The different measurement strategies are compared and judged on the basis of the frequency of occurrence of bad results, as well as the standard uncertainties (type A and type B added in quadrature) obtained for the noise parameters. Results that differ by a few percent or less are not significant; differences of more than about 5 % are significant.

#### B. Input Uncertainties

The simulation program accepts as input not only the values of the all the parameters, but also the standard uncertainties in the parameters that are directly measured, including the DUT S-parameters, the reflection coefficients of all the terminations, the noise temperatures of all the terminations, the output reflection coefficients  $\Gamma_{2,n}$  in Fig. 1, and the output noise temperatures. We refer to the uncertainties in these underlying measurements as the input uncertainties. Although the values obtained for the noise-parameter uncertainties will depend on the input uncertainties, we will concentrate on whether the uncertainties are significantly improved by a given measurement strategy, rather than on the actual values of the uncertainties. Nonetheless, we need to specify the input uncertainties.

Most of the input uncertainties are those used in [2], which also discusses the reasoning behind the values chosen. In treating correlations, which are of crucial importance, we work in terms of correlated and uncorrelated uncertainties, defined by the relations

$$u(y_i)^2 = u_{unc}(y_i)^2 + u_{cor}(y_i)^2$$

$$\rho_{ij} = \frac{u_{cor}(y_i)u_{cor}(y_j)}{u(y_i)u(y_j)},$$
(2)

where "cor" and "unc" refer to correlated and uncorrelated, and  $\rho_{ij}$  is the correlation coefficient for errors in  $y_i$  and  $y_j$ . Normal distributions are used for all the measured variables except the ambient temperature, for which a rectangular distribution is used, in order to more accurately represent the effect of thermostatic control.

The real and imaginary parts of the reflection coefficient are treated separately, and the same  $u(\Gamma)$  is used for each, where  $u(\text{Re}\Gamma) = u(\text{Im}\Gamma) \equiv u(\Gamma)$ . For reflection-coefficient measurements, a larger value of uncertainty is used for large  $|\Gamma|$  than for small  $|\Gamma|$ . For  $|\Gamma| \leq 0.5$ , we use  $u_{cor} = 0.0025$  and  $u_{unc} = 0.001$ , corresponding to  $u(\Gamma) = 0.002693$  and  $\rho = 0.8621$ . For larger values of  $|\Gamma|$ , we use  $u_{cor} = 0.004$  and  $u_{unc} = 0.001$ , corresponding to  $u(\Gamma) = 0.004123$  and  $\rho = 0.9412$ . All S-parameters other than  $S_{21}$  are treated the same way as reflection coefficients. The value used for  $S_{21}$  is not very important because its magnitude is treated as a fitting parameter,  $G_0 = |S_{21}|^2$ ; we use  $u(\text{Re}S_{21}) = u(\text{Im}S_{21}) = 0.01$ .

For the ambient temperature we use a rectangular distribution centered at the nominal laboratory temperature of 296.15 K, extending from 295.65 K to 296.65 K, with no correlation between separate measurements (since a considerable time period intervenes between separate measurements). For the noise temperatures of the input terminations, we use a fractional uncertainty of 0.005 for hot or cold terminations. For ambient or near-ambient (*i.e.*, within 20 K of ambient) terminations, we use the uncertainty in the ambient temperature.

One departure from the previous input uncertainties occurs for the measurement of output noise temperatures. In the past, we used a simple parameterization depending only on the value of the noise temperature being measured, unless an adapter was present. That parameterization relied on the output reflection coefficient not being too large. In order to treat poorly matched amplifiers, we have modified the uncertainty in measuring the output noise temperatures to include more details of the DUT and the measurement process. The new model includes estimates of the five principal contributions to noise-temperature measurement uncertainties (at least at NIST): the cryogenic standard, the ambient standard, the evaluation of the mismatch factor(s), the ratio of efficiencies for the different measurement paths, and the instrument linearity. These five contributions are combined in quadrature to yield the standard uncertainty. For large output reflection coefficients, the new model yields a somewhat larger value for the measurement uncertainty than did the previous model.

#### C. LNAs and Input States

We do not want our results to depend on specific features of the DUT, but on the other hand, the simulator requires specific values for the DUT scattering and noise parameters. We therefore apply each measurement strategy to three different amplifiers, whose properties span a wide range of values of interest. We label the three amplifiers A1, A2, and A3. Their scattering and noise parameters are given in Tables 1 and 2. (Phases of S-parameters are omitted to save space.) Amplifier A1 has a low noise figure, A3 has a high noise figure, and A2 lies between. A1 and A2 have gains in the range of 32 dB to 33 dB, whereas A3 has lower gain, around 23 dB. A1 and A2 are reasonably well matched, but A3 has  $|S_{11}| \approx 0.47$ . All three amplifiers have  $|\Gamma_{opt}|$  around 0.2. All three sets of properties are realistic in the sense that they were obtained in measurements on real amplifiers in the 1-12 GHz range.

Table 1. DUT S-parameters (to three significant places).

DUT	$ S_{11} $	$ S_{12} $	$ S_{21} $	$ S_{22} $
A1	0.248	0.00245	41.3	0.181
A2	0.180	0.0005	43.5	0.113
A3	0.469	0.0041	14.6	0.127

Table 2. DUT noise parameters (to three significant places).

					$\psi_{opt}$	$r_{min}$
DUT	$G_0$	$T_{e,min}(K)$	$R_n(\Omega)$	$ \Gamma_{opt} $	(degr)	(dB)
A1	1740	59.7	6.55	0.199	35.3	0.813
A2	1890	115	5.68	0.194	151	1.112
A3	220	291	19.8	0.226	91.8	3.021

We must also specify the input terminations to be used. Most of the strategies considered below differ in the set of input terminations used. Figure 2 plots the location in the complex plane of the reflection coefficients of the terminations used in this study, with labels to allow convenient reference. There are eight highly reflective terminations (R1 – R8), seven less reflective terminations (R1' – R7'), six "interior" points (I1 – I6), and four nearly reflectionless loads clustered around the origin—one ambient (a), two hot (h1, h2), and one cold (c). Unless otherwise specified, all the R, R', and I terminations have ambient noise temperature. Most of our results will concern the efficacy of using various sets of input terminations (or input states) in the noise-parameter measurements.

#### III. SIMULATIONS AND RESULTS

#### A. Base Configuration(s)

In order to establish a baseline for comparing the results obtained with different strategies, we choose a base set of input states, which will be labelled "B." Since we are fitting for five parameters (four noise parameters plus  $G_0$ ), at least five different input states are required. At least one additional state is required if we are to have meaningful type A uncertainties. Because we are including  $G_0$  in the fitting parameters, we need at least two different input noise tempera-

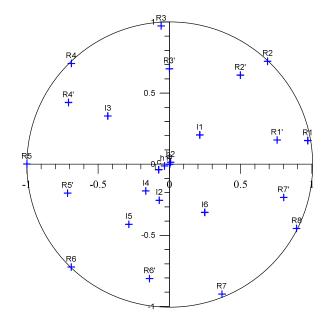


Fig. 2 Reflection coefficients of input states used in study.

tures. The base set that we choose consists of  $B = \{a, h1, R1, R3, R5, R7\}$ , *i.e.*, one ambient and one hot matched load plus four highly reflective terminations. In principle, it is possible that these specific reflection coefficients could conspire with the particular noise parameters that we have chosen and "accidentally" yield especially good or bad results that were not representative of the general situation. To guard against that possibility, we also consider a second base set  $B2 = \{a, h1, R2, R4, R6, R8\}$  and check that results obtained with B and with B2 are not dramatically different.

Simulation results obtained with input sets B and B2 for the three amplifiers A1, A2, and A3 are summarized in Table 3. We have shown results for the IEEE parameters and for magnitude and phase of  $\Gamma_{opt}$ , since they are probably the most familiar. It is clear that the results are consistent, and therefore fears that we have accidentally chosen special values or states for B are unfounded. In Table 3 all uncertainties are standard uncertainties  $(1 \sigma)$ , and BadFrac is the fraction of the simulated measurement sets that produced bad results, either a poor fit for the noise parameters or a violation of one or more physical or mathematical constraints, as mentioned in II.A. The rather large values for BadFrac, particularly for A1, may be somewhat unsettling. Note that A1 is a rather challenging device to measure, with high gain and low noise temperature, and the base sets contain fewer input terminations than would normally be used. It is also possible that the input uncertainties that we use are more conservative than is necessary or realistic. For purposes of this study, however, what is important is not actual value of BadFrac, but whether it is better or worse for different sets of input states or different measurement strategies.

#### B. Other Non-Ambient Matched Loads

We first consider the choice of the non-ambient matched load(s). The noise temperature of the hot load h1 in the base set is 1232 K, which is a typical temperature for a hot load in such measurements. We have run simulations using a

Table 3. Comparison of results for two different base sets.

<u>DUT</u>	Bad		$u(T_{min})$	$u(R_n)$		
Input	Frac	$u(G_0)$	(K)	$(\Omega)$	$u( \Gamma_{opt} )$	$u(\varphi_{opt})$
<u>A1</u>						
В	0.35	17.8	4.1	0.091	0.0093	0.61
B2	0.34	17.7	4.1	0.088	0.0091	0.61
<u>A2</u>						
В	0.16	19.6	4.7	0.080	0.0048	0.40
B2	0.18	19.6	4.7	0.080	0.0048	0.41
<u>A3</u>						
В	0.17	2.5	7.5	0.23	0.0044	0.12
B2	0.17	2.5	7.4	0.22	0.0039	0.13

cryogenic load (c, noise temperature  $T_c = 99$  K) either in place of or in addition to h1. We have also considered cooler (h2,  $T_{h2} = 750$  K) and hotter (h3,  $T_{h3} = 5000$  K) hot loads and various combinations of h1, h2, h3, and c. Some results of those simulations are given in Table 4. In the entries under "Input," B represents the base set, a minus sign indicates that the following state was removed from B, and a plus sign indicates that the following state was added to B. Thus, for example, B-h1+c represents an input state consisting of B without h1 but with c, *i.e.*, the set {a, c, R1, R3, R5, R7}.

Many effects can be gleaned from a detailed examination of Table 4. We will note only the most salient. Changes of the non-ambient input state(s) have a negligible effect on uncertainties in  $\Gamma_{opt}$ . Not surprisingly, the biggest effects are on the determination of  $G_0$  and  $T_{min}$ . For amplifiers whose value of  $T_{min}$  is significantly below  $T_{amb}$ , using the cold input termination c instead of the hot termination h1 results in a significant reduction in the uncertainty in  $T_{min}$ , accompanied by a small increase in  $u(G_0)$ . Using the cold input in addition to h1 results in major improvements in  $u(T_{min})$  (more than a factor of two for A1 and A2) and a small improvement in

Table 4. Simulation results for different non-ambient input noise sources.

<u>DUT</u>	Bad		$u(T_{min})$	$u(R_n)$		
Input	Frac	$u(G_0)$	(K)	$(\Omega)$	$u( \Gamma_{opt} )$	$u(\varphi_{opt})$
<u>A1</u>						
В	0.35	<mark>17.8</mark>	<mark>4.1</mark>	0.091	0.0093	0.61
B-h1+c	0.35	<mark>18.8</mark>	<mark>2.3</mark>	0.091	0.0093	0.61
B-h1+h2	0.35	<mark>22.5</mark>	<mark>5.2</mark>	0.105	0.0093	0.61
B-h1+h3	0.35	<mark>14.8</mark>	<mark>3.2</mark>	0.083	0.0093	0.61
B+c	0.30	13.6	<mark>1.8</mark>	0.080	0.0094	0.62
B+h2	0.39	<mark>16.0</mark>	<mark>4.0</mark>	0.088	0.0094	0.62
B+h2+c	0.34	12.3	1.7	0.078	0.0095	0.62
<u>A2</u>						
В	0.16	<mark>19.6</mark>	<mark>4.7</mark>	0.080	0.0048	0.40
B-h1+c	0.16	<mark>22.6</mark>	<mark>3.1</mark>	0.084	0.0048	0.40
B-h1+h2	0.16	<b>25.1</b>	<mark>6.0</mark>	0.093	0.0048	0.40
B-h1+h3	0.16	15.9	<mark>3.6</mark>	0.072	0.0048	0.40
B+c	0.15	15.4	<mark>2.2</mark>	0.071	0.0049	0.41
B+h2	0.25	<mark>17.7</mark>	<mark>4.6</mark>	0.077	0.0049	0.41
B+h2+c	0.20	13.9	<b>2.0</b>	0.069	0.0049	0.41
<u>A3</u>						
В	0.17	<mark>2.5</mark>	<mark>7.5</mark>	0.23	0.0044	0.12
B-h1+c	0.17	<mark>3.9</mark>	<mark>8.2</mark>	0.35	0.0044	0.12
B-h1+h2	0.17	<mark>3.3</mark>	10.2	0.31	0.0044	0.12
B-h1+h3	0.17	<mark>1.9</mark>	<mark>5.5</mark>	0.17	0.0044	0.12
B+c	0.14	<mark>2.1</mark>	<mark>4.6</mark>	0.19	0.0045	0.13
B+h2	0.22	<mark>2.3</mark>	<mark>7.5</mark>	0.22	0.0045	0.13
B+h2+c	0.17	1.9	<b>4.3</b>	0.17	0.0045	0.13

 $u(G_0)$ . In general, the higher the noise temperature of the hot source, the smaller are the uncertainties in  $G_0$  and  $T_{min}$ . Using a cold input source in addition to the hot source is a clear recommendation, particularly since it is not particularly difficult (if a cold noise source is available). Because of the input uncertainties used for the input noise sources, the cold input noise source c is assumed to be a calibrated synthetic noise source (see, e.g., [7] - [9]), rather than a cryogenic standard.

#### C. Additional Reflective Terminations

We next turn our attention to the question of whether it is useful to include additional reflective terminations. The results depend to some extent on the reflection coefficient(s) of the additional terminations and the properties of the amplifiers, so we have done the following. Starting with the base set B, we added one reflective termination R2 and performed the simulations on B+R2. We then added a different reflective termination R4 and obtained results for B+R4. This was done for each of the four resistive terminations not already included in B, that is, for R2, R4, R6, and R8. We averaged the results of those four sets of simulations to get representative results for adding one additional reflective termination. We then repeated the process adding two reflective terminations at a time, in all possible combinations, and averaging them, and then doing the same for three additional terminations. Finally, we added all four additional terminations, B+B2. Results are tabulated in Table 5, where we have used B+1R to represent the average of the results with one reflective termination added to B, etc.

The effect of adding additional reflective terminations is not very dramatic. It has no significant effect on the uncertainties in  $R_n$  or  $\Gamma_{opt}$ ; and for  $G_0$ ,  $T_{min}$ , and BadFrac, the effect is small or insignificant. Although the effect is small for these three quantities, it warrants some discussion because it is rather counter-intuitive. In some cases (highlighted entries in Table 5), adding one or more additional reflective terminations seems to make matters worse, albeit by a small amount. This effect is the result of two features of the computations. The principal cause is probably the fact that we are adding terminations with reflection coefficients that are very close to the edge of the unit circle compared to the uncertainty in measuring them, and the calculations are quite sensitive to these reflection coefficients, due to the occurrence of factors like  $(1-|\Gamma|^2)^{-1}$ . A simple check of this explanation is to reduce the relevant input uncertainties and see whether that reduces or removes the peculiar results. We performed that test, and it confirms the explanation. As a further check, we have performed the simulations using terminations that were somewhat less reflective, and again the peculiar results disappeared. We should also remember that the simulated measurement sets with "bad" results contribute to BadFrac, but they are excluded from the uncertainty computations.

Table 5. Simulation results with added reflective terminations.

Input Frac $u(G_0)$ (K) $(\Omega)$ $u( \Gamma_{opt} )$ $u$	$(\varphi_{opt})$
<u>A1</u>	
B 0.35 17.8 4.1 0.091 0.0093 (	0.61
B+1R 0.38 18.6 4.3 0.093 0.0093 0	0.61
B+2R 0.40 18.8 4.4 0.093 0.0092 0	0.61
B+3R 0.42 19.2 4.5 0.093 0.0091 0	0.60
B+4R <mark>0.44 19.4 4.6</mark> 0.093 0.0090 (	0.59
<u>A2</u>	
B 0.16 <mark>19.6 4.7</mark> 0.080 0.0048 (	0.40
B+1R 0.16 20.3 4.9 0.081 0.0048 (	0.40
B+2R 0.14 20.5 5.0 0.082 0.0048 0	0.40
B+3R 0.13 20.8 5.1 0.081 0.0047 (	0.40
B+4R 0.12 21.0 5.1 0.081 0.0047 (	0.40
<u>A3</u>	
B 0.17 2.5 <mark>7.5</mark> 0.23 0.0044 (	0.12
B+1R 0.14 2.6 7.8 .23 0.0043	0.12
B+2R 0.11 2.6 8.0 .23 0.0043	0.12
B+3R 0.090 2.6 8.1 .24 0.0042 0	0.12
B+4R 0.078 2.6 8.2 .24 0.0041 0	0.11

Therefore, we exclude some of the simulated measurements with the largest errors.

In view of the simulation results and the preceding discussion, we conclude that with our input uncertainties, the inclusion of additional reflective terminations in the input set leads to no significant improvement in the measurement uncertainties or the fraction of bad measurements.

#### D. Additional Interior Points

So far, the only input states that we have considered have been either highly reflective or nearly matched. Most practical measurements also include input reflection coefficients distributed in the interior of the unit circle. We have run simulations with input sets that included one or more interior (but not matched) reflection coefficients (I1 – I6 in Fig. 2). Results are tabulated in Table 6. In a similar manner as was done for the reflective terminations, we use B+1I to refer to the results obtained by adding one interior point to the base set, averaged over four different choices (I1, I3, I5, I6) for the additional interior terminations. B+2I refers to the inclusion of two interior points, etc. The results of Table 6 indicate that there is a significant benefit to including several interior points among the input terminations. Because of our imposition of the various checks, the benefit is manifest primarily as a decrease in the occurrence of bad measurements. We conclude that there is good reason for the common practice of having

Table 6. Simulation results with added interior terminations.

<u>DUT</u> Input	Bad Frac	$u(G_0)$	$u(T_{min})$ (K)	$u(R_n)$ $(\Omega)$	$u( \Gamma_{opt} )$	$u(\varphi_{opt})$
		(-0)			·· (1 0pt1)	· (
<u>A1</u>						
В	0.35	17.8	4.1	0.091	0.0093	0.61
B+1I	<mark>0.26</mark>	18.2	3.9	0.093	0.0094	0.62
B+2I	0.21	18.3	3.8	0.094	0.0094	0.62
B+3I	<mark>0.17</mark>	18.4	3.8	0.094	0.0096	0.62
B+4I	<mark>0.14</mark>	18.5	3.8	0.094	0.0095	0.63
<u>A2</u>						
В	<mark>0.16</mark>	19.6	4.7	0.080	0.0048	0.40
B+1I	0.12	20.1	4.5	0.081	0.0048	0.40
B+2I	0.090	20.1	4.4	0.081	0.0048	0.41
B+3I	0.070	20.2	4.3	0.081	0.0049	0.41
B+4I	0.058	20.4	4.3	0.081	0.0049	0.41
<u>A3</u>						
В	<mark>0.17</mark>	2.5	7.5	0.23	0.0044	0.12
B+1I	0.12	2.5	7.2	0.23	0.0044	0.13
B+2I	<mark>0.081</mark>	2.5	7.1	0.23	0.0045	0.13
B+3I	0.057	2.5	6.9	0.23	0.0045	0.13
B+4I	0.042	2.5	6.9	0.23	0.0045	0.13

input reflection coefficients distributed throughout the unit circle (or across the Smith chart).

#### E. Reverse Measurements

Various authors have suggested direct measurement of the noise emanating from the input port of an amplifier or transistor, as depicted in Fig. 3 [10], [11]. Our simulation program allows inclusion of such measurements, and we have investigated the effect of including one or more such "reverse" measurements among the measurement results to be fit. In terms of the wave-representation, a reverse measurement yields a good determination of  $X_1$ . (The expression for  $T_2$  for reverse measurements is, of course, different from that for forward measurements. Both can be found in [2].) Simulation results when a reverse measurement is included are shown in Table 7.The results of Table 7 show a marked improvement in the uncertainty for  $T_{min}$ , especially for the two lower-noise

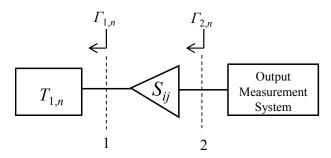


Fig. 3 Configuration for reverse measurements.

Table 7. Simulation results with a reverse measurement.

<u>DUT</u>	Bad		$u(T_{min})$	$u(R_n)$		
Input	Frac	$u(G_0)$	(K)	$(\Omega)$	$u( \Gamma_{opt} )$	$u(\varphi_{opt})$
<u>A1</u>						
В	0.35	17.8	<mark>4.1</mark>	0.091	0.0093	0.61
B+Rev	0.32	15.7	<mark>2.2</mark>	0.080	0.0094	0.62
<u>A2</u>						
В	0.16	19.6	<mark>4.7</mark>	0.080	0.0048	0.40
B+Rev	0.17	17.2	<mark>2.5</mark>	0.076	0.0048	0.40
<u>A3</u>						
В	0.17	2.5	7.5	0.23	0.0044	0.12
B+Rev	0.13	2.3	<mark>5.1</mark>	0.21	0.0044	0.13

amplifiers, where the improvement is almost a factor of two. There are also small improvements in the  $G_0$  and  $R_n$ uncertainties. At first, these results would seem to conflict with the results of [12], [13], which found that the reverse measurement did not improve uncertainties for amplifier noise-parameter measurements. The difference is due to the fact that the earlier results were obtained with the output reflection coefficient  $\Gamma_{2,i}$  computed from cascade, whereas the current results assume that they are measured directly, for reasons that will become apparent in the next subsection. When the output reflection coefficients are measured directly, the inclusion of a reverse measurement does improve the uncertainties for the amplifier noise measurements. Unfortunately, a reverse measurement requires a different measurement configuration than the usual measurements, and therefore it entails non-negligible additional time and effort.

#### F. Measurement of Output Reflection Coefficient

One of the options offered by the simulator is the choice of how the output reflection coefficients  $\Gamma_{2,i}$  are determined. They can either be measured directly, or they can be computed by cascading the input reflection coefficients  $\Gamma_{1,i}$  with the DUT S-parameters  $S_{i,j}$ . We ran simulations with the same sets of input states (B and B+II, where II represents the four interior points I1, I3, I5, I6) with the output reflection coefficients determined in the two different ways, and Table 8 compares the uncertainties obtained with them measured and computed from cascade. (The results with the output reflection coefficients computed are indicated by (C) following the designation of the input set.)

The results for BadFrac in Table 8 clearly show that measuring the output reflection coefficients is much better than computing them from the other measured quantities, particularly for low-noise devices. As with the inclusion of additional reflective terminations in subsection III.c above, we might think that this effect would disappear if the input

Table 8. Results with output reflection coefficients computed (C), compared to results with them measured.

Table 9. Results of including multiple enhancements simultaneously.

<u>DUT</u>	Bad		$u(T_{min})$	$u(R_n)$			<u>DUT</u>	Bad		$u(T_{min})$	$u(R_n)$		
Input	Frac	$u(G_0)$	(K)	$(\Omega)$	$u( \Gamma_{opt} )$	$u(\varphi_{opt})$	Input	Frac	$u(G_0)$	(K)	$(\Omega)$	$u( \Gamma_{opt} )$	$u(\varphi_{opt})$
<u>A1</u>							<u>A1</u>						
В	<mark>0.35</mark>	17.8	4.1	0.091	0.0093	0.61	B+II	0.14	18.5	<mark>3.8</mark>	0.094	0.0095	0.63
B(C)	<mark>0.83</mark>	18.2	4.3	0.14	0.017	0.90	B+II+c	0.15	12.5	<mark>1.8</mark>	0.074	0.0094	0.63
B+II	<mark>0.14</mark>	18.5	3.8	0.094	0.0095	0.63	B+II	0.17	<mark>15.8</mark>	<mark>2.2</mark>	0.078	0.0095	0.63
B+II(C)	<mark>0.90</mark>	19.0	3.9	0.084	0.0095	0.58	+Rev						
							B+II+c	0.17	13.1	<mark>1.6</mark>	0.073	0.0094	0.62
<u>A2</u> B							+Rev						
В	<mark>0.16</mark>	19.6	4.7	0.080	0.0048	0.40							
B(C)	<mark>0.316</mark>	19.9	4.7	0.35	0.016	0.68	<u>A2</u>						
B+II	<mark>0.057</mark>	20.4	4.3	0.081	0.0049	0.41	B+II	0.057	<mark>20.4</mark>	<mark>4.3</mark>	0.081	0.0049	0.41
B+II(C)	0.4 <mark>7</mark>	21.1	4.6	0.20	0.011	0.50	B+II+c	0.064	<mark>14.4</mark>	<mark>2.3</mark>	0.069	0.0049	0.41
							B+II	0.079	17.3	<mark>2.6</mark>	0.075	0.0049	0.41
<u>A3</u>							+Rev						
В	<mark>0.17</mark>	2.5	7.5	0.23	0.0044	0.12	B+II+c	0.083	<b>15.2</b>	<mark>2.0</mark>	0.070	0.0048	0.41
B(C)	<mark>0.29</mark>	2.5	7.7	0.25	0.0071	0.28	+Rev						
B+II	0.04 <mark>2</mark>	2.5	6.9	0.23	0.0045	0.13							
B+II(C)	<mark>0.10</mark>	2.6	7.0	0.26	0.0072	0.30	<u>A3</u>						
							B+II	0.042	<mark>2.5</mark>	<mark>6.9</mark>	.23	0.0045	0.13
uncertain	ties for	reflection	n coefficie	ents wer	e smaller. V	We have	B+II+c	0.034	<mark>2.1</mark>	<mark>4.8</mark>	.19	0.0045	0.13
run the	simulat	ions wi	th the i	nput re	flection-co	efficient	B+II	0.036	<mark>2.4</mark>	<mark>5.3</mark>	.22	0.0045	0.13
uncertain	ties red	uced by	a factor	of two,	and altho	ugh the	+Rev						

B+II+c

+Rev

0.029

uncertainties for reflection coefficients were smaller. We have run the simulations with the input reflection-coefficient uncertainties reduced by a factor of two, and although the effect is somewhat smaller, the qualitative behavior remains. Even for the smaller uncertainties, it is better to measure rather than compute the output reflection coefficients.

#### G. Combined Strategies

In the preceding subsections, we considered various possible enhancements of noise-parameter measurement methods, treating them one at a time and comparing the results to those obtained with a base set of input terminations. We now test whether additional improvements are realized by implementing more than one strategy at a time. Based on the results of the preceding subsections, the enhancements that we consider are additional interior points, addition of a cold (i.e., well below ambient) matched load, and inclusion of a reverse measurement. Since it is common practice to use additional interior points, we will compare to the results obtained with the B+II input set (hot and ambient matched loads, four reflective terminations, and four not very reflective terminations). All simulations are done with the output reflection coefficients determined by direct measurement rather than cascade computation. We consider the addition of a cold input source (B+II+c), a reverse measurement (B+II+Rev), and both a cold input source and a reverse measurement (B+II+c+Rev).

Results are tabulated in Table 9. We see that addition of either a cold input source or a reverse measurement leads to significant improvement in the uncertainties for  $G_0$  and  $T_{min}$ ,

and a smaller improvement for  $R_n$ . Including both a cold input source and a reverse measurement leads to a small further improvement for  $T_{min}$ , but not for  $G_0$  or  $R_n$ . Because it is generally easier to add a cold input source than to perform a reverse measurement, the conclusion is that it is certainly worthwhile to add a measurement with a cold input source, but that adding a reverse measurement may not be worth the extra effort.

.19

0.0045

0.13

#### IV. SUMMARY

We have developed a simulator for noise-parameter measurements and used it to compare uncertainties obtained with several different possible measurement enhancements. The results were obtained on three different amplifiers, with differing properties, and with various different input states, in an attempt to distill general features, not subject to the influence of accidental conspiracies among the detailed characteristics.

Some of the general results can be summarized as follows. The noise temperature of the input hot matched load should be as far from ambient as possible (while still keeping the DUT and output measurement system in their linear operating ranges). It is very helpful to use a cold (cryogenic) input matched load, particularly for low-noise devices. Substituting

a cold load for the hot input load yields some improvements for many amplifiers, but use of a cold load in addition to the hot load yields larger improvements in the uncertainties for all amplifiers considered. The common practice of including interior points (neither reflective nor matched) does indeed lead to better results. The output reflection coefficients should definitely be measured rather than computed by cascade. Additional (beyond four) reflective input terminations do not help and may in fact hurt. Inclusion of a reverse measurement helps, but it requires a different measurement configuration. The practical recommendation that emerges is to add a cold (cryogenic) matched load to the usual set of input terminations; for low-noise devices it will reduce the uncertainty in  $T_{min}$  by a factor of about two.

We next plan to perform a similar investigation for onwafer noise-parameter measurements on transistors.

#### REFERENCES

- J. Randa, "Simulator for amplifier and transistor noiseparameter measurement," 2010 Conference on Precision Electromagnetic Measurements Digest, pp. 555 – 556, June 2010.
- [2] J. Randa, "Uncertainty analysis for noise-parameter measurements at NIST," *IEEE Trans. Instrum. Meas.*, vol. 58, no. 4, pp. 1146 – 1151, April 2009.
- [3] G. Caruso and MM. Sannino, "Computer-aided determination of microwave two-port noise parameters," *IEEE Trans. Microw. Theor. Tech.*, vol. 26, no. 11, pp. 639 642, 1978.
- [4] A.C. Davidson, B.W. Leake, and E. Strid, "Accuracy improvements in microwave noise parameter measurements,"

- *IEEE Trans. Microw. Theor. Tech.*, vol. 37, no. 11, pp. 1973 1978, 1989.
- [5] S. Van den Bosch and L. Martens, "Improved impedancepattern generation for automatic noise-parameter determination," *IEEE Trans. Microw. Theor. Tech.*, vol. 46, no. 11, pp. 1673 – 1678, 1998.
- [6] J. Randa, "Amplifier and Transistor Noise-Parameter Measurements," in Wiley Encyclopedia of Electrical and Electronics Engineering, edited by John Webster, 2014.
- [7] R. Frater and D. Williams, "An active 'cold' noise source," IEEE Trans. Microw. Theor. Tech., vol. MTT-29, no. 4, pp. 344 – 347, April 1981.
- [8] L. Dunleavy, M. Smith, S. Lardizabal, A. Fejzuli, and R. Roeder, "Design and characterization of FET based cold/hot noise sources," *IEEEE MTT-S Digest*, pp. 1293 1296, May 1997
- [9] P. Buhles and S. Lardizabal, "Design and characterization of MMIC active cold loads," *IEEE MTT-S Digest*, pp. 29 – 32, June 2000.
- [10] D. Wait and G. Engen, "Application of radiometry to the accurate measurement of amplifier noise," *IEEE Trans. Instrum.* and Meas., vol. 40, no. 2, pp. 433 – 437, April 1991; correction: *ibid*, vol. 42, no. 1, p. 78, Feb. 1993.
- [11] S. Wedge and D. Rutledge, "Wave techniques for noise modeling and measurement," *IEEE Trans. Microwave Theory & Tech.*, vol. 40, no. 11, pp. 2004 – 2012, Nov. 1992.
- [12] J. Randa, "Noise-parameter uncertainties: a Monte Carlo simulation," J. Res. NIST, vol. 107, pp. 431 – 444, Sept. 2002; correction: ibid, vol. 111, p. 461, Nov. 2006.
- [13] J. Randa, T. McKay, S.L. Sweeney, D.K. Walker, L. Wagner, D.R. Greenberg, J. Tao, and G.A. Rezvani, "Reverse noise measurement and use in device characterization," 2006 IEEE Radio Frequency Integrated Circuits (RFIC) Symp. Dig., pp. 345 – 348, June 2006.

## On-wafer differential Noise Figure measurement without couplers on a Vector Network Analyzer

Yogadissen Andee\*†, Alexandre Siligaris\*†, François Graux‡ and François Danneville§

\*Univ. Grenoble Alpes, F-38000 Grenoble, France

†CEA, LETI, MINATEC Campus, F-38054 Grenoble, France

Email: yogadissen.andee@cea.fr

‡Rohde&Schwarz, 9-11, rue Jeanne Braconnier, 92366 Meudon-la-Forêt, France

§IEMN, UMR CNRS 8520, Av Poincaré, BP 60069, 59652 Villeneuve d'Ascq cedex, France

Abstract—This papers presents a measurement technique for the noise figure of on-wafer differential amplifiers using 4-port network analyzers. The approach is based on the determination of the correlation of output noise waves in terms of the 4-port S-parameters and of the output noise powers. The measurement setup is simple as it does not require any hybrid coupler or calibrated noise source. Measurement results of an on-wafer differential LNA demonstrate the validity of the new technique.

Index Terms—Noise figure, differential amplifier, on-wafer, mixed-mode, network analyzer.

#### I. Introduction

Differential circuits are more and more replacing traditional single-ended ones in many radio-frequency and other highfrequency applications. This is due to their better immunity to common-mode noise and interference. Futhermore, the maximum differential voltage swing is almost twice that in single-ended operation, which is interesting for integrated circuits that can only cope with low supply voltages. It is nowadays possible to easily characterize the small-signal behavior (differential signal gain, common-mode rejection ratio, etc) of these circuits using commercially available network analyzers. In contrast, the noise characterization of differential circuits remains a challenging subject. This is due to the fact that the noise waves at the outputs of these circuits are correlated. Correlated output noise complicates, for instance, the measurement of the noise figure of differential amplifiers. In [1], noise figure measurements are performed with couplers. These extra equipment offers the possibility to measure the differential noise figure without the need of calculating the correlation. However, the couplers are bandwidth limited and requires a proper de-embedding which is quite complex [2],[3],[4]. In [5], the correlation is removed by referring the inherent noise sources of the differential amplifier to its input ports. This technique is interesting but is quite time-consuming as a lot of single-ended measurements are made using the Yfactor method [6]. In [7], a theoretical approach based on the determination of the correlation of the output noise waves is proposed. Our paper makes use of this approach to develop a measurement procedure for the noise figure of on-wafer amplifiers. Our new technique relies on the measurements of the S-parameters and of the output noise powers using a 4-port network analyzer. It does not require any coupler or calibrated noise source. The theoretical approach to the differential noise

figure is briefly presented in section II. The measurement setup and procedure are developed in section III. The measurement results are discussed in section IV and concluding remarks are given in section V.

#### II. THEORY

An analytical expression of the differential noise figure of a 4-port device is given in [7]. This expression is derived from the noise-wave formalism [8], illustrated in Fig. 1, and the mixed-mode S-parameters described in [9]. The expression of the noise figure is valid for a system where the sources and the loads are reflectionless ( $\Gamma_i = 0$ ).

The differential noise figure given in [7] is:

$$F_{diff} = \frac{\overline{|b_3|^2} + \overline{|b_4|^2} - 2\Re e(\overline{b_3 \cdot b_4^*})}{2kT_0\Delta f(|S_{dd21}|^2 + |S_{dc21}|^2)}$$
(1)

where  $S_{dd21}$  and  $S_{dc21}$  are the mixed-mode gains which can be calculated from the classical S-parameters [9]. The term  $kT_0\Delta f\left(|S_{dd21}|^2+|S_{dc21}|^2\right)$  is the output noise power of the differential mode due to the two input sources. These two sources have both an available noise power of  $kT_0\Delta f$  and are uncorrelated.  $\overline{|b_3|^2}$  and  $\overline{|b_4|^2}$  are the noise powers at the output ports 3 and 4 respectively. The term  $\overline{b_3} \cdot \overline{b_4}^*$  represents the correlation between the output noise waves. It is the only term in the expression that cannot be measured using commercially-available equipment.

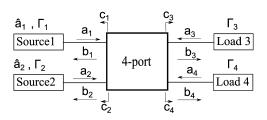


Fig. 1. Noise wave formalism for a 4-port circuit, where  $a_i$  is incident noise wave at port i,  $b_i$  is the outgoing noise wave and  $c_i$  is the internal noise wave. The input ports are connected to 2 sources with generator wave  $\hat{a}_i$  and reflection coefficient of  $\Gamma_i$ .

The correlation of the noise waves at the output ports of a differential amplifier can be determined in terms of the input-referred noise powers and of the S-parameters:

$$\overline{b_3 \cdot b_4^*} = S_{31} S_{41}^* \overline{|a_{s1}|^2} + S_{32} S_{42}^* \overline{|a_{s2}|^2}$$
 (2)

where the input-referred noise powers can be calculated in terms of the output noise powers as:

$$\overline{|a_{s1}|^2} = \frac{|S_{42}|^2 \overline{|b_3|^2} - |S_{32}|^2 \overline{|b_4|^2}}{|S_{31}|^2 ||S_{42}|^2| - |S_{41}|^2 ||S_{32}|^2|} 
\overline{|a_{s2}|^2} = \frac{|S_{31}|^2 \overline{|b_4|^2} - |S_{41}|^2 \overline{|b_3|^2}}{|S_{31}|^2 ||S_{42}|^2| - |S_{41}|^2 ||S_{32}|^2|}$$
(3)

These expressions are derived by representing the differential amplifier as a 4-port noise-free circuit connected at its inputs to 2 uncorrelated input-referred noise sources [5]. The differential noise figure is then determined from (1), (2) and (3). These equations have been validated in [7] by ADS simulation of a differential amplifier. The aim of this work is to use the equations to construct a measurement procedure for the noise figure measurement of on-wafer differential amplifiers.

#### III. MEASUREMENT PROCEDURE

An RF differential low-noise amplifier (LNA) from CEA-LETI [10] serves as the device under test (DUT) in this work. Fig. 2 shows the micrograph of the LNA chip fabricated in a 0.25um SiGe BiCMOS process.

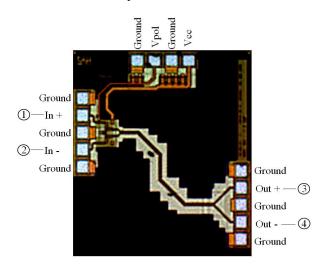


Fig. 2. Micrograph of the differential LNA with a die size of  $1.32 \times 1mm^2$ . The input ports are denoted by 1&2 and the output ports are represented by 3&4.

#### A. S-parameters measurement

The measurements are made with a commercially-available wafer probe station. A DC probe is used for the transistors biasing with a collector voltage Vcc of 3V and an emitter voltage Vpol of -1V. Two Cascade Infinity GSGSG probes are placed at the inputs and outputs of the LNA, as shown on Fig. 3.

The first step consists of measuring the 4-port S-parameters of the LNA. A Rohde&Schwarz 4-port Vector Network Analyzer (VNA) is used. Measurements are done in the frequency band of 1 to 6 GHz. 4-port SOLT (Short-Open-Load-Through) calibrations are performed on a standard impedance substrate in order to place the reference planes at the probe tips. The 4x4 matrix of S-parameters is then acquired and used

to calculate the mixed-mode parameters according to the following equations [9].

$$S_{dd21} = \frac{1}{2}(S_{31} + S_{42} - S_{32} - S_{41})$$

$$S_{dc21} = \frac{1}{2}(S_{31} - S_{42} + S_{32} - S_{41})$$
(4)

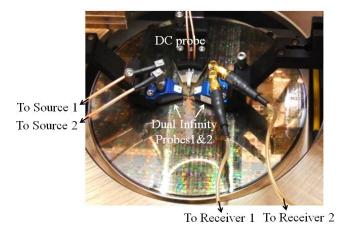


Fig. 3. On-wafer measurement setup with the input and output ports of the LNA connected to the 4-port Vector Network Analyzer via the Dual Infinity probes.

#### B. Noise measurement

The next step consists of measuring the noise powers at the output ports of the differential LNA. A block diagram of the setup is shown in Fig. 4. The input ports of the LNA are connected via the input probe to two  $50\Omega$  sources of the VNA. The sources have both an available noise power per hertz of  $kT_0$ . The output ports of the LNA are connected via the output probe to two  $50\Omega$  receivers of the VNA. Low noise pre-amplifiers are placed between the LNA and the VNA in order to reduce the noise figure of the receivers. The VNA receivers have a high noise figure of about 40 dB and tend therefore to mask the noise generated by the LNA. By placing the 25dB pre-amplifiers before the VNA, the noise figures of the receiver systems are reduced by about 25dB.

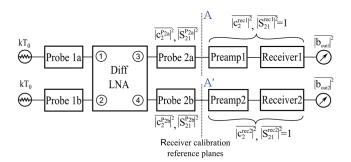


Fig. 4. Block diagram of the test setup for the noise measurement of the on-wafer differential amplifier

The probes, pre-amplifiers and receivers contribute to the output noise measured by the VNA. These contributions have

to be compensated for the determination of the output noises  $\overline{|b_3|^2}$  and  $\overline{|b_4|^2}$ . In Fig. 4, the 2 paths of the output dual probe are represented as Probe 2a and Probe 2b. The losses in the 2 paths are denoted by  $|S_{21}^{P_{2a}}|^2$  and  $|S_{21}^{P_{2b}}|^2$ . The noise powers generated in both paths due to these losses are represented by  $|\overline{c_2^{P_{2a}}}|^2$  and  $|\overline{c_2^{P_{2b}}}|^2$ . As the probe is a passive component with well-matched inputs and outputs, these inherent noise powers are given by:

$$\frac{\overline{|c_2^{P_{2a}}|^2}}{|c_2^{P_{2b}}|^2} = (1 - |S_{21}^{P_{2a}}|^2)kT_0\Delta f 
\overline{|c_2^{P_{2b}}|^2} = (1 - |S_{21}^{P_{2b}}|^2)kT_0\Delta f$$
(5)

The noise generated by the pre-amplifiers and the receivers are determined after receiver power calibrations are performed. The calibrations are done in the reference planes A and A' (Fig. 4) using an R&S thermal power sensor. By doing the calibration in these references planes, the pre-amplifiers are considered to be part of the receiver systems. The transfer characteristics  $|S_{21}^{rec1}|^2$  and  $|S_{21}^{rec2}|^2$  are equal to 1 due to the receiver power calibration. The inherent noise produced by the receiver systems are denoted by  $|c_2^{rec1}|^2$  and  $|c_2^{rec2}|^2$ . They are measured directly by connecting  $50\Omega$  match at the input ports of the receiver systems.

The noise powers  $\overline{|b_{out1}|^2}$  and  $\overline{|b_{out2}|^2}$  measured at the output of the whole system can be expressed in terms of the elements described above:

$$\frac{\overline{|b_{out1}|^2}}{\overline{|b_{out2}|^2}} = |S_{21}^{P_{2a}}|^2 \overline{|b_3|^2} + \overline{|c_2^{P_{2a}}|^2} + \overline{|c_2^{rec1}|^2} 
\overline{|b_{out2}|^2} = |S_{21}^{P_{2b}}|^2 \overline{|b_4|^2} + \overline{|c_2^{P_{2b}}|^2} + \overline{|c_2^{rec2}|^2}$$
(6)

#### IV. MEASUREMENT RESULTS

The noise powers  $\overline{|b_{out1}|^2}$  and  $\overline{|b_{out2}|^2}$  are measured by the VNA with a measurement bandwidth of 5 MHz. The noise powers  $\overline{|b_3|^2}$  and  $\overline{|b_4|^2}$  at the output ports of the different LNA are then determined from (5) and (6). Fig. 5 shows the two output noise powers and the input-referred noise powers  $\overline{|a_{s1}|^2}$  and  $\overline{|a_{s2}|^2}$  obtained from the measurement data and (3).

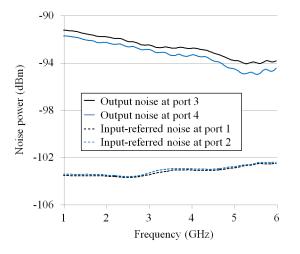


Fig. 5. Noise powers obtained at the output ports of the differential LNA and the corresponding input-referred noise powers

The correlation of the output noise waves is then obtained from the input-referred noises and is injected in (1) for the determination of the differential noise figure. This noise figure is illustrated in Fig. 6 and is compared to the differential noise figure obtained using the classical coupler technique [1].

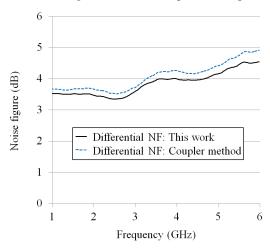


Fig. 6. Comparison between the differential noise figure measured with our technique and the one obtained with the coupler method [1]

Indeed, for completeness, noise figure measurements of the differential LNA have been done using 180° hybrid couplers. The differential LNA is placed between two hybrid couplers so as to be in a single-ended (SE) configuration where the SE noise figure is determined using the Y-factor method [6]. Measurements are performed with a Noisecom Noise Source and R&S Signal Analyzer. The differential noise figure is deembedded using an extension of Friis equation to the cascade of 3-port and 4-port circuits.

Fig. 6 demonstrates that there is a close agreement between the two noise figures. A differential noise figure of 3.5-4.5 dB is obtained with our method while a differential noise figure of 3.7-4.9 dB is given by the coupler method. The agreement between the noise figures confirms the validity of our new approach. The small differences between the traces are likely due to several factors such as the measurement uncertainties in the noise power measurements, the errors caused by the amplitude/phase unbalances in the couplers and additional common-mode noise that is not totally rejected by the LNA.

#### V. CONCLUSION

A noise figure measurement technique is proposed for on-wafer differential amplifiers. The differential noise figure is expressed in terms of the correlation between the output noise waves. The correlation is calculated from the input-referred noise powers which are measured using a procedure developed in this paper. The technique has been tested on a 1-6 GHz on-wafer differential LNA. Measurement results have proven the accuracy and repeatability of our new approach. The target application is the implementation on 4-port Network Analyzers of a fast and user-friendly method for differential noise figure measurements without the use of a noise source or couplers.

#### REFERENCES

- A. Abidi and J. Leete, "De-embedding the noise figure of differential amplifiers," *IEEE J. Solid-State Circuits*, vol. 34, no. 6, pp. 882-885, Jun. 1999.
- [2] O. Garcia-Perez, L. E. Garcia-Munoz, V. Gonzalez-Posadas and D. Segovia-Vargas, "Noise-Figure Measurement of Differential Amplifiers Using Nonideal Baluns," *IEEE Trans. Microw. Theory Tech.*, vol. 59, no. 6, pp. 1658-1664, Jun. 2011.
  [3] L. F. Tiemeijer, R. M. T. Pijper and E. van der Heijden, "Complete
- [3] L. F. Tiemeijer, R. M. T. Pijper and E. van der Heijden, "Complete On-Wafer Noise-Figure Characterization of 60-GHz Differential Amplifiers," *IEEE Trans. Microw. Theory Tech.*, vol. 58, no. 6, pp. 1599-1608, Jun. 2010.
- [4] M. Robens, R. Wunderlich, and S. Heinen, "Differential Noise Figure De-Embedding: A Comparison of Available Approaches," *IEEE Trans. Microw. Theory Tech.*, vol. 59, no. 5, pp. 1397-1407, May 2011.
- [5] L. Belostotski and J. W. Haslett, "A technique for differential noise figure measurement of differential LNAs," *IEEE Trans. Instrum. Meas.*, vol. 57, no. 7, pp. 1298-1303, Jul. 2008.
- [6] Agilent Technologies: "Noise Figure Measurement Accuracy: The Y-Factor Method", Application Note 57-2, 2004
- [7] Y. Andee, J. Prouvée, F. Graux and F. Danneville, "Determination of noise figure of differential circuits using correlation of output noise waves," *Electronic Letters*, vol. 50, no. 9, pp. 665-667, Apr. 2014.
- [8] J. Randa, "Noise characterization of multiport amplifiers," *IEEE Trans. Microw. Theory Tech.*, vol. 49, no. 10, pp. 17571763, Oct. 2001.
- [9] D. E. Bockelman and W. R. Eisenstadt, "Combined differential and common-mode scattering parameter": Theory and simulation," *IEEE Trans. Microw. Theory Tech.*, vol. 43, no. 7, 1995, pp. 1530-1539, Jul. 1995.
- [10] M.-A. Dubois, Ch. Billard, C. Muller, G. Parat, and P. Vincent, "Integration of High-Q BAW Resonators and Filters Above IC," ISSCC Dig. of Tech. Papers, pp. 392-393, 2005.

## Novel Flexible Dielectric Waveguide for Millimeter and Sub-Millimeter Frequencies – Design and Characterization

Hans-Ulrich Nickel and Janno Zovo

Spinner GmbH, Aiblinger Str. 30, 83620 Feldkirchen-Westerham, Germany {uli.nickel; janno.zovo}@spinner-group.com

Abstract — This paper is about a novel design of flexible dielectric waveguides that can be employed as multi-purpose connecting lines in test and measurement setups for mm- and sub-mm-wave frequencies. The waveguide design presented here differs from prior art basically in two features: the application of a protective tube composed of standardized segments and the use of strings for supporting and centering the dielectric ribbon waveguide within that tube. Following the proposed design allows building a waveguide that can be bent and twisted simultaneously while exhibiting only small changes in its electrical behavior. Besides the novel design we present experimental results that demonstrate its suitability for various mm-wave test applications.

Index Terms — Dielectric waveguide, measuring line, mm waves, sub-mm waves, flexible, bending, twisting, dielectric ribbon, string support.

#### I. INTRODUCTION

Measuring lines used to connect RF test instruments like network analyzers, signal generators, power meters or spectrum analyzers to a device under test (DUT) are faced with two generally contradictory demands: Mechanical flexibility and electrical stability. While the mechanical flexibility of a measuring line is often indispensable in order to connect a DUT after calibrating a test instrument, the stability of a measuring line's electrical behavior over flexing is the key issue for de-embedding its influence.

Depending on the radio frequency range under consideration different technologies for flexible measuring lines are available. Frequencies of up to about 100 GHz allow the use of coaxial cables or flexible metallic waveguides. Optical frequencies are generally covered by flexible fiberoptic cables. For the upper millimeter and the lower submillimeter wave frequencies between roughly 100 GHz and 1 THz however, there does not exist a flexible low-loss transmission line which provides a satisfactory electrical stability.

The aim of the reported work is to develop a family of practicable flexible measuring lines covering in total a frequency range from 75 to 600 GHz. The lines are to be equipped with built-in transitions to standard hollow rectangular waveguides (WR-10 to WR-1.9). Nine frequency sub-ranges were chosen in accordance with the nominal frequency bands of these waveguides. A main development goal is a basic design applicable to all sub-ranges by using

only repeated or proportionally scaled parts. In an initial stage of the project only the lowest frequency sub-range from 75 to 110 GHz (WR-10) was to be fabricated and characterized in detail.

In particular the lines need to meet the following mechanical demands:

- 1) Flexible in two degrees of freedom, i.e. bendable and twistable.
- Flexibility degrees of freedom limited by mechanical means.
- 3) "Flex-stable", in the sense that once set up, the line's form does not collapse due to influence of gravity.
- 4) Protection from damage, dust and liquids.
- 5) Configurable in length.

A set of electrical requirements must be met. Each of them has to be valid for the rectangular waveguide's entire nominal frequency range:

- 6) Excellent flexing stability of transmission and reflection behavior.
- 7) Transmission loss lower than that of any coaxial cable and any single-mode metallic waveguide.
- 8) Sufficiently high return loss.
- 9) Sufficiently low dispersion.
- 10) Electric shielding.

Furthermore, from a production point of view the line must be easy to assemble.

#### II. DESIGN

The novel flexible measuring line consists of a dielectric waveguide section that is connected to metallic waveguide transitions on both sides. In detail the design is as follows:

#### A. Dielectric Waveguide

In order to reach the flexibility and loss requirements we chose the "dielectric wire" transmission principle described on a theoretical basis more than 100 years ago by Hondros and Debye [1]. For the dielectric wire a number of cross sections and materials were considered but finally we decided to use a simple polymer ribbon of rectangular cross section made out of a high-density-polyethylene (HDPE or PE-HD). This configuration has already been investigated by various authors, e.g. [2] and [3].

Fig. 1 shows a longitudinal section of the dielectric waveguide. The polymer ribbon (40) is surrounded by a protective tube (14) which is of innovative design. The tube is composed of a number of identical segments (20) made out of a moderately absorbing polymer. At its ends each segment has a male and a female portion of a ball joint which allows it to be clinched to its neighbors. In this way the protective tube becomes bendable and twistable. Both degrees of freedom are limited by integrated stop dogs.

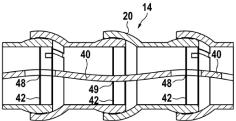


Fig. 1. Longitudinal section of dielectric waveguide.

Another feature of the segments is that they carry an integrated support structure for the polymer ribbon based on thin strings. The string diameter must be kept small compared to the wavelength so that the disturbance in wave propagation remains insignificant. These string supports are indicated as (41) and (42) in Figs. 1 and 2. Each string support is positioned at the center of a ball joint. Most strings are chosen to have a cross hair shape as shown in Fig. 2. Here the polymer ribbon is supported from its lower left side or its upper right side. Along the axis of the waveguide the support directions are chosen to alternate from segment to segment leading to a pre-undulation of the ribbon.

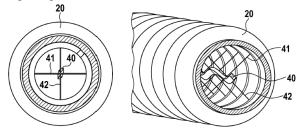


Fig. 2. Cross section of dielectric waveguide.

The presented method of supporting the ribbon has several distinct advantages:

- Extremely low reflectivity due to small dimensions of strings.
- Ribbon is kept on the "neutral fiber" of the protective tube, hence minimizing length changes during flexing.
- Pre-undulation serves as a length buffer for the ribbon, thus preventing axial forces to the waveguide transitions during flexing.

By applying the presented segments the dielectric waveguide becomes easy to assemble in a stepwise manner.

#### B. Waveguide Transitions

To convert the  $TE_{10}$  mode of the rectangular input port into the desired fundamental mode of the dielectric waveguide a

suitably broadband transition has been designed. This transition starts with the rectangular waveguide and ends in a nonlinear tapered horn section. The end of the polymer ribbon is scarfed in a symmetrical way in order to get a continuous transition of the wave onto the ribbon. The pointed end is fixed within the rectangular waveguide section.

#### C. Assembled Waveguide Samples

For an experimental verification of our design we initially restricted ourselves to the lowest frequency sub-range of 75 to 110 GHz, which is the nominal frequency band of the WR-10 waveguide. For this band laboratory samples with different line lengths have been realized.

The following design parameters have been chosen for the tubular segments of the protective tube:

- Insertion length: 25 mm
- Minimum bending radius: 75 mm
- Maximum twisting angle per ball joint: ±5°

The support strings are made out of polyamide with a diameter of approximately 0.1 mm.



Fig. 3. Flexible dielectric waveguide assembly with WR-10 interfaces (300 mm total length, 7 standard segments).



Fig. 4. Flexible dielectric waveguide assembly with WR-10 interfaces connected to a VNA frequency extender unit (575 mm total length, 18 standard segments).

Fig. 3 shows a short sample with 7 standard segments which has a total line length of 300 mm. The line shown in Fig. 4 is composed of 18 standard elements which result in a total

length of 575 mm. Fig. 4 explicitly illustrates the "flex-stable" nature of the line.

#### III. CHARACTERIZATION

A vector network analyzer setup composed of Anritsu ME7808C/37297D with two frequency extenders Anritsu 3742A-EW covering 65 to 110 GHz was used for the experimental characterization (Fig. 5).

The measurement results presented in Figs. 6, 7, 8, and 10 use 801 frequency points and a smoothing aperture of 3 points (112.5 MHz or 0.25%).



Fig. 5. 575 mm dielectric waveguide assembly with WR-10 interfaces connected between two VNA frequency extender units.

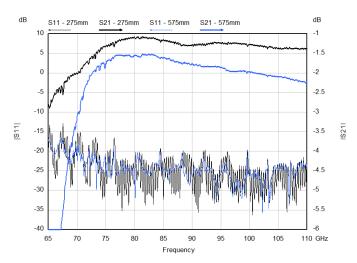


Fig. 6. Transmission and reflection of straightened waveguide assemblies (275 mm and 575 mm).

Fig. 6 compares the magnitudes of the transmission and reflection behavior of a short (275 mm) and a long (575 mm) line sample in straightened form. Within the specified WR-10 frequency range of 75 to 110 GHz the transmission loss does not exceed a value of 1.5 dB for the short and 2.3 dB for the

long sample. The return loss is typically around 20 dB or better.

Fig. 7 compares the magnitudes of the transmission and reflection behavior of the 275 mm line when bending over its H-plane. The curves for six deflection angles -90°, -60°, -30°, 0°, 30°, and 60° are plotted. Increasing the deflection angle from the axis of the straightened waveguide leads to a decreasing bending radius. The insert in Fig. 7 gives the geometrical arrangement for a deflection angle of -90° (positive deflection angles indicate bending in the opposite direction). In case of the 275 mm line a 90° deflection angle corresponds to the minimum bending radius of 75 mm. Within the frequency range of 80 to 110 GHz the variations of the transmission loss are less than 0.1 dB. For the lower portion of the specified frequency band ranging from 75 to 80 GHz we observed slightly higher loss variations of up to 0.2 dB. Variations of the return loss due to H-plane bending can hardly be observed. We always reach return loss values around 20 dB or better.

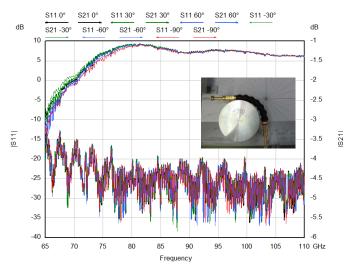


Fig. 7. Transmission and reflection stability over H-plane bending (275 mm line).

It should be noted that the curves in Figs. 6 and 7 exhibit a set of weakly developed resonances with a period of about 4 GHz. They can be explained by Bragg reflections at the periodically spaced string supports according to

$$\Delta f = \frac{c_0}{2l\sqrt{\varepsilon_r}} \approx \frac{3 \times 10^8 \text{ m s}^{-1}}{2 \times 25 \text{ mm} \times \sqrt{2.3}} \text{ GHz} \approx 4 \text{ GHz}.$$
 (1)

Due to their weak occurrence these resonances will not be markedly disturbing in practical applications.

Fig. 8 compares the group delay of the 275 mm line when bending over its H-plane. Again six curves are plotted representing the same bend configurations as above. Fig. 8 illustrates that the variation of the group delay due to bending does not exceed 0.04 ns for any frequency within the entire 75 to 110 GHz band.

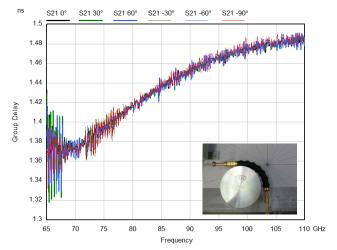


Fig. 8. Group delay stability over H-plane bending (275 mm line).

In order to put the absolute group delay into perspective, Fig. 9 compares the measured performance of the dielectric waveguide with the theoretical group delays of an air-filled TEM line and an air-filled WR-10 waveguide. The theoretical curves are calculated for the length of the measured dielectric waveguide (i.e. 275 mm).

Figure 9 demonstrates the nearly TEM-like dispersion behavior of the dielectric waveguide. While the group delay of the rectangular waveguide increases dramatically near its cut-off frequency, the group delay of the dielectric waveguide experiences only a minor decrease at these frequencies.

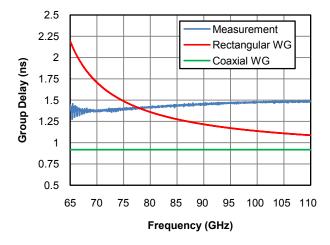


Fig. 9. Group delay comparison of the dielectric waveguide to conventional air-filled metallic waveguides.

First investigations of bending the dielectric waveguide over its E-plane and of twisting were found to result in similar variations of the electrical performance as with bending it over its H-plane. This is demonstrated with the 575 mm line in Fig. 10 comparing transmission and reflection behavior of the straight configuration with that of the curved configuration shown in Fig. 5. This configuration includes three E-plane bends at the line's minimum bending radius of 75 mm

(deflection angles: 45°, -90° and 45°). The E-plane bends are combined with various twists distributed randomly along the waveguide in a way that the total twisting cancels out.

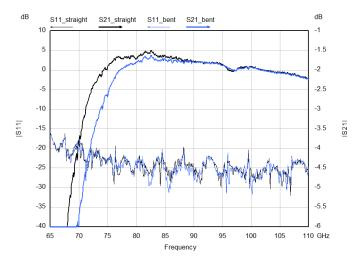


Fig. 10. Transmission and reflection of the 575 mm line in straight configuration compared to that of the curved configuration in Fig. 5.

Within the frequency range of about 80 to 110 GHz the transmission curves in Fig. 10 differ only very slightly. At the lower end of the specified frequency band however, between 75 and about 80 GHz, the transmission loss increases by up to 0.8 dB. This is caused by the weak guiding of the transmitted waves at these frequencies.

#### IV. CONCLUSION

A novel concept for flexible dielectric waveguides covering mm- and sub-mm-wave frequencies has been developed. As a proof of concept a waveguide for 75 to 110 GHz (WR-10) has been designed, analyzed, and manufactured. By experimental characterization we were able to demonstrate its low transmission loss and its high degree of electrical stability over bending and twisting. Both features make the waveguide ideally suited as a universal measuring line in this frequency range.

Applying the proposed waveguide design to higher frequencies we expect similar promising results. This is to be confirmed in future work.

#### REFERENCES

- D. Hondros, and P. Debye, "Elektromagnetische Wellen an dielektrischen Drähten," *Annalen der Physik*, vol. 32, no. 4, pp. 465-476, 1910.
- [2] W. Schlosser, and H.-G. Unger, "Partially filled waveguides and surface waveguides of rectangular cross section," in L. Young (Ed.), Advances in Microwaves, New York: Academic Press, pp. 319-387, 1966.
- [3] H. Brand, and J. Weinzierl, "Design, characteristics and applications of dielectric waveguides at millimeter wave frequencies," *Frequenz*, vol. 55, no. 1-2, pp. 3-8, 2001.

# Evaluating the Effect of Using Precision Alignment Dowels on Connection Repeatability of Waveguide Devices at Frequencies from 750 GHz to 1.1 THz

N M Ridler<sup>1</sup> and R G Clarke<sup>2</sup>
<sup>1</sup>National Physical Laboratory, UK; <sup>2</sup>University of Leeds, UK

Abstract—This paper describes an investigation into the effects of using additional precision alignment dowel pins on the connection repeatability performance of waveguide interfaces submillimeter-wave frequencies. The waveguide interface type that was used for this investigation is an adapted version of the 'precision' UG-387 (i.e. based on the MIL-DTL-3922/67 design), manufactured by Virginia Diodes, Inc. The investigation was undertaken in the WM-250 waveguide band (i.e. at frequencies ranging from 750 GHz to 1.1 THz). Connection performance is compared with and without the use of added precision dowel pins in the inner dowel holes of this flange type. The repeatability of the measurements is assessed using statistical techniques, in terms of the experimental standard deviation in both the real and imaginary components of the complex-valued linear reflection coefficient.

Index Terms—Measurement repeatability, Submillimeter-wave measurements, VNA measurements, Waveguide flanges, Waveguide interfaces, Waveguide measurements

#### 1. INTRODUCTION

Two recent papers [1, 2] have presented investigations into the connection repeatability of some waveguide devices operating from 750 GHz to 1.1 THz (i.e. in the WM-250 waveguide size [3]). In both these earlier investigations, the waveguide flanges were aligned during connection using four alignment dowel holes and dowel pins situated on the front faces of the flanges. These alignment dowel pins are permanently fitted to the flanges. During the connection of two waveguide flanges, two dowel pins on one of the flanges fit into two dowel holes on the other waveguide flange, and vice versa.

This connection strategy follows the so-called UG-387 flange design (described in [4] and earlier editions, e.g. [5, 6], etc), which has been in existence for many years. However, the performance of this

flange design has long been known to be poor at high submillimeter-wave millimeter-wave and frequencies, where the relatively loose tolerances on the specified diameters of the dowel pins and dowel holes cause performance degradation in the electrical measurements (i.e. significant mismatch and lack of connection repeatability). This has led to various improvements being made to this original design by different manufacturers. These improvements can broadly be described as being of two types: (i) the use of tighter tolerances on the above-mentioned outer alignment dowel holes and dowel pins; and/or (ii) the inclusion of two additional inner alignment dowel holes situated immediately above and below the waveguide aperture. These inner alignment dowel holes allow additional dowel pins to be inserted into both flange faces during connection.

Fig. 1 shows a photograph of a flange that features both the outer dowel pins and dowel holes (used for the traditional UG-387 connection strategy) and the additional inner alignment dowel holes (to which additional dowel pins are inserted during connection). The other holes shown in this Figure (situated at north, south, east and west positions around the flange face) are threaded holes to enable screws to be used to tighten the connection between two flange faces.

The flanges used in the earlier investigations [1, 2] feature both above-mentioned alignment improvements. However, only the outer dowel pins and dowel holes were used for aligning the flanges during these earlier investigations.

The purpose of the work described in this paper is to investigate the effect on flange connection repeatability of using dowel pins in the two inner alignment dowel holes. This work used the same VNA test port and devices under test (DUTs) that were used for the previous investigations [1, 2]. This enabled comparisons of connection repeatability performance to be made directly with these earlier investigations.

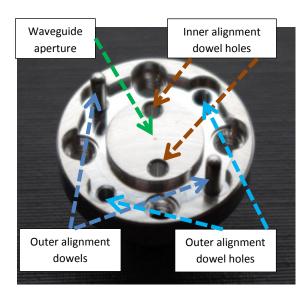


Fig. 1. Waveguide flange showing the outer alignment dowel pins and dowel holes, and, the inner alignment dowel holes. The WM-250 rectangular waveguide aperture is 250  $\mu$ m  $\times$  125  $\mu$ m - barely visible to the naked eye

The investigation described in this paper used the inner alignment dowel holes in conjunction with two different types of dowel pin:

- Typical dowel pins for use with these dowel holes, found in some manufacturers' calibrations kits;
- (ii) Dowel pins that emulate a connection strategy that is being developed in a new IEEE standard [7]. This connection strategy uses dowel pins with different nominal diamaters.

This paper compares the connection repeatability performance achieved using both the above types of dowel pins, and also compares the achieved performance with the connection repeatability performance reported previously in [2]. Flange connection performance is assessed by calculating the experimental standard deviation of a series of repeated flange connections. Results are presented as graphs showing experimental standard deviation versus frequency.

#### 2. METHOD

#### 2.1 Experimental set-up

The VNA system used for the investigation comprised an Agilent Technologies PNA-X VNA connected to WM-250 (WR-01) waveguide extender heads, manufactured by Virginia Diodes, Inc (VDI).

This is the same system and set-up that was used for the previous repeatability investigations [1, 2]. Following the procedure adopted in [2], the extender head was arranged so that the waveguide test port pointed vertically upwards. This arrangement minimizes any effect due to gravity on the alignment of the waveguide flanges. As with the previous investigations [1, 2], the power used to measure each Device Under Test (DUT) was around -35 dBm (0.3 µW) and the VNA's IF bandwidth was set to 30 Hz with no numerical averaging. The VNA system and set-up, shown in Fig. 2, is situated in the Roger Pollard High Frequency Measurements Laboratory (this being a temperature-controlled laboratory) at the School of Electronic and Electrical Engineering, University of Leeds, UK.

The VNA system was calibrated using a one-port 'three-known-loads' calibration technique. The 'known loads' (i.e. calibration standards) were an offset short-circuit, a 'flush' short-circuit and 'near-matched' load (from a VNA calibration kit supplied by VDI). The offset short-circuit and near-matched load were used subsequently as the DUTs for the repeatability investigation. It was not possible to use the flush short-circuit as a DUT for this investigation because the flange did not include the two inner alignment dowel holes. The offset short-circuit and near-matched load were the same DUTs that were used in [1, 2].

The connection repeatability procedure followed that given in [2], where the repeatability exercise includes connections of the DUTs where the orientation of the flange is inverted before being reconnected to the VNA test port. By inverting the waveguide flange, the imperfect position of the alignment dowel pins and dowel holes will, in principle, cause a systematic change in the VNA's electrical measurements. This systematic change will be present in the repeatability data sets along with the random changes cause by the tolerances on the diameters of the alignment dowel pins and dowel holes.

For each flange connection orientation (i.e. either inverted or non-inverted), the complex-valued linear reflection coefficient of each DUT was measured 12 times, disconnecting and re-connecting the DUT between each re-measurement. This produced a set of 12 separate determinations of reflection coefficient for each DUT in each of the two orientations. Therefore, a total of 24 dis-connect / reconnect measurements were made for each of the two DUTs. All measurements were made from 750 GHz to 1.1 THz at regular intervals of 1.75 GHz across the band.



Fig. 2. The 750 GHz to 1.1 THz VNA system used for the measurements

#### 2.2 Flange connection methods

(a) Same-diameter inner dowel pins: This flange connection method used two additional dowel pins inserted into the flanges' inner alignment dowel holes. The two dowel pins used for this connection method were of the same nominal diameter. The purpose of this flange connection method is to emulate the conventional use of these inner alignment dowel holes. Some manufacturers supply these types of dowel pin in VNA calibration kits and so two such dowel pins (in this case, from a calibration kit manufactured by Flann Microwave Ltd) were used for this purpose.

A measurement of the diameter of both of these dowel pins, made using a digital micrometer, showed the diameter of one pin to be 1.555 mm and the other pin to be 1.556 mm.

(b) Different-diameter inner dowel pins: This flange connection method also used two additional dowel pins inserted into the flanges' inner alignment dowel holes. However, for this connection method, each dowel pin was chosen to have a different diameter. This is to emulate the connection strategy being proposed for a flange design in a draft IEEE standard [7] that is currently under development. This strategy uses two dowel pins with different diameters. The dowel pin with the larger diameter achieves a very close fit to the flanges' dowel holes and provides planar alignment for the waveguide apertures. This is called the "Planar Alignment Dowel" pin. The dowel pin with the smaller diameter achieves a looser fit to the flanges' dowel holes and

provides angular alignment for the waveguide apertures. This is called the "Angular Alignment Dowel" pin.

The IEEE flange design uses inner dowel holes of a specific diameter, and associated dowel pins to fit these holes accordingly. The nominal diameter of the IEEE flange inner dowel holes is 1.570 mm. The nominal diameter of the IEEE flange Planar Alignment Dowel pin is 1.566 5 mm and the nominal diameter of the Angular Alignment Dowel pin is 1.556 mm.

The engineering drawing for the flange type used for the VNA test ports and DUTs (both manufactured by VDI), used in this exercise, is shown in Fig. 3. This Figure shows that the nominal diameter of the inner alignment dowel holes is 0.0625 inches (i.e. 1.588 mm) – i.e. this is not the same diameter that is proposed in the draft IEEE standard [7]. So it is not possible to follow exactly the connection strategy advocated by the IEEE standard for this particular flange design.

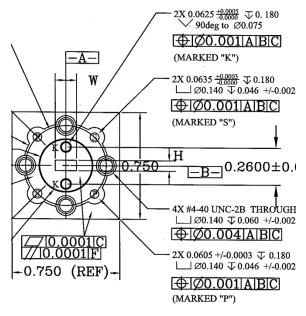


Fig. 3. Engineering drawing extract of the flange used for this investigation. The inner dowel hole diameter value (0.0625") is shown in the top right-hand corner of the drawing

However, the connection strategy can be emulated by selecting dowel pins that, as far as possible, perform a similar role to the planar and angular alignment dowel pins used with the IEEE flange design. In order to do this, a series of dowel pins of various diameters, ranging from 1.550 mm to 1.625 mm in 0.005 mm step sizes, was obtained. These dowel pins were inserted into the flanges'

dowel holes – starting with the smallest diameter dowel pin and using increasingly larger diameter dowel pins until a diameter size was found that provided the closest fit to the dowel hole size. This dowel was then considered to perform a role similar to the Planar Alignment Dowel pin used for the connection strategy described in the draft IEEE standard [7]. A measurement, made using a digital micrometer, of the diameter of the selected dowel pin showed the diameter to be 1.586 mm. (The nominal diameter for the selected dowel pin was 1.590 mm, i.e. showing the measured value to be within 4  $\mu$ m of the nominal value.)

A second dowel pin was then selected with a nominal diameter of 10  $\mu m$  less than the Planar Alignment Dowel (i.e. with a nominal diameter of 1.580 mm). This 10  $\mu m$  difference in the pin diameters is similar to the difference in diameter between the Planar and Angular Alignment Dowels used in the draft IEEE standard (i.e. 10.5  $\mu m$ ). Therefore, the 1.580 mm diameter dowel pin was considered to perform a similar role as the Angular Alignment Dowel pin in the draft IEEE standard [7]. A measurement of the diameter of this dowel pin, made using a digital micrometer, showed the diameter to be 1.576 mm (i.e. within 4  $\mu m$  of the nominal value).

(c) No inner dowel pins: The repeatability exercise reported in [2] did not use the flange inner alignment holes for aligning the flanges during connection. Instead, only the outer alignment dowel pins and holes were used during that exercise. However, this earlier exercise used the same test port flanges and the same DUTs as used during this current investigation. Therefore, the results obtained in the earlier exercise [2] can be used to provide equivalent repeatability data for these flanges when used without the aid of the inner alignment dowel pins and holes.

#### 2.3 Data Analysis

The analysis uses calculations of the experimental standard deviation (as used previously in [1, 2]) as the measure of variability in the observed values due to flange connection repeatability. This computation is applied separately to both the real and imaginary components of the complex-valued linear reflection coefficient. An analysis based on using the magnitude and phase components of the reflection coefficient is avoided due to problems with such calculations that have been described in [8].

Let  $\Gamma$  be the complex-valued linear reflection coefficient written in terms of its real,  $\Gamma_R$ , and imaginary,  $\Gamma_I$ , components as follows (with  $j^2 = -1$ ):

$$\Gamma = \Gamma_R + j \Gamma_I \tag{1}$$

For *n* repeated determinations of  $\Gamma$ , the arithmetic mean of  $\Gamma_R$  is given by:

$$\overline{\Gamma}_{R} = \frac{1}{n} \sum_{i=1}^{n} \Gamma_{R_{i}} \tag{2}$$

and the experimental variance is given by:

$$s^{2}\left(\Gamma_{R_{i}}\right) = \frac{1}{n-1} \sum_{k=1}^{n} (\Gamma_{R_{k}} - \overline{\Gamma_{R}})^{2}$$
(3)

The experimental standard deviation,  $s(\Gamma_{R_i})$ , is equal to the positive square root of  $s^2(\Gamma_{R_i})$ .

Similarly, the arithmetic mean of  $\Gamma_I$  is given by:

$$\overline{\Gamma}_{I} = \frac{1}{n} \sum_{i=1}^{n} \Gamma_{I_{i}} \tag{4}$$

and the experimental variance is given by:

$$s^{2}\left(\Gamma_{I_{i}}\right) = \frac{1}{n-1} \sum_{j=1}^{n} (\Gamma_{I_{j}} - \overline{\Gamma_{I}})^{2}$$
 (5)

The experimental standard deviation,  $s(\Gamma_{I_i})$ , is equal to the positive square root of  $s^2(\Gamma_{I_i})$ .

For each DUT at each frequency, values of  $s(\Gamma_{R_i})$  and  $s(\Gamma_{l_i})$  are calculated for the following three situations:

- (i) Using the 12 repeat measurements of the flange when connected in the non-inverted orientation. Following the convention used in [2], we use a superscript N to indicate this 'Non-inverted' situation i.e.  $\Gamma_R^N$  for the real component, and  $\Gamma_I^N$  for the imaginary component;
- (ii) Using the 12 repeat measurements of the flange when connected in the inverted orientation. Following the convention in [2], we use a superscript I to indicate this 'Inverted' situation i.e.  $\Gamma_R^I$  for the real component, and  $\Gamma_I^I$  for the imaginary component;
- (iii) Using all 24 repeated measurements of the flange connected in both inverted and non-inverted orientations. Following the convention in [2], we use a superscript *IN* to indicate this 'Inverted and Non-inverted' situation i.e.  $\Gamma_{R}^{IN}$  for the real component, and  $\Gamma_{I}^{IN}$  for the imaginary component.

#### 3. RESULTS

For each of the three flange connection methods, for both the offset short-circuit and the near-matched load, we can compare calculated values of the experimental standard deviations in the real component,  $s(\Gamma_{R_i}^N)$ ,  $s(\Gamma_{R_i}^I)$  and  $s(\Gamma_{R_i}^{IN})$ , and, we can compare the calculated values of the experimental standard deviations for the imaginary component  $s(\Gamma_{I_i}^N)$ ,  $s(\Gamma_{I_i}^I)$  and  $s(\Gamma_{I_i}^{IN})$ .

This is shown in Figs. 4 to 15, where the labels 'Same-diameter pins', 'Different-diameter pins' and 'No pins' are used to identify the three flange connections methods described in sub-section 2.2, i.e. (a) 'same-diameter inner dowel pins', (b) 'different-diameter inner dowel pins' and (c) 'no inner dowel pins', respectively.

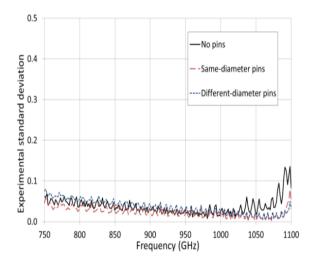


Fig. 4.  $s(\Gamma_{R_i}^N)$  for the offset short-circuit

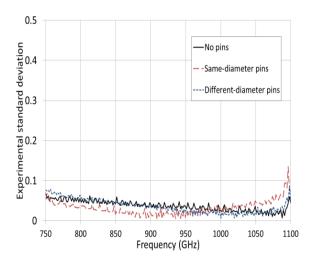


Fig. 5.  $s(\Gamma_{R_i}^I)$  for the offset short-circuit

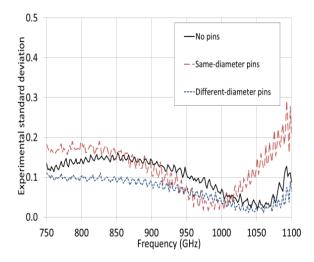


Fig. 6.  $s(\Gamma_{R_i}^{IN})$  for the offset short-circuit

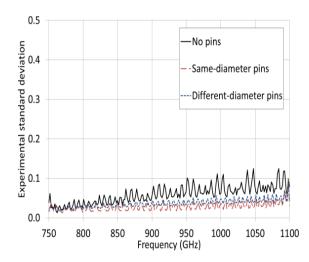


Fig. 7.  $s(\Gamma_{I_i}^N)$  for the offset short-circuit

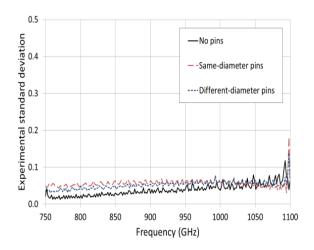


Fig. 8.  $s(\Gamma_{I_i}^I)$  for the offset short-circuit

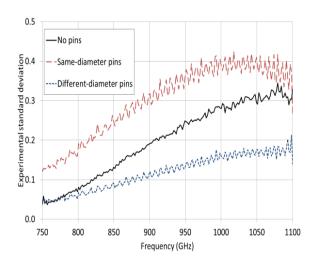


Fig. 9.  $s(\Gamma_{I_i}^{IN})$  for the offset short-circuit

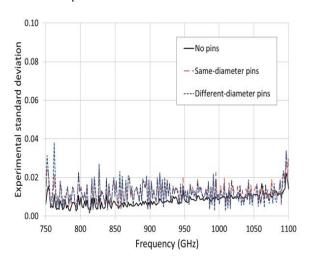


Fig. 10.  $s(\Gamma_{R_i}^N)$  for the near-matched load

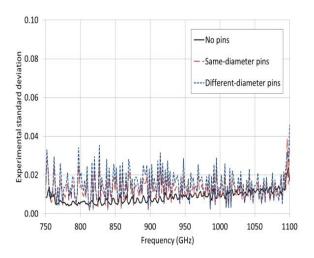


Fig. 11.  $s(\Gamma_{R_i}^I)$  for the near-matched load

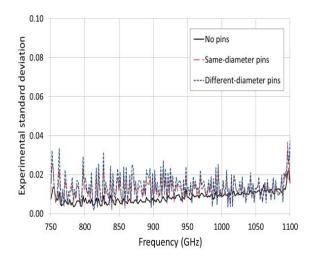


Fig. 12.  $s(\Gamma_{R_i}^{IN})$  for the near-matched load

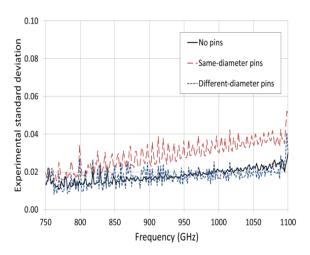


Fig. 13.  $s(\Gamma_{I_i}^N)$  for the near-matched load

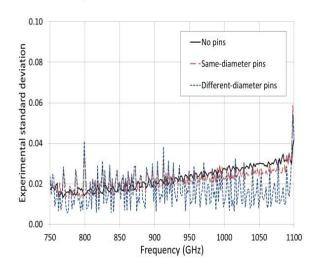


Fig. 14.  $s(\Gamma_{I_i}^I)$  for the near-matched load

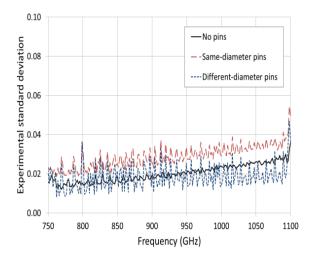


Fig. 15.  $s(\Gamma_{I_i}^{IN})$  for the near-matched load

#### 4. DISCUSSION

The results presented in Figs. 4 to 15 show that, for all three flange connection methods, there is no clear and obvious 'best' connection method (in terms of the achieved standard deviations due to the repeatability of flange connections) for the situations examined in this investigation. There are some instances (e.g. in Figs. 6, 9, 13 and 15) where the connection using same-diameter inner dowel pins exhibits inferior repeatability. However, there are also instances (e.g. in Figs. 4 and 7) where the same connection method performs as good as, or better than, the other methods. Similar types of observation could be made about the other connection methods. There are also instances where flange connection repeatability for all three methods appears to be significantly worse than for other instances - see, for example, Figs. 6 and 9. However, this type of behaviour has been explained in a previous investigation [2], where this effect was attributed to imperfect positioning of the flange alignment dowel pins and holes, and so the waveguide apertures of the DUT and the VNA test port will be misaligned (systematically) by different amounts, depending on the orientation used for the connection of the DUT.

Since all three methods achieve quite similar connection performance, it is instructive to examine the methodologies behind these types of connection. As mentioned previously, the relatively loose tolerances that make the conventional UG-387 flange design [4-6] unacceptable for use at high millimeterwave and submillimeter-wave frequencies has led to two different strategies for improving this design:

- 1. Use tighter tolerance specifications for the outer alignment dowel holes and pins so that these holes and pins are suitable as the primary alignment mechanism for the flange;
- 2. Use inner alignment dowel holes and pins with relatively tight tolerance specifications as the primary mechanism for achieving the required alignment precision. For these designs, the loose tolerance outer alignment dowel holes and pins remain as legacy features of the flange, but do not play a significant role in the alignment process.

Table I summarizes the alignment properties for the conventional UG-387 flange design [4]. The table gives the specified range of diameter values for both the outer dowel holes and pins. These values are used to calculate a worst-case difference between these two diameters (i.e. between the largest hole-size and the smallest pin-size). This difference indicates how well the alignment pins fit the holes – the larger the difference, the worse the likely flange alignment. Table I shows a worst-case diameter difference for the UG-387 flange of 0.216 mm.

TABLE I
Diameters for the outer dowel pins and holes for conventional UG-387 flange

	conventional e d 307 mange							
	Nominal	Tolerance	Range					
	(mm)	(mm)	(mm)					
Holes	1.702	+0.025, -0.000	1.702→1.727					
Pins	1.524	±0.013	1.511→1.537					
Worst case diameter difference between nin and hole								

Worst case diameter difference between pin and hole: (1.727 - 1.511) mm = 0.216 mm

Table II shows similar information for the outer alignment dowel pins and holes for the VDI flange type used during the investigation reported in this paper. This information is derived from values given in Fig. 3 (although the values in Fig.3 are specified in inches). Table II shows a worse-case diameter difference for this VDI flange of 0.092 mm, which is considerably better than the conventional UG-387 flange summarized in Table I.

TABLE II
Diameters for the VDI flange outer dowel pins and holes

	Nominal	Tolerance	Range			
	(mm)	(mm)	(mm)			
Holes	1.613	+0.008, -0.000	1.613 → 1.621			
Pins	1.537	±0.008	1.529 → 1.545			
Worst assa diameter difference between nin and hole:						

Worst case diameter difference between pin and hole: (1.621 - 1.529) mm = 0.092 mm

We can use a similar method to examine the alignment properties of the two connection methods described in this paper that used the inner dowel holes and pins. This information is shown in Tables III and IV for the 'same-diameter inner dowel pins' method and the 'different-diameter inner dowel pins' method, respectively. These tables show worsecase diameter differences of 0.046 mm for the samediameter inner dowel pin method and 0.015 mm for the different-diameter inner dowel pin method. This would imply that the connection methods using the inner alignment holes and pins should provide better alignment than the use of the outer pins alone. However, the results from this investigation (in terms of achieved repeatability) suggest that the alignment provided by the tighter tolerance outer alignment dowel pins and holes for the VDI flange design is such that adding additional alignment mechanisms (i.e. using the inner alignment holes) does not improve significantly the overall alignment of the waveguide apertures. It therefore remains to be seen whether the connection strategy proposed in the new IEEE standard [7] (i.e. just using high-precision inner alignment holes and pins, along with loose tolerance outer holes and pins, as specified in the conventional UG-387 flange design) will result in improved connection repeatability compared to the repeatability performance obtained in this paper. The investigation of this type of connection strategy will need to wait until the flanges specified in the new IEEE standard [7] become available commercially and are used for waveguide components operating these frequencies.

TABLE III

Diameters for the inner dowel pins and holes involved in the 'same-diameter inner dowel pins' connection method

connection method							
	Nominal	Tolerance	Range				
	(mm)	(mm)	(mm)				
Holes	1.588	+0.013, -0.000	$1.588 \rightarrow 1.601$				
		Measured (mn	1)				
Pins	1.555 (and 1.556)						
Worst case diameter difference between pin and hole:							

(1.601 - 1.555) mm = 0.046 mm

#### TABLE IV

Diameters for the inner dowel pins and holes involved in the 'different-diameter inner dowel pins' connection method

Commented in the most									
	Nominal	Tolerance	Range						
	(mm)	(mm)	(mm)						
Holes	1.588	+0.013, -0.000	1.588 → 1.601						
		Measured (mm)							
Pins		1.586							
Worst case diameter difference between pin and hole:									
	(1.601	-1.586) mm $-0.014$	5 mm						

#### 5. CONCLUSIONS

This paper has presented a detailed investigation and analysis of the connection repeatability performance that can be achieved from using waveguide flanges that are currently available on VDI waveguide extender heads for VNAs in the WM-250 waveguide size.

The investigation has concentrated on assessing likely improvements in connection repeatability due to the use of the inner alignment dowel holes found on these flanges. The use of different sizes of dowel pin has been evaluated as part of this exercise.

The results show that, for the flange types manufactured by VDI, there is no clear advantage, in terms of the achieved connection repeatability, in using these inner alignment dowel holes when making connections with these flange types.

It remains to be seen whether the use of the flange design that is currently being specified in the ongoing draft IEEE standard [7] will improve upon the connection repeatability observed during this and earlier investigations [1, 2].

#### **ACKNOWLEDGEMENT**

The authors would like to thank Dr Jeffrey Hesler (Virginia Diodes, Inc) for helpful discussions concerning aspects of the VDI flange type used in this paper and for permission to use the engineering drawing shown in Fig. 3.

The work described in this paper was jointly funded by the European Metrology Research Programme (EMRP) Project SIB62 'HF-Circuits', and, the National Measurement System Directorate of the UK government's Department for Business, Innovation and Skills. The EMRP is jointly funded by the EMRP participating countries within EURAMET and the European Union.

#### **REFERENCES**

- [1] N M Ridler and R G Clarke, "Investigating Connection Repeatability of Waveguide Devices at Frequencies from 750 GHz to 1.1 THz", *Proc.* 82<sup>nd</sup> ARFTG Microwave Measurement Conference, pp 87-99, Columbus, OH, USA, Nov. 2013.
- [2] N M Ridler and R G Clarke, "Further Investigations into Connection Repeatability of Waveguide Devices at Frequencies from 750 GHz to 1.1 THz", Proc. 83<sup>rd</sup> ARFTG Microwave Measurement Conference, pp 83-89, Tampa, FL, USA, June 2014.
- [3] IEEE Std 1785.1-2012, "IEEE Standard for Rectangular Metallic Waveguides and Their Interfaces for Frequencies of 110 GHz and Above—Part 1: Frequency Bands and Waveguide Dimensions", Mar. 2013.
- [4] "Detailed Specification Sheet Flanges, Waveguide (Contact) (Round, 4-hole) (Millimeter)", MIL-DTL-3922/67E with Amendment 1, May 2014.
- [5] "Detailed Specification Sheet Flanges, Waveguide (Contact) (Round, 4-hole) (Millimeter)", MIL-DTL-3922/67C, June 2004.
- [6] "Detailed Specification Sheet Flanges, Waveguide (Contact) (Round, 4-hole) (Millimeter)", MIL-DTL-3922/67D, Dec. 2009.
- [7] IEEE Std 1785.2 (draft), "IEEE Standard for Rectangular Metallic Waveguides and Their Interfaces for Frequencies of 110 GHz and Above—Part 2: Waveguide Interfaces".
- [8] N M Ridler and M J Salter, "Evaluating and expressing uncertainty in complex S-parameter measurements", Proc. 56<sup>th</sup> ARFTG Microwave Measurement Conference, Boulder, CO, USA, Dec. 2000.

## Accuracy and Repeatability of Automated Non-Contact Probes for On-wafer Characterization

Cosan Caglayan\*, Georgios C. Trichopoulos, and Kubilay Sertel
The ElectroScience Laboratory, The Ohio State University
1330 Kinnear Rd, Columbus, OH 43212
E-mail: {caglayan.1, trichopoulos.1, sertel.1}@osu.edu

Abstract—We present significant performance improvements of non-contact probes for the mmW and sub-mmW device characterization. Repeatability and accuracy of the measurement setup is studied using an automated non-contact probe system and compared with conventional contact-probes. Owing to the planar, non-contact nature of the new setup, only 2-axis automated positioning is required, as compared to typical 3-axis manipulators, including precise contact-force control used in commercially available systems. We demonstrate repeatability studies for the 140-220 GHz band using a precision servo system, which can be fully automated using a software-controlled aligner for wafer-scale measurements. This fully-automated system also allows for periodic re-calibrations that are typically required for reliable sub-mmW measurements.

#### I. INTRODUCTION

The demand on ultrafast integrated circuits (ICs) for the sub-millimeter wave region continues to grow as key applications, including medical and securit imaging, high-speed communications, spectroscopy, are being adopted in practice. In particular, effective development of sub-mmW devices (e.g. diodes, transistors, passives, mixers, etc. operating above 300 GHz) require reilable and accurate, on-wafer metrology approaches to enable device testing at the intended operation frequency. However, this has become a challenge due to much smaller feature sizes at such high frequencies. Currently, contact probes are the state of the art for testing at sub-mmW frequencies up to 1.1THz [1]. This technology is primarily based on aggresive scaling of coplanar contact probes that are widely used in microwaves. Scaling requirements of contact probes result in high manufacturing and repair costs, as well as extreme fragility. For example, if the contact force between the probe tip and test wafer is not controlled precisely, this can result in poor repeatability or fast deterioration of the probe tips [2]. In an effort to circumvent such fundamental drawbacks, we recently proposed non-contact probes based on

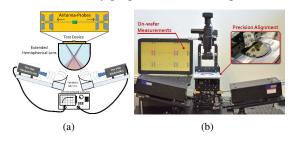


Fig. 1. (a) Illustration of the non-contact probe setup for on-wafer characterization in the THz and mmW bands (b) Photograph of the non-contact probe setup prototype

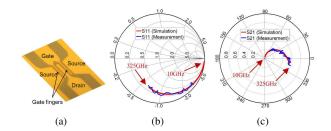


Fig. 2. Non-contact characterization of cold HEMT external parasitics: (a) Micrograph of the on-chip HEMT layout, (b) Smith Chart representation of the measured reflection  $(S_{11})$  (c) Smith Chart representation of the measured transmission coefficient  $(S_{21})$ 

efficient, quasi-optical coupling of the test signals into and out of the coplanar environment of the test device [3]. The concept is illustrated in Fig. 1(a) where a pair of diagonal horn antennas and a high-resistivity hemispherical Silicon lens is utilized for the quasi-optical wireless link. Effective coupling into the co-planar waveguide (CPW) environment is achieved using broadband, butterfly shaped double slot antennas integrated with the test device. These on-wafer antennas act as virtual probe tips and the measurement signals are quasi-optically focused onto the input and output ports of the device under test using Gaussian-like beams, as illustrated in Fig. 1(a).

A single test die or a complete test wafer can be characterized by placing the respective test structure over the hemispherical lens allowing for two isolated signal links between input and output ports. Since only the position of the test wafer is varied to collect the calibration and measurement data, the quasi-optical link is kept unchanged. As such, the non-contact test-bed can be automated easily by incorporating servo controlled precision manipulators instead of manual micromanipulators, as shown in Fig. 1(b). A relatively simple, software-controlled, commercially-available servos suffices to implement fully-automated measurements. In this work, we investigate the accuracy and repeatability of the non-contact test bed operated with servo-controlled manipulators and demonstrate the performance of fully-automated, on-wafer sub-mmW measurements for the first time.

### II. ACCURACY AND REPEATABILITY OF AUTOMATED NON-CONTACT PROBES

A key feature of non-contact probes is the effective radiative coupling of the test signal in and out of the device under test without resorting to electrical contact with the device wafer. To do so, we use wideband planar antennas integrated with the CPW device environment. As illustrated in Fig. 1(a), the incident beam radiated from the horn antenna at the to VNA input port is focused upon the "on-chip" probe antenna at the input port of CPW line. The hemispherical lens is used to achieve a tight focus (with approximately  $\lambda/3$  in diameter) on the probe antenna. The test signal received by the on-chip antenna feeds the CPW environment of the test device. Subsequently, transmitted signal that may be attenuated or amplified by the test device is re-radiated out of the opposite on-chip antenna, enabling transmission parameters ( $S_{12}$ ,  $S_{21}$ ) measurements. Moreover, the signal reflected by the device couples back to the input port via the same optical path as the incident beam, enabling reflection ( $S_{11}$  and  $S_{22}$ ) measurements. The incidence angle between optical axis and receiving/transmitting antenna beams is kept small, ensuring effective coupling into the planar antennas at broadside. We also note that relatively high refractive index of the high-resistivity silicon lens allows for much smaller on-wafer antenna sizes, minimizing chip space required to fabricate the virtual probe tips.

As an initial demonstration of the non-contact probe setup for device characterization, we recently studied a high electron mobility transistor (HEMT) layout to model its external parasitics. A SOLT-type on-wafer calibration is performed using well-known offset-short and thru standards. As seen in Fig. 2, there is excellent agreement between the full-wave simulations (HFSS) and non-contact measurements over the entire 90-325 GHz, spanning 3 successive waveguide bands. We note that the quasi-optical alignment of the non-contact probe setup was kept the same and only the frequency extenders were replaced to collect the data, illustrating the modularity of the proposed setup.

### III. REPEATABILITY PERFORMANCE OF NON-CONTACT PROBES

Following the above initial demonstration, we next focus on identifying and quantifying the main sources of non-repeatable errors in the non-contact probing process. It is expected that the virtual probe tip placement under the beam spot will slightly differ for each of the calibration, as well as test device measurements. The placement relies on the precision of the alignment of the virtual probe tip under the microscope. Moreover, this probe alignment is also limited by the manipulating precision. As such, manual placement of the virtual probe tip under the marked beam spot better than 1 micron is not typically possible in both of the manipulation axes. However, this precision can be significantly improved using a software-controlled automated test-bed.

In addition, the instrument drift is another source of measurement error. Due to temperature sensitivity of the electronic components used in multipliers and mixers in VNA frequency extenders, they exhibit varying degrees of magnitude and phase drift over time, mainly due to fluctuations in the environment. For our current 2-port configuration in the WR 5.1 band, 3% of magnitude drift and  $\pm 4^{\circ}$  phase drift over 1 hour time span is specified according to the manufacturer (Virginia Diodes Inc.).

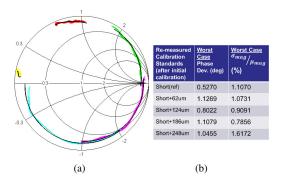


Fig. 3. 1-port repeatability of semi-automatic non-contact probe test bed in WR 5.1: (a) Smith Chart scatter plot (colored) of re-measured standards, black lines representing the ideal response. (b) Worst case phase and magnitude deviations tabulated for each standard.

The following experimental procedure was implemented to study the 1-port repeatability of our non-contact probe system: After an initial on-wafer calibration, the "standards" feature set, which consists of 5 offset short CPW lines and a through standard, was measured 25 times over a time span of 1.5 hours in typical laboratory conditions. The Smith Chart representation of the collected 25 measurements is shown in Fig. 3(a) as a scatter plot. As seen in Fig. 3(b), the worst case phase deviation is about 1° and the worst case magnitude deviation is 1.6%. According to manufacturer specifications, 1-port stability of the frequency extenders in the WR5.1 band is expected to be 5 times better than the 2-port configuration. As seen in this example, the measured repeatability of the non-contact probes, which is the combined effect two factors discussed above, is indeed very close to the instrument limitations. In a fully automated test-bed, repeatability is expected to further improve compared to semi-automatic version presented here.

#### IV. CONCLUSION

An initial study on reliability and repeatability of non-contact probes is presented. 1-port repeatability performance was calculated and shown to be very close to instrument drift, which demonstrates the effectiveness and ease of use of the non-contact probes. Owing to relatively simple, quasi-optical non-contact nature of this new approach, the non-contact probe system is cost-effective and free from fragility and wear/tear issues of traditional contact-based probes. Most importantly, they can be easily automated to enable large-scale wafer-level multi-port characterization of on-chip devices and ICs in the mmW and sub-mmW frequencies.

#### REFERENCES

- [1] M. Bauwens, N. Alijabbari, A. Lichtenberger, N. Barker, and R. Weikle, "A 1.1 THz micromachined on-wafer probe," 2014 IEEE MTT-S International Microwave Symposium (IMS), pp. 1–4, June 2014.
- [2] T. Reck, L. Chen, C. Zhang, A. Arsenovic, C. Groppi, A. Lichtenberger, R. Weikle, and N. Barker, "Micromachined probes for submillimeter-wave on-wafer measurements part I: Mechanical design and characterization," *IEEE Transactions on Terahertz Science and Technology*, vol. 1, no. 2, pp. 349–356, November 2011.
- [3] C. Caglayan, G. Trichopoulos, and K. Sertel, "Non-contact probes for on-wafer characterization of sub-millimeter-wave devices and integrated circuits," *IEEE Transactions on Microwave Theory and Techniques*, vol. PP, no. 99, pp. 1–11, 2014.

## On high frequency/mm-wave IMD measurements with small tone spacing

J. Martens

Anritsu Company, 490 Jarvis Drive, Morgan Hill, CA 95037 US

Abstract — Small-tone-spacing intermodulation distortion (IMD) measurements, needed for some memory-effect modeling studies in particular, are traditionally challenging because of the stresses on source phase noise, isolation, measurement system memory effects and dynamic range. These effects are exacerbated in broadband and mm-wave measurements due to (typically) more frequency multiplication and reduced source chain isolation. Through a series of studies on automatic level control (ALC) bandwidth modulation, isolation effects, source coherence improvements and receiver memory control, an improved system will be presented having residual measurement system third-order intercept products (IP3) in excess of 25 dBm at 70 GHz and >20 dBm at 110 GHz with a 100 Hz tone spacing.

Index Terms — Intermodulation distortion, measurement, memory effects.

#### I. Introduction

Intermodulation distortion measurements, and in particularly IMD asymmetry, have been a useful tool for exploring memory effects and other wide-time-constantrelated model elements in devices, circuits and subsystems (e.g., [1]-[4]). Among the possible mechanisms are thermal, thermo-mechanical relaxation, bias system effects and Thermal and thermo-mechanical relaxation processes can be very slow depending on the structure with time constants sometimes exceeding 1 ms. While most direct bias tee and bias driver time constants are faster, the bulk power supply system can sometimes be part of the dynamic and, again, time constants above 1 ms can occur. Trapping processes cover the gamut of time constants as well.

Since the tone spacing ( $\Delta$ ) in an IMD measurement exercises time constants on the order of  $1/\Delta$ , small-tone-spacing IMD measurements may sometimes be critical for this type of analysis and model development. The challenges in small- $\Delta$  measurements at lower carrier frequencies have been covered before (e.g., [1], [5]) since they have particularly been an issue when characterizing narrowband communications systems where both stimulus tones had to fit in a channel bandwidth on the order-of-a few kHz wide. Potential issues for the measurement include poor tone (or receiver LO) phase noise so that the desired products were obscured in the phase noise skirts, tone pulling (remodulation, either in a phase or amplitude sense, by one tone on another) due to inadequate isolation between sources, measurement system memory effects (tones interacting in the IF in particular) and limited

dynamic range in general. The prescription was logical: cleaner sources, more source chain isolation (using isolators or isolation amplifiers), more linear IFs, etc. In broadband and mm-wave applications that are increasingly common, however, these prescriptions can sometimes be difficult to fill: multiplication stages are often used for system reaching 100 GHz or more thus degrading phase noise, isolation amplification stages covering more than an octave may be expensive and/or have inadequate drive power on their own, and receivers themselves may be more limited in their flexibility.

Further methods of tone cancellation or filtering have been used for enhanced dynamic range at lower frequencies (e.g., [6]) and particularly for passive intermodulation distortion measurements. With the bandwidths involved here, filtering is perhaps not practical and, with the absolute frequencies and bandwidths, feedforward cancellation would often have stability and control issues. For these reasons, those enhancement techniques will not be considered further in this paper.

This paper will look at methods of improving this measurement scenario using system IMD residuals as the primary metric. Approaches to be investigated include

The use of dynamic leveling loop bandwidth to minimize induced remodulation without adding more isolation

The use of source synchronization to reduce contributed phase noise and the effects of the reference clock

The consideration of IF and receiver memory effects

The measurement stimulus structure to be used is relatively classical involving two synthesizers and a passive combiner. The ALC detection system, which is going to play a role in the measurements of this paper, will be isolated by coupler directivity from the main tone path (as suggested in Fig. 1) but not actively isolated for bandwidth and power reasons. Millimeter-wave modules are shown for broadband operation but operate in a pass-through mode for low frequency coverage [7]. The receiver, sources and leveling circuitry are all contained within the VNA. The combiner was internal in some cases and external in others for logistical reasons but in both cases, isolation was about 20 dB over the frequencies of interest. Both combiners used had over 70 GHz of bandwidth.

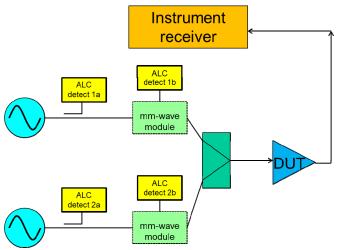


Fig. 1. The measurement structure to be used for the analysis in this paper is shown above (most of which is within a VNA). Depending on the mode and frequency range, different ALC detection paths would be employed.

# II. POWER LEVELING, SOURCE ISOLATION AND THE IMPLICATIONS

Communication (in a distortive sense) between sources in an IMD measurement has long been known to be an issue for smaller tone spacings. In the era of unsynthesized sources, this was sometimes literally due to frequency pulling of the oscillators (e.g., [8]). More germane, usually, is interaction of the ALC systems where the lower second-order product (generated by the DUT or by the detection system) can enter the leveling loop and remodulate onto the tones creating frequencies at the locations of 3<sup>rd</sup> (and other odd) order products.

# A. Explicit isolation and its limits

The classical solution is to add more isolation in the individual tone arms, through better combiners, amplifier-pad combinations or isolators. These certainly help and are often adequate in narrowband applications. In broadband measurements or in certain high power cases, however, this may be problematic. On the latter point, if high power tones are required and it is desired to level them for power accuracy (more on this in section II.C), it may be prohibitive for cost or technological reasons to add isolation after the power stage. Thus if isolation is limited, the leveling system itself should be addressed.

# B. Loop behavior and dynamic parameter control

A simplified block diagram of the leveling loop used in the measurement system of Fig. 1 is shown in Fig. 2 and is not atypical. The loop has some bandwidth set by a number of poles (but often dominated by effects of a quasi-integrator)

that is often designed for a particular settling time and dynamic response pattern. For the purposes of IMD, the primary effect of interest is some AC signal is introduced at the detection plane corresponding to the tone spacing (from mixing in the detection system or from the DUT in a reflective sense). If this signal is within the bandwidth of the loop, the loop will attempt to correct for its presence by applying a misphased signal of that frequency to the modulator. This will produce sidebands on the tone, one of which corresponds to the frequency of a 3<sup>rd</sup> order product. Depending on loop and modulator linearity, this may also spawn signals at 5<sup>th</sup> order and higher product locations. Since ALC loop bandwidths are often on the scale of a few MHz or less, this is more likely to be an issue when the tone spacing (and hence the frequency of the lower 2<sup>nd</sup> order product) is small.

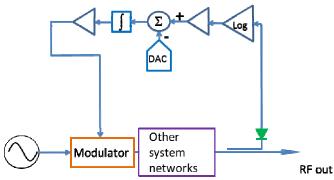


Fig. 2. A simplified ALC loop block diagram is shown here. The second main IMD tone can enter back through the 'RF out' point and mix with the first main tone within or before the loop.

This loop structure was simulated in time domain with a 2<sup>nd</sup> order product injection to view the response characteristics. In Fig. 3 are simulations of an internal ALC loop node voltage near the integrator showing the effect of a requested increase in output power (to exercise the loop dynamics as well) at the 500 µs time point. An IMD measurement with a tone spacing of 50 kHz and a measured 2<sup>nd</sup> order conversion level (at 60 GHz center frequency) into the loop was used in the simulations. The solid trace was for a nominal loop with a wide (100 KHz) bandwidth. Two other traces show the effect of reduced loop bandwidth (to 50 and 10 kHz) with some reduction in measurement speed. The effect of a 20 dB isolation increase is also shown using the measured change in the 2<sup>nd</sup> order conversion efficiency of the detection system. The isolation and bandwidth reduction changes are similar but the former may not be practical as discussed earlier and does also change the loop dynamics somewhat more drastically (presumed due to the embedding environment of the detection system).

The results of Fig. 3 are not unexpected. A next step is to measure residual IMD product levels versus tone spacing for a variety of loop bandwidths and compare (at least in one case) to simulated results using the measured conversion efficiency of the loop modulator. These results are shown in Fig. 4 and the bandwidth requirement based on tone spacing is somewhat

intuitive. The agreement with simulation is better than 2 dB and is believed to be limited by the accuracy of the 2<sup>nd</sup> order injection measurements and the modulator efficiency measurements.

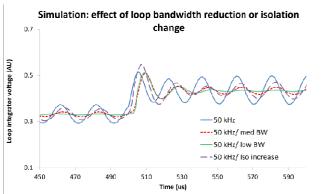


Fig. 3. Simulated ALC internal integrator node voltages for a step in requested power, including tone-spacing-related leakage, are shown here for different loop configurations.

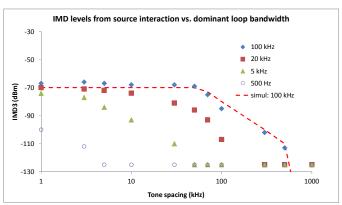


Fig. 4. Residual IMD products (due to source interaction) are shown here versus ALC loop bandwidth and tone spacing. All except the dashed line are measured 3<sup>rd</sup> order residuals. The measurements in this case were at 60 GHz.

# C. Open-loop power control and its ramifications

In view of the dependencies shown in the previous section, it may be worth considering using power control in a different mode. Particularly in the higher mm-wave frequency ranges, a variety of leveling approaches have been used including open-loop and quasi-open-loop approaches (e.g., [9]). Here the latter term is used to refer to (usually software-based) approaches where the power is not corrected real-time relative to the measurement but on a slower time scale. While this certainly can remove leveling loop effects (except possibly on extremely long time scales), it can introduce a different problem related to the inherent absolute level sensitivity of the IMD or IPn measurement.

In the simplest sense, the computation of the intercept point has a fairly well-behaved sensitivity to a tone power error measurement of 0.5 for the 3<sup>rd</sup> order product measurement and 1.5 for the main tone power measurement (when expressed in

dB/dB terms). What is practically more interesting is the sensitivity to an input power error, which might occur from operating open-loop, on the intercept point due to a state change in the DUT. As an example, a 90 GHz IMD swept power measurement was made of a DUT with a somewhat anomalous third order response (left panel of Fig. 5). The input power sweep in this case ranged over -30 to -10 dBm and the tone spacing was 1 MHz.

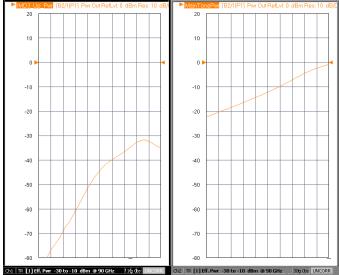


Fig. 5. Measured third order upper product (left panel) and main tone (the two main tones were equal to within 0.5 dB; right panel) are plotted vs. input power at 90 GHz

The sensitivity to that input power error is plotted in Fig. 6 for this DUT (over the upper half of the power sweep range used in Fig. 5). In the anomalous portion, the sensitivity exceeds 2 even for this class AB mm-wave amplifier that is better behaved than many higher efficiency structures.

This tends to suggest that, if the ALC loop bandwidth can be dynamically adjusted adequately, such operation may be preferable to open-loop operations in the interests of accuracy.

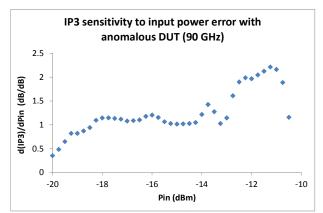


Fig. 6. The sensitivity of the measured OIP3 of the amplifier in Fig. 5 at 90 GHz to an error in input power is plotted here. Particularly when the intermodulation product behavior is non-classical, the penalty for an input power error can be exacerbated.

# III. SOURCE NOISE AND RECEIVER MEMORY EFFECTS

Aside from leveling loop issues, two other potential concerns associated with small spacing measurements are phase noise (will the noise skirts of the sources and LO obscure the IMD products to be measured?) and the receiver memory responses (often in the IF).

# A. Phase noise effects

Since common synthesizer phase noise levels are in the range of -100 dBc/Hz at 10 kHz offset and 20 GHz center frequency, it is not surprising that phase noise may become a limitation on small-spacing measurements in the higher microwave and mm-wave range. It is not the intent of this paper to explore synthesizer architecture and design but only to look at two items that may pertain to the IMD measurement more generally: correlation between tones and LO and the timebase cleanliness (which in turn can affect correlation).

If the tones and LO have essentially independent synthesis structures (connected only via a timebase, often at 10 MHz), the individual phase noise levels will contribute to the residual noise floor on a largely uncorrelated basis. If, however, these signals are derived from a higher frequency source, the correlation levels can increase considerably and the resultant residual IF floor can be reduced. This effect is shown in Fig. 7 for a 1 kHz tone spacing measurement over roughly a 70 GHz center frequency bandwidth. The dashed curve represents the residual 3<sup>rd</sup> order product for independent synthesis structures. The solid curve is for the case when the tones and receiver LO are derived from another synthesizer in the 5 GHz range. The residual dynamic range improvement is on the order of 10 dB.

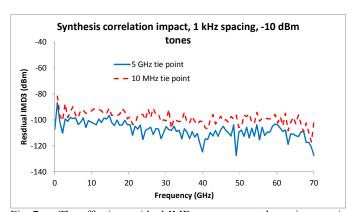


Fig. 7. The effective residual IMD measurement dynamic range is shown here for two synthesis structures where the only variable was the correlation between tones and LO.

Particularly at the smaller tone spacings (< 1 kHz), there are many practical cases when the timebase cleanliness itself may become relevant. This effect is shown in Fig. 9 where the IMD3 residual floor is plotted for a nominal 10 MHz timebase (-110 dBc/Hz at 10 Hz offset) and a higher specification unit (-145 dBc/Hz at 10 Hz offset). The average improvement in

the 1 kHz spacing measurement of Fig. 8 was about 4 dB. The more uncorrelated synthesis structure was used for the measurement of Fig. 8.

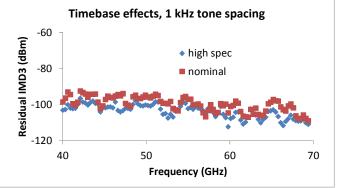


Fig. 8. The effect of a higher specification 10 MHz timebase on the residual measurement floor is shown here.

# B. Receiver (IF) memory effects

If the receiver chain has any memory effects, whether those are from biasing, thermalization or variable gain reasons, the residual floor would also be affected. In this particular case, the front-end bias systems were well-isolated down to the sub-100 Hz level and, once source effects were isolated, no floor distortions to the -120 dBm level were detected (and overall residual receiver IP3 exceeds 30 dBm at larger spacings [7]). If variable gain decisions at the IF are based on integrated signal level, then again no distortions were observed. If the gain decisions are based on narrowband amplitude, then a pseudo-memory effect occurs where the IF amplifiers are sent into compression as the tone spacing decreases. Using that approach increased the residual IMD floor to -80 dBm for -10 dBm tones in the limit of small spacing. Aside from one trace on Fig. 11, the measurements in this paper used the integrated power decision basis.

# IV. MEASUREMENTS

Bringing together the ALC loop bandwidth control, phase noise correlation and reference changes and dynamic IF filtering, one can look at the composite residual floors over broadband and some mm-wave ranges as well as look at the impact on DUT measurements. The residual floor is plotted in Fig. 9 for a low frequency to 70 GHz span for a variety of tone spacings ranging from 1 MHz down to 100 Hz. For the -10 dBm tones used, this translates to 25-30 dBm residual IP3 values over the range at a 100 Hz tone spacing.

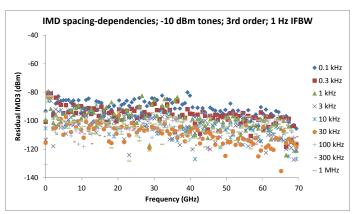


Fig. 9. The residual IMD floor for the receiver is shown here over a 70 GHz bandwidth using the leveling, phase noise and receiver optimizations discussed.

For a mm-wave configuration, there is a different leveling location so the effective isolation is somewhat higher than for the baseband 70 GHz setup but the same ALC bandwidth controls were used. The multipliers for the final tone frequencies are higher so the net phase noise levels are elevated by 6-10 dB. The residual floor is thus a bit higher as shown in Fig. 10. The residual IP3 in this case is then > 20 dBm at a 100 Hz offset up to 110 GHz.

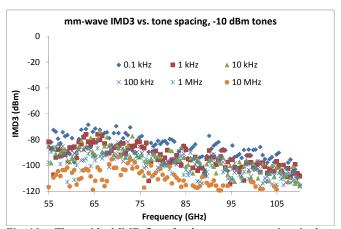


Fig. 10. The residual IMD floor for the mm-wave receiver is shown here up to 110 GHz using the leveling and phase noise optimizations discussed. The leveling position is different from Fig. 9 and the multipliers are higher so the values do not overlap directly.

A common reason for looking at these small-spacing measurements is to investigate DUT memory effects that may originate from several different mechanisms. An example 75 GHz bandwidth amplifier assembly DUT had an active resonance in its bias structure at about 10 kHz. The IMD of this device was measured as part of an investigation and the system described above was used in its final state and with some of the modifications removed. These results are shown in Fig. 11. The nominal measurement (blue diamond trace) shows an expected response in the 12-14 kHz spacing range. With some the phase noise degraded by reference and correlation change removal, the signature is still visible although the measurement floor is elevated. If the receiver

memory and dynamic ALC bandwidth changes are removed, a large step in the residual floor occurs and the DUT signature is much more difficult to detect.

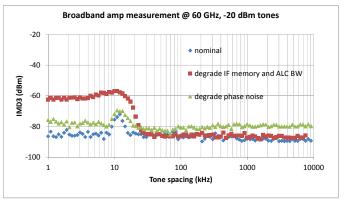


Fig. 11. Measurements of the IMD of a broadband DUT (with a known memory oddity) at 60 GHz but with variable tone spacing are shown here for various states of the measurement system.

#### V. CONCLUSION

Challenges to making small-tone-spacing IMD measurements are well-known and can become worse in broadband and mm-wave scenarios. Some system improvements have been discussed that can improve the residual measurement floor and allow the detection of potentially interesting memory effects in wideband devices.

- [1] J. P. Martins and N. B. Carvalho, "Multitone phase and amplitude measurement for nonlinear device characterization," *IEEE Trans. Mic. Theory Techn.*, vol. 53, pp. 1982-1989, June 2005
- [2] J. H. K. Vuolevi, T. Rahkonen, and J. P. A. Manninen, "Measurement technique for characterizing memory effects in RF power amplifiers," *IEEE Trans. Micr. Theory Techn.*, vol. 49, pp. 1383-1389, Aug. 2001.
- [3] Y. Yang, J. Yi, J. Nam, B. Kim, and M. Park, "Measurement of two-tone transfer characteristic of high-power amplifiers," *IEEE Trans. Micr. Theory Techn.*, vol. 49, pp. 568-571, Mar. 2001.
- [4] J. S. Kenney and P. Fedorenko, "Identification of RF power amplifier memory effect origins using third-order intermodulation distortion amplitude and phase asymmetry," 2006 Int. Micr. Symp. Dig., pp. 1121-1124, June 2006.
- [5] "Intermodulation Distortion (IMD)", Anritsu Application Note 11410-00213, April 2000.
- [6] A. Walker, M. Steer and K. G. Gard, "A vector intermodulation analyzer applied to behavioral modeling of nonlinear amplifiers with memory," *IEEE Trans. Micr. Theory and Techn.*, vol. 54, pp. 1991-1999, May 2006.
- [7] J. Martens, "On high resolution, pulse-profiled mm-wave intermodulation measurements," 2013 Eur. Micr. Conf. Dig., Oct. 2013.
- [8] "RF and microwave designers' handbook," Watkins-Johnson Company, pp. 449-451, 1996.
- [9] J. Martens, "Improved power leveling in mm-wave/sub-THz systems," 2012 Eur. Mic. Conf. Dig., Nov. 2012.

# A test set-up for the analysis of multi-tone intermodulation in microwave devices

J.P Teyssier<sup>(1)</sup>, J. Sombrin<sup>(2)</sup>, R. Quéré<sup>(1)</sup>, S. Laurent<sup>(1)</sup>, F. Gizard<sup>(3)</sup>

(1) XLIM-CNRS-University of Limoges, France,

(2) LABEX-ΣLim University of Limoges, France,

(3) CNES Toulouse, France

Abstract — This paper proposes a multi-tone signal pattern designed for accurate and easy measurements of nonlinear devices linearity factors of merit. The stimulus signal we propose ensures that DUT's third order intermodulation products won't overlap. Thus, the relative phases of source tones do not affect the amplitudes of intermodulation products. The usual metrics for linearity factors, ACPR (Adjacent Channel Power Ratio) or NPR (Noise Power Ratio), can be acquired with a greater accuracy only with amplitude measurements. This work has been carried out with a sampler-based receiver, using FFT (Fast Fourier Transform) filtering for tone separation.

Index Terms — ACPR, Linearity factor, Multi-tone, Nonlinear devices, NPR.

# I. INTRODUCTION

Multi-tone intermodulation (IM) analysis still represents a challenge for linearity assessment of microwave devices, notably when they are fed by complex modulated signals, like involved in Orthogonal Frequency Multiplexing (OFDM) systems. Investigations on efficient stimulus signals for linearity tests have been made for a while [1]. In OFDM case it is interesting to separate the IM products from injected frequencies. Many attempts have been made to draw formula from multi-tone signals constituted of a number of equally spaced frequencies [2]. However the separation of the different IM products which appear at the same frequencies is only possible for well-known nonlinearities. Recently it has been proposed [3] to generate a frequency pattern which allows separating all the IM products of third order (IM3) both from the injected signals and the different IM3 products themselves.

This paper describes a measurement set up that allows to generate a signal with this tone frequency pattern and to measure accurately the different IM products both in amplitude and phase. Moreover the four channels system allows performing network measurements on wafer for microwave transistors. Then it will be possible to evaluate the impact of low frequency memory effects on the linearity of transistors and to improve their models.

# II. THE INPUT SIGNAL

Generally the input signal is constituted of n equally spaced frequency tones such as the  $k^{th}$  frequency is given by:

$$f_k = f_1 + (k-1)\Delta f \qquad 1 \le k \le n \tag{1}$$

We make use of random phases;  $f_1$  is the first microwave frequency; and  $\Delta f$  can be adjusted depending of the number n of frequencies and the bandwidth. Intermodulation products can be measured directly if their frequencies are different from carrier frequencies, e.g. in a notch for NPR or outside the signal bandwidth for ACPR. They can also be computed from correlation of input and output signals. In both cases, a large number of random throws of carrier phases must be performed to achieve correct values of the intermodulation ratio after averaging the results of the different throws because the standard deviation on each measurement is quite high.

We propose a set of frequencies chosen such as the k<sup>th</sup> frequency is given by:

$$f_k = f_1 + (k-1)\Delta f + \varepsilon_k \quad 1 \le k \le n \tag{2}$$

The frequency shift  $\varepsilon_k$  is small, so that all the IM3 products appear at frequencies that are different from each other and also different from carrier frequencies. The separation frequency  $\Delta f$  as well as the frequency shifts  $\varepsilon_k = n_k \varepsilon$  are integer multiples of a base frequency  $\varepsilon$ . This  $\varepsilon$  frequency is the Fourier transform grid tone spacing of the measurement system, so that an exact Fourier Transform without any windowing (i.e. no amplitude error) can be performed on the signal to be measured. Moreover those frequency shifts are chosen as small as possible to keep some compatibility with classical signal and to keep the size of the Fourier Transform reasonable. An example of a three-tone signal is given in table I, we show the RF frequency column, together with the relevant IM3 products; our list of n<sub>k</sub> for this example is {0, 9 and 27). We get 9 IM3 frequencies for such a three-tone signal. We propose different measurement columns, depending on the source power setting. The more we increase the source power, the more the RF amplifier is nonlinear and produces intermodulation products.

TABLE I FREQUENCY TABLE FOR 3 STIMULUS FREQUENCIES,  $\varepsilon=976.6625~Hz$ , FFT SIZE = 131072

Carrier type	RF frequency	Meas 1,	Meas 2,	Meas 3,	Meas 4,	Meas 5,
		-10 dBm	+6 dBm	+13 dBm	+16 dBm	+16 dBm,
						pre-
						distortion
$f_1$	2002500000.000	-25.2	-9.25	-2.33	+0.64	+0.64
$f_2$	2002776367.188	-25.4	-9.28	-2.36	+0.61	+0.61
$f_3$	2003237304.688	-25.5	-9.33	-2.40	+0.56	+0.56
$2f_i - f_j$	2002223632.813	-84.3	-79.2	-63.4	-54.9	-74.4
$2f_i - f_j$	2001762695.313	-82.5	-79.5	-63.2	-54.8	-74.9
$2f_i - f_j$	2003052734.375	-83.7	-81.8	-64.4	-56.2	-70.9
$2f_i - f_j$	2002315429.688	-85.5	-79.6	-62.6	-54.7	-71.9
$2f_i - f_j$	2003974609.375	-84.2	-81.8	-64.5	-56.1	-68.8
$2f_i - f_j$	2003698242.188	-81.5	-79.1	-64.7	-56.3	-70.0
$f_i + f_j - f_k$	2002039062.500	-86.0	-82.3	-57.1	-49.1	-66.9
$f_i + f_j - f_k$	2002960937.500	-84.3	-82.1	-58.2	-49.9	-65.7
$f_i + f_j - f_k$	2003513671.875	-81.9	-81.4	-58.7	-50.3	-64.0
Fig of merit		+63.4	+68.2	+58.5	+53.2	+68.9

If we move to an 8-stimulus tone signal, we end up with 224 RF frequencies; this is still compatible with our hardware. It has been shown by [3] that with 8 stimulus tones, the signal statistics in terms of spectral density and peak to average are almost perfect (like a continuous spectrum signal). Another result from our experiments: the figure of merit we get is not sensitive to the phase of the stimulus frequencies. There is a good reason for that: there is no addition of tones anywhere. The figure of merit is derived from the ratio of IM3 power over the stimulus frequencies power.

# III. THE TEST SET-UP

The test set-up consists in a AWG (Arbitrary Wave Generator) RF source with IQ modulation capabilities, a sampler-based NVNA (we are proposing here VTD/Agilent SWAP results. We have checked we achieve the same results with HP/Maury LSNA). We are using the pretty flat IF bandwidth of the SWAP (10 MHz IF bandwidth) and its one-shot acquisition capability to get, thanks to an inverse fast Fourier transform, all the frequencies of interest amplitudes and relative phases information from a single large ADC record.

This approach is suitable for 50 Ohm matched devices or real transistors with an impedance tuning system in a network approach.

For the purpose of this summary, our nonlinear DUT is the power amplifier of the AWG source, when we increase the output power, we get more and more power at IM3 products (see table 1, meas. 1 to 4 columns). Obviously, next step consists in measuring an external amplifier. With the network

capability of the system, we can measure simultaneously the input and output of the DUT. We can compensate for the AWG nonlinearities with a pre-distortion algorithm (see below).

For meas1, the amplifier is driven to provide -10 dBm, the IM3 frequencies are in the floor noise of the system. Meas2 gives the best figure of merit, as we can see the stimulus frequencies have higher amplitudes but the IM3 products are still in the vicinity of the noise level. When we reach 13 dBm, the power amplifier is clearly in nonlinear mode. We get an expected result: the f1+f2-f3 products are 6 dB higher than 2f1-f2 products. At 16 dBm, the 6 dB law is not so well respected. It means we just begin to have IM5 products popping up. This is illustrated in fig. 2 that shows the measured spectrum. One can notice the 3 stimulus tones, the 9 IM3 products, 3 of them are -49dBm and 6 of them are 6 dB below. The first IM5 products are roughly at -61dBm.

We have to note here that some nonlinear effects can come from the receiver part of the system if we drive the receivers in the vicinity of their compression. We have checked for that to avoid such an issue. Adding a fixed wideband attenuator at the receiver input lets us know if the IM3 products popping up are coming from the DUT or the receiver system.

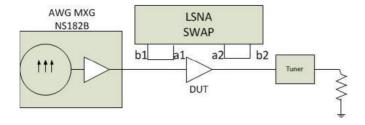


Fig. 1. Measurement set-up with sampler-based receiver.

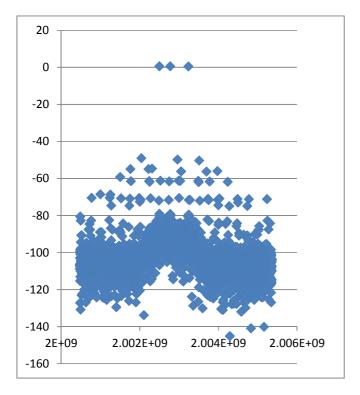


Fig. 2. Measure 4, source set to +16dBm, no pre-distortion.

# IV. DIGITAL PRE-DISTORTION

As the generated multi-tone signal is fed through an amplifier, at high power levels this amplifier generates its own IM products. To minimize the input IM products it is necessary to make as perfect as possible the multi-tone generator. This is done by an optimization process where the digital I/Q data sent to the AWG are updated after measurement by the set-up. This pre-distortion is computed from measured amplitudes and calculated phases in the plane of the I/Q generator.

The last column of the table I shows the results we get when driving the amplifier at 16 dBm, with a pre-distortion signal applied at IM3 product frequencies. We have optimized the amplitudes and the phases of 9 small additive tones at the 9 IM3 frequencies, and added these tones inside the AWG.

We can notice that the figure of merit has increased from 53.2 to 68.9 dBs. We show here that we can compensate for a

large part of the RF source power amplifier nonlinear effects. This result shows we can pre-calibrate a measurement setup to make it mostly linear, even for high power measurements.

# V. CONCLUSION, PERSPECTIVES

We are proposing a new way to get a linearity figure of merit. This approach gives results very consistent with ACPR or NPR measurements. It gives results consistent with EVM measurements of modulated signals too. Our approach is a very good compromise between 2-tone IM3, that is too sensitive to the tone spacing, and real signals that are very complex and require complex stimulus, acquisition and demodulation procedures to get a figure of merit. Our approach is easier to generate and easier to measure than a real modulated signal, it is less sensitive to relative phases of stimulus signal. With a careful choice of  $n_k \varepsilon$  values, and 8 stimulus frequencies, it is possible to get a very good coverage of all the low frequency memory effects.

In order to improve our measurement quality, we will need to apply an IF (Intermediate Frequency) calibration.

We think this work paves the way for a better and more general definition of linearity factor for RF active devices.

- M. Begue, "Testing new Digital RF Communications with Smart Stimulus and Analysis", Hewlett-Packard Tech note, 1995
- [2] N.B. De Carvalho, "On the use of multitone techniques for assessing RF components intermodulation distortion", IEEE trans. On MTT, vol 47, n12, 1999
- [3] J. Sombrin, "Future test benches for the optimization of spectrum and energy efficiency in telecom nonlinear RF components and amplifiers", ARFTG Invited talk, Montreal, 2012

# Via-Adjusted Microstrip Launch for Sub-Terahertz Wafer Probing

Kooho Jung and John Ebner

Cascade Microtech Inc., Beaverton, OR 97008 USA

Abstract — A new design for a microstrip launch is proposed to improve the measurement repeatability at sub-THz frequencies. Performance improvement is achieved by adjusting the ground vias' position to the rear of the launch by which it becomes less sensitive to probe-tip placement compared to conventional launches using microstrip or co-planer waveguides. The investigation was done using HFSS, 3-D finite-elementmethod based electromagnetic simulation software, with tight convergence criteria to meet the required tolerances. The proposed design can be applied to other RF interfaces that required high repeatability such as pads for wire-bonds and footprints for surface-mount components, without increasing cost or compromising RF performance.

Index Terms — coplanar-waveguide, HFSS, launch, microstrip, probe, sub-THz, via.

# I. INTRODUCTION

Coplanar-Waveguides (CPW) have been transmission-lines at probe interfaces in integrated circuits and calibration standards ever since wafer probing was introduced [1]. CPW provides a convenient launch structure that well matches the coplanar like ground-signal-ground probe-tip. Over the past few decades, wafer probing technology has advanced to meet the increasing demand for higher frequencies, and in many cases CPW is still used. However, using CPW may compromise measurements at high frequencies [2], if the wavelengths become comparable to the gaps between the signal trace and the two grounds. This is due to CPW's radiation and the substrate's slab waveguide modes as reported in [3-4]. Such non-transverse-electromagnetic (non-TEM) modes are difficult to predict due to their dependence on the surrounding structures which can act as scattering sites.

To avoid these unpredictable non-TEM modes, microstrips have become the preferred transmission-line at the launch [5-6]. Vias are generally needed in microstrip launches in order to connect the lower ground to the top pads exposed for the probe-tip, although there are ways to avoid them in narrowband applications [7]. If the vias are at the center of the pads they provide an unintended but important benefit, making the electrical characteristics of the launch less sensitive to probe-tip placement which can be roughly ±3 to ±6 µm depending on the operator's skill and the probe-station's mechanical stability. This is because the vias provide fixed electrical paths to the ground, hence are more immune to probe-tip placement. Such desensitization is beneficial because it helps the launch (which is part of the error-network that needs to be calibrated) to be consistent during calibration and post-calibration

measurements. However, further desensitization is desired at sub-THz frequencies and beyond, due to their extremely short wavelength; for example at 500 GHz, the quarter-wavelength is about 50  $\mu$ m when using an alumina substrate.

A new design is proposed in order to further desensitize the electrical characteristics of the launch to probe-tip placement at sub-THz frequencies. This is achieved by adjusting the vias' positions as shown in Section II. The results of adjusting the vias are discussed in Section III and further potential application of the proposed design are presented in Section IV. All investigations were done using HFSS [8], 3-D finite-element-method based electromagnetic simulation software, which can provide valid results for such simple structures as long as the convergence criteria are set appropriately to meet the required tolerances.

# II. VIA ADJUSTED MICROSTRIP LAUNCH

A microstrip launch is shown in Fig.1 along with its transparent view which shows the vias connecting the backside grounds to the top pads. The pad size is 50 µm by 30 um, which are considered the minimum to allow the probe-tip to safely land and skate the minimum distance needed to ensure repeatable electrical contact. The 3 grey structures at the top pads represent the ground-signal-ground structure of the probe-tip. The microstrip region is 300 µm long which is enough for the injected signal at the probe-tip to settle into the microstrip's TEM mode. This microstrip was designed with a 44 µm wide trace on a 20 µm thick substrate that has a dielectric constant of 3.5. This will make the characteristic impedance 50  $\Omega$  with the phase-delay characteristics shown in Fig. 2, where 1 µm in length accounts for 1 degree of phasedelay at 500 GHz. This provides convenient conversion which will be used in the next section.

Fig. 3 shows the cross-sectional views along the dashed lines labeled as A and B in Fig. 1(a). The variables v and x represent the amount of the vias' adjustment and the probetip's displacement, respectively. The green dashed-lines represent their nominal center positions (v = 0, x = 0), while the blue solid-lines and the red dotted-lines represent their maximum considered variations. The vias' adjustment was taken to range from -15 to 15  $\mu m$ . Although placing the vias at the pads' edges may violate layout design rules, it was simulated to such extremes to observe the effects. The probetip's displacements were taken to range from -6 to 6  $\mu m$  as mentioned in the previous section.

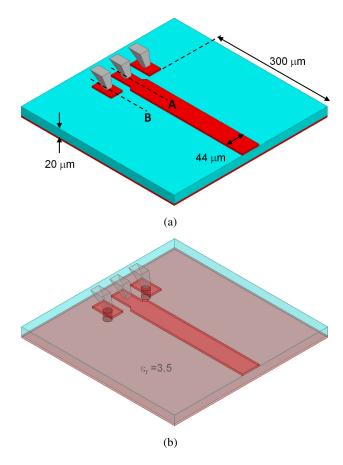


Fig. 1. Microstrip launch for wafer probes; (a) solid view; (b) transparent view.

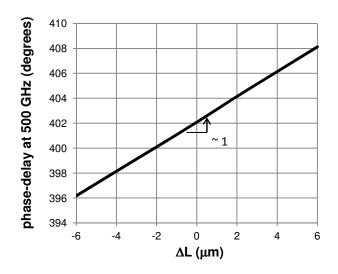


Fig. 2. Phase-delay of a 400  $\mu m$  +  $\Delta L$  long microstrip transmission-line shown in Fig. 1.

In order to minimize simulation time only one side of the symmetric structure is simulated in HFSS, as shown in Fig. 4. The surface that was the plane of symmetry is assigned with perfect-H symmetry boundary condition, and other surfaces

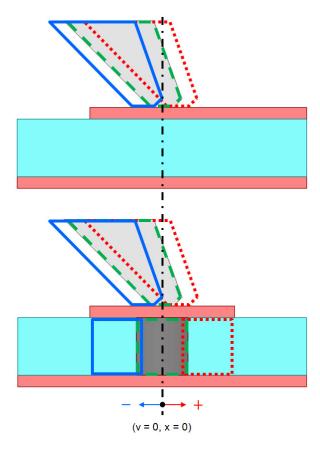


Fig. 3. Cross-section of microstrip launch with maximum considered adjustments of the vias, V and the probe-tip's displacement, X; most rear (solid blue-line), center (dashed greenlines), most front (dotted red-lines); the upper and lower figures are the those along the lines labeled as A and B in Fig. 1(a), respectively.

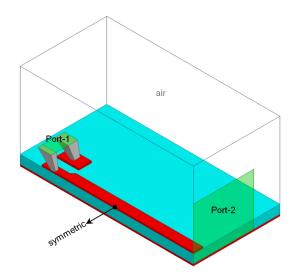


Fig. 4. Simulation setup of the microstrip launch using perfect-H symmetry boundary condition.

are assigned with radiation boundary conditions. Port-1 and Port-2 are 50  $\Omega$  referenced lump-port and wave-port, respectively. Any mode-mismatches of the lump-port assigned

at Port-1 can be considered as the non-ideal transition to the probe's tip from the short transmission-line section inside the probe.

In this HFSS model, the vias and probe-tip are moved from their center position using the variables V and X that are implemented consistently with Fig. 3. Since the simulation results need to correctly distinguish the effects of the small changes in these variables, tight convergence criteria is forced by requiring at least 2 consecutive passes that meet the S-parameter tolerance spec of 0.001. Using Intel's 3.6 GHz Xeon® processor with 34 GB RAM, it took about 30 minutes of simulation time for initial convergences at 500 GHz.

#### III. SIMULATION RESULTS

The effects of adjusting the vias at 500 GHz are shown in Fig. 5. The X-axis is the probe-tip's displacement and the Yaxis is the resulting variation of the phase-delay, -phase( $S_{21}$ ). It shows that the phase-delay becomes less sensitive to the probe-tip's displacement when the vias are adjusted to the most rear position,  $V = -15 \mu m$ . In this position, displacing the probe-tip by ±6 µm changes the phase-delay from -0.7 to 1.5 degrees. This is equivalent to having the microstrip's length vary from -0.7 to 1.5 μm, since 1 μm in length of the designed microstrip accounts for 1 degree of phase-delay as mentioned in the previous section. Note that if the launch was designed for CPW that has similar phase velocity, one will need to place the probe-tips within ±2 µm to achieve such level of repeatability, which will be difficult without using an automated probe-station with embedded vision processing software.

Maximum desensitization to probe-tip placement occurred when the vias were adjusted to the most rear, because the electrical path change on the signal pad was compensated by

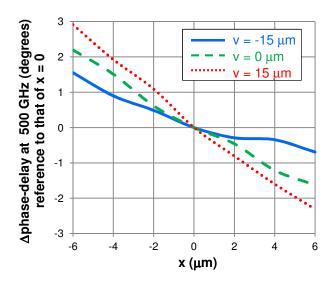
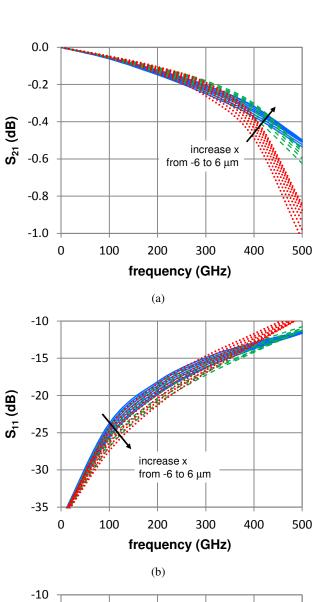


Fig. 5. Phase-delay variations of microstrip launch due to probetip's displacement at various via adjustments.



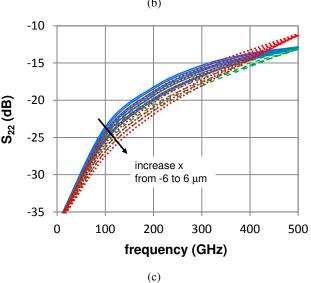


Fig. 6. S-parameter magnitude variations of microstrip launch at various via adjustments;  $V = -6 \mu m$  (solid blue-lines),  $V = 0 \mu m$  (dashed green-lines),  $V = 6 \mu m$  (dotted red-lines); multiple lines in each case are due to varying probe-tip's displacement, X.

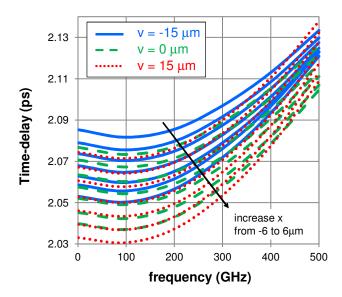


Fig. 5. Time-delay variations of microstrip launch at various via adjustments, v; multiple lines in each case are due to varying probetip's displacement, x.

the change on the two adjacent ground pads. For example, if the probe-tip is displaced towards the front (if x is positive) the electrical path on the signal pad decreased while those on the two adjacent ground pads increased, because the currents have to travel back to the rear where the vias are located. Such desensitization also occurred for the RF magnitude as shown in Fig. 6, which can be explained by the same reason. For  $V = -15 \mu m$  (blue solid-lines), the multiple lines representing the probe-tip's displacement are close to each other, while those for V = 0 (green dashed-lines) and  $V = 15 \mu m$  (red dotted-lines), are further apart. Note that one would normally redesign the launch for optimum RF performance for each via location. However, the redesign is not done here in order to observe the effects of their adjustments, which resulted in slightly degraded RF performance for  $V = 15 \mu m$ .

In order to verify that the investigated via adjusted launches are suitable for broadband applications, dispersion characteristics were investigated, as shown in Fig. 7. The coding of the lines' color and type represents the via adjustments in the same way as in Fig. 5 and 6, while the multiple lines in each case represent the probe-tip's displacement. The Y-axis is the time-delay of the launch including the 300  $\mu$ m long microstrip. This is calculated using (1) where,  $t_{\text{delay}}$ ,  $\phi$ , and f are the time-delay, phase(S<sub>21</sub>), and frequency, respectively, with the units defined in their subscripts.

$$t_{\text{delay,ps}} = -\frac{1}{0.36} \cdot \frac{\phi_{\text{deg}}}{f_{\text{GHz}}} \tag{1}$$

The results did not show much difference except for  $V=-15~\mu m$  where the time-delay varied slightly less over frequency (hence, less dispersive) and also less over probe-tip's displacement. This makes it even more desirable to adjust the vias to the rear of the launch.

# IV. FURTHER POTENTIAL APPLICATIONS

Further desensitization of the probe-tip placement is expected by adjusting the vias' position more to the rear with lengthened ground pads. This can be done in applications where high measurement repeatability is required such as in calibration standards or test structures for characterizing deembedded transistors. Adjusting the vias to the rear can also be applied to general RF interfaces such as pads for wirebonds and footprints for surface-mount components. It is expected have a wide range of potential application because it provides higher repeatability and does not compromise RF performance nor add production cost.

#### ACKNOWLEDGEMENT

The first author would like to thank Dr. Youngoo Yang at Sungkyunkwan University for encouragement on completing and publishing this work.

- [1] K. E. Jones, E. W. Strid, and K. R. Gleason, "mm-Wave Wafer Probes Span 0 to 50 GHz," *Microwave J.*, vol. 30, no. 4, pp. 177 - 183, Apr. 1987.
- [2] F. J. Schmiickle, *et al.*, "Radiation, Multimode Propagation, and Substrate Modes in W-Band CPW Calibrations," *Proc. 41st European Microw. Conf.*, pp. 297 300, Oct. 2011.
- [3] M. Y. Frankel, et al., "Terahertz Attenuation and Dispersion Characteristics of Coplanar Transmission Lines," *IEEE Trans. Microw. Theory Tech.*, vol. 39, no. 6, pp. 910 - 915, Jun. 1991.
- [4] W. Heinrich, F. Schnieder, and T. Tischler, "Dispersion and Radiation Characteristics of Conductor-Backed CPW with Finite Ground Width," *Proc. IEEE MTT-S* 2000, vol. 3, pp. 1663 - 1666, Jun. 2000.
- [5] D. F. Williams et al., "Calibration-Kit Design for Millimeter-Wave Silicon Integrated Circuits," *IEEE Trans. Microw. Theory Tech.*, vol. 61, no. 7, pp. 2685 - 2694, Jul. 2013.
- [6] D. Harvey, "A Lumped Coplanar to Microstrip Transition Model for De-Embedding S-Parameters Measured on GaAs Wafers," Proc. 29th Automated RF Tech. Group Conf., pp. 204-217, Jun. 1987.
- [7] D. F. Williams and T. H. Miers, "A Coplanar Probe to Microstrip Transition," *IEEE Trans. Microw. Theory Tech.*, vol. 36, no. 7, pp. 1219 - 1223, Jul. 1988.
- [8] HFSS, Version 14.0.1, Ansys Inc., Southpointe 275 Technology Dr., Canonsburg, PA 15317 USA, Feb. 2012.

# Adaptive Estimation of Complex Calibration Residual Errors of Wafer-Level S-Parameters Measurement System

Aleksandr A. Savin<sup>1)</sup>, Vladimir G. Guba<sup>2)</sup>, Andrej Rumiantsev<sup>3)</sup>, Benjamin D. Maxson<sup>4)</sup>, Dirk Schubert<sup>5)</sup> and Uwe Arz<sup>5)</sup>

<sup>1)</sup>Tomsk State University of Control Systems and Radioelectronics, 634050, Tomsk, Russia <sup>2)</sup>NPK TAIR, a subsidiary of Copper Mountain Technologies, 634041, Tomsk, Russia <sup>3)</sup>MPI Corporation, Advanced Semiconductor Test Division, 30267, Chu-Pei City, Taiwan <sup>4)</sup>Copper Mountain Technologies, 46268, Indianapolis, USA <sup>5)</sup>Physikalisch-Technische Bundesanstalt (PTB), 38116, Braunschweig, Germany

Abstract — This article presents a method for determining complex residual errors of calibrated two-port vector network analyzers. It utilizes the time-domain technique. Calibration residual errors are extracted from a distance-frequency system model using a special estimation algorithm based on the quasi-optimal unscented Kalman filter. Because the method requires only three measurement conditions, it is in particular beneficial for on-wafer applications, as three test conditions can be obtained from using only one transmission line. Moreover, the length of the line can be relatively short. Experimental studies were performed and verified the proposed method.

Index Terms — S-parameters, vector network analyzer (VNA), verification, residual errors, on-wafer measurements, unscented Kalman filter (UKF).

# I. INTRODUCTION

The estimation of the vector network analyzer (VNA) calibration residual errors is a crucial step in establishing S-parameter measurement assurance. An analysis of different methods was made and the new method of measuring complex calibration residual errors was introduced in [1]. The method required six measurement conditions obtained from reference standards (such as a transmission line and two offset reflection elements) with fully-known electrical characteristics. It was verified for coaxial and wafer-level applications. To increase the estimation accuracy at the wafer-level, the reflection verification elements should be realized as long lines terminated with a short at one end. As a consequence, the verification chip takes undesirably large space of the wafer real estate making the implementation of the proposed method less practical.

This work introduces an adaptive algorithm that allows using reference reflection elements with only partly-known reflection coefficients. As a result, estimation of the calibration residual errors of a wafer-level measurement system can be completed using only one verification element, such as a long transmission line with known characteristic impedance  $Z_0$  and propagation constant  $\gamma$ . The measurement sequence can be completed as follows. First, the RF probe connected to the VNA port 1 contacts the verification line, and

the reflection coefficient of the line opened at its second end is measured (this condition is often called an "open stub"). Next, the RF probe connected to the second VNA port contacts the verification line at its second end and four S-parameters of the line are measured. Last, the first RF probe is elevated in the air and the reflection coefficient of the line is measured using the second RF probe. An accurate model of the open stub measurement condition is not required.

#### II. SYSTEM ERROR MODEL AND OBSERVED SIGNALS

The calibrated S-parameter measurement system can be described as shown in Fig. 1, where  $D_i$ ,  $T_i$ ,  $M_i$  and  $R_i$  are calibration residual errors at port i of the VNA (i=1, 2).

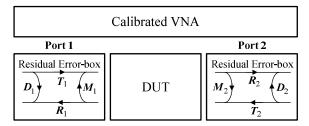


Fig. 1. The model of a two-port calibrated measurement system.

We describe the calibration residual error model of the VNA in the time domain as a set of ten networks, so-called "reflectors". Each reflector has known distance (time delay) and unknown frequency characteristics. For example, Fig. 2 shows the set of samples for A (reference values  $A_1$ ,  $A_2$ ,  $A_3$ ) and B (reference values  $B_1$ ,  $B_2$ ,  $B_3$ ) reflectors in the distance-frequency plane.

In Fig. 2,  $f_1$  is the start frequency, while  $f_2$  and  $f_3$  are other reference frequencies,  $\Delta f$  is the frequency step between samples,  $l_A$  is the distance of A from the reference plane of VNA,  $l_B$  is the distance of B, and  $\Delta l$  is the distance step between reflectors depending on the length of the on-wafer transmission line. Cubic splines are used to interpolate the frequency characteristics of the reflectors and to calculate  $A_k$  and  $B_k$ .

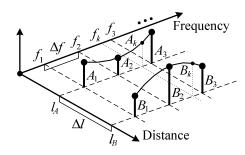


Fig. 2. Distance-frequency model of the measurement system.

The first (reflection) measurement condition gives:

$$\Gamma_1 \approx D_1 + T_1 R_1 \cdot (L^2 \cdot G) + M_1 \cdot T_1 R_1 \cdot (L^2 \cdot G)^2$$
, (1)

where L – the transmission coefficient of the line; G – the reflection coefficient at the second (opened) end of the line. L and G can be written as:  $L = L_C \cdot \Delta L$  and  $G = G_C \cdot \Delta G$ , where  $L_C$  and  $G_C$  are calculated (approximated) parameters,  $\Delta L$  and  $\Delta G$  are approximation uncertainties. Thus, (1) includes three unknown reflectors  $D_1$ ,  $T_1R_1 \cdot (\Delta L^2 \cdot \Delta G)$  and  $M_1 \cdot T_1R_1 \cdot (\Delta L^2 \cdot \Delta G)^2$  separated from each other in the time domain.

The second measurement condition gives:

$$S_{11} \approx D_1 + M_2 \cdot T_1 R_1 \cdot L^2$$
 (2)

$$S_{21} \approx T_1 R_2 \cdot L \ . \tag{3}$$

where  $S_{11}$  and  $S_{21}$  are the measured reflection and transmission coefficients of the verification line, respectively. Thus, (2) and (3) include two new unknown reflectors  $M_2 \cdot T_1 R_1 \cdot \Delta L^2$  and  $T_1 R_2 \cdot \Delta L$ .

The equations for the second residual error box are obtained in a similar way from the reverse direction of the second measurement condition and the third measurement condition.

# III. ALGORITHM

The algorithm for estimating the frequency characteristics of reflectors was developed using the Markov theory of nonlinear filtering. The algorithm is based on the unscented transformation, and is also known as Unscented Kalman Filter (UKF) [1, 2]. Thus, ten reflectors are calculated using this special time-domain filtering technique:

$$\begin{split} x_1 &= D_1 \; ; \; x_2 = T_1 R_1 \cdot (\Delta L^2 \cdot \Delta G) \; ; \; x_3 = M_1 \cdot T_1 R_1 \cdot (\Delta L^2 \cdot \Delta G)^2 \; ; \\ x_4 &= M_2 \cdot T_1 R_1 \cdot \Delta L^2 \; ; \; x_5 = T_1 R_2 \cdot \Delta L \; ; \\ x_6 &= D_2 \; ; \; x_7 = T_2 R_2 \cdot (\Delta L^2 \cdot \Delta G) \; ; \; x_8 = M_2 \cdot T_2 R_2 \cdot (\Delta L^2 \cdot \Delta G)^2 \; ; \\ x_9 &= M_1 \cdot T_2 R_2 \cdot \Delta L^2 \; ; \; x_{10} = T_2 R_1 \cdot \Delta L \; . \end{split}$$

Estimates  $x_1$  and  $x_6$  give the effective directivity of the VNA ports. Estimates  $x_5$  and  $x_{10}$  define the transmission tracking with the accuracy factor  $\Delta L$ . Combining estimates, one can find:

$$\Delta L \cdot \Delta G = \sqrt{\frac{x_2 \cdot x_7}{x_5 \cdot x_{10}}}$$
 (4)

Assuming that both  $\Delta L$  and  $\Delta G$  are close to 1, the root-square problem of (4) can be solved. Combining  $x_2$ ,  $x_7$  and (4):

$$T_1 R_1 \cdot \Delta L = x_2 / (\Delta L \cdot \Delta G)$$
, (5)

$$T_2 R_2 \cdot \Delta L = x_7 / (\Delta L \cdot \Delta G). \tag{6}$$

Therefore, all four residual tracking parameters are found up to the factor  $\Delta L$ . Next,  $M_1$  and  $M_2$  can be found from  $x_4$ ,  $x_9$ :

$$M_2 \approx M_2 \cdot \Delta L = \frac{x_4}{x_2} \cdot (\Delta L \cdot \Delta G) ,$$
 (7)

$$M_1 \approx M_1 \cdot \Delta L = \frac{x_9}{x_7} \cdot (\Delta L \cdot \Delta G)$$
 (8)

# IV. EXPERIMENTAL RESULTS AND DISCUSSION

The goal of the experiments was to verify the proposed method when a verification line has relatively short length, and to evaluate the approximation uncertainties  $\Delta L$ ,  $\Delta G$ . We used the GaAs Reference Material RM8130 and the multiline TRL method from NIST for calibration of the experimental setup [3, 4]. RM8130 includes five lines in a coplanar waveguide design from which we selected the 19.7 mm (L19) and 6.562 mm (L6) long lines as verification elements. All line lengths are indicated as additional lengths relative to 0.5 mm long thru standard.

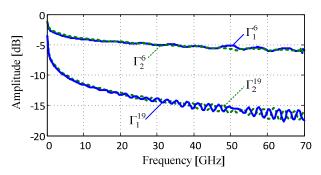


Fig. 3. The measured reflection coefficients of the verification lines open stub conditions corrected by the first calibration series.

All the systematic errors of the measurement setup were calculated from the same set of measured data. Three calibration conditions were investigated: first series – using all available lines, second series – using all available lines except line L6, and third series – using all available lines except line L19. The first (complete) calibration series provided the reference data, as this calibration is expected to be the most accurate. Measurement frequencies covered the band from 100 MHz to 70 GHz with 286 frequency steps. Figures 3-6 show the verification measurements using L6 and L19 as verification lines in the frequency and in the time domain,

respectively. Residual errors and their products can be well identified in the time domain diagrams (Fig. 5, 6).

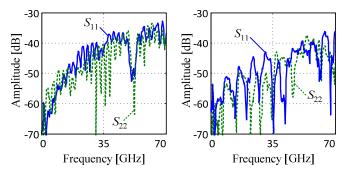


Fig. 4. The measured reflection coefficients of L19 (left) and L6 (right), first calibration series.

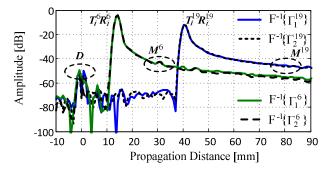


Fig. 5. Reflection time domain diagrams of the open stub conditions for the two verification lines L19 and L6.

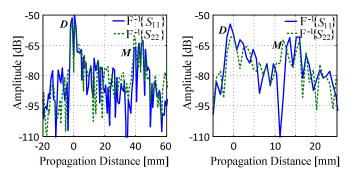


Fig. 6. Reflection time domain diagram of  $S_{11}$  and  $S_{22}$  of the verification lines L19 (left) and L6 (right).

Next, the calibration residual error terms of the test system were calculated. The minimal frequency step  $\Delta f$  for calculated reference points depends on the length of the verification line and is  $\Delta f_{\rm L19}$ =2.8 GHz for L19 and  $\Delta f_{\rm L6}$ =8.4 GHz for L6. The use of a short reference line is an obvious practical advantage, however, it may reduce the estimation accuracy, as  $\Delta f_{\rm L19} < \Delta f_{\rm L6}$ . In Fig. 7 we compare residual errors of the first (reference) calibration series when using L19 as verification line with  $\Delta f$ =2.8 GHz and  $\Delta f$ =8.4 GHz frequency steps. The comparison demonstrates that the choice of  $\Delta f$ =8.4 GHz introduces only negligible calculation errors, except for the residual directivity  $D_1$  at frequencies around f=51 GHz (Fig. 7). The cause of the

observed anomalous drop in  $D_1$  is probably specific to our measurement setup.

In the following, further comparisons of L6 and L19 verification results are performed using the same frequency step  $\Delta f$ =8.4 GHz. This may slightly overestimate the residual directivity  $D_1$  in the frequency range from 45 GHz to 55 GHz.

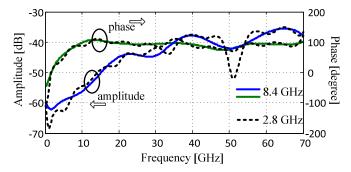


Fig. 7. The magnitude and the phase of the residual error  $D_1$  of the first calibration series estimated using L19 as verification line with  $\Delta f$ =8.4 GHz (solid lines) and  $\Delta f$ =2.8 GHz (dotted lines).

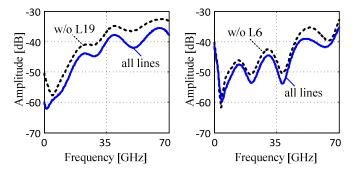


Fig. 8. The magnitude of the residual directivity  $D_1$  using the verification lines L19 (left) and L6 (right) for the three calibration series. Calibration accuracy degrades when fewer lines are involved in the calibration process.

We calculated residual errors of the three calibration series from verification measurement data of both lines L6 and L19. Fig. 8 shows the forward residual directivity  $D_1$ , while Fig. 9 shows residual reflection and transmission tracking  $T_1R_1$  and  $T_1R_2$ , respectively. Other parameters demonstrated a similar relationship. As expected, the accuracy of the calibration degrades when fewer lines are included in the calibration step. The longest line L19 influences the calibration process the most.

We observed a slight variation of the obtained residual errors for the reference calibration series when L6 and L19 were used for the verification measurement (Fig. 9). The method assumes that the propagation constant of both lines is identical. However, as it was discussed in [5], possible coupling of the verification line with nearby structures through the substrate as well as its interference with the probe tip may lead to the propagation of higher-order modes and thereby to a slight distortion of the propagation constant.

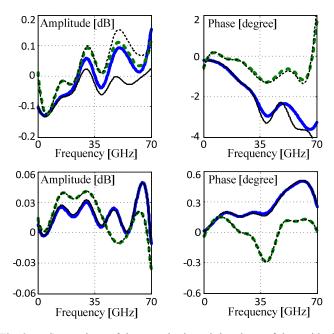


Fig. 9. Comparison of the magnitude and the phase of the residual reflection tracking  $T_1R_1$  (top) and the residual transmission tracking  $T_1R_2$  (bottom) for several verification and calibration cases: 1) L19, first series (solid thick lines); 2) L19, third series (solid thin lines); 3) L6, first series (dotted thick lines); and 4) L6, second series (dotted thin lines).

We also verified our initial assumption about  $\Delta L$  and  $\Delta G$  made when solving (4). The magnitude and the phase of the product  $\Delta L \Delta G$  are given in Fig. 10. It is important to note that this product is originally unknown, similarly to the reflection coefficient of the reflect standard used for TRL calibrations.

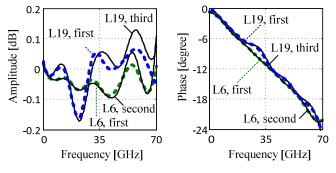


Fig. 10. Magnitude (left) and phase (right) of  $\Delta L \Delta G$  as calculated by (4) for L6 and L19 as verification lines (all calibration series).

Often, the calibration reference impedance  $Z_{\rm REF}$  and the characteristic impedance  $Z_0$  of the verification line are different. In this case, the calculated calibration residual errors can be easily transformed into the system of the desired reference, in a manner similar to that proposed in [6]. We used the characteristic impedance  $Z_0$  of L6 and L19 extracted from previous experiments (Fig. 11, right) and transformed the results to  $Z_{\rm REF}$ =50  $\Omega$ . Fig. 11, left shows  $D_1$  obtained from the first measurement series, with L19 as the verification line,

before and after impedance transformation. Above 12 GHz, the influence of the impedance transformation on  $D_1$  seems negligible.

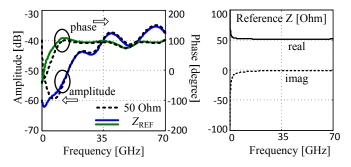


Fig. 11. Comparison of magnitude and phase of the residual directivity  $D_1$  (left) before (solid lines) and after (dotted lines) impedance transformation (first calibration series, L19).

# V. CONCLUSION

In this paper we presented an algorithm for estimation of complex residual errors of a calibrated two-port VNA requiring only one transmission line. The algorithm significantly reduces both the measurement time and the cost of the verification procedure. Experimental results demonstrated suitability of the new method for wafer-level applications.

# ACKNOWLEDGEMENT

The authors thank Sergey Zaostrovnykh and Alex Goloschokin from Copper Mountain Technologies, Indiana, USA for support of this work and for their helpful discussions.

The work was supported by Russian Foundation for Basic Research RFBR Project 14-07-31312.

- [1] A. A. Savin, V. G. Guba, A. Rumiantsev, and B. D. Maxson, "Estimation of Complex Residual Errors of Calibrated Two-Port Vector Network Analyzer," 83rd ARFTG Microwave Measurement Conference, 2014, Tampa, Florida, USA.
- [2] A. A. Savin, "A Novel Factor Verification Technique for One-Port Vector Network Analyzer," Proceedings of the 43rd European Microwave Conference, 7-10 October 2013, Nuremberg, Germany, pp. 60-63.
- [3] "Reference Material 8130. Coplanar waveguide calibration set," NIST, Gaithersburg, MD 20899, USA, 1998.
- [4] R. B. Marks, "A multi-line method of network analyzer calibration," *IEEE Trans. Microwave Theory Tech.*, vol. 39, no. 7, pp. 1205-1215, January 1991.
- [5] A. Rumiantsev and R Doerner, "Method for estimating probedependent residual errors of wafer-level TRL calibration," 83rd ARFTG Microwave Measurement Conference, 2014, Tampa, Florida, USA.
- [6] R. B. Marks and D. F. Williams, "A general waveguide circuit theory," Journal of research of the National Institute of Standards and Technology, vol. 97, pp. 533-562, September-October 1992.

# LZZM: An Extension of the Theory of the LZZ Calibration Technique

<sup>1</sup>Centro de Investigación Científica y de Educación Superior de Ensenada (CICESE). Ensenada, B.C., Mexico. <sup>2</sup>Microsemi, Corp. Santa Rosa, CA 95403, United States.

<sup>3</sup>Centro de Investigación y de Estudios Avanzados del I.P.N (CINVESTAV). Guadalajara, Jal., Mexico.

Abstract — In this paper, the theory of the recently introduced line, offset-open, offset-short (LZZ) calibration technique is extended to develop a calibration procedure comparable to the LRRM calibration technique, the line, open, short, unknown load (LZZM). The LZZM uses as standards a known transmission line, two pairs of unknown reflecting loads and a load of unknown impedance (match) connected at one of the two ports of the vector network analyzer. Already-existing LRRM calibration procedures assume that the real part of the impedance of the load used as match standard is frequency-independent and known prior to the calibration. The LZZM compares favorably with previously reported LRRM procedures in the sense that it allows using loads of unknown and frequency-dependent impedance (real and imaginary parts) as match standard. In order to avoid redundancies in the LZZM calibration process, the impedance of the load used as the match standard has to be different from the characteristic impedance of the transmission line.

Index Terms — Vector Network Analyzer, LZZ calibration, LRRM calibration, ABCD-parameters.

# I. INTRODUCTION

Accurate S-parameter measurements of linear devices at microwave frequencies are performed using a calibrated vector network analyzer (VNA). A number of VNA calibration techniques have been proposed in the literature. them, the line-reflect-reflect-match calibration technique [1]-[3] is acknowledged as one of the most accurate VNA calibration techniques. Previously reported LRRM procedures [1]-[3] use as standards a transmission line, two pairs of highly reflecting loads and a load of partially known impedance Zma. The LRRM procedures reported in [1]-[3] determine the imaginary part of Zma during the calibration process provided that its real part, assumed as frequency-independent, is known prior to the calibration. Nevertheless, when the real part of Zma is dispersive, assuming it as frequency-independent introduces errors in the calibration.

The line, offset-open, offset-short (LZZ) calibration technique [4] allows calibrating the VNA using a known transmission line of arbitrary characteristic impedance and two offset reflecting loads of unknown impedance. In the LZZ calibration procedure, algorithmic issues arise when solving for some of the calibration terms in which choosing the correct root from a quadratic equation is involved, namely  $\overline{A_X}/\overline{C_X}$ ,  $\overline{B_X}$  and  $\overline{C_X}$ .

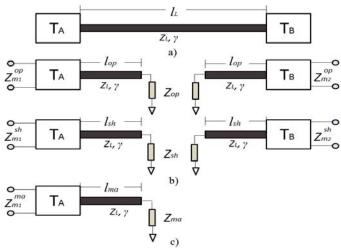


Fig. 1. LRRM calibration elements: a) one transmission line, b) two pairs of highly reflecting loads and c) one match standard.

In this paper the theory of the LZZ calibration technique is extended to develop a calibration procedure comparable to the LRRM calibration technique: the line, open, short, unknown load (LZZM). The LZZM uses as standards a known transmission line, two pairs of unknown reflecting loads and a load of unknown impedance (match), which may be dispersive. The impedance of the load used as the match standard has to be different from the characteristic impedance of the line; otherwise the information provided by the load is redundant.

The use of a load in the LZZM allows developing a more reliable procedure for determining the terms  $\overline{A_X}$  /  $\overline{C_X}$ ,  $\overline{B_X}$  and  $\overline{C_X}$ . The sign ambiguity in the calculation of  $\overline{C_X}$  (eq. (45) of [4]) is eliminated in the LZZM. Furthermore, unlike the LZZ calibration, in which a heuristic criterion was used for choosing  $\overline{A_X}$  /  $\overline{C_X}$  and  $\overline{B_X}$  from a quadratic equation (eq. (44) of [4]), the LZZM uses the measurement of the load to derive an analytical criterion to solve this issue.

This paper is organized as follows. Section II gives a comprehensive analytical derivation of the LZZM calibration procedure. In section III, experimental results verifying the usefulness of the LZZM are presented. The conclusions are presented in section IV.

# II. LZZM CALIBRATION PROCEDURE

The LZZM uses the 8-term error model and the ABCD-parameters to represent the VNA and the calibration standards. When using the 8-term error model, a two-port VNA measures the following product of matrices

$$\mathbf{M}_{\mathbf{D}} = \mathbf{T}_{\mathbf{A}} \mathbf{T}_{\mathbf{D}} \mathbf{T}_{\mathbf{B}} \tag{1}$$

where  $T_A$  and  $T_B$  are matrices modeling the errors in ports one and two of the VNA.  $M_D$  and  $T_D$  are matrices representing the measured and the actual behavior of a DUT, respectively.

# A. The use of the Transmission Line

The equivalent ABCD parameters matrix of the structure shown in Fig. 1a may be expressed as

$$\mathbf{M_L} = \mathbf{T_A} \mathbf{T_L} \mathbf{T_B} = \begin{bmatrix} p_{11} & p_{12} \\ p_{21} & p_{22} \end{bmatrix}. \tag{2}$$

According to [5], the ABCD parameters matrix representation of a transmission line of length lL, characteristic impedance ZL, and propagation constant  $\gamma$ , may be expressed as

$$\mathbf{T}_{\mathbf{L}} = \mathbf{T}_{\mathbf{Z}} \mathbf{T}_{\lambda} \mathbf{T}_{\mathbf{Z}}^{-1} \,, \tag{3}$$

where  $T_Z$  and  $T_{\lambda}$  are given by

$$\mathbf{T}_{\mathbf{Z}} = \begin{bmatrix} Z_L & -1 \\ 1 & Z_L^{-1} \end{bmatrix}; \quad \mathbf{T}_{\lambda} = \begin{bmatrix} \lambda_L & 0 \\ 0 & \lambda_L^{-1} \end{bmatrix}$$
 (4)

with  $\lambda_L = e^{\gamma l_L}$ . Thus, by substituting (3) in (2), **M**L becomes

$$\mathbf{M}_{\mathbf{L}} = \mathbf{T}_{\mathbf{X}} \mathbf{T}_{\mathbf{\lambda}} \mathbf{T}_{\mathbf{V}} , \qquad (5)$$

where

$$\mathbf{T_X} = \mathbf{T_A} \mathbf{T_Z} = \begin{bmatrix} A_X & B_X \\ C_X & D_X \end{bmatrix} = D_X \overline{\mathbf{T_X}}; \overline{\mathbf{T_X}} = \begin{bmatrix} \overline{A_X} & \overline{B_X} \\ \overline{C_Y} & 1 \end{bmatrix}, \quad (6)$$

$$\mathbf{T}_{\mathbf{Y}} = \mathbf{T}_{\mathbf{Z}}^{-1} \mathbf{T}_{\mathbf{B}} = \begin{bmatrix} A_{\mathbf{Y}} & B_{\mathbf{Y}} \\ C_{\mathbf{Y}} & D_{\mathbf{Y}} \end{bmatrix} = D_{\mathbf{Y}} \overline{\mathbf{T}_{\mathbf{Y}}}; \overline{\mathbf{T}_{\mathbf{Y}}} = \begin{bmatrix} \overline{A_{\mathbf{Y}}} & \overline{B_{\mathbf{Y}}} \\ \overline{C_{\mathbf{Y}}} & 1 \end{bmatrix}.$$
(7)

Then, by solving (1) for  $T_D$  and using the definitions given in (6)-(7), the following expression is obtained

$$\mathbf{T_D} = (D_X D_Y)^{-1} \mathbf{T_Z} \overline{\mathbf{T_X}}^{-1} \mathbf{M_D} \overline{\mathbf{T_Y}}^{-1} \mathbf{T_Z}^{-1}.$$
 (8)

Since the elements of  $T_Z$  have to be known prior to the calibration, it can be noted from (8) that seven terms have to be known to determine the ABCD parameters of a DUT: the

elements of the matrix  $\overline{\mathbf{T_X}}$ , the elements of the matrix  $\overline{\mathbf{T_Y}}$  and the product  $D_X D_Y$ . By solving (5) for  $\mathbf{T_Y}$  and using (6)-(7), the elements of  $\overline{\mathbf{T_Y}}$  along with  $D_X D_Y$  may be expressed as

$$\overline{A_Y} = \frac{1}{\overline{C_X}} \frac{p_{11} - \overline{B_X} p_{21}}{-p_{12} + \overline{A_X} / \overline{C_X} p_{22}} \lambda_L^{-2}, \qquad (9)$$

$$\overline{B_Y} = \frac{1}{\overline{C_Y}} \frac{p_{12} - \overline{B_X} p_{22}}{-p_{12} + \overline{A_Y} / \overline{C_Y} p_{22}} \lambda_L^{-2}, \qquad (10)$$

$$\overline{C_Y} = \frac{-p_{11} + \overline{A_X} / \overline{C_X} p_{21}}{-p_{12} + \overline{A_Y} / \overline{C_Y} p_{22}},$$
(11)

$$D_X D_Y = \frac{-p_{12} + \overline{A_X} / \overline{C_X} p_{22}}{\overline{A_X} / \overline{C_X} - \overline{B_X}} \lambda_L.$$
 (12)

Thus, in order to accomplish the calibration, the values of  $\overline{A_X}/\overline{C_X}$ ,  $\overline{B_X}$  and  $\overline{C_X}$  have to be determined according to the procedure presented next.

# B. The Use of the Loads

In the LZZM three loads are used as standards: an open circuit, a short circuit and a load of arbitrary impedance (match). In the following, subscripts op, sh, ma will denote, respectively, these loading conditions. As shown in Fig. 1b-c an offset load is represented by a line of impedance ZL terminated with a load of impedance ZP, P=op, sh, ma. According to [4], the impedance at the input of ports one and two of the VNA,  $Z_{m1}^P$  and  $Z_{m2}^P$ , when they are loaded with an offset load (Fig. 1a-c) may be expressed as

$$Z_{m1}^{P} = \frac{Y_{L}(Z_{L} + Z_{P})\lambda_{P}^{2}\overline{A_{X}} + (Z_{L} - Z_{P})\overline{B_{X}}}{Y_{L}(Z_{L} + Z_{P})\lambda_{P}^{2}\overline{C_{Y}} + (Z_{L} - Z_{P})}$$
(13)

and

$$Z_{m2}^{P} = \frac{Y_{L}(Z_{P} - Z_{L}) + (Z_{L} + Z_{P})\lambda_{P}^{2}\overline{B_{Y}}}{Y_{L}(Z_{P} - Z_{L})\overline{C_{Y}} + (Z_{L} + Z_{P})\lambda_{P}^{2}\overline{A_{Y}}}.$$
 (14)

where  $\lambda_P = e^{\gamma l_P}$ . From (13) and (14), by connecting an open circuit of impedance  $\left|Z_{op}\right| >> \left|Z_L\right|$  at both ports of the VNA, the following expressions are obtained

$$\overline{C_X} = \frac{Z_L}{\lambda_{op}^2} \frac{Z_{m1}^{op} - B_X}{Z_{m1}^{op} - \overline{A_X} / \overline{C_X}}$$
(15)

$$\overline{A_Y} = \frac{Y_L}{\lambda_{on}^2} \frac{Z_{m2}^{op} \overline{C_Y} - 1}{\overline{B_Y} / A_Y - Z_{m2}^{op}} . \tag{16}$$

Then, by connecting a short circuit of impedance  $|Z_{sh}| \ll |Z_L|$  at ports of the VNA, the following expressions are obtained

$$\overline{C_X} = -\frac{Z_L}{\lambda_{sh}^2} \frac{Z_{m1}^{sh} - \overline{B_X}}{Z_{m1}^{sh} - \overline{A_X} / \overline{C_X}}$$
(17)

$$\overline{A_Y} = -\frac{Y_L}{\lambda_{sh}^2} \frac{Z_{m2}^{sh} \overline{C_Y} - 1}{\overline{B_Y} / A_Y - Z_{m2}^{sh}} . \tag{18}$$

According to [4], by equating (15) with (17), provided that  $\lambda_{op} = \lambda_{sh}$ , one can identify the following expression

$$n_1 a_1 + n_2 a_2 = W_a \,, \tag{19}$$

where

$$a_1 = Z_{A1} (20)$$

$$a_2 = -2 \tag{21}$$

$$n_1 = \overline{A_X} / \overline{C_X} + \overline{B_X} \tag{22}$$

$$n_2 = \overline{A_X} / \overline{C_X} \cdot \overline{B_X} \tag{23}$$

$$W_a = 2Z_{B1} \tag{24}$$

with  $Z_{Ai}$  and  $Z_{Bi}$ , , defined as  $Z_{Ai} = Z_{mi}^{sh} + Z_{mi}^{op}$  and  $Z_{Bi} = Z_{mi}^{sh} \cdot Z_{mi}^{op}$ . An expression similar to (19) is obtained by equating (16) with (18) and using (9)-(12) as

$$n_1 b_1 + n_2 b_2 = W_b (25)$$

where

$$b_1 = 2Z_{B2}p_{11}p_{22} + 2p_{12}p_{22} - Z_{A2}(p_{11}p_{22} + p_{12}p_{21})$$
 (26)

$$b_2 = -2(Z_{B2}p_{21}^2 + p_{22}^2 - Z_{A2}p_{21}p_{22}) (27)$$

$$W_b = 2(Z_{B2}p_{11}^2 + p_{12}^2 - Z_{A2}p_{11}p_{12}). (28)$$

The set of two simultaneous equations formed by (19) and (25), may be solved for the two unknowns,  $n_1$  and  $n_2$ . Then, using the definitions given in (22)-(23), a quadratic equation whose roots are  $\overline{A_X}/\overline{C_X}$  and  $\overline{B_X}$  may be formed, with solutions given by

$$\overline{A_X} / \overline{C_X}, \overline{B_X} = \frac{1}{2} \left( n_1 \pm \sqrt{n_1^2 - 4n_2} \right).$$
 (29)

Unlike the LZZ calibration [4], in which the heuristic criterion  $\overline{A_X}/\overline{C_X} > \overline{B_X}$  was used for choosing  $\overline{A_X}/\overline{C_X}$  and  $\overline{B_X}$ , the LZZM uses the measurement of an offset load (Fig.1c) to derive an analytical criterion. From (13) it may be observed that if the value of  $Z_{ma}$  were identical to  $Z_L$ , the value of  $\overline{A_X}/\overline{C_X}$  may be straightforwardly calculated as  $\overline{A_X}/\overline{C_X} = Z_{m1}^{ma}$ . This condition is difficult to achieve at high

frequencies. Nevertheless, when  $Z_{ma}$  is not so far from  $Z_L$ , the value of  $Z_{m1}^{ma}$  approximates the value of  $\overline{A_X}/\overline{C_X}$  and the following expression may be identified

$$\left| \overline{A_X} / \overline{C_X} - Z_{m1}^{ma} \right| < \left| \overline{B_X} - Z_{m1}^{ma} \right|. \tag{30}$$

Note that, as long as  $\lambda_{op} = \lambda_{sh}$ , the procedure used to determine  $\overline{A_X}/\overline{C_X}$  and  $\overline{B_X}$ , presented in (15)-(30), holds independently of the value of  $\lambda_P$ , P = op, sh. Thus, the phase shift of the reflecting loads may be arbitrary;  $\lambda_P$  may even be equal to the unity. Hence, the loads may be either offset loads or non-offset loads.

So far, the only unknown to be determined is  $\overline{C_X}$ . From (13) and by using the measurement of a load of impedance  $Z_{ma} \neq Z_L$  (Fig.1c), an expression for calculating  $\overline{C_X}$  may be derived as

$$\overline{C_X} = \left(\frac{Z_{ma} / Z_L - 1}{Z_{ma} / Z_L + 1}\right) \frac{Z_L}{\lambda_{ma}^2} \frac{Z_{m1}^{ma} - \overline{B_X}}{Z_{m1}^{ma} - \overline{A_X} / \overline{C_X}}.$$
 (31)

Note that for calculating  $\overline{C_X}$  from (31), the value of the ratio  $Z_{ma}/Z_L$  is required. The ratio  $Z_{ma}/Z_L$  may be calculated by equating (15) with (31) as<sup>1</sup>

$$\frac{Z_{ma}}{Z_L} = \frac{1+\xi}{1-\xi},\tag{32}$$

where

$$\xi = \left(\frac{\lambda_{ma}}{\lambda_{op}}\right)^{2} \frac{\left(Z_{m1}^{op} - \overline{B_{X}}\right) \left(Z_{m1}^{ma} - \overline{A_{X}} / \overline{C_{X}}\right)}{\left(Z_{m1}^{ma} - \overline{B_{X}}\right) \left(Z_{m1}^{op} - \overline{A_{X}} / \overline{C_{X}}\right)}.$$
 (33)

The calculation of  $Z_{ma}/Z_L$  from (32)-(33) requires that the ratio  $\lambda_{ma}/\lambda_{op}$  be known, which in the case of two equally shifted loads (or non-offset loads) is reduced to unity. Since  $Z_L$  is known prior to the calibration, from (32) the value of  $Z_{ma}$  may be calculated.

Note that when  $Z_{ma}=Z_L$ , the value of  $\overline{C_X}$  cannot be calculated from (31). Instead, as previously mentioned, the expression  $\overline{A_X}/\overline{C_X}=Z_{m1}^{ma}$  may be derived, which provides redundant information since  $\overline{A_X}/\overline{C_X}$  has been previously calculated from (29). An alternative procedure for determining  $\overline{C_X}$  may be derived, as in the LZZ calibration [4], from the measurement of a symmetrical reflecting load connected at both ports of the VNA. By solving (13) and (14) for  $Z_P$  and equating the resulting expressions, one has

<sup>&</sup>lt;sup>1</sup> Since in the LZZM the value of ZL is known prior to the calibration, as a byproduct of the calibration process, Zma may be calculated once the ratio ZL/Zma is known. Calculating Zma is not required in the LZZM to determine the calibration terms.

$$\overline{C_X} = \pm \frac{Z_L}{\lambda_L} \sqrt{\frac{\overline{B_X}^2 k_0^{RL} + \overline{B_X} k_1^{RL} + k_2^{RL}}{\left(\overline{A_X} / \overline{C_X}\right)^2 k_0^{RL} + \overline{A_X} / \overline{C_X} k_1^{RL} + k_2^{RL}}} , \quad (34)$$

where

$$k_0^{RL} = p_{22} - p_{21} Z_{m2}^{RL} (35)$$

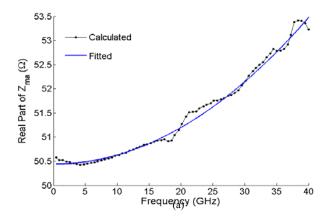
$$k_1^{RL} = p_{21} Z_{m1}^{RL} Z_{m2}^{RL} - p_{22} Z_{m1}^{RL} + p_{11} Z_{m2}^{RL} - p_{12}$$
 (36)

$$k_2^{RL} = p_{12} Z_{m1}^{RL} - p_{11} Z_{m1}^{RL} Z_{m2}^{RL} , (37)$$

with RL=op, sh. Using (34) for determining  $\overline{C_X}$  avoids calculating the ratio  $Z_{ma}/Z_L$  and in such a case the load of impedance  $Z_{ma}$  is only used for choosing the root in (29). The advantage of calculating  $\overline{C_X}$  using (31) instead of (34) is the elimination of the sign ambiguity due to the square root in (34).

# III. EXPERIMENTAL RESULTS

In order to verify the theoretical analysis presented in previous sections, the LZZM calibration was implemented by using microstrip structures included in the substrate model CM05 from J Micro Technology. Measurements were performed by using a HP8510C VNA in the frequency range of 0.045-40 GHz.



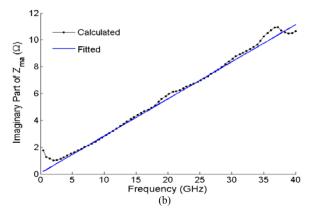


Fig. 2. Calculated and fitted impedance of the load used as match standard: a) real part and b) imaginary part.

The accuracy of the LZZM was assessed by comparing it to the TRL procedure reported in [6] and the LRRM procedure reported in [3]. The TRL was implemented using a zero-length thru, a 0.06cm length transmission line and symmetrical short circuit. The LRRM and the LZZM were implemented using a 0.06 cm length transmission line, symmetrical open circuit, symmetrical short circuit and a load connected at port one. Both reflecting loads and the load used as the match standard are non-offset loads, i.e. they are measured at the calibration reference plane.

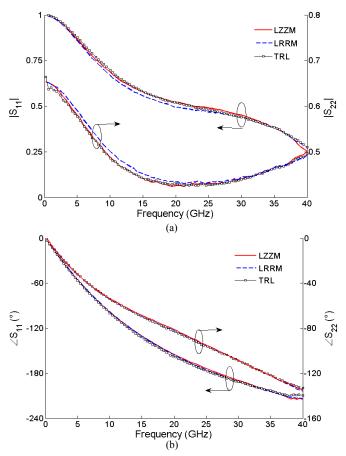


Fig.3.  $S_{11}$  and  $S_{22}$  parameters of an HFET transistor ( $V_{DS}$  = 1 V;  $V_{GS}$  = -1 V) corrected using the LZZM, LRRM and TRL: a) magnitude and b) phase.

The propagation constant of the transmission line used as calibration element was calculated using two transmission lines of different lengths [7]. Meanwhile, the characteristic impedance of the line was determined from its capacitance and propagation constant [8]-[9]. The impedance of the load used as match standard was determined by using the procedure presented in section II-B. The ratio  $Z_{ma}/Z_L$  was calculated from (33); then using the known value of  $Z_L$ , the value of  $Z_{ma}$  was determined.

The calculated real and imaginary parts of  $Z_{ma}$  are shown in Fig. 2. From Fig.2 it can be observed that at frequencies below 3 GHz the value of  $Z_{ma}$  was not accurately calculated. To mitigate this problem, the load was modeled as described next. It is observed that the behavior of the real part of  $Z_{ma}$ 

varies quadratically with the frequency, which according to [10], is not atypical of planar resistors. The real part of  $Z_{ma}$  was fitted to a quadratic function:  $\text{Re}(Z_{ma}) = R_{dc} + g\omega^2$ , with  $\omega = 2\pi f$  as the angular frequency. A value of  $R_{dc} = 50.45~\Omega$  and a fitting factor  $g = 4.8 \times 10^{-23}$ , predict  $\text{Re}(Z_{ma})$  reasonably. The imaginary part of  $Z_{ma}$  was fitted to a linear function:  $\text{Im}(Z_{ma}) = \omega L_{ma}$ . A value of  $L_{ma} = 44 \times 10^{-12}$  predict  $\text{Im}(Z_{ma})$  reasonably.

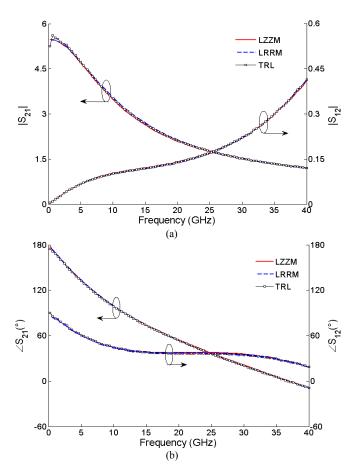


Fig.4.  $S_{12}$  and  $S_{21}$  parameters of an HFET transistor ( $V_{DS}$ = 1 V;  $V_{GS}$ = -1 V) corrected using the LZZM, LRRM and TRL: a) magnitude and b) phase.

A FET transistor was used as DUT. Figs. 3-4 show the magnitude and phase of the DUT S-parameters corrected using the LZZM, the TRL as well as the LRRM. High correlation is observed between the S-parameters corrected using the LZZM and the S-parameters corrected using the reference TRL. The LRRM procedure reported in [3] assumes that the real part of  $Z_{ma}$  is frequency-independent; then it determines its imaginary part during the calibration process. From Fig. 3 it can be observed that the  $S_{11}$  and  $S_{22}$  parameters of the DUT corrected using the LRRM slightly differs from those obtained using the TRL. From Fig. 4 it is observed that the magnitude and phase of  $S_{12}$  and  $S_{21}$  parameters corrected using the LZZM, LRRM and TRL show good correlation. This result indicates that the transmission parameters are less

sensitive to the dispersion of the real part of  $Z_{ma}$ . Greater advantages of the LZZM over the LRRM are expected when the real part of  $Z_{ma}$  is highly dispersive and of value very different from  $50\Omega$ .

# IV. CONCLUSION

In this paper, the LZZM calibration procedure, which is an extension of the theory of the LZZ calibration technique, was introduced. The LZZM allows using loads of unknown and frequency-dependent impedance as match standard; it was demonstrated to be useful for improving the accuracy of the calibration when highly dispersive loads are used as match standard.

- A. Davidson, K. Jones, E. Strid, "LRM and LRRM Calibrations with Automatic Determination of Load Inductance," *ARFTG Conference Digest-Fall*, 36th, pp.57-63, Nov. 1990.
- [2] F. Purroy, L. Pradell, "New theoretical analysis of the LRRM calibration technique for vector network analyzers," *IEEE Trans. Instrum. Meas.*, vol. 50, no. 5, pp. 1307–1314, Oct. 2001.
- [3] L. Hayden, "An Enhanced Line-Reflect-Reflect-Match calibration," ARFTG Conference Digest, 67th, Jun. 2006, pp. 146-149.
- [4] M.A. Pulido-Gaytan, J.A. Reynoso-Hernandez, A. Zarate-de Landa, J.R. Loo-Yau and M. C. Maya-Sánchez, "Vector Network Analyzer Using a Line and Two Offset Reflecting Loads," *IEEE Trans. Microw. Theory Tech.*, vol. 61, no. 9, pp.3417-3423, Sep. 2013.
- [5] J.A. Reynoso-Hernandez, M.A. Pulido-Gaytan, M. C. Maya-Sánchez, J.R. Loo-Yau, "What can the ABCD parameters about the TRL?" ARFTG Conference Digest, 79th, Jun. 2012, pp. 1-4.
- [6] J.A. Reynoso-Hernandez, M.A. Pulido-Gaytan; A. Zarate-de Landa; J.E. Zuniga-Juarez.; J.R. Monjardin-Lopez; A. Garcia-Osorio; Orozco-D. Navarro; J.R. Loo-Yau; M.C. Maya-Sanchez, "Using lines of arbitrary impedance as standards on the TRL calibration technique," *Microwave Measurement Conference (ARFTG)*, 81st ARFTG, pp.1-4, June 2013.
- [7] J.A. Reynoso-Hernandez, "Unified method for determining the complex propagation constant of reflecting and nonreflecting transmission lines," *IEEE Microw. and Wireless Components Letters*, vol.13, no.8, pp.351-353, Aug. 2003.
- [8] D.F. Williams, "Characteristic Impedance Determination Using Propagation Constant Measurement," *IEEE Microw. Guided Wave Lett.*, vol.1, no.6, pp. 141-143, Jun. 1991.
- [9] D.F. Williams, R.B. Marks, A. Davidson, "Transmission Line Capacitance Measurement," *Microwave and Guided Wave Letters*, *IEEE*, vol.1, no.9, pp. 243-245, Sep. 1991.
- [10] Walker, D.C.; Williams, D.F.; Morgan, J.M., "Planar Resistors for Probe Station Calibration," ARFTG Conference Digest-Fall, 40th, pp.1,9, Dec. 1992.

# Study of reflection effect at fixture interfaces on permittivity measurements using the transmission/reflection method

# Yuto KATO\* and Masahiro HORIBE\*

\*National Institute of Advanced Industrial Science and Technology 1-1-1 Umezono, Tsukuba, Ibaraki, 305-8568, Japan {y-katou, masahiro-horibe}@aist.go.jp

Abstract—We have evaluated the reflection effect at fixture interfaces in permittivity measurements using the transmission/reflection (T/R) method. In the T/R method, permittivity is derived from measured quantities without taken into account the reflections at fixture ends, thus they generate deviations of the results. From numerical calculations, we confirmed ripples due to multiple reflections are more pronounced in the frequency characteristic of the permittivity with increasing the reflection coefficient at fixture ends. We also performed permittivity measurements with the T/R method using four different types of fixtures. By comparing the resulting frequency characteristics of the permittivity, and by evaluating the uncertainties due to the connecting repeatability of fixtures, we clarified fixture-type dependence of the reflection effect on results of the T/R method.

Index Terms—Permittivity measurement, Uncertainty, Transmission/Reflection method, Connecting repeatability, S-parameter, Network analyzer

# I. INTRODUCTION

The frequency bands of electromagnetic (EM) waves utilized as social infrastructure are broadening every year. A wide range of application of EM waves has become common. At the same time, the expansion of the utilization of EM waves and their broadened frequency bands have complicated electromagnetic compatibility (EMC) problems. For the development of radio-wave absorbents and electromagnetic interference (EMI) prevention components, knowing the permittivity of high-loss materials is of the utmost importance. The trasmission/reflection (T/R) method is the most common method of measuring the permittivity of high-loss materials [1].

In the T/R method, a sample is inserted into either a coaxial line or a waveguide as shown in Fig. 1, and the permittivity is calculated from measured S-parameters at the fixture interfaces and dimensions of a sample and a fixture. According to the transmission-line theory, S-parameters at the sample interfaces are written as

$$S_{11} = S_{22} = \frac{\Gamma(1 - z^2)}{1 - \Gamma^2 z^2} , \qquad (1)$$

$$S_{21} = S_{12} = \frac{z(1 - \Gamma^2)}{1 - \Gamma^2 z^2} , \qquad (2)$$

where  $z=\exp(-\gamma L)$ , L is the sample length,  $\gamma$  is the propagation constant in a sample, and  $\Gamma$  is the reflection coefficient at a sample incidence plane. Right-hand sides of Eqs. (1) and (2) are functions of the permittivity of a sample, so the permittivity can be calculated by solving Eqs. (1) and

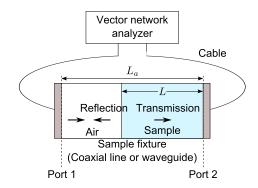


Fig. 1. Schematic drawing of a fixture of the transmission/reflection method.

(2). We should note, however, that reflections at connections between a fixture and cables are not considered in deriving Eqs. (1) and (2), so the resulting permittivity can be deviated by the reflection effect which is inevitably appeared in actual measurements [2]. In this paper, we studied the effect of reflections at fixture ends on permittivity measurements with the T/R method, and also clarified its fixture-type dependence.

# II. NUMERICAL CALCULATIONS

In this section, we discuss the effect of reflections at fixture interfaces by performing numerical calculations. For simplicity, we assume S-parameters at connectors of a fixture by

$$S^{\text{Ref}} = \begin{pmatrix} p & \sqrt{1-p^2} \\ \sqrt{1-p^2} & p \end{pmatrix} , \qquad (3)$$

where  $p \in \mathbb{R}$  is the reflection coefficient at connectors, and we calculate combined S-parameters of connectors, a fixture, and a sample for the frequency band ranging from 1 to 18 GHz. Next, we derive S-parameters at sample interfaces by transforming reference planes where reflections at fixture ends are not taken into account. Finally, the permittivity of a sample is calculated by iteratively solving a following equation;

$$S_{21}S_{12} - S_{11}S_{22} = \frac{z^2 - \Gamma^2}{1 - \Gamma^2 z^2} , \qquad (4)$$

where  $S_{ij}$  are S-parameters at sample interfaces. We let the sample length L=5 mm, and a coaxial line fixture having the fixture length  $L_a=40$  mm is considered in calculations.

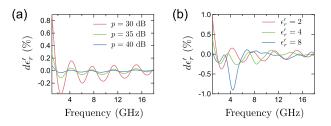


Fig. 2. Deviations of the relative permittivity calculated from S-parameters without considering reflections at fixture interfaces. In (a) and (b), traces for different p ( $\epsilon_r^{/\mathrm{set}}=2$  is fixed), and those for different  $\epsilon_r^{/\mathrm{set}}$  (p=-30 dB is fixed), are plotted against the frequency, respectively.

Figure 2 shows deviations of the relative permittivity,  $d\epsilon'_r = \left(\epsilon'_r^{\rm cal} - \epsilon'_r^{\rm set}\right)/\epsilon'_r^{\rm set}$ , where  $\epsilon'_r^{\rm cal}$  and  $\epsilon'_r^{\rm set}$  are calculated and setup values of the relative permittivity, respectively. For all calculations, the loss tangent of a sample is fixed;  $\tan \delta = 0.01$ . In Fig. 2(a) and (b), traces for different p ( $\epsilon'_r^{\rm set} = 2$  is fixed), and those for different  $\epsilon'_r^{\rm set}$  (p = -30 dB is fixed), are plotted against the frequency, respectively.

From Fig. 2(a), we can confirm ripples in the frequency characteristic of the permittivity due to multiple reflections are more pronounced with increasing p, especially in the low-frequency region. For the setups of this numerical demonstrations, a fixture whose reflection coefficient at connectors is similar to or less than -40 dB is preferable.

By increasing the relative permittivity, deviation properties become complicated as shown in Fig. 2(b), because the reflection coefficient at sample interfaces becomes large for high permittivity samples, which obscures resonance conditions of multiple reflections.

#### III. MEASUREMENT SYSTEM AND METHOD

In this section, we show results of permittivity measurements with the T/R method using different types of fixtures. The four fixtures used in this study are shown in Fig. 3. Fixtures named (a) PC7-long, (b) PC7-short, and (c) N-long are air-dielectric 7-mm coaxial lines (airlines). Connector types are PC-7 and type N, and for PC-7, fixtures having two different lengths are used. Fixture lengths,  $L_a$ , of PC7long, PC7-short, and N-long are about 40 mm, 7 mm, and 50 mm, respectively. Connection structures of these fixtures are different in the contact structures of center conductors. The center conductor of the type N fixture is made of a single metal part, and its pin is fixed. The center conductors of PC-7 fixtures have, by contract, double-layered structures. Their pins, which are inserted in collets of cable ends, are movable by spring structures. Therefore, compared to a fixed-type fixture, there are concerns about the repeatability of connection and the effect of reflections at connectors; further, the pin's axis of PC7-short is not stable, because the miniaturized center conductor has a problem with the machining accuracy of the double-layered structure. A typical measurement setup using a coaxial line fixture is shown in Fig. 4(a). We evaluate the effects of these differeces of fixture structures on permittivity measurements.

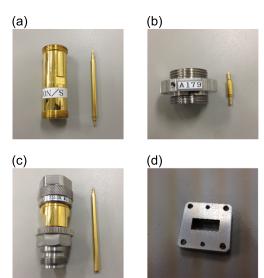


Fig. 3. Photos of fixtures used in this study. (a) PC-7 coaxial fixture of  $L_a\sim 40\,$  mm (PC7-long), (b) PC-7 coaxial fixture of  $L_a\sim 7\,$  mm (PC7-short), (c) type N coaxial fixture of  $L_a\sim 50\,$  mm (N-long), and (d) X-band waveguide fixture of  $L_a\sim 10\,$  mm (X-band WG)

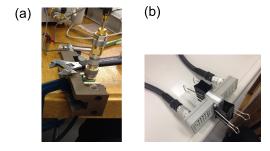


Fig. 4. Photos of measurement setups of (a) a coaxial line fixture and (b) a waveguide fixture.

We also compare coaxial airline fixtures with a X-band waveguide fixture of  $L_a \sim 10$  mm (named as X-band WG, see Fig. 3 (d)). The waveguide fixture and waveguide to coaxial adapters at cable ends are fixed and aligned by using clips and rods (see Fig. 4(b)).

After performing a calibration on a vector network analyzer (VNA) (the open-short-load-through (OSLT) calibration with a sliding load termination is used on coaxial line measurements, whereas the through-reflect-line (TRL) calibration is used on waveguide measurements), a toroidal-shaped PTFE sample is measured by using PC7-long, PC7-short, and N-long fixtures, and a cuboid-shaped PTFE sample is measured by using the X-band WG fixture. Both samples are machined from the same bulk, and both sample legths are about 5 mm. For each fixture, we repeatedly (6 times) measured S-parameters, where we remove and rotate a fixture (by about 60 degrees for coaxial line fixtures, and 180 degrees for a waveguide fixture), and re-connect a fixture to cables in each interval between two consecutive measurements.

From measured S-parameters and dimensions, we calculate

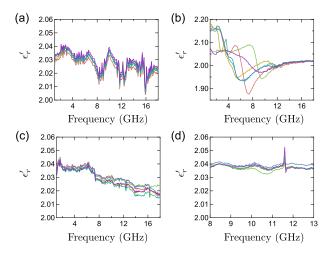


Fig. 5. 6 pairs of the relative permittivity  $\epsilon'_r$  traces for PTFE samples calculated from results of repeated measurements of S-parameters using (a) PC7-long, (b) PC7-short, (c) N-long, and (d) X-band WG fixtures.

the permittivity of a sample by iteratively solving Eq. (4). Note that Eq. (4) is independent of a position of a sample in a fixture.

# IV. MEASUREMENT RESULTS AND DISCCUSION

Figure 5 shows 6 pairs of the relative permittivity  $\epsilon'_r$ traces calculated from results of repeated measurements of S-parameters. Measured frequency bands are 1 to 18 GHz and 8 to 13 GHz for coaxial line fixtures (Fig. 5(a)-(c)) and a waveguide fixture (Fig. 5(d)), respectively. By comparing Fig. 5(a) and (b) with Fig. 5(c), we can clearly see ripples due to multiple reflections at connectors in permittivity results for PC-7 fixtures, which can be attributed to an unstable metal contact between a pin with a string structure and a collet at a cable end. Also, PC7-short fixture gives a worse connecting repeatability than other fixtures especially in the low-frequency region (< 12 GHz), which can be explaind by an instability of the axis of pins of PC7-short; the connecting repeatability is not established sufficiently, and the effect of a stray capacitance of an air gap caused by a misalignment of the axis become pronounced in the low-frequency region.

Compared to three coaxial line fixtures, X-band WG fixture gives the most flat results without large repples, except a resonance of uncertain cause located near 11.6 GHz, as shown in Fig. 5(d).

We focus two types of uncertainty factors for permittivity measurements with the T/R method in this study. One is the connecting repeatability between a fixture and cables. This contribution is evaluated from the standard deviation of the 6 pairs of permittivities calculated from results of repeated measurements of S-parameters;

$$u_R(\epsilon_r') = \sqrt{\frac{\sum_{i=1}^N \left(\epsilon_{r,i}' - \hat{\mu}\right)^2}{N-1}} , \qquad (5)$$

where N=6 is the number of measurements,  $\epsilon'_{r,i}$  is the relative permittivity calculated from *i*-th S-parameter results,

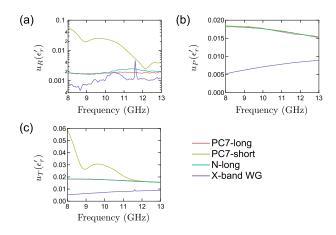


Fig. 6. Calculated permittivity uncertainties of (a) the connection-repeatability contribution  $u_R(\epsilon_r')$ , (b) the uncertainty-propagation contribution  $u_P(\epsilon_r')$ , and (c) the total uncertainty  $u_T(\epsilon_r')$  corresponding to four different fixtures.

and  $\hat{\mu} = \sum_{i=1}^{N} \epsilon'_{r,i}/N$ . The permittivity uncertainty due to the connecting repeatability depends on fixtures, as is qualitatively apparent from results shown in Figure 5.

The other uncertainty factor focused in this study is the propagation of uncertainties of measured quantities, i.e. Sparameters and dimensions of a sample and a fixture. The permittivity uncertainty due to the uncertainty propagation is evaluated by using a following equation;

$$u_{P}(\epsilon_{r}')^{2} = \sum_{i,j} \left\{ \left| \frac{\partial \epsilon_{r}'}{\partial |S_{ij}^{F}|} \right|^{2} u(|S_{ij}^{F}|)^{2} + \left| \frac{\partial \epsilon_{r}'}{\partial \theta_{ij}^{F}} \right|^{2} u(\theta_{ij}^{F})^{2} \right\}$$

$$+ \left| \frac{\partial \epsilon_{r}'}{\partial L} \right|^{2} u(L)^{2} + \left| \frac{\partial \epsilon_{r}'}{\partial L_{a}} \right|^{2} u(L_{a})^{2} , \qquad (6)$$

where  $i=\{1,2\},\,j=\{1,2\},\,S^{\rm F}_{ij}$  is the measured S-parameter at fixture interfaces,  $\theta^{\rm F}_{i,j}$  is the phase of  $S^{\rm F}_{i,j}$ , and u(X) denotes the uncertainty of X. In this study, we substitute averaged values of S-parameters calculated from results of 6-repeated measurements to Eq. (6), and  $u(|S^{\rm F}_{ij}|)$  and  $u(\theta^{\rm F}_{ij})$  are evaluated from the residual deviations of the pre-calibration owing to the incompleteness of calibration standards [3]–[5], and we let  $u(L)=u(L_a)=10~\mu{\rm m}$ .

Reflecting the fact that uncertainties of S-parameters vary depending on calibration methods used on a VNA, the accuracy of permittivity measurements also depends on a VNA calibration method [6]; the uncertainty of the permittivity, for example, can be reduced by using the TRL calibration instead of the OSLT calibration.

Figure 6 shows permittivity uncertainties of (a) connecting-repeatability contribution  $u_R(\epsilon_r')$ , (b) uncertainty-propagation contribution  $u_P(\epsilon_r')$ , and (c) the total uncertainty calculated from  $u_T(\epsilon_r') = \sqrt{u_P(\epsilon_r')^2 + u_R(\epsilon_r')^2}$ , corresponding to four different fixtures. The frequency range is limited to X band, 8 to 13 GHz.

Among three coaxial line fixtures, PC7-long and N-long provide comparable  $u_R(\epsilon_r')$ , but PC7-short shows a substantial  $u_R(\epsilon_r')$  in the low-frequency region. In contrast,  $u_P(\epsilon_r')$  for

three coaxial line fixtures are nearly equal, because  $u_P(\epsilon'_r)$ depends on a VNA calibration method which dominantly determines the uncertainties of S-parameters, but it is independent of a fixture type. From Fig. 6(c), we can see both PC7-long and N-long provide about the same  $u_T(\epsilon_r)$ , because  $u_P(\epsilon'_r)$  is the dominant uncertainty factor for the case of these two fixtures, but  $u_R(\epsilon_r)$  for PC7-short is the dominant uncertainty factor in the low-frequency region (< 12 GHz), thus PC7-short provides a much larger  $u_T(\epsilon'_r)$  as large as more three times of those for PC7-long and N-long for the most significant case. Therefore, we can conclude that N-long is the most desirable coaxial line fixture among three, in order to establish the connecting repeatability of a fixture, and to avoid ripples in the frequency characteristic of the permittivity due to multiple reflections. Note that deviations, or ripples, caused by reflections at fixture interfaces are partly included in  $u_R(\epsilon'_r)$ , but possibly they should be considered in a more complete way in uncertainty evaluations.

Compared to coaxial line fixtures, X-band WG provides a better  $u_R(\epsilon_r')$  except near the resonance point, which is attributed to a larger contact area at connection points of a waveguide fixture, and to a smaller reflection coefficient at connectors. Also, X-band WG shows smaller  $u_P(\epsilon_r')$  as small as less than one-third of those for coaxial line fixtures for the most significant case. Because of differences in calibration kits between coaxial line measurements and waveguide measurements, different calibration methods are used on a VNA, which affect the uncertainties of the S-parameters and that of the permittivity. Since the TRL calibration used in waveguide measurements provides better accuaracy,  $u_P(\epsilon_r')$  for X-band WG is quite reduced. Therefore,  $u_T(\epsilon_r')$  for X-band WG is smallest among those for fixtures used in this study.

# V. CONCLUSION

For permittivity measurements obtained by using the T/R method, the effect of reflections at fixture interfaces is considered by doing numerical calculations and by performing experimental measurements using four different fixtures. According to numerical calculations, reflections at fixture ends generate ripples in the frequency characteristic of the permittivity caused by multiple reflections. From comparisons of measurement results using four fixtures, we quantitatively confirmed that it is preferable to use a fixture whose reflection coefficient at connectors and connecting repeatability are sufficiently low and high, respectively. We clarified that a waveguide fixture is suitable for the T/R method, because it has a good connecting repeatability, and because the uncertainties of the S-parameters for waveguide measurements can be reduced by using the TRL calibration on a VNA. Although it is unable to disregard the fact that a coaxial line fixture has the advantage that broadband measurements can be performed by using a single pair of a coaxial line fixture and a sample, and the fact that a waveguide fixture has the disadvantage that rather large samples are needed in for measurements the low-frequency region using a waveguide fixture, it is worthwhile to consider the use of a waveguide fixture in the high-frequency region because of the reduced uncertainty of the permittivity.

- J. Baker-Jarvis, "Transmission/Reflection and Short-Circuit Line Permittivity Measurements," NIST Technical Note 1341, 1990.
- [2] IEEE 287-2007 IEEE Standard for Precision Coaxial Connectors (DC to 110 GHz)
- [3] D. Rytting, "Advances in microwave error correction techniques," Hewlett-Packard RF & Microwave Symposium, Jun 1987.
- [4] "Guidelines on the evaluation of vector network analysers (VNA)," Tech. Rep. EURAMET/cg-12/v.01, EURAMET, Jul 2007.
- [5] J. P. M. de Vreede, "Proposed Revision to the EA Guidelines on Evaluation of Vector Network Analysers (VNA) to include Uncertainty in Phase," ANAMET Report 038, Aug 2003.
- [6] Y. Kato, M. Horibe, M. Ameya, S. Kurokawa, and Y. Shimada, "New uncertainty analysis and simplified verification method for permittivity measurements using the Transmission/Reflection method by utilizing a weighted factor," The 2014 Conference on Precision Electromagnetic Measurements, Mo-P110-P61, Rio de Janeiro, 2014.

# Free-space reconstruction of the electrical properties of carbon nanotube based composites in the Q-band range

Ahmed M. Hassan<sup>1</sup>, Jan Obrzut<sup>2</sup>, Edward J. Garboczi<sup>3</sup>.

<sup>1</sup>Engineering Laboratory, Materials and Structural Systems Division

<sup>2</sup>Material Measurement Laboratory, Materials Science and Engineering Division National Institute of Standards and Technology, Gaithersburg, MD 20899

<sup>3</sup>Material Measurement Laboratory, Applied Chemicals and Materials Division National Institute of Standards and Technology, Boulder, CO 80305

Abstract — A free-space transmission-reflection measurement method for the non-destructive electrical characterization of carbon nanotube based composites was developed. Specifically, this versatile method measures the dielectric properties of the sample in the Q-band, corresponding to a frequency range of 30 GHz to 50 GHz, and can be used with specimens that are either thinner or thicker than the radiation penetration depth. This method also involves an error correction model in order to accurately reconstruct the constitutive dielectric properties of the composites from the measured scattering parameters. In order to perform the error-correction only two reference scattering parameters measurements are required: one from a metal plate of known reflection coefficient and the other from air with no specimen. The simplicity of our error-correction model makes the method attractive for research, development, and for quality control in the manufacturing environment.

Index Terms — Free space measurement; microwave errorcorrection model; nanocarbon composites; non-destructive testing

# I. INTRODUCTION

Carbon nanotubes (CNTs) composites have been incorporated in a wide range of applications, especially in the aerospace and automotive industries [1-3]. The mechanical, thermal, and electrical properties of these composites are predominantly determined by the properties of the CNTs and their dispersion in the embedding polymer matrix [2-3]. A technique to evaluate the properties of these composites is based on quantifying the free-space microwave scattering parameters.

However, free-space microwave characterization is plagued by the mismatch between the two antennas and free space, the multiple reflections between the antennas and the material under test (MUT), and the diffraction of the waves in free space. Therefore, free space systems require elaborate procedures to extract the electrical properties of the MUT. These procedures can involve the movement of the antennas, the movement of the MUT, and the measurement of the scattering parameters from multiple references [4-5].

One of the standard calibration techniques is the Thru-Reflect-Line (TRL) calibration technique [4-5]. However, the main challenge in this calibration is the need to move the antennas disturbing the alignment/coupling between them. The Line-Network-Network (LNN) procedure is another calibration technique that does not require a reflect standard [5]. Instead, this methodology corrects the measurement using four measurements: one thru and three MUT locations separated by an equal distance  $\Delta x$  [5]. However, it is difficult to implement the multiple shifting of the MUT in the quality control of high-thru-put unrolling thin film materials in a manufacturing line.

In this paper, we present a free-space Q-band experimental system for non-destructive non-contact characterization of CNT composites. For this system, we have devised a simple and accurate error correction model that mitigates the limitations of the previous calibration techniques. Only two reference scattering parameters measurements are required: one from a metal plate of known reflection coefficient and the other from air with no specimen. The use of microwaves in the Q-band, defined to be between 30 GHz and 50 GHz, is a broadband technique that is capable of providing both the real and imaginary parts of the complex dielectric permittivity constant, which can be related to the dispersion of the CNTs in the polymer matrix. The technique is relatively simple and, therefore, attractive for non-destructive quality control in the manufacturing environment.

# II. EXPERIMENTAL SETUP

Our Q-band non-contact microwave measurement system utilizes two horn antennas connected to a vector network analyzer. The distance between the antennas was 225 mm and the beam radius at the MUT plane in the middle between the antennas was roughly 52.5 mm. A holder, with an aperture in its center larger than the beam width, was utilized and

attached to a motorized stage for precise positioning of the MUT between the antennas. All the MUTs considered in this work had lateral dimensions of 300 mm x 300 mm or larger minimizing surface wave propagation and parasitic edge effects.

# III. ERROR CORRECTION MODEL

The scattering parameters of the MUT  $\{T_{11}, T_{21}, T_{22}, T_{12}\}$ are measured by the system, which is initially calibrated at the coaxial ends connected to the antennas (see Fig. 1). Therefore, the measurements are affected by propagation through antennas A1 and A2, as well as propagation in free space between the antennas and interfaces 1 and 2. In order to account for these effects and move the reference planes of the measurements from the coaxial ends to the plane of the MUT, two additional measurements are performed using references with known propagation characteristics. Specifically, these references are (i) a metal plate, for which we denote the scattering parameters as  $\{M_{11}, M_{21}, M_{22}, M_{12}\}$  and (ii) the scattering parameters from air or where no MUT is inserted between the two antennas,  $\{L_{11}, L_{21}, L_{22}, L_{12}\}$ . The corrected transmission,  $S_{21}^{MUT}$ , and the corrected reflection,  $S_{11}^{MUT}$ , from the MUT are:

$$S_{21}^{MUT} = \frac{G[T_{21}]}{G[L_{21}]} e^{-j\beta_0 d}$$
 (1)

$$S_{11}^{MUT} = \frac{G[T_{11} - L_{11}]}{G[M_{11} - L_{11}]} (-1),$$
 (2)

where G refers to time gating, d is the MUT thickness,  $j^2 = -1$  is the imaginary unit and  $\beta_0 = \omega/c_0$  is the calculated plane wave propagation factor in air. The time gating correction is performed by transforming the scattering parameters measurements from frequency domain to the time domain using the Inverse Fast Fourier Transform (IFFT). The first reflection/transmission is then isolated by multiplying the time domain measurement with a Gaussian window centered at the same time instant as the maximum of the first reflection/transmission. The width of the Gaussian window, typically in the range of about 15 ns, is selected to reject any additional spurious multiple reflections/transmissions.

In (1), the denominator  $G[L_{21}]$  normalizes  $S_{21}^{MUT}$  and deconvolutes the antenna response, while  $e^{-j\beta_0d}$  adjusts the reference plane to interface 2 of the MUT. In (2), the subtraction of  $L_{11}$  removes any mismatch between the antenna and the connecting cable whereas the division with  $G[M_{11}-L_{11}]$  normalizes the reflection from the MUT,  $S_{11}^{MUT}$ . The metal plate reference reflects all the incident waves and, therefore, it is assumed to have a reflection magnitude of unity. The multiplication by -1 in (2) is performed to account for the fact that the reflection from the metal plate is 180 ° out of phase from the incident wave. Following the correction of  $S_{21}^{MUT}$  and  $S_{11}^{MUT}$  using (1) and (2), the complex relative

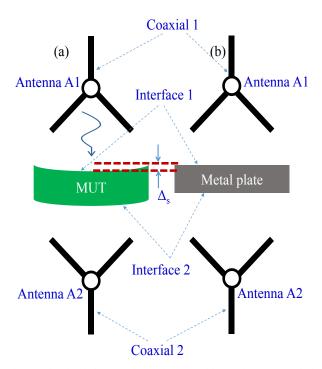


Fig. 1. Sketch of the experimental setup with (a) the MUT and (b) the calibrating metal plate inserted between the two antennas.

dielectric permittivity  $\varepsilon_r = \varepsilon_r' + j\varepsilon_r''$  can be extracted through a root searching algorithm [5-6].

# IV. EXPERIMENTAL RESULTS

In order to validate our error correction model, which is summarized in (1) and (2), we used a poly(methyl methacrylate) (PMMA) MUT with known complex relative dielectric permittivity  $\varepsilon_r \approx 2.5$  [7]. The PMMA MUT had a thickness d = 1.95 mm. The measured transmission and reflection from the MUT were corrected using (1) and (2) and the corresponding  $\varepsilon_r$  are plotted in Fig. 2. For comparison, the LNN procedure reported in [5] was used to correct the measured scattering parameters and the corresponding value of  $\varepsilon_r$  is also plotted in Fig. 2. The LNN error-correction model does not involve a metal plate standard and, therefore, is completely independent from our error-correction model developed in (1) and (2). The close agreement between both values of the complex relative dielectric permittivity  $\varepsilon_r$  in Fig. 2 validates our error-correction model. Furthermore, the reconstructed permittivity values are in good agreement with those reported for Plexiglas in [7].

In Fig. 3 we present the complex permittivity of a lossy CNT composite having thickness d = 1.95 mm. Fig. 3 shows that the CNT composite has a significant imaginary part in the relative permittivity indicating considerable losses. Again, good agreement is achieved between the simple calibration developed herein and the LNN calibration. Even though the MUT in Fig. 3 was lossy, the skin depth of the CNT composite is larger than the MUT thickness and, therefore,

significant  $S_{21}^{MUT}$  was measured. These MUTs are labelled as microwave transparent in comparison to microwave nontransparent MUTs with negligible  $S_{21}^{MUT}$ . We also measured other CNT composites with skin depth comparable to or less than the MUT thickness from which  $S_{21}^{MUT}$  is negligible. These results will also be presented.

#### V. UNCERTAINTY ANALYSIS

Several uncertainty factors such as instrumentation, dimensional uncertainty of the MUT geometry, and roughness of the MUT surfaces contribute to the combined uncertainty of the measurements. Typically, the standard uncertainty in the measured scattering parameters can be assumed to be within the manufacturer's specification for the network analyzer, about  $\pm$  0.05 dB for the magnitude and  $\pm$  0.5 ° for the phase. The largest contributing factor to the combined uncertainty is the uncertainty in the distribution of the film thickness and/or sagging of the thin film MUT, which is depicted by the bending in the interfaces of the MUT in the sketch shown in Fig. 1. The error-correction model assumes that the interfaces of the MUT and the metal plate are placed at precisely the same location. However, any thickness inhomogeneity or sagging in the thin film MUT can lead to a shift between the locations of the interfaces of the MUT and the interfaces of the metal plate. This shift is shown as  $\Delta_s$  in Fig. 1 and can distort the error correction model. However, this shift is on the order of  $\Delta_s$  < 100  $\mu$ m, which can be estimated to cause a maximum uncertainty of 5 % in  $\varepsilon_r$ .

# VI. MODELING OF THE ELECTRICAL PROPERTIES OF CARBON NANOTUBE COMPOSITES

understand the experimental measurements from CNT composites detailed in the previous sections, composite 2D models of CNTs embedded in a dielectric slab are developed similar to those reported in [8]. The basis of the model was to implement the CNT composite as multiple random arrays of infinitesimally thin wire antennas with the equivalent impedance of CNT. These random wire arrays were then embedded in a dielectric slab to account for the effect of the matrix of the composite on the electromagnetic signature of the CNTs. The model showed that the reflected power from the composite was sensitive to the exact locations of the CNTs and to their locations with respect to the interfaces of the dielectric slab [8]. This sensitivity to the location is one of the possible explanations for the variability in the measurements from different CNT composites exhibited in this work.

# VII. CONCLUSION

A Simple free-space calibration technique for the reconstruction of the relative dielectric properties of carbon nanotube based composites is developed and verified in the Q-

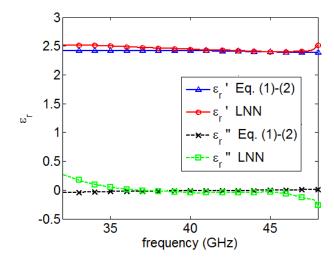


Fig. 2: Complex relative dielectric permittivity of a PMMA specimen obtained using the correction model in (1) and (2) (real  $\epsilon_r$ ' shown as  $\Delta$  and imaginary  $\epsilon_r$ " shown as  $\times$ ) versus the LNN calibration (real  $\epsilon_r$ ' shown as  $\alpha$  and imaginary  $\alpha$  are shown as  $\alpha$ ).

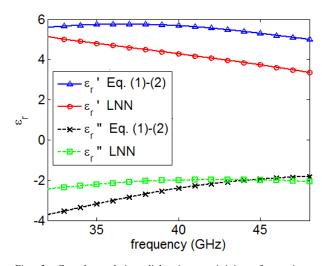


Fig. 3: Complex relative dielectric permittivity of a microwave transparent CNT composite obtained using the correction model in (1) and (2) (real  $\epsilon_r$ ' shown as  $\Delta$  and imaginary  $\epsilon_r$ " shown as  $\times$ ) versus the LNN calibration (real  $\epsilon_r$ ' shown as  $\sigma$  and imaginary  $\sigma$  shown as  $\sigma$ ).

band. The presented error correction procedure involves only two reference measurements: a *metal* plate and *air* with no MUT present. The reconstructed relative dielectric properties agree favorably with the values achieved using the previously reported LNN calibration technique, which requires four measurements, three MUT locations and an air measurement with no MUT present. In the future, we will develop electromagnetic models to correlate the measured dielectric properties with the constituents and internal structure of the CNT composites.

- [1] M. De Volder, S. Tawfick, R. Baughman, and A. Hart, "Carbon Nanotubes: Present and Future Commercial Applications," *Science*, vol. 339, pp. 535-539, 2013.
- [2] P. Maa, N. Siddiqui, G. Marom, J. Kim, "Dispersion and functionalization of carbon nanotubes for polymer-based nanocomposites: A review," *Composites: Part A*, vol. 41, 1345– 1367, 2010.
- [3] www.appliednanostructuredsolutions.com.
- [4] P. Bartley, Jr. and S. Begley, "Improved Free-Space S-Parameter Calibration," *Proceedings of the IEEE Instrumentation and Measurement Technology Conference*, pp. 372-375, 2005.
- [5] C. Orlob, T. Reinecke, E. Denicke, B. Geck, and I. Rolfes, "Compact Unfocused Antenna Setup for X-Band Free-Space Dielectric Measurements based on Line-Network-Network Calibration Method," *IEEE Transactions on Instrumentation* and Measurement, vol. 62, no. 7, 2013.
- [6] J. Baker-Jarvis, E. Vanzura, and W. Kissick, "Improved Technique for Determining Complex Permittivity with the Transmission / Reflection Method," *IEEE Transactions on Microwave Theory and Techniques*, vol. 38, no. 8, pp. 1096-1103, 1990.
- [7] P. Goldsmith, Quasioptical Systems: Gaussian Beam Quasioptical Propagation and Applications, Wiley-IEEE Press, page 81, 1998.
- [8] A. Hassan and E. Garboczi, "Electromagnetic scattering from randomly-centered parallel single-walled carbon nanotubes embedded in a dielectric slab," *IEEE Trans. on Antennas and Propag.*, vol. 62, no. 10, pp. 5230-5241, 2014.

# A calibration procedure for electronic calibration units

J. Stenarson<sup>†</sup>, C. Eiø<sup>‡</sup>, K. Yhland<sup>†</sup>

<sup>†</sup>SP Technical Research Institute of Sweden

<sup>‡</sup>NPL National Physical Laboratory, UK

Abstract — This paper presents a procedure for calibrating a Vector Network Analyzer (VNA) calibration kit, mechanical short, open, and load or electronic calibration unit, as a black box. The uncertainty is associated with each connector type in the calibration kit in the form of an uncertainty two-port. The method is validated by comparing results using different VNA test set configurations as well as a comparison to a traditional ripple technique.

Index Terms — VNA, Calibration, Electronic Calibration Unit, Uncertainty

# I. INTRODUCTION

In the past decade electronic calibration units (ECU) for vector network analyzers (VNA) have become important tools in the microwave industry. ECUs simplify the calibration procedure by reducing the number of connections necessary for a calibration. This is especially important for multi-port measurements where the number of connections can become very large when using mechanical calibration kits.

The traditional procedures for establishing traceability [1] are not adapted to ECUs. In [2] a procedure is described to characterize an ECU. It gives S-parameters and uncertainties for all ECU states. From a traceability perspective this seems as an obvious choice but for the end user it is quite demanding to propagate the uncertainties (and their correlations) through the calibration algorithm of choice although there do exist third party software that provide this capability [3, 4].

We propose a procedure where the uncertainties of all ECU states are collected into an uncertainty two-port associated with each ECU port. Nominally this uncertainty two-port is an ideal thru connection but its S-parameters have uncertainties. This simplifies the uncertainty calculation for the end user. The proposed procedure is based on the calibration comparison technique in [5] and association of uncertainty two-ports with calibration standards introduced in [6, 7].

For the end-user, it turns out that the expressions used to compute uncertainty in S-parameters using the uncertainty two-port approach has a lot in common with the traditional residual error model as used in [1]. This makes it easier to adopt.

# II. UNCERTAINTY MODEL

We propose to use an uncertainty two-port associated with each connector in a calibration kit, Fig. 1. For a standard mechanical calibration kit this means associating an uncertainty two-port with each connector sex, for an ECU it means associating an uncertainty two-port with each port of the ECU.

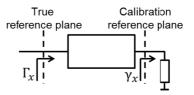


Fig. 1 Uncertainty two-port associated with reflection standard

This approach is very close to the one in [6, 7] but the difference is that the place of the true and model reference planes have been exchanged in this work. This new way of placing the reference planes aligns better with the guide to the expression of uncertainty in measurement (GUM) [8] where the true value is usually said to equal the estimated value with an uncertainty.

The true value of a calibration standard thus becomes

$$\Gamma_{\chi} = D + \frac{\gamma_{\chi}(1+T)}{1-M\gamma_{\chi}} \tag{1}$$

where  $\Gamma_x$  and  $\gamma_x$  is the true value and model value of standard x respectively.

After calibration using the calibration standard with an associated uncertainty two-port an estimated calset e that is the cascade connection of the true calset E, and the uncertainty two-port DTM is obtained, see Fig. 2.

For the case of a one-port calibration kit with three standards there is a one-to-one correspondence between the uncertainty two-port model and the method where an uncertainty is associated with each standard. It is assumed that it is possible to use the uncertainty two-port even when using more than three one-port standards per port. We believe this is reasonable and verification measurements done using different VNA configurations, reported later in this paper, indicate that this works in practice as well.

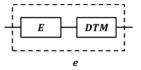


Fig. 2 After calibration the estimated calset, e, is the cascade of the true calset, E, and the uncertainty two-port DTM.

# A. Transfer calibration procedure

What is meant by transfer calibration procedure here is the process where the known uncertainties associated with a master calibration kit are transferred to a calibration kit under test, which is characterized but without associated uncertainties.

The transfer calibration procedure starts with two calibrations of the VNA resulting in two estimated calsets e (for the master kit) and e' (for the kit under test). For the purpose of deriving the expressions here all variables are viewed as being input quantities that require assignment of uncertainties at some point but for the purpose of deriving the expressions it can be assumed that they are regular variables.

The known uncertainty two-port for the master kit is given by

$$DTM = \begin{pmatrix} D & \sqrt{T} \\ \sqrt{T} & M \end{pmatrix} \tag{2}$$

and the unknown uncertainty two-port for the DUT kit

$$dtm = \begin{pmatrix} d & \sqrt{t} \\ \sqrt{t} & m \end{pmatrix} \tag{3}$$

By de-embedding the estimated calsets e and e' from each other an estimate of the difference between the calibrations can be obtained

$$\delta \tau \mu = e^{-1} \otimes e' \tag{4}$$

where the elements of  $\delta \tau \mu$  are given by

$$\delta \tau \mu = \begin{pmatrix} \delta & \sqrt{\tau} \\ \sqrt{\tau} & \mu \end{pmatrix} \tag{5}$$

Using the relations for e and e' we also obtain

$$\delta \tau \mu = e^{-1} \otimes e' = (E \otimes DTM)^{-1} \otimes (E \otimes dtm) = DTM^{-1} \otimes E^{-1} \otimes E \otimes dtm = DTM^{-1} \otimes dtm$$
 (6)

Now solve for the unknown two-port dtm

$$d = D + \frac{T\delta}{1 - M\delta} \tag{7}$$

$$t = \frac{\tau T}{(1 - M\delta)^2} \tag{8}$$

$$m = \mu + \frac{M\tau}{1 - \delta M} \tag{9}$$

The nominal value of the unknown two-port can be computed by (7)-(9) setting any uncertainties to zero. The sensitivity coefficients for d, t, and m are given in Table 1.

TABLE 1 SENSITIVITY COEFFICIENTS FOR D, T, AND M

Variable	Sensitivity	Nominal DTM	DTM with values
	∂d ∂D	1	1
d	∂d ∂T	δ	$\frac{\delta}{1-\delta M}$
	∂d ∂M	$\delta^2$	$\frac{T\delta^2}{(1-\delta M)^2}$
t	$\frac{\partial t}{\partial T}$	τ	$\frac{\tau}{(1-\delta M)^2}$
· ·	<u>∂t</u> ∂M	$2 au\delta$	$\frac{2\tau T\delta}{(1-\delta M)^3}$
m	<u>∂m</u> ∂M	τ	$\frac{\tau}{(1-\delta M)^2}$

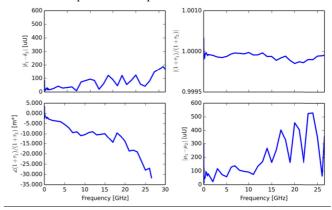
This means the transfer calibration will give both values (7)-(9) and sensitivities to compute uncertainties from Table 1 for each of d, t, and m.

# B. Verification of validity of the uncertainty model

In order to verify that the uncertainty model is valid we compare two cases:

- 1.  $\delta_1$ ,  $\tau_1$ , and  $\mu_1$  for the case where the VNA was calibrated at the front panel using a test port adapter
- 2.  $\delta_2$ ,  $\tau_2$ , and  $\mu_2$  for the case where the VNA was calibrated at the end of a long test port cable.

In both cases the coaxial 3.5 mm test port was calibrated using an ECU and a mechanical calibration kit (short-openload technique using table based models) and the transfer calibration equation (6) was used to compute the difference in the calibration sets. This difference should be independent of the VNA configuration. In Fig. 3 the differences,  $|\delta_1 - \delta_2|$ ,  $\frac{1+\tau_1}{1+\tau_2}$ , and  $|\mu_1 - \mu_2|$ , between the two cases are plotted. It can be seen that the difference is well below normal uncertainties for calibrations in a 3.5 mm connector interface. The calibration sequence was repeated 4 times.



As an additional verification the two-port ripple technique [6, 7] estimation of a DUT calibration kit (Type-N with broad band load) has been compared to the calibration transfer technique where the uncertainties of the master calibration kit were determined using the two-port ripple technique.

Fig. 4 shows the result for d. The black curve is the estimated value of d from the calibration transfer and the red field is the associated uncertainty that was estimated using the two-port ripple technique on the master kit, the green lines are the two-port ripple technique applied to the DUT kit. When using the two-port ripple technique the envelope of the air-line ripple gives the estimate of the residual error [7] which means we expect the envelope of the ripple to coincide with the estimated value using the method presented in the paper.

There is very good agreement between the two methods and just as good agreement for  $m_s$  see Fig. 5.

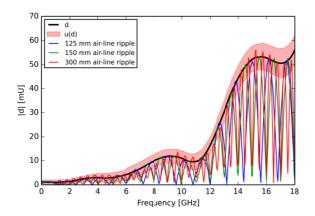


Fig. 4 Comparison of two-port ripple technique using three air-lines and calibration transfer for the *d* term.

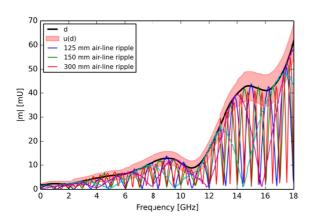


Fig. 5 Comparison of two-port ripple technique using three air-lines and calibration transfer for the *m* term.

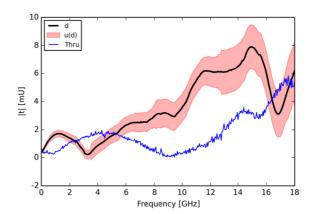


Fig. 6 Comparison of two-port ripple technique estimation of *t* using the thru standard and calibration transfer for the *t* term.

As can be seen in Fig. 6 there is rather poor agreement for the tracking term but this is expected since the tracking term is poorly estimated by the two-port ripple technique when using sexed connectors.

# III. MODEL EQUATIONS FOR UNCERTAINTY TWO-PORT USING SOLT AND SOLR

Using the uncertainty two-port for a SOLT or SOLR calibration kit, equations relating the error corrected  $(s_{ij})$  S-parameters to the true-values  $(S_{ij})$  can be derived. This derivation is done assuming the only uncertainty components are associated with the calibration standards.

# A. Model equations using SOLT

The full model equations for the SOLT case are included in an appendix. Here we present the sensitivity coefficients with respect to the dtm parameters obtained in the transfer calibration procedure

TABLE 2 SENSITIVITY COEFFICIENTS FOR SOLT

Variable	Sensitivity	Nominal dtm sensitivities
	$\frac{\partial S_{11}}{\partial d_1}$	$1 - s_{12} s_{21}$
$S_{11}$	$\frac{\partial S_{11}}{\partial t_1}$	<i>s</i> <sub>11</sub>
	$\frac{\partial S_{11}}{\partial m_1}$	$s_{11}^2$
C	$\frac{\partial S_{12}}{\partial d_2}$	$-s_{11}s_{12}$
$S_{12}$	$\frac{\partial S_{12}}{\partial m_2}$	$s_{12}s_{22}$
$S_{12}$	$\frac{\partial S_{21}}{\partial d_1}$	$-s_{21}s_{22}$

	$\frac{\partial S_{21}}{\partial m_1}$	s <sub>11</sub> s <sub>21</sub>
$S_{22}$	$\frac{\partial S_{22}}{\partial d_2}$	$1 - s_{12} s_{21}$
	$\frac{\partial S_{22}}{\partial t_2}$	S <sub>22</sub>
	$\frac{\partial S_{22}}{\partial m_2}$	$s_{22}^{2}$

# B. Model equations using SOLR

Just like for the SOLT case the full equations are included in an appendix and here we present the sensitivity coefficients with respect to the dtm parameters obtained in the transfer calibration procedure

TABLE 3 SENSITIVITY COEFFICIENTS FOR SOLR

TABLE 3 SENSITIVITY COEFFICIENTS FOR SOLR				
Variable	Sensitivity	Nominal dtm sensitivities		
	$\frac{\partial S_{11}}{\partial d_1}$	1		
S <sub>11</sub>	$\frac{\partial S_{11}}{\partial t_1}$	$s_{11}$		
	$\frac{\partial S_{11}}{\partial m_1}$	$s_{11}^{2}$		
	$\frac{\partial S_{11}}{\partial m_2}$	$S_{12}S_{21}$		
	$\frac{\partial S_{12}}{\partial m_1}$	$S_{11}S_{12}$		
$S_{12}$	$\frac{\partial S_{12}}{\partial m_2}$	$S_{12}S_{22}$		
3 <sub>12</sub>	$\frac{\partial S_{12}}{\partial t_1}$	$\frac{s_{12}}{2}$		
	$\frac{\partial S_{12}}{\partial t_2}$	$\frac{s_{12}}{2}$		
	$\frac{\partial S_{21}}{\partial \mathbf{m}_1}$	$S_{11}S_{21}$		
$S_{21}$	$\frac{\partial S_{21}}{\partial m_2}$	$s_{21}s_{22}$		
321	$\frac{\partial S_{21}}{\partial t_1}$	$\frac{s_{21}}{2}$		
	$\frac{\partial S_{21}}{\partial t_2}$	$\frac{s_{21}}{2}$		
	$\frac{\partial S_{22}}{\partial d_2}$	1		
_	$\frac{\partial S_{22}}{\partial t_2}$	s <sub>22</sub>		
$S_{22}$	$\frac{\partial S_{22}}{\partial m_1}$	$S_{12}S_{21}$		
	$\frac{\partial S_{22}}{\partial m_2}$	$s_{22}^2$		

# C. Influence of the Thru standard

To get a complete model equation for the influence of the calibration standards the uncertainties associated with the thru standard should also be included, which is typically (but not always) a flush thru for the SOLT algorithm and a reciprocal component for the SOLR algorithm. This will be addressed in a later paper.

The uncertainties associated with the flush thru come from connector imperfections like pin depth, difference in connector cross-section and alignment etc. The uncertainties associated with the reciprocal device will come from the non-reciprocity of the device and should be negligible for reasonable devices.

# IV. CONCLUSION

We have shown that it is reasonable to associate an uncertainty two-port with both a normal mechanical calibration kit and an ECU that has three or more reflection standards for each port. The verification was done by ensuring that the calibration transfer is the same for a calibration at the front panel and at the end of a long test-port cable. A comparison was also made against a standard ripple technique.

We have also derived equations that can be used to compute uncertainties in measurements using the uncertainty two-port method for both the SOLT and SOLR calibration algorithms. The effects of non-ideal thru will be investigated in a later paper.

# ACKNOWLEDGEMENT

This work was funded through the European Metrology Research Programme (EMRP) Project SIB62 "Metrology for New Electrical Measurement Quantities in High-frequency Circuits". The EMRP is jointly funded by the EMRP participating countries within EURAMET and the European Union.

- [1] "Guidelines on the Evaluation of Vector Network Analysers (VNA)," Euramet EURAMET/cg-12/v.01, 2007.
- [2] J. A. Jargon, D. F. Williams, T. M. Wallis, D. X. LeGolvan, and P. D. Hale, "Establishing traceability of an electronic calibration unit using the NIST Microwave Uncertainty Framework," in Microwave Measurement Conference (ARFTG), 2012 79th ARFTG, 2012, pp. 1-5.
- [3] H. Sagl, "Multiport S-parameters Software MMS4."
- [4] M. Wollensack, J. Hoffmann, J. Ruefenacht, and M. Zeier, "VNA Tools II: S-parameter uncertainty calculation," in Microwave Measurement Conference (ARFTG), 2012 79th ARFTG, 2012, pp. 1-5.
- [5] D. F. Williams, R. B. Marks, and A. Davidson, "Comparison of On-Wafer Calibrations," in ARFTG Conference Digest-Winter, 38th, 1991, pp. 68-81.
- [6] J. Stenarson and K. Yhland, "Residual error models for the SOLT and SOLR VNA calibration algorithms," in 69th ARFTG Conference, Honolulu Hawaii, 2007.

- [7] J. Stenarson and K. Yhland, "A new assessment method for the residual errors in SOLT and SOLR calibrated VNAs," in 69th ARFTG Conference, Honolulu Hawaii, 2007.
- [8] JCGM, "Evaluation of measurement data Guide to the expression of uncertainty in measurement," JCGM JCGM 100:2008, 1993.
- [9] N. Ridler and M. Salter, "A generalised approach to the propagation of uncertainty in complex S-parameter measurements," in 64th ARFTG Microwave Measurements Conference, Fall 2004, 2004, pp. 1-14.
- Conference, Fall 2004, 2004, pp. 1-14.
  [10] N. M. Ridler and M. J. Salter, "An approach to the treatment of uncertainty in complex S-parameter measurements," Metrologia, vol. 39, pp. 295-302, 2002.
- [11] K. Yhland and J. Stenarson, "A simplified treatment of uncertainties in complex quantities," in Conference on Precision Electromagnetic Measurements, London, 2004, pp. 652-653.

# APPENDIX A SOLT MODEL EQUATIONS

These are the equations that are linearized to obtain the sensitivity coefficients in Table 2

$$\begin{split} S_{11} &= \frac{d_1^2(-m_1\Delta_s + m_1^2s_{11} - m_1 + s_{22}) + d_1t_1(-2m_1s_{11} + \Delta_s + 1) + s_{11}t_1^2}{d_1(-m_1\Delta_s + m_1^2s_{11} - m_1 + s_{22}) - m_1s_{11}t_1 + t_1} \\ S_{12} &= \frac{s_{12}t_2}{d_2(-m_2\Delta_s + m_2^2s_{22} - m_2 + s_{11}) - m_2s_{22}t_2 + t_2} \\ S_{21} &= \frac{s_{21}t_1}{d_1(-m_1\Delta_s + m_1^2s_{11} - m_1 + s_{22}) - m_1s_{11}t_1 + t_1} \\ S_{22} &= \frac{d_2^2(-m_2\Delta_s + m_2^2s_{22} - m_2 + s_{11}) + d_2t_2(-2m_2s_{22} + \Delta_s + 1) + s_{22}t_2^2}{d_2(-m_2\Delta_s + m_2^2s_{22} - m_2 + s_{11}) - m_2s_{22}t_2 + t_2} \end{split}$$

Where  $\Delta s = s_{11}s_{22} - s_{12}s_{21}$ .

# APPENDIX B SOLR MODEL EQUATIONS

These are the equations that are linearized to obtain the sensitivity coefficients in Table 3

$$\begin{split} S_{11} &= \frac{m_2 \Delta_s (t_1 - d_1 m_1) + d_1 (m_1 s_{11} + m_2 s_{22} - 1) - s_{11} t_1}{-m_1 m_2 \Delta_s + m_1 s_{11} + m_2 s_{22} - 1} \\ S_{12} &= \frac{s_{12} \sqrt{t_1} \sqrt{t_2}}{m_1 m_2 \Delta_s - m_1 s_{11} - m_2 s_{22} + 1} \\ S_{21} &= \frac{s_{21} \sqrt{t_1} \sqrt{t_2}}{m_1 m_2 \Delta_s - m_1 s_{11} - m_2 s_{22} + 1} \\ S_{22} &= \frac{m_1 \Delta_s (t_2 - d_2 m_2) + d_2 (m_1 s_{11} + m_2 s_{22} - 1) - s_{22} t_2}{-m_1 m_2 \Delta_s + m_1 s_{11} + m_2 s_{22} - 1} \end{split}$$

# Offset-Short Vector-Network-Analyzer Calibration with Simultaneous Modeling of Calibration Standards

Arkadiusz Lewandowski\*, Wojciech Wiatr\*, Paweł Barmuta\*†
\*Institute of Electronic Systems, Warsaw University of Technology
00-665 Warsaw, Poland
†Department of Electrical Engineering, KU Leuven
B-3001 Leuven, Belgium
E-mail: a.lewandowski@elka.pw.edu.pl

Abstract—We present an improved offset-short vector-network-analyzer calibration method which allows to identify broadband equivalent-circuit models of the offset-short standards and an imperfect thru connection. Our approach is based on the multi-frequency formulation of the vector-network-analyzer calibration problem in which parameters of the models are identified simultaneously with the vector-network-analyzer calibration coefficients at all frequencies. Thus, the impact of the constraints imposed by the models is also reflected in the calibration coefficients. We illustrate our approach with experimental results for an offset-short calibration in coaxial 3.5 mm connector. These results demonstrate that our method reduces the impact of measurement errors, and extends the bandwidth of the calibration.

# I. INTRODUCTION

In this paper, we report on an improved offset-short vectornetwork-analyzer calibration method which identifies broadband models of calibration standards along with the vectornetwork-analyzer (VNA) calibration coefficients. The offsetshort calibration considered in this work is a special case of the multi-reflect-thru calibration [1] which uses multiple offsetreflects and a thru connection. An offset-reflect is constructed by terminating a transmission-line section with a highlyreflective load, typically realized as a short or an open circuit. It is assumed that offset-reflects attached to a given VNA port have transmission-line sections with the same unknown propagation constant, and that all offset-reflects have the same unknown terminating impedance. The unknown propagation constant and terminating impedance are then determined along with the VNA calibration coefficients. Thus, the multi-reflectthru method may be considered as dual with respect to the multiline thru-reflect-line (TRL) [2], since both methods use unknown transmission-line sections and an unknown highlyreflective load, but in a different manner.

In the traditional offset-short method, the propagation constant and reflection coefficient of the terminating impedance are determined separately at each measurement frequency. Thus, any broadband constraints on these parameters, such us causality, or constraints resulting from a underlying physical model cannot be accounted for. On the other hand, due to a large impact of connection nonrepeatability on measurements of highly-reflective loads [3], the propagation constant

identified in the offset-shorts method is more vulnerable to those errors than in the multiline TRL method. Thus, artifacts may appear in this constant that do not reflect the actual behavior of the transmission lines. Also, the imperfection of thru connection in coaxial measurements affects the estimate of the reflection coefficient of the offset-short terminating impedance [4].

In this work, we present an improved offset-short calibration method which allows to impose broadband models on the propagation constant, short-circuit impedance, and an imperfect thru connection. Our approach is based on the multi-frequency formulation of the VNA calibration problem in which parameters of the these model are identified simultaneously with the VNA calibration coefficients at all frequencies [5], [6].

# II. THEORY

# A. Multi-frequency calibration

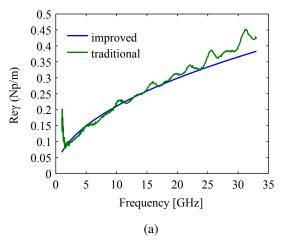
In the multi-frequency formulation of the VNA calibration problem, we use the maximum-likelihood estimation method [7], with the likelihood function given by [5]:

$$L\left(\boldsymbol{\theta}_{1},\ldots,\boldsymbol{\theta}_{K},\boldsymbol{\varphi},\sigma_{1}^{2},\ldots,\sigma_{K}^{2}\right)=\prod_{k=1}^{K}L_{k}\left(\boldsymbol{\theta}_{k},\boldsymbol{\varphi},\sigma_{k}^{2}\right),\quad(1)$$

where the vectors  $\theta_1, \ldots, \theta_K$  denote the unknown VNA calibration coefficients for frequencies  $f_k$ , for  $k=1,\ldots,K$ , the vector  $\varphi$  contains the unknown parameters of the calibration standard models, while the likelihood function at the frequency  $f_k$  is written as:

$$L_k(\boldsymbol{\theta}_k, \boldsymbol{\varphi}, \sigma_k^2) = p(\mathbf{r}_k(\boldsymbol{\theta}_k, \boldsymbol{\varphi})), \qquad (2)$$

where the  $\mathbf{r}_k\left(\boldsymbol{\theta}_k, \boldsymbol{\varphi}\right)$  denotes the residual error (*i.e.*, a difference between a calibration standard definition and its prediction from a raw measurement),  $p(\cdot)$  is the probability density function of the measurement errors, and  $\sigma_1^2, \ldots, \sigma_K^2$  are unknown residual error-variances. We can show that maximization of (1) with respect to  $\sigma_1^2, \ldots, \sigma_K^2$  may be performed



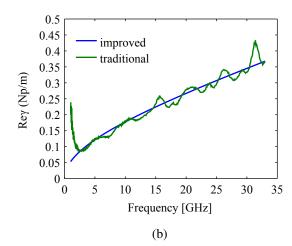
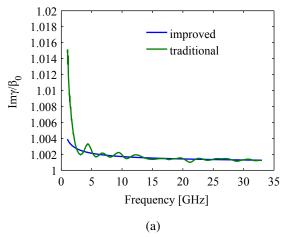


Figure 1. Attenuation constant  $\text{Re}\gamma$  for (a) male and (b) female coaxial 3.5 mm offset-shorts determined by the traditional offset-short method (solid green) and by our improved method with calibration-standard modeling (solid blue).



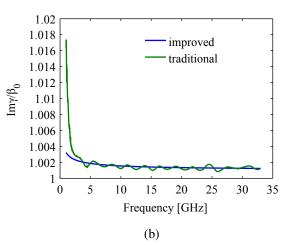


Figure 2. Phase constant  $Im\gamma$  normalized to phase constant  $\beta_0$  of vacuum for (a) male and (b) female coaxial 3.5 mm offset-shorts determined by the traditional offset-short method (solid green) and by our improved method with calibration-standard modeling (solid blue).

analytically [5], and therefore the original problem may be equivalently expressed as minimizing the following function:

$$e(\boldsymbol{\theta}_{1}, \dots, \boldsymbol{\theta}_{K}, \boldsymbol{\varphi}) = \sum_{k=1}^{K} \ln \left[ \mathbf{r}_{k}^{T} \left( \boldsymbol{\theta}_{k}, \boldsymbol{\varphi} \right) V_{k}^{-1} \mathbf{r}_{k} \left( \boldsymbol{\theta}_{k}, \boldsymbol{\varphi} \right) \right], \quad (3)$$

where  $V_k$  are the covariance matrices of measurement errors (known up to a scalar factor). Now, since the frequency-independent parameters in the vector  $\varphi$  affect simultaneously the residual error at all frequencies, we cannot solve the VNA calibration problem independently at each frequency, thus all of the unknown parameters need to be identified simultaneously. As the direct minimization of (3) is infeasible due to the large number of unknown parameters, we reduce the problem dimensionality by exploiting the structure of the Jacobian matrix, and apply a modified Levenberg-Marquardt algorithm. Details are given elsewhere [5].

# B. Calibration-standard models

We assume that the transmission-line sections in the offsetshorts have low loss, and thus model the propagation constant by use of the classical skin-depth model with the Hammerstadt correction for surface roughness [8]:

$$\gamma = (1 + j) \alpha + j\beta, \tag{4}$$

$$\alpha = \alpha_1 \sqrt{f} \left( 1 + \frac{2}{\pi} \arctan \alpha_2 f \right), \ \beta = \beta_1 \frac{2\pi f}{c},$$
 (5)

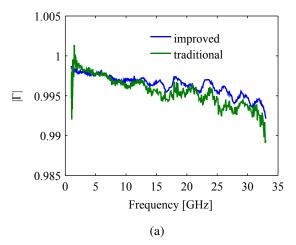
where c is speed of light in vacuum, and  $\alpha_1$ ,  $\alpha_2$ , and  $\beta_1$  are real-valued model parameters.

We further model the terminating impedance of the offset shorts as the surface impedance of a conductor. We also include the Hammerstadt correction for surface roughness, which yields the following model:

$$Z_T = (1+j)R_s, (6)$$

$$R_s = r_1 \sqrt{f} \left( 1 + \frac{2}{\pi} \arctan r_2 f \right), \tag{7}$$

where  $r_1$  and  $r_2$  are real-valued model parameters. Since the shorting plane and the surface of outer and inner conductors



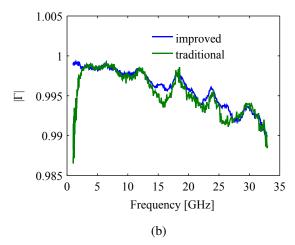
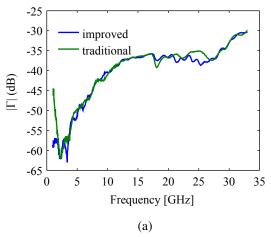


Figure 3. Magnitude of reflection coefficient for (a) male and (b) female coaxial 3.5 mm open circuit determined by the traditional offset-short method (solid green) and by our improved method with calibration-standard modeling (solid blue).



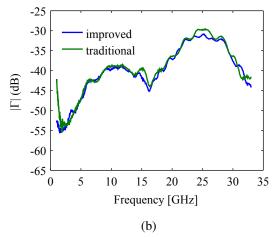


Figure 4. Magnitude of reflection coefficient for (a) male and (b) female coaxial 3.5 mm matched termination determined by the traditional offset-short method (solid green) and by our improved method with calibration-standard modeling (solid blue)

are manufactured in the same process, we assume the same impact of the surface roughness, thus we set  $r_2 = \alpha_2$ .

Finally, we assume that the imperfection of the direct-thru connection results from how the center-conductor pin-gap is lumped into the VNA calibration coefficients. The "mean" gap lumped into the calibration coefficients on each VNA port contains the port gap along with a "mean" gap of the offset-short standards. On the other hand, for the thru connection we see only the sum of both port pin-gaps. Consequently, this connection can be represented as a "negative" gap [4]. The simplest model for the pin-gap consists of a series inductance [9], therefore we model the direct thru connection as a small negative series inductance:

$$\mathbf{S}_{thru} = \begin{bmatrix} -j\frac{x}{2} & 1 + j\frac{x}{2} \\ 1 + j\frac{x}{2} & -j\frac{x}{2} \end{bmatrix}, \tag{8}$$

where  $x=\mathrm{j}\omega\tau$ , and the time constant  $\tau$  is a real-valued model parameter.

## III. EXPERIMENTS

We verified our approach experimentally. We performed an offset-short calibration in the frequency range 1-33 GHz with a set of male and female 3.5 mm coaxial offset-shorts, and the thru connection realized as a direct connection of VNA ports. Each set of shorts consisted of standards with lengths 5.004, 8.369, 12.349, 17.488, 29.980, and 59.1 mm. The offset shorts were manufactured by Maury Microwave. The length of the longest offset-short was chosen based on the approach [10], [11].

In Fig. 1 we show the attenuation constant for male and female offset shorts determined with the traditional offset-short method and with our improved method. We note that the results from the traditional offset-short method method contain significant ripples that are removed by our approach. We also note that the attenuation constant is slightly different for male and female shorts which may result from manufacturing tolerances on metal properties and offset-short length errors.

We further see in Fig. 2 that also phase constant obtained from the traditional offset-short method has ripples which

are removed by our approach. The phase constant obtained for male and female shorts is also slightly different which may be caused by offset-short length errors and connection repeatability errors.

In order to verify our approach, we measured two verification devices: an open circuit and a matched termination. In Fig. 3 and Fig. 4, we show the reflection-coefficient magnitude of these devices obtained after calibrating the VNA with the traditional and our improved offset-short method. We see that our approach allows to obtain smoother results, in particular for the open circuit. We also note that the results from the traditional offset-short method have large errors at lower frequencies due to the bandwidth limitation of this calibration. Our method, by imposing broadband models on the calibration standards, allows to extend the measurement bandwidth to lower frequencies.

## IV. CONCLUSIONS

We presented an improved offset-short method which allows to identify broadband models of the propagation constant, offset-short terminating impedance, and imperfect thru connection simultaneously with the determination of the VNA calibration coefficients. Our method uses the multi-frequency formulation of the calibration problem [5]. Experimental results for the offset-short method calibration with 3.5 mm coaxial offset-shorts show that our method, by imposing broadband models of the calibration standards, improves the calibration accuracy and extends the measurement bandwidth.

## V. ACKNOWLEDGMENT

This work has been supported by the Polish National Science Center in the framework of the project no. 2011/03/D/ST7/01731.

#### REFERENCES

- W. Wiatr, "Statistical VNA calibration technique using thru and multiple reflect terminations," in *Proc. of* 17<sup>th</sup> Int. Conf. on Microwaves, Radar and Wireless Communications, pp. 1–2, May 19–21, 2008.
- [2] R. Marks, "A multiline method of network analyzer calibration," *IEEE Trans. Microw. Theory Techn.*, vol. 39, pp. 1205–1215, July 1991.
- [3] J. Juroshek, "A study of measurements of connector repeatability using highly reflecting loads (short paper)," *IEEE Trans. Microw. Theory Techn.*, vol. 35, no. 4, pp. 457–460, 1987.
- [4] W. Wiatr, "Insight into models of coaxial standards applied for millimeter-wave VNA calibrations," in *Proceedings of Agilent Technolo*gies Metrology Workshop 2008, Berlin, Germany, pp. 1–30, 2008. CD-ROM.
- [5] A. Lewandowski, Multi-frequency approach to vector-network-analyzer scattering-parameter measurements. PhD thesis, Warsaw University of Technology, 2010.
- [6] A. Lewandowski, W. Wiatr, and D. Williams, "Multi-frequency approach to vector-network-analyzer scattering-parameter measurements," in *Proc. European Microwave Conf. (EuMC 2010)*, pp. 260–263, 2010.
- [7] Y. Bard, Nonlinear parameter estimation. Academic Press, New York, 1974.
- [8] E. Hammerstad and O. Jensen, "Accurate models for microstrip computer-aided design," in *Microwave Symposium Digest*, 1980 IEEE MTT-S International, pp. 407–409, May 1980.
- [9] B. B. Szendrenyi, "Effects of pin depth in LPC 3.5 mm, 2.4 mm, and 1.0 mm connectors," in *Proc. IEEE MTT-S International Microwave Symposium Digest*, vol. 3, pp. 1859–1862, 11–16 June 2000.
- [10] W. Wiatr, "Line-length optimization of offset-short standards for broad-band VNA calibration," in Proc. of 18<sup>th</sup> Int. Conf. on Microwaves, Radar and Wireless Communications (MIKON 2010), Vilnius, Lithuania, June 14–16, 2010.
- [11] A. Lewandowski, W. Wiatr, L. Opalski, and R. Biedrzycki, "Accuracy and bandwidth optimization of the overdetermined offset-short reflectometer calibration." submitted to IEEE Trans. Microw. Theory Techn.

# Two Port Calibration Insensitive to Flange Misalignment

Alexander Arsenovic, Robert M. Weikle II, Jeffrey Hesler

Abstract—As waveguide measurements continue to push upwards in frequency, waveguide misalignment becomes a severe problem. In this paper we combine two known calibration algorithms; the SDDL [1] and Unknown Thru, to create a two-port calibration insensitive to flange misalignment. The resultant algorithm, termed MRC, is tested both numerically and experimentally. While the numerical simulation show that MRC works as intended, the experimental results indicate that there are other measurement errors which need to be taken into account.

## I. Introduction

S waveguide measurements continue to push upwards in frequency, waveguide misalignment caused by mechanical tolerances becomes a severe problem [2]. Not only does misalignment produce reflections at each flange connection, but it creates measurement inaccuracies by inducing calibration error[3], [4]. While improving the mechanical alignment mechanism is being addressed by the IEEE P1875 working group[5], new calibration algorithms have been developed to operate in the presence of such misalignment[1]. The original solution to a reflectometer calibration utilizing delayed shorts of unknown phase was given in [6]. Lui and Weikle helped to generalize this solution by allowing the load to be arbitrary[1]. Their formulation, coupled with the modeling of a radiating rectangular waveguide [7], produced a one-port calibration that was insensitive to flange misalignment. This algorithm has been referred to by as SDDL, an acronym for the standard set; Short Delay Delay Load.

While one-port measurements are of interest, full two-port capabilities are desirable. Currently, two-port calibrations at frequencies above 100GHz, are generally made using either SOLT, or TRL. Above 500GHz, the quarter-wave line required by TRL becomes difficult to manufacture and use without damage. The accuracy of measurements corrected using these algorithms depends on the ability to realize either perfectly matched transmission

standards, or precisely known reflect standards. By combining the SDDL technique[1] with the Unknown Thru [8], a two-port calibration insensitive to flange misalignment is possible. It is acknowledged that a calibration insensitive to flange misalignment will not correct for the misalignment present in subsequent measurements. However, it will eliminate flange misalignment as source of calibration error, an important step towards improving measurement accuracy in the waveguide medium. As a byproduct, this algorithm yields a direct measurement of the flange alignment.

This paper is organized as follows. In Section II a procedure to create two-port calibration insensitive to flange misalignment. by combining SDDL with the Unknown Thru is described. The resultant algorithm, termed Misalignment Resistant Calibration (MRC), is verified numerically as well as tested experimentally in rectangular waveguide at 325-500GHz (WR-2.2, WM-570). A circuit simulation incorporating the entire processes of calibration is detailed in Section III and used to compare with the measurement results given in Section IV. Comparisons of the various calibrations are made through a set of verification standards corrected using standard calibration algorithms

## II. TWO-PORT CALIBRATION (UNKNOWNTHRU)

While SDDL can tolerate misalignment on reflect standards[1], at least one transmissive connection is needed to correct two-port measurements. The calibration algorithm known as Unknown Thru[8] provides precisely the self-calibration capabilities needed to handle misalignment on the thru standard. Specifically, the Unknown Thru requires that the thru standard be reciprocal and have a transmission phase known within  $\pi$ . Exact knowledge of transmission standards' s-parameters are not required. The Unknown Thru algorithm can be broken up into three discrete steps:

1) One-port calibration on port 1 (yields 3 -terms)

- 2) One-port calibration on port 2 (yields 3 -terms)
- 3) Measurement of reciprocal Thru (yields 1-term)

The Misalignment Resistant Calibration (MRC) is created by modifying the UnknownThru to use the SDDL solution described in the previous section for steps 1 and 2. The third step is described in [8], and need not be repeated here.

## A. Implementation and Availability

The SDDL, MRC, and other conventional algorithms have all been implemented as part of the open-source python module scikit-rf[9]. All algorithms have been tested numerically with a linear circuit simulation to verify the solutions are correct and stable. Details of the numerical verification is described in the following section.

## III. SIMULATION

## A. Numerical Verification

The Unknown Thru is part of a family of calibration algorithms known as the error box model, or 8-term model [10], [11]. In this model, the true response of a two-port device  ${\bf T}$  is embedded within unknown networks  ${\bf X}$  and  ${\bf Y}$ , illustrated in Figure 1. As is common to most applications employing the error-box model, the s-parameters are transformed into wave cascading matrices which allows the combined response to be calculated through matrix multiplication.

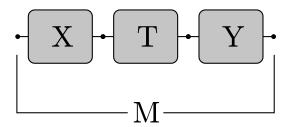


Figure 1. Diagram of the error box model

The relation between the true response of a two-port and it's measured response is expressed algebraically by

$$\mathbf{M} = \mathbf{X}\mathbf{T}\mathbf{Y} \tag{1}$$

Where

- ullet M is the measured response
- ullet T is the true response
- **X**, **Y** is the embedding networks representing the intervening circuitry

In simulation, all of the networks M, T, X and Y are observable, which allows the accuracy of the calibration algorithm to be verified.

A calibration is tested as follows. First, random matrices are created for the error networks  $\mathbf{X}$  and  $\mathbf{Y}$ . Next, the appropriate set of calibration standards  $\{\mathbf{T}\}$  are sandwiched in between the  $\mathbf{X}$  and  $\mathbf{Y}$ , producing a corresponding set of fictitious measurements  $\{\mathbf{M}\}$ . The algorithm under test is given the measurement set  $\{\mathbf{M}\}$ , and the assumed ideal responses  $\{\mathbf{I}\}$ . For self-calibration algorithms, such as the UnknownThru, SDDL, and MRC, the ideal standards are different from their true response, ie  $\{\mathbf{T}\} \neq \{\mathbf{I}\}$ . For example, to correctly test SDDL, it was given an ideal standard set containing delay shorts of lengths  $45^{\circ}$  and  $90^{\circ}$ , while the actual responses used to generate the corresponding measurements were of lengths  $30^{\circ}$  and  $120^{\circ}$ .

Once a calibration algorithm has run, it can produce a corrected response from a measured device under test (DUT). For an algorithm to be considering working, it must correctly determine, inasmuch as possible, the parameters of the embedding networks **X** and **Y** as well as random DUTs within a reasonable numerical accuracy. This entire process is built into the calibration test-suit of scikit-rf.

While numerical simulation may be used to verify that an algorithm is producing a valid solution, it also provides a way to model measurements results. In the next section, an experimental comparison of SOLT, UnknownThru and MRC is given, followed by a simulation of the results.

## IV. EXPERIMENTAL RESULTS

## A. Measurement Procedure

To test the calibration algorithm, measurements were made in the 325-500GHz (WR-2.2 , WM-570) frequency band using a pair of Virginia Diodes extender heads (VNAX TXRX-TXRX), driven by a Agilent PNA-X. The flanges at the test ports were altered by reaming out the alignment holes to a diameter of .0066" to induce a larger amount of misalignment. The resultant amount of alignment tolerance was chosen to equal the flange's designed tolerances when used in the WR-1.0 (WM-250) band, i.e. the worst-case expected misalignment. In order to prevent the need to ream out the calibration standards, the alignment pins were removed from the test-port flanges. A picture of the modified test-ports is shown in Figure 2 .



Figure 2. Picture of the test-ports with alignment pins removed.

The MRC calibration was created from measurements of a flush short, two delay shorts (realized with delay shims), the radiating open, and a flush thru. Because the alignment pins were removed from the test-ports, the inner dowel holes were used to provide alignment during the thru measurement. For comparison, 12-term and Unknown Thru algorithms were created from the identical measurement data with the exception that the radiating open was replaced by a matched load. In order for the calibration kits to be as similar as possible, the same four reflect standards were used in the 12-term and Unknown Thru calibrations. Both of these calibrations used an overdetermined least squares algorithm similar to that described in [12] for the one-port stages of calibration.

Although various metrics have been used to demonstrate calibration quality, we find the measurement of verification standards to be the most interpretable and relevant. A series of devices were measured and corrected using all three of the calibrations, producing a set of data which can be directly compared. Both transmissive and reflective devices were measured to accurately represent the algorithms performance on a whole. These results are shown in Figures 4-6.

#### B. Results

Figure 4 shows the corrected reflection coefficient from a 1" straight waveguide terminated with a flush short on the far port. Also shown is the theoretical response of an ideal rectangular waveguide 1" long with finite conductivity on the waveguide walls. A resistivity of  $2.8e^{-8}\Omega m$ , and surface roughness of  $.05\mu m$  RMS was chosen as reasonable values which most closely match the measurements. Both 12-term and Unknown Thru produce identical responses,

as is expected for non-transmissive devices. All traces are similar with the exception that MRC produces a smaller ripple at the lower end of the band.

Figures 5 and 6 show the corrected response of a 1" straight waveguide measured in transmission. Figure 6 demonstrates that MRC shows the best agreement with the theoretical response. It can be seen that the 12-term algorithm produces high frequency ripples of about  $\pm .5 dB$ , about the theoretical response, while the Unknown through algorithm has a different frequency dependence and smaller ripple of about  $\pm .1 dB$ .

## C. Modeling results through simulation

Figures 7 through 9 present simulations corresponding to the measurements in Figures 4-6. A numerical simulation, as described in Section III was constructed, and the true calibration standards where perturbed heuristically until simulated results agreed with the measurements. In these simulations the embedding networks **X** and **Y** were taken from a previous calibration, created from with experimental measurements. The exact responses of **X** and **Y** are not needed to capture the general effects of the observed measurements, just their approximate values.

The *true* calibration standards were perturbed by cascading a model of the misaligned flange in front of the delay shorts. Initially, the flange model was also cascaded with the thru measurement, but was removed to produce better agreement with measurements. It is hypothesized that this is because the inner dowels were used during the thru measurement, thereby providing excellent alignment.

The response of the misaligned flange was approximated by an equivalent circuit consisting of a constant shunt susceptance [13], as shown in figure 3. More sophisticated models of a misaligned waveguide which produce frequency-dependent values for the susceptance can be used, but for our purposes simple lumped circuit elements appear to be sufficient. The nominal values of the shunt capacitance and inductance can be chosen based upon the expected amount of misalignment. These values were then adjusted within reason until agreement with measurements was achieved. Eventually, values of 2fF and 4nH were chosen.

In addition to the flange perturbations, zero-mean white gaussian phase noise was added to the fictitious measurements. To accurately reflect observed noise characteristics, different amounts of noise was added to the transmission than to the reflective s-parameters. The phase noise is characterized by standard deviations of reflection coefficient  $(\sigma_{\angle S_{ii}})$  and transmission  $(\sigma_{\angle S_{ij}})$ . In summary, values chosen for the adjustable parameters used in the simulation were,

- $\sigma_{\angle S_{ij}} = .8^{\circ}$
- $\sigma_{\angle S_{ii}} = .2^{\circ}$
- C = 2fF
- L = 4nH

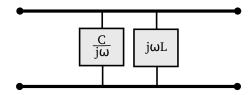


Figure 3. Circuit model used to approximate a misalignment flange

## D. Observations

By comparing figures 4-11 with figures 7-13 it is clear that the simulated performance of the MRC algorithm is substantially better than the measured results. This suggests the existence of additional sources of uncertainty other than flange misalignment. Some specific comments about the results:

- It was not possible to degrade MRC's corrected results given the types of perturbations used in this simulation. One exception is the reflection from an ideal 1" waveguide, as shown in figure 8. MRC's result is directly proportional to the amount of phase noise in the simulation.
- MRC's corrected response in figure 4 differs greatly from the simulation in figure 7.
- Regarding the theoretical responses in figures 4 and 11: It was not possible to simultaneous achieve the best fit between theory and measurement, given a single value for waveguide loss and roughness. The cause of this discrepancy is unknown.

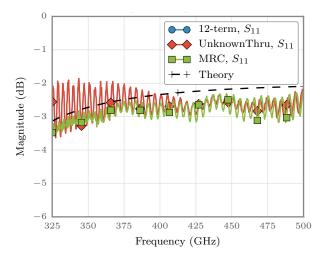


Figure 4. Corrected measurement of the reflection coefficient from a 1" straight waveguide terminated with a short (SOLT and Unknown-Thru, produce identical results as expected)

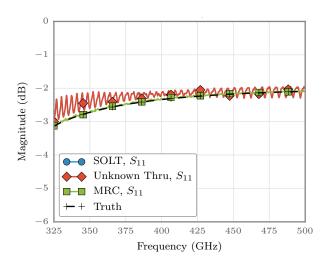


Figure 7. Simulation of corrected measurement of the reflection coefficient from a 1" straight waveguide terminated with a short (SOLT and UnknownThru, produce identical results as expected)

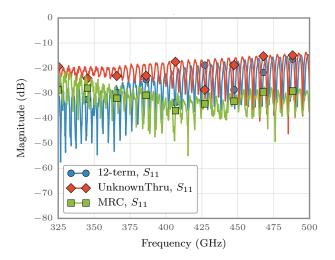


Figure 5. Corrected measurement of the reflection coefficient from a 1" straight waveguide  $\,$ 

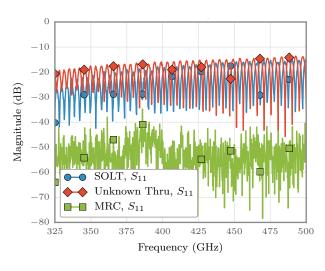


Figure 8. Simulation of corrected measurement of the reflection coefficient from a 1" straight waveguide

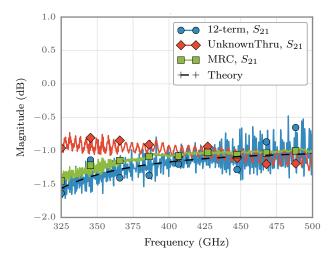


Figure 6. Corrected measurement of the transmission coefficient through a 1" straight waveguide

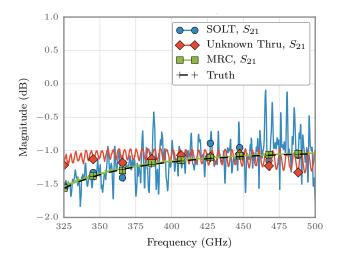


Figure 9. Simulation of corrected measurement of the transmission coefficient through a 1" straight waveguide

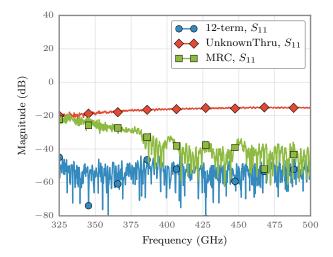


Figure 10. Corrected measurement of the reflection coefficient from a flush thru connection

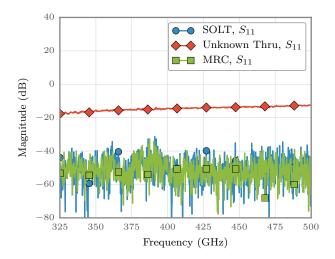


Figure 12. Simulated measurement of the reflection coefficient from a flush thru connection  $\,$ 

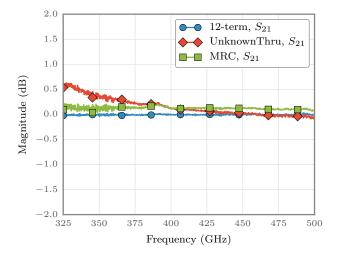


Figure 11. Corrected measurement of the transmission coefficient from a flush thru connection

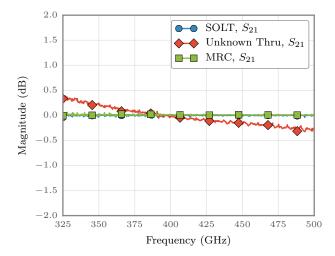


Figure 13. Simulated measurement of the transmission coefficient from a flush thru connection

## E. Absolute measurement of the flange misalignment

A unique characteristic of MRC algorithm is it's ability to measure the absolute flange misalignment between a pair of test-ports. In an attempt to demonstrate this, the flush through was measured a second time, without being used in the calibrations. The reflection and transmission coefficient of the flush through is shown in figures 10 and 11, respectively. Note that the result of the 12-term calibration is expected to be very close to ideal, as it is only a measure of repeatability. The 12-term response does yield a way to estimate an appropriate noise level. Accompanying simulations of a perfect flush thru are shown in figures 12 and 13. These results demonstrate good agreement of with 12-term and Unknown Thru, the MRC provides better results in the simulation than is observed in the measurements.

## F. Summary

Although the MRC calibration appears to improve calibration quality for some verification standards, these improvements are less than expected from corresponding simulations. The inconsistency between simulated and measured performance indicate that there are other problems with the measurement system beyond flange misalignment.

## V. Conclusion

The SDDL algorithm has been combined with the Unknown Thru to create a two-port calibration insensitive to flange misalignment. The resultant calibration algorithm, termed MRC, has been testing both numerically and experimentally. While the numerical simulation show that MRC works as intended, the experimental results indicate that there are other measurement errors which need to be taken into account. Although the MRC, and SDDL algorithms are designed to operate in the presence of flange misalignment, they may be applicable to other measurement mediums and scenarios where similar partially known reflective standards are advantageous. All algorithms have been implemented and tested as part of the open-source python module scikit-rf.

## REFERENCES

 Z. Liu and R. Weikle, "A reflectometer calibration method resistant to waveguide flange misalignment," *Microwave Theory* and *Techniques, IEEE Transactions on*, vol. 54, pp. 2447 –2452, June 2006.

- [2] E. W. A. R. Kerr and N. Horner, "Waveguide flanges for alma instrumentation," Nov 1999.
- [3] A. Arsenovic and R. Weikle, "Comparison of competing designs for delay-short calibration standards at wr-1.5," International Conference on Infrared, Millimeter, and Terahertz Waves, September 2012.
- [4] D. F. Williams, "500 GHz 750 GHz rectangular-waveguide vector-network-analyzer calibrations," *Terahertz Science and Technology*, *IEEE Transactions on*, vol. 1, pp. 364 –377, Nov. 2011.
- [5] N. Ridler, "IEEE begins work on waveguide standards above 110 GHz [MTT-S society news]," *IEEE Microwave Magazine*, vol. 10, p. 122, Feb. 2009.
- [6] W. Sigg and J. Simon, "Reflectometer calibration using load, short and offset shorts with unknown phase," *Electronics Letters*, vol. 27, pp. 1650 –1651, aug. 1991.
- [7] D. F. Williams, M. T. Ghasr, B. Alpert, Z. Shen, A. Arsenovic, R. M. Weikle, and R. Zoughi, "Legendre fit to the reflection coefficient of a radiating rectangular waveguide aperture," *Antennas* and *Propagation*, *IEEE Transactions on*, vol. 60, pp. 4009 – 4014, aug. 2012.
- [8] A. Ferrero and U. Pisani, "Two-port network analyzer calibration using an unknown 'thru'," *IEEE Microwave and Guided Wave Letters*, vol. 2, no. 12, pp. 505–507, 1992.
- [9] scikit-rf Development Team, "scikit-rf: Open source rf engineering," 2009-present. http://www.scikit-rf.org.
- [10] R. B. Marks, "Formulations of the basic vector network analyzer error model including switch-terms," in ARFTG Conference Digest-Fall, 50th, vol. 32, pp. 115-126, Dec. 1997.
- [11] H.-J. Eul and B. Schiek, "A generalized theory and new calibration procedures for network analyzer self-calibration," Microwave Theory and Techniques, IEEE Transactions on, vol. 39, pp. 724 –731, apr. 1991.
- [12] J. Bauer, R.F. and P. Penfield, "De-embedding and unterminating," Microwave Theory and Techniques, IEEE Transactions on, vol. 22, pp. 282 – 288, mar. 1974.
- [13] R. F. Harrington, Time-Harmonic Electromagnetic Fields (IEEE Press Series on Electromagnetic Wave Theory). Wiley-IEEE Press, 2001.

## Residual Error Analysis of a Calibrated Vector Network Analyzer

Faisal Mubarak and Gert Rietveld

Van Swinden Laboratorium (VSL), Thijsseweg 11, 2629 JA Delft, The Netherlands; fmubarak@vsl.nl

Abstract—With S-parameter measurement uncertainties reaching accuracy limits far beyond those previously achieved, uncertainty evaluation methods need to be advanced as well. A method based on Fourier analysis is presented for uncertainty analysis of one-port Vector Network Analyzer (VNA) measurements. The new uncertainty assessment method is validated using a system-level VNA model designed in Advanced Design System (ADS) software. The model replicates a one-port airline measurement system and allows for simulation of typical measurement scenarios including different residual error levels. The simulated airline measurement data is used to validate the proposed uncertainty assessment algorithm and to find the right gating window in the Fourier analysis. One of the main analysis results for 3.5 mm precision connectors is that airlines of 15-cm length should be used in uncertainty analysis of calibrated one-port VNAs using the Fourier analysis method. For short airlines the frequency dependence of the residual errors and airline termination lead to much higher estimated VNA uncertainties.

Index Terms—S-parameter, VNA, VNA calibration, VNA verification, airline, ripple technique, residual error, assessment technique.

## I. INTRODUCTION

Vector Network Analyzers (VNAs) are the key tools for Sparameter measurements needed in for example precision network analysis. Technological advancements have resulted in the development of a new generation of VNAs with measurement capabilities far beyond those of their predecessors. Besides the availability of these state-of-the-art VNAs, much improvement has also been achieved recently in the fabrication and characterization of devices used to calibrate VNAs. This two-fold progress paves the way to a significant improvement of the uncertainties achieved in Sparameter measurements. However, such an improvement not only requires better hardware but also calls for a re-assessment and improvement of existing uncertainty evaluation methods. The method outlined in the present EURAMET guideline on the uncertainty evaluation of vector network analyzers [1] is not applicable for the frequency range currently covered with new generation of VNAs and the uncertainties presently achieved. Therefore new uncertainty evaluation methods need to be developed in order to fully exploit the capabilities of the latest generation of VNAs.

This work was funded through the European Metrology Research Program (EMRP) Project SIB62 'Metrology for New Electrical Measurement Quantities in High-frequency Circuits' and the Dutch Ministry of Economic Affairs. The EMRP is jointly funded by the EMRP participating countries within EURAMET and the European Union.

One particular new approach in VNA uncertainty evaluation, outlined in [2] and [3], belongs to the 'ripple' class and relies on elaborative signal processing techniques using Fourier analysis. However, the actual applicability of such Fourier-based methods in S-parameter measurements so far is severely hindered by unknown interaction of different residual VNA errors in the time domain. It is the aim of this paper to provide more insight in the effect of such residual errors and to find the best way for achieving high accuracy in Fourier-based VNA uncertainty evaluations.

The structure of the paper is as follows. After a short description of the process and error parameters in one-port VNA calibration, the method for measurement of the residual errors is presented, followed by an explanation of the basic analysis algorithm. The core of the paper is the description of a system-level model of a VNA, built in Advanced Design System (ADS) software. Through this model known residual errors are induced in the calibration of the VNA and their effect on system-level airline ripple measurements is determined via simulations. Based on the results of different simulation scenarios, the most suitable measurement technique is proposed for investigation of the residual uncertainty of each VNA error-term, as well as the best parameter settings in the uncertainty assessment algorithm. Finally, an indication is given of the best achievable uncertainties in VNA calibrations using the proposed method.

## II. VNA ONE-PORT CALIBRATION

The one-port re-presentation of a VNA is based on the three error-term model. The parameters in this model are determined via a calibration using the short-open-load (SOL) method, see figure 1a. The SOL method relies on the use of three calibration devices with known electrical properties  $\Gamma_{i}$ , resulting in three independent measurements  $\Gamma_{meas(i)}$  with three unknown error-terms, which are calculated using the following equation:

$$\begin{bmatrix} 1 & \Gamma_{1} \cdot \Gamma_{meas(1)} & -\Gamma_{1} \\ 1 & \Gamma_{2} \cdot \Gamma_{meas(2)} & -\Gamma_{2} \\ 1 & \Gamma_{3} \cdot \Gamma_{meas(3)} & -\Gamma_{3} \end{bmatrix} \cdot \begin{bmatrix} e_{00} \\ e_{11} \\ \Delta \end{bmatrix} = \begin{bmatrix} \Gamma_{meas(1)} \\ \Gamma_{meas(2)} \\ \Gamma_{meas(3)} \end{bmatrix}$$

$$\Delta = e_{00}e_{11} - e_{10}e_{01}$$

$$(1)$$

Here, the error-terms  $e_{00}$ ,  $e_{11}$ , and  $e_{10}e_{01}$  respectively represent directivity, source match, and reflection tracking of the calibrated VNA. The reflection coefficient  $\Gamma$  at the  $f_1$  calibration reference plane (see figure 1) can then be calculated using equation (2):

$$\Gamma = \frac{\Gamma_{meas} - e_{00}}{e_{10}e_{01} + e_{11} \cdot (\Gamma_{meas} - e_{00})}$$
 (2)

The uncertainty in the electrical properties of the calibration devices propagates as residual errors in the error terms of the VNA. These residual errors for of each error term can be described as:

$$e_{00} = e'_{00} + \varepsilon_{00}$$

$$e_{11} = e'_{11} + \varepsilon_{11}$$

$$e_{10}e_{01} = e'_{01}e'_{10} + \varepsilon_{10}$$
(3)

with  $e_{00}'$ ,  $e_{11}'$  and  $e_{01}'e_{10}'$  representing the error-free directivity, source match, and reflection tracking of the calibrated VNA respectively and  $\varepsilon_{00}$ ,  $\varepsilon_{11}$  and  $\varepsilon_{10}$  their respective residual errors. These residual errors impact the accuracy of the reflection coefficient measurement values. Therefore, the sensitivity of the reflection coefficient at the calibration reference plane  $f_1$  is investigated for such errors. For a typical one-port calibration of a VNA, the following approximations hold:  $e_{00}$ ,  $e_{11} \approx 0$  and  $e_{10}e_{01} \approx 1$ . The sensitivity coefficients can then be derived as follows [4]:

$$\frac{\partial \Gamma}{\partial e_{00}} \approx -1$$
  $\frac{\partial \Gamma}{\partial e_{11}} \approx -\Gamma_{\text{meas}}^2$   $\frac{\partial \Gamma}{\partial e_{10}e_{01}} \approx -\Gamma_{\text{meas}}$  (4)

The uncertainty in the directivity  $\varepsilon_{00}$  is the most dominant uncertainty term in reflection coefficient measurements of matched devices. The exact contribution of the uncertainties in  $\varepsilon_{11}$  and  $\varepsilon_{10}$  strongly depends on the magnitude of the reflection coefficient being measured. In practice, these uncertainties only contribute for highly mismatched devices such as short and open circuit devices.

## III. MEASUREMENT OF UNCERTAINTY TERMS

The measurement of the VNA uncertainty terms via the airline ripple assessment technique relies on the fundamental assumption of extending the measurement reference plane of a calibrated VNA, see figure 1b. Through this technique, VNA residual errors become visible in the measured reflection coefficient. In practice this measurement is performed using a precision bead-less airline with a suitable electrical length. The second port of the airline is terminated with a suitable one-port device. In figure 1a the complete system-level flow-graph of one-port airline measurement is shown schematically.

The complete VNA calibration process is as follows. First, the VNA is calibrated up to reference plane  $\dot{r}_1$  using the SOL calibration method. The error-terms of the VNA account for

the errors up to this point. The subsequent use of a precision airline is assumed to extend the measurement reference plane up to the reference plane f2. The extension of the measurement reference plane increases the phase in each residual error of the measurement system. This induced phase shift causes a circular rotation of the error vector, which results in visible ripple in the reflection coefficient of an airline measurement. The magnitude of the error vector serves as a measure for the uncertainty component of the respective residual error of the measurement system.

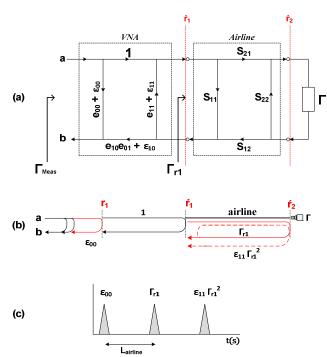


Figure 1. (a) Flow-graph of reflection coefficient measurement of a coaxial airline with its  $2^{nd}$  port being terminated using a one-port device. Parameter f1 serves as the calibration reference plane and f2 denotes the second reference plane at the  $2^{nd}$  port of the airline. (b) A flow-graph of residual error components, separated as result of additional time delay caused by the airline. (c) Time domain representation of the residual errors as function of displacement caused by the airline.

The problem of this method is that the sensitivity coefficients derived via equation (4) exhibit correlation between the different residual error terms. It thus is impossible to assess each individual residual uncertainty in the frequency domain. To allow for an orthogonal analysis of the VNA residual uncertainty, a time-domain analysis technique is proposed using Fourier transforms [3].

One of the well-known problems with the application of Fourier transforms of S-parameter frequency signals into the time domain is that frequency dependence of the different VNA error terms results in interaction in the time domain. So in order to achieve reliable results with good uncertainty, the time-domain analysis technique should carefully take into account these interactions between different components. The

origin of the interaction lies in the frequency dependence associated with all VNA residual uncertainties, the properties of the precision airline and of the one-port device used to terminate the airline. A complicating factor is that any significant change in the frequency response of these components changes its interaction with other components in the time-domain representation of the measurement as well.

The second important parameter to be considered by the analysis technique is the length of the precision coaxial airline. As shown in figure 1b the Fourier transform into the time-domain in principle allows for separation of the VNA residual errors. The distance between the errors in the time domain is determined by the length of the precision airline, see figure 1c. Whereas one thus at first instance might aim to use very long length airlines, in practice the length of metrology-grade airlines is limited in order to meet all tolerance limits in the dimensional parameters defining the airline. It therefore is important to evaluate to what extent the errors can still be separated in the time domain for practical airline lengths.

For evaluation of the  $\varepsilon_{00}$  term a matched 50  $\Omega$  device is used to terminate the airline. As explained in the previous section, in this case the contribution of the residual terms  $\varepsilon_{11}$  and  $\varepsilon_{10}$  can be ignored. The  $\varepsilon_{11}$  uncertainty of source-match error term is evaluated using a high-reflect standard, such as a short-circuit device. The source-match uncertainty term requires an additional correction for the tracking term (see figure 4).

For correct assessment of the residual errors the geometry of the airline connectors is important as well. Any unknown discrepancy in the connection between the test-port and the airline connector will directly propagate in  $\varepsilon_{00}$ . Since it is not possible to separate this error in the time domain, prior knowledge of the airline connectors is necessary. Thus, for a precise evaluation of the effect of residual errors to VNA uncertainties, an airline with high-precision connectors and small dimensional parameters tolerances is required.

Table 1 shows the VNA measurement frequency settings for a series of different coaxial connectors. Note that it is important to have constant frequency steps over the complete frequency range to allow for correct Fourier transform of the measurement data.

TABLE I.	VNA Frequency parameter S	SETTINGS
----------	---------------------------	----------

	Frequen		
connector	min – max	step	points
N	0.025 - 18.0	0.025	720
3.5 mm	0.025 - 33.0	0.025	1320
2.92 mm (K)	0.025 - 40.0	0.025	1600
2.4 mm	0.025 - 50.0	0.025	2000
1.85 mm	0.025 - 65.0	0.025	2600

## IV. ANALYSIS ALGORITHM

Time domain representation of the measurement data possesses some distinct advantages in comparison with frequency domain representation. It enables orthogonal analysis of desired error components as a function of time delay. This property is exploited in the proposed algorithm, where the frequency domain measurement data undergoes a number of signal processing steps for accurate evaluation of the desired residual uncertainty term.

The general approach of the algorithm is depicted in figure 2. First the signal is transformed into the time domain, enabling separation of the desired error component. Then gating is applied to extract the desired component from the time domain trace which is subsequently transformed back into the frequency domain. The frequency domain representation of the residual error finally is used as a measure to quantify the analyzed uncertainty term.

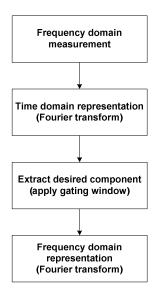


Figure 2. Flow-chart of the residual error analysis algorithm.

In the practical implementation of the algorithm, a Fourier transform is applied to convert the frequency signal into the time domain and vice versa. Standard FFT and IFFT functions in Matlab software are used for this Fourier transformation. The frequency domain measurement is performed with frequency settings as shown in table 1 for each connector type suitable for measurements up to 67 GHz.

As already mentioned above, the desired residual error component is extracted from the time domain trace using gating functions. Due to the frequency dependent response of the residual terms and the limited width of the gating function, side lobes are induced at the outer edges of the extracted residual term. In our algorithm, a number of different gating windows are considered, such as a rectangular window [5], Hamming window [5], Nutall window [6], and combined

rectangular Nutall window (RN), in order to find the optimal window response for our application.

#### V. SYSTEM LEVEL SIMULATION

For finding the best VNA measurement parameters as well as the best settings in the analysis algorithms, a system-level model of the measurement system is designed in Advanced Design System (ADS) software. The model is used to replicate an airline measurement connected to a calibrated one-port VNA. With known residual errors induced in the calibration of the VNA, a simulation of the airline measurement is used to generate reference data for validation of the signal processing algorithm.

The VNA model is based on the two sampler architecture as shown in figure 3. The samplers are assumed to be ideal and imperfections due to down-conversion hardware are not considered. First, the one-port VNA system model is calibrated using the SOL method based on ideal calibration devices. This results in nominal system error terms represented by cascade e-term matrix  $[E_{ideal}]$ . A second calibration of the VNA is performed using non-ideal calibration devices, by introducing known errors to the ideal reference data of the three (SOL) calibration devices. This results in a new set of system error terms  $[E_{cal}]$ . This second set of error-terms includes the residual error for each VNA error-term. Finally, using the error-free  $[E_{ideal}]$  e-terms and the error-prone  $[E_{cal}]$  e-terms the VNA residual errors  $[E_{error}]$  can be computed as follows:

$$[E_{error}] = [E_{ideal}] - [E_{cal}]$$
With  $[E] = \begin{bmatrix} \Delta & e_{00} \\ -e_{11} & 1 \end{bmatrix}$ , see (1).

As already indicated in section III, a well-known drawback associated with the application of Fourier transform technique for S-parameter uncertainty assessment is interaction between the different components in the time domain representation of the VNA measurement data. This effect is caused by frequency dependent response of the components, such as VNA residual errors, airline connectors, and the device used to terminate the airline. The length of the airline plays a crucial role as well as it increases the spacing between different error components in the time domain representation.

The VNA model simulations are used to investigate the uncertainty assessment limitations caused by this time-domain interaction of different components present in the measurement system. The particular VNA model for the simulation results presented here is based on the measurement system as used for measurements in 3.5 mm coaxial connectors with a maximum measurement frequency of 33 GHz (see table 1 for the exact frequency settings).

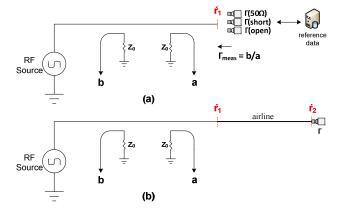


Figure 3. A system-level block diagram of (a) one-port VNA based on two sampler architecture calibrated using the SOL method. (b) airline ripple measurement using precision coaxial airline. f1 denotes the reference plane determined with the SOL calibration and f2 denotes the new reference plane set by the coaxial airline. a and b denote VNA outgoing and reflected waves.

For assessment of the  $\varepsilon_{00}$  directivity uncertainty term, an airline ripple measurement is simulated with a 50- $\Omega$  load as airline termination. In figure 4 the resulting time domain signals of the airline ripple simulations are shown, with  $\varepsilon_{00}$  marked as A. The simulations are performed for a 5-cm and 15-cm long airline. For each airline two simulations are performed: one with frequency independent, constant, residual errors and airline termination, and one with frequency dependent residual errors and airline termination, such as typically found for 3.5-mm coaxial devices. The three different VNA error terms as defined in equation 3 are indicated in the time domain traces with A, B, and C respectively. Note that the derivation of  $\varepsilon_{10}$  and  $\varepsilon_{11}$  from peak B and C require some additional correction terms.

In a similar way, the source-match uncertainty  $\varepsilon_{11}$  is assessed using airline ripple simulated with a high-reflect short for termination of the airline. In figure 5 the resulting time domain representation of the airline ripple simulations are shown, with  $\varepsilon_{11}$  marked as C. Again the results of four simulations are shown, for two difference airline lengths and for both constant and frequency dependent errors and airline termination.

As expected, the results in figures 4 and 5 clearly show the increased distance between the error terms for the 15-cm airline with respect to the 5-cm airline. The major new finding of the simulations is that the results show the very significant effect of the frequency dependence of residual errors and airline termination. Especially for the  $\varepsilon_{11}$  assessment using the high-reflect short and a 5-cm airline, the effect is considerable: uncertainty measurement is limited to above the -50 dB level, typical for present VNA uncertainties, making the  $\varepsilon_{11}$  error essentially indiscernable in the time trace.

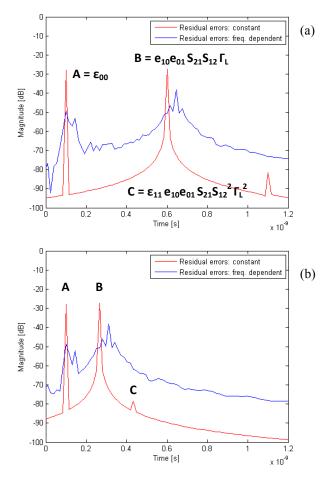


Figure 4. Time-domain representation of the airline ripple measurement simulation, for frequency-independent, constant, residual errors and airline termination (red line) and for frequency-dependent errors such as typically found in practice. The airline is terminated with a matched 50  $\Omega$  device. (a) Airline simulation is performed with a 15-cm long airline. (b) Airline simulation results for a 5-cm long airline. Error terms are marked with A, B, and C.

## VI. RESULTS & DISCUSSION

Simulation data for configuration described in figure 4 is analyzed for assessment of  $\varepsilon_{00}$  uncertainty using the proposed signal processing scheme. Discrepancies caused by interaction between uncertainties and airline termination reduces assessment accuracy, see figure 4 and 5. Accuracy of the algorithm is significantly reduced due this interaction between uncertainties, when compared with results of a measurement system with frequency independent residual errors, see figure 4 and 5. Assessment errors of directivity uncertainty  $\varepsilon_{00}$  are shown in figure 6a for 15 cm and 5 cm long airlines. Airline terminated with a short device results in much higher assessment error and is not suitable for evaluation of  $\varepsilon_{00}$  uncertainties realized.

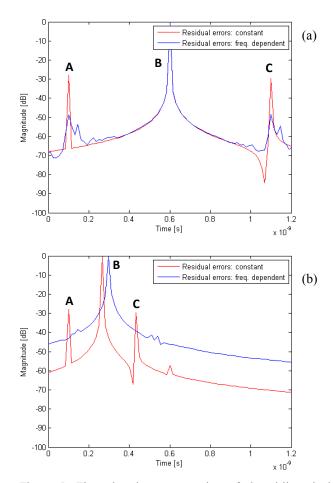
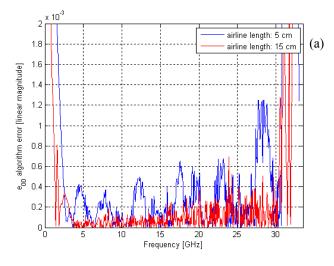


Figure 5. Time domain representation of the airline ripple measurement simulation, for frequency-independent, constant, residual errors and airline termination (red line) and for frequency-dependent errors such as typically found in practice. The airline is terminated with a high reflect short device. (a) Airline simulation is performed with 15-cm long airline. (b) Airline simulation results for 5-cm long airline. Error terms are marked with A, B, and C.

Source match uncertainty  $\varepsilon_{11}$  assessment results are shown in figure 6b. Simulation data for configuration described in figure 5 is analyzed using the proposed signal processing scheme. The airline was terminated with a frequency dependent short device. The algorithm assessment accuracy decreases for the shorter airline.

The response of the gating window introduces side lobes in the evaluated uncertainty component. A number of gating windows were considered in the analysis and best results were found for a rectangular window with window transition as that of a Nutall window (RN). This effect can be reduced by extrapolation of the data before transformation of the evaluated uncertainty component back to the frequency domain.



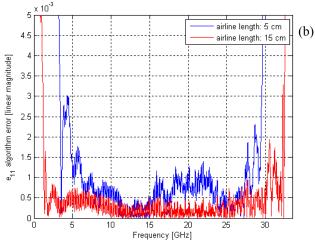


Figure 6. A comparison between the induced and assessed residual errors is shown for airline of 5 cm and 15 cm electrical length. The residual errors are induced in the VNA calibration using the ADS based model of the measurement system. (a) Directivity uncertainty  $e_{00}$  is determined using a typical frequency dependent 50 ohm termination. (b) Source match uncertainty  $e_{11}$  is measured using a frequency dependent short termination.

## VII. CONCLUSIONS

A study has been performed on the suitability of Fourieranalysis based evaluation of the uncertainties of VNAs. A major concern with the use of Fourier techniques for VNA uncertainty assessment purposes is the interaction between different uncertainty sources. Such interactions can easily lead to incorrect representation of the uncertainty by analyzed terms resulting from the Fourier analysis.

To assess the uncertainties of calibrated VNAs using Fourier transforms, a complete system-level model is designed of a one-port VNA. The model simulates an airline measurement using a calibrated VNA with different airline termination devices. The model has been used to investigate the interaction between the uncertainty sources due to

frequency dependency of the residual VNA error terms and airline termination, as well as the impact of the airline length on the accuracy of the analysis algorithm.

The results of the simulations in 3.5 mm connector for frequencies up to 33 GHz show that the frequency response of the residual VNA error terms and airline termination indeed greatly influence the magnitude of the VNA uncertainty terms. However, it appears that the length of the airline can play a crucial role in reducing this effect: longer airline lengths results in larger spacing between different error components in the time trace of the airline ripple measurements.

The simulations further show that for directivity uncertainty  $\varepsilon_{00}$  assessment the best accuracy is achieved for 50- $\Omega$  device termination of the airline, whereas the best results for the source match uncertainty  $\varepsilon_{11}$  assessment are achieved with a high-reflect short termination. Especially for accurate source match uncertainty  $\varepsilon_{11}$  determination the airline should be as long as possible; the simulation results achieved for a commercially available metrology grade airline of 15-cm length is very significantly better than used for a 5-cm long airline.

#### ACKNOWLEDGEMENT

The authors acknowledge Johannes Hoffman (METAS) and Marco Spirito (Delft University of Technology) for many useful discussions and support.

## REFERENCES

- [1] EURAMET Technical Committee for Electricity and Magnetism, "Guidelines on the evaluations of Vector Network Analyzers (VNA)", EURAMET cg-12, Version 2.0 (03/2011). Online available via <a href="https://www.euramet.org">www.euramet.org</a>.
- [2] Gerd Wubbeler, Clemens Elster, Thomas Reichel, and Rolf Judaschke, "Determination of the Complex Residual Error Parameters of a Calibrated One-Port Vector Network Analyzer", IEEE Trans. on Instrumentation and Measurement, Vol 58, No.9, pp. 3238 – 3244, September 2009.
- [3] Aleksandr A. Savin, "A Novel Factor Verification Technique for One-Port Vector Network Analyzer", Proc. of the 43<sup>rd</sup> European Microwave Conference, October 2013
- [4] B.D. Hall, "Using Uncertain Complex Numbers With VNA Measurements", 2008 IEEE MTT-S International Microwave Symposium Digest, pp. 26 – 31, June 2008.
- [5] Oppenheim, Alan V., Ronald W. Schafer, and John R. Buck, "Discrete-Time Signal Processing", Upper Saddle River, NJ: Prentice Hall, 1999
- [6] Nuttall, Albert H. "Some Windows with Very Good Sidelobe Behavior." IEEE Transactions on Acoustics, Speech, and Signal Processing. Vol. ASSP-29, February 1981, pp. 84–91.

# Evaluation and Validation of a National WR-15 (50 to 75 GHz) Power Measurement System

Xiaohai Cui<sup>1</sup>, Yu Song Meng<sup>2</sup>, Yueyan Shan<sup>2</sup>, Wenze Yuan<sup>1</sup>, Chao Ma<sup>1</sup>, and Yong Li<sup>1</sup>

National Institute of Metrology, Beijing, China, e-mail: cuixh@nim.ac.cn

<sup>2</sup>National Metrology Centre, Agency for Science, Technology and Research (A\*STAR), Singapore, e-mail: meng\_yusong@nmc.a-star.edu.sg, shan\_yueyan@nmc.a-star.edu.sg

Abstract — In this paper, we present some preliminary results from evaluation and validation of a national WR-15 (50 to 75 GHz) power measurement system, which has been upgraded for thermistor sensor (thermistor mount) measurements recently. The system is a physical realization of direct comparison transfer technique for microwave power sensor calibration. It has been evaluated and validated referring to a WR-15 microcalorimeter measurement system. Good performance has been observed preliminary, and some necessary improvement works have been planned in near future.

Index Terms — Direct comparison transfer, microcalorimeter, power measurement, thermistor mount.

#### I. INTRODUCTION

Recently, a trilateral comparison of WR-15 (50 to 75 GHz) waveguide power sensor measurement and calibration has been planned to be performed among the National Institute of Metrology (NIM) of China, the National Institute of Standards and Technology (NIST) of USA, and the National Metrology Centre (NMC) of the Agency for Science, Technology and Research (A\*STAR) of Singapore in 2014. The main motivation of this trilateral comparison is a desire to demonstrate the precision measurement capabilities and validate the equivalence of WR-15 power sensor calibration at the three National Metrology Institutes (NMIs). This exercise is also meaningful because, to the best of our knowledge, there is only one international key comparison with the same waveguide size which was performed about 15 years ago, but only at 62 GHz [1].

For this comparison, commercially available temperature-compensated thermistor mount, Hughes 45774H-1100, has been planned as the traveling standard. For its measurements, NIM and NIST will use their own-designed and well-established WR-15 microcalorimeter [2-4]. However, the measurement system at NMC, A\*STAR was previously developed for the diode sensor (e.g., V8486A power sensor) measurements [5], and therefore the system needs to be modified slightly for measuring the thermistor mounts. Correspondingly, the measurement uncertainty also needs to be re-evaluated.

In this paper, preliminary results from evaluation and validation (i.e., a pre-comparison system checking) of the

improved/modified WR-15 power sensor measurement system at NMC, A\*STAR will be discussed and presented.

## II. MEASUREMENT METHODOLOGIES

## A. Measurement System at NMC, A\*STAR

NMC, A\*STAR uses a typical measurement setup [5-6] implemented with a direct comparison transfer technique which was proposed by the NIST [7]. The schematic diagram of the calibration system is shown in Fig. 1(a). The reference standard (with a calibration factor  $K_{STD}$ ) is measured on Port 2 of a directional coupler which is used to minimize the source mismatch of a microwave synthesizer [8], and then replaced with the device under test (DUT). A monitoring power sensor is connected to Port 3 of the coupler for power leveling.

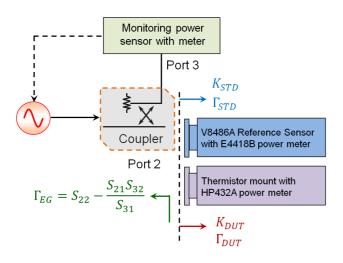
The calibration factor  $K_{DUT}$  of the DUT can be determined through,

$$K_{DUT} = K_{STD} \times \frac{P_{DUT}}{P_{STD}} \times \frac{P_{3STD}}{P_{3DUT}} \times \frac{|1 - \Gamma_{DUT}\Gamma_{EG}|^2}{|1 - \Gamma_{STD}\Gamma_{EG}|^2}$$
 (1)

Here,  $P_{DUT}$  and  $P_{3DUT}$  are the powers measured at Port 2 using the DUT and that at Port 3 using a monitoring power sensor respectively.  $P_{STD}$  and  $P_{3STD}$  are the powers measured at Port 2 using the reference standard and that at Port 3 using the same monitoring power sensor.  $\Gamma_{STD}$  is the reflection coefficient of the reference standard, and  $\Gamma_{DUT}$  is the reflection coefficient of the DUT.  $\Gamma_{EG}$  is the equivalent source match term of Port 2 [9], and equal to

$$\Gamma_{EG} = S_{22} - \frac{S_{21}S_{32}}{S_{31}},\tag{2}$$

where  $S_{ij}$  (i, j = 1, 2 or 3) are the scattering parameters of the directional coupler. A more detailed description of eq. (1) can be obtained in [6-7], and the derivation of eq. (2) can be found in [9]. As introduced in [5], the existing system at NMC, A\*STAR was developed for measuring the diode sensor (i.e., V8486A waveguide power sensor) with an Agilent EPM series power meter.





(a) Schematic diagram of the calibration system

(b) Practical setup

Fig. 1. Calibration of a thermistor mount by the method of direct comparison transfer using a coupler at NMC, A\*STAR.

For this trilateral comparison, a temperature-compensated thermistor mount, Hughes 45774H-1100 which is provided by NIM, China has been selected as the traveling standard due to its good stability and then works as the DUT in this study.

The existing system at NMC, A\*STAR therefore has to be slightly modified. A HP432A power meter is used together with the thermistor mount as shown in Fig. 1. Its recorder output is connected to a HP34401A multimeter for automatic data recording.

## B. Measurement Methods at NIM/NIST

The thermistor mount is tested and calibrated at NIM/NIST using a microcalorimeter system which serves as a primary power standard at many NMIs. The microcalorimeter measures the effective efficiency  $\eta_e$  of a mount, through determining the ratio of the changes in the direct current (DC) power (or DC substitution power) to the absorbed millimeterwave power.

The effective efficiency  $\eta_e$  of the thermistor mount (Hughes 45774H-1100 in this study) at each frequency of interest can be calculated using the following recommendation,

$$\eta_e = g \frac{1 - \left(\frac{V_2}{V_1}\right)^2}{\frac{e_2}{e_1} - \left(\frac{V_2}{V_1}\right)^2}.$$
 (3)

Here  $V_1$  and  $e_1$  are the output voltages of the power meter and thermopile with only the DC applied to the mount, and  $V_2$  and

 $e_2$  are the same voltages with both the RF and DC applied. The detailed derivation of eq. (3) can be obtained in [10].

As discussed in [3-4], g in eq. (3) is the correction factor of the microcalorimeter, and can be measured and characterized through inserting a foil short between the test port and the DUT in the microcalorimeter. Moreover as reported in [4], the correction factor g is the main uncertainty contribution for the effective efficiency measurements using a microcalorimeter.

Furthermore since the reference standard at NMC, A\*STAR (V8486A waveguide power sensor) has a traceable calibration factor  $K_{STD}$ , the calibration factor  $K_{DUT}$  of the thermistor mount is therefore used for performance evaluation.  $K_{DUT}$  can be obtained through

$$K_{DUT} = \eta_e (1 - |\Gamma_{DUT}|^2), \qquad (4)$$

in terms of the effective efficiency  $\eta_e$  and the reflection coefficient  $\Gamma_{DUT}$  of the thermistor mount (i.e., the DUT).

## III. PRELIMINARY RESULTS AND ANALYSIS

Some preliminary measurement results (calibration factor K) for the Hughes thermistor mount have been shown in Fig. 2, with the associated expanded uncertainty at a level of confidence of approximately 95%. The results have found to be agreed well with the historical data of this thermistor mount maintained and kept at NIM, China, using their own designed WR-15 microcalorimeter measurement system.

The analysis of uncertainty sources shows that, currently uncertainty of the traceable reference standard is one of the

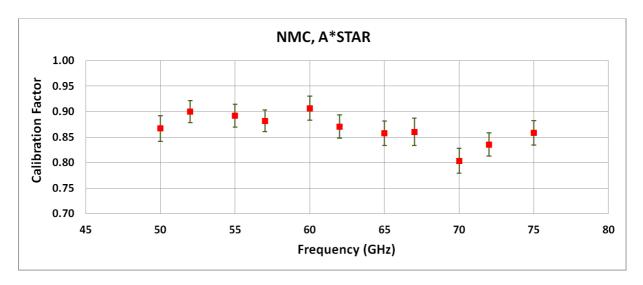


Fig. 2. Measurement results of calibration factor and its expanded uncertainty for a Hughes thermistor mount.

major uncertainty contributions. The standard uncertainty of the reference standard is from 0.95% to 1.25%, depending on the frequency. Another major uncertainty contribution is from the HP432A power meter. Its recorder output used in this study has an accuracy of 0.5% [11].

Therefore to improve the performance of the calibration system using direct comparison transfer technique at NMC, A\*STAR (a relatively economical calibration method for measuring the thermistor mounts comparing to the microcalorimeter method), the uncertainty of the reference standard can be much improved. Moreover through using other outputs, the accuracy of HP432A power meter could achieve up to 0.2% and will be applied later.

## IV. CONCLUSION

In this paper, some preliminary results for evaluating and validating a national WR-15 (50 to 75 GHz) power sensor measurement system at NMC, A\*STAR were reported.

The existing system has been upgraded for calibrating the thermistor sensors. A thermistor mount, Hughes 45774H-1100 was tested for performance evaluation of the improved system, referring to a WR-15 microcalorimeter at NIM, China. Good performance has been observed preliminary with some improvement plans suggested in the near future.

## REFERENCES

- [1] J. Achkar, B. Mellouet, L. Velasco, S. Swarnowski, A. N. Akhiezer, V. P. Seredniy, Y. F. Pavlenko, and J. R. Juroshek, "The GT-RF/95-1 key comparison of power measurements at 62 GHz," *IEEE Trans. Instrum. Meas.*, vol. 50, no. 2, pp. 406-408, Apr. 2001.
- [2] T. P. Crowley and X. H. Cui, "Design and evaluation of a WR-15 (50 to 75 GHz) microcalorimeter," in 2008 Conference on

- Precision Electromagnetic Measurements, Broomfield, CO, Jun. 2008, pp. 420-421.
- [3] X. H. Cui and T. P. Crowley, "Comparison of experimental techniques for evaluating the correction factor of a rectangular waveguide microcalorimeter," *IEEE Trans. Instrum. Meas.*, vol. 60, no. 7, pp. 2690-2695, Jul. 2011.
- [4] X. H. Cui, Y. Li, X. Gao, Z. Song, and W. Sun, "Correction factor evaluation technique for a rectangular waveguide microcalorimeter," in 2013 82<sup>nd</sup> ARFTG Microwave Measurement Conference, Columbus, OH, Dec. 2013.
- [5] Y. S. Meng, Y. Shan, and H. Neo, "Development of a waveguide microwave power sensor calibration system at NMC," in 2012 Asia-Pacific Symposium on Electromagnetic Compatibility, Singapore, May 2012, pp. 745-748.
- [6] Y. Shan, Y. S. Meng, and Z. Lin, "Generic model and case studies of microwave power sensor calibration using direct comparison transfer," *IEEE Trans. Instrum. Meas.*, vol. 62, no. 6, pp. 1834-1839, Jun. 2013.
- [7] M. P. Weidman, "Direct comparison transfer of microwave power sensor calibration," *NIST Technical Note 1379*, Jan. 1996.
- [8] G. F. Engen, "Amplitude stabilization of a microwave signal source," *IRE Trans. Microw. Theory Tech.*, vol. 6, no. 2, Apr. 1958, pp. 202-206.
- [9] A. Fantom, Radio Frequency and Microwave Power Measurement, IEE Electrical Measurement, ser. 7, Peter Peregrinus Ltd., UK, 1990.
- [10] J. W. Allen, F. R. Clague, N. T. Larsen, and M. P. Weidman, "NIST microwave power standards in waveguide," *NIST Technical Note* 1511, Feb. 1999.
- [11] Agilent Technologies, *HP432A Power Meter Operating and Service Manual*, Part No. 00432-90079.

## A Near-Field Scanning Microwave Microscope for measurement of the permittivity and loss of high-loss materials

A P Gregory<sup>1</sup>, J F Blackburn<sup>1</sup>, K Lees<sup>1</sup>, R N Clarke<sup>1</sup>, T E Hodgetts<sup>2</sup>, S M Hanham<sup>3</sup>, N Klein<sup>3</sup>

<sup>1</sup>National Physical Laboratory (NPL), <sup>2</sup>Consultant to NPL, <sup>3</sup>Imperial College London

Abstract — The design and calibration of a Near-Field Scanning Microwave Microscope (NSMM) for measurement of permittivity and loss on the small scale are described. The instrument described uses a wire probe electromagnetically coupled to a resonant cavity. Using an electrostatic model based on image charges (Gao and Xiang 1998) permittivity and loss may be determined. The paper describes progress in two specific areas: (i) The implementation of an optical beam-deflection method for obtaining contact mode between the probe tip and specimens. (ii) Improvements to the calibration process to improve the traceability and accuracy of the measurement of loss by using the Laplacian 'complex 'frequency' in the image-charge model. This is demonstrated by measurements on polar liquids.

Index Terms — Dielectric measurement, microwave microscope, complex frequency.

#### I. INTRODUCTION

A Near-Field Scanning Microwave Microscope (NSMM) can be used for obtaining images of dielectric permittivity or microwave conductivity on the micron scale [1-6]. NSMMs have found applications in the electronics industry, and in combinatorial studies for the development of new functional materials and low-loss electroceramics [7]. There are two main types of NSMM, both based on a probe that makes contact with specimens: (1) Instruments that measure the complex reflection coefficient of the probe directly, and (2) instruments that measure the perturbation of the resonant frequency and Q-factor of a cavity coupled to the probe. To set the work in context, we provide a brief overview of each type:

(1) By using a Vector Network Analyzer (VNA), the complex reflection coefficient of a sharp probe with a matching network is measured. A microscope working on this principle would normally be integrated with an AFM to allow scanning in *contact mode*. Such instruments are described in a recent and thorough review [1]. A typical application is for imaging the microwave conductivity of semiconductors at the *nanometer scale*. They are not well-suited for measurement of permittivity as stray capacitances associated with the AFM cantilever are difficult to compensate for, although there has been significant progress in developing methods of calibration [6][8].

(2) Permittivity and loss are determined from shifts in the resonant frequency and Q-factor of the resonator. The probe can be a wire, or a sharpened stripline [5][9] (which may be self-resonant with no separate cavity). A calibration procedure, based on measurement of reference specimens that are highly polished and uniform on the small scale, is required. An electrostatic analysis, based on an image-charge analysis of a conducting sphere in proximity to a dielectric lamina [2][10], can be used to relate the shifts in resonant frequency and Q-factor to permittivity and loss.

The NSMM which is described in this paper is of the cavity perturbation type (Fig. 1), using wire probes with a spherical tip approximately 0.1 mm in diameter. Using such probes measurement resolution is on the micron scale (which is significantly smaller than the tip diameter as the field is concentrated in the region closest to specimens, especially when the permittivity is high). One of the main motivations for this work was to make an instrument that offers accurate and traceable measurements of dielectric loss, for which two main problems can be identified: (i) limitations in the electrostatic theory [2] are apparent (particularly for high-loss materials for which it was not designed), (ii) suitable solid calibration reference specimens that have significant loss have yet to be identified. In this paper a new design of NSMM, new calibration algorithms, and the use of polar liquids as calibration reference materials are described. The use of a Laplacian 'complex-frequency' in the calibration and calculation of results for the first time enables accurate measurements of the loss of high loss materials.

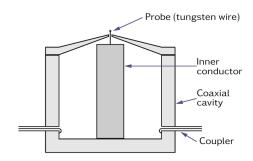


Fig. 1: Coaxial cavity with wire probe. The top of the cavity is sloped to allow the gap between tip and specimens placed above to be observed by using a camera system to assist setting up.

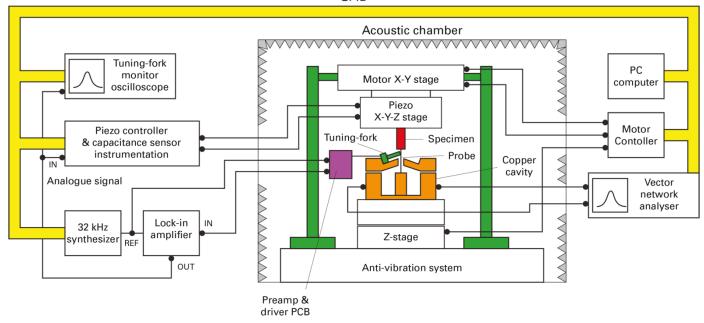


Fig. 2: Schematic of the NSMM (with tuning fork system for obtaining contact mode).

The paper is arranged as follows: in Section II, an overview of the design of the microscope is presented. This is based on raster scanning to allow images to be obtained. Instrumentation is required to obtain contact mode with minimal pressure between specimens and the probe tip (this is needed during scanning and calibration). As this is the most technically demanding part of building a microscope it is discussed in some detail (Section II). Calibration processes and some initial results are described in Sections III and IV. The results are analyzed in Section V, and Section VI is the Conclusion.

## II. OVERVIEW OF THE NSMM

The NSMM (Fig. 2) is built into an acoustically-shielded chamber with an active anti-vibration table. The combined power supply and control unit for the anti-vibration table is located externally to reduce temperature rises inside the chamber. Physik Instrumente (PI) type M-605 X & Y motorized stages with 0.3 μm resolution allow large area scans (50 x 25 mm). Coarse control of the separation between the specimen and probe tip is provided by means of a motorized Z stage (range 0 – 12.5 mm). Fine-scale movement (100x100x10 μm) of the specimens is provided by a three-axis closed-loop piezo stage (PI 733.3CD). The Z-axis of the piezo can be controlled by means of a control loop using external circuitry to maintain contact mode. The movement range of the Z axis of the piezo stage is only 10 μm, so if the control loop should become unlocked it is unlikely that significant

damage will occur. All of the stages have capacitive feedback sensors to allow positions to be read by the control computer using the GPIB.

Specimens are attached to a microscope slide using acetonesoluble wax (glycol phthalate, trade name 'Quartz' wax). Small magnets are used to attach this to the piezo XYZ stage. Several specimens (including calibration specimens) can be secured to the microscope slide. The strategy used in the control software is that measurement positions are set up manually and stored by the software for reuse. This is achieved by using a joystick attached to the PI C-848 motor controller to set Z-axis height and a CCD camera with a zoom lens to view the tip and specimen. The motorized XYZ stages can be moved to any of the memorized positions using buttons on the software interface. This enables measurements to be made in the minimal amount of time (to reduce drift) and with minimal disturbance to the system. The motorized Z stage can be raised in micrometer steps via the software user-interface to allow the user to adjust the specimen/tip separation.

The cavity resonant frequency and Q-factor are obtained by fitting swept measurements of complex transmission coefficient (typically at 51 frequencies) to a resonance model [11]. These measurements are made using a Vector Network Analyzer (VNA). To improve accuracy, the leakage vector, which accounts for signal paths between the two ports of the VNA that bypass the resonant circuit, is a fitted parameter.

## A. Cavity and probe tip design

In this paper the resonator is a quarter-wave cavity. The wire probe passes through a small hole  $(1-mm\ \emptyset)$  in the cavity lid. Experiments have shown that the wire must be placed centrally in the hole, otherwise the microwave Q-factor is much reduced. The probe's spherical tip was formed by electro-discharge machining (EDM) [12]. A spherical tip is chosen as this is calculable geometry by the image-charge technique (Section III). The surfaces of the EDM probe tips are of high quality, which is important in this application. In the work described the tip diameter was  $0.18\ mm$ .

Image scans are made in contact mode. Unlike AFM systems, in which contact mode can be obtained using weight under gravity, this requires an active system to be implemented. In the experiment which is the subject of this paper, it is obtained by detection of shear-force interaction [13-15] between the tip and specimen using a highly-sensitive detector. For measurements in an air atmosphere, a thin layer coating of water [13] is the most likely cause of the shear force. The observed range of interaction is ~10 nm. The piezo controller (PI E-710) is used to control the Z-axis of the piezo stage in closed-loop mode using an 'error voltage' that is normally derived by reference to a built-in distance sensor (resolution 0.3 nm). Under GPIB control, the controller can be switched so that the source of the error voltage is an input socket on the panel of the instrument, which is connected to the shear force detector. Therefore a subsystem that maintains contact mode can be constructed. Once contact mode has been established, the corresponding reading of the Z axis of the piezo stage can be obtained from the distance sensor.

Two systems were devised for shear-force detection: a tuning fork system [16] and an optical beam deflection system [14]. Both use a low-frequency synthesizer (Yokogawa FG200) to supply a sine-wave signal, and a lock-in amplifier as a detector. The output signal is connected to the piezo controller. By adjustment of the output DC offset of the lock-in amplifier and the synthesizer frequency, a 'lock' to contact mode can be established. Low mechanical Q-factors (~150) are obtained.

## B. Shear-force detection with a tuning fork

In the initial phases of this work, a tuning-fork [1][16] was used for detecting the shear force. This makes use of a (nominally) 32.7 kHz quartz-crystal watch tuning fork (*IQD* type XTAL002995). The can of the tuning fork must be removed (with the aid of a needle file) to produce a bare fork. In the authors' design, the wire probe is mechanically coupled to one prong of the tuning fork by means of a strip of polymer which is secured with cyanoacrylate adhesive (Fig. 3). Shear force caused by close proximity of the probe tip and specimens raises the frequency of the tuning fork resonance and reduces its Q-factor.

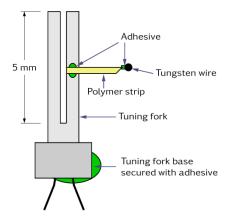


Fig. 3: Top view of the tuning fork assembly. In practice, the fork must be slightly tilted to provide adequate clearances.

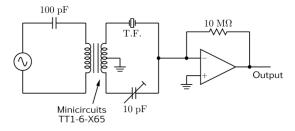


Fig. 4: Bridge and amplifier circuitry [16] for detection of shear force using a tuning fork.

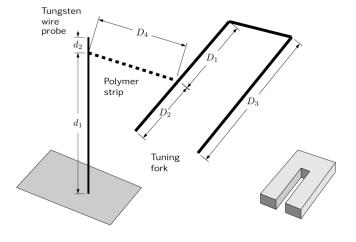


Fig. 5: Dimensions of tuning fork and probe assembly (diagram based on reference [17]).

This can be detected as a change in impedance by means of a simple bridge circuit (Fig. 4) driven at a constant frequency [16]. Similar structures are used in Scanning Near-field Optical Microscopy (SNOM) [17]; however for a microwave microscope the probe tip should ideally be separated from the tuning fork (which is metallized and will therefore cause disturbance to the fields). Satisfactory operation requires the probe to have a vibrational mode which resonates at almost the same frequency as the tuning fork assembly [17], i.e. ~32 kHz. This is a significant disadvantage as the design of the microwave cavity does not easily allow an adjuster for tuning the mechanical resonant frequency of the probe to be implemented. The elasticity, dimensions and positioning of the polymer strip (Fig. 5) are critical; our most successful design used a strip (cross-section 0.3x0.3 mm) cut from heatshrink tubing. For a probe made from tungsten wire 0.13-mm diameter, successful assemblies could be made with approximate dimensions  $D_1 = D_2 = D_4 = d_1 = 2.5 \text{ mm}$ d<sub>2</sub>=0.2 mm. To obtain a strong resonance d<sub>2</sub> must be as short as practicable. For dielectric resonator cavities, the wire can be anchored into the hole in the cavity lid by placing it concentrically and filling the gap with adhesive. For coaxial cavities, it is attached to the inner-conductor inside the cavity, but if it is necessary to shorten the length d<sub>1</sub> to change the resonant frequency it can also be secured to the lid. It was not possible to control dimensions accurately enough to produce a repeatable and reliable fabrication process by hand-assembly techniques. However, the design does have one very useful aspect; the tuning fork signal is observed to be remarkably unaffected by external vibrations.

## C. Shear force detection by optical beam deflection

On account of the difficulty of obtaining working tuningfork assemblies, it was decided also to implement an optical beam-deflection system [14]. This uses optical detection of resonances in a cantilever, which are excited by a piezoelectric actuator (referred to as a dither piezo). Talanov et al [5] use a similar method in an NSMM that uses a stripline instead of a wire probe. The dither frequency can be set arbitrarily to suit whatever resonances are available, which makes it much easier to construct than a tuning-fork system for the reasons given in Subsection B. To implement the beam deflection system a modified coaxial cavity which contains a cantilever in the inner conductor (Fig. 6) has been constructed. The Q-factor of the cantilever is low ( $\sim$ 150) so strong excitation is needed. For this reason it is necessary to locate the dither piezo on the inner conductor rather than on the outside of the cavity. A power amplifier (op-amp type OPA452) is used to boost the sine wave signal from the synthesizer to drive the piezo (Thorlabs TA0505D024W) with 10V peak amplitude. The resulting vibrational amplitude of the piezo is ~300 nm. The cantilever is illuminated by light from a 635 nm semiconductor laser with stabilized 1 mW output power (Edmund Optics #53-227). The system devised is unusual in that movement is detected using the shadow of the cantilever seen in transmission, rather than by the more conventional method of using reflection of the beam from the cantilever. The transmission approach means that the holes  $(1.5 \text{ mm } \emptyset)$  in the cavity wall through which the light must pass can be on a diameter, which eases assembly. The dither piezo is driven at approximately 9 kHz (the lowest resonance of the cantilever). Applying a voltage to the piezo was observed to shift the resonance of the microwave cavity, so it was necessary to shield it by using copper foil. The wire probe was attached to the inner-conductor with conducting paint. To minimize disturbance to the electromagnetic fields in the cavity, wires connections to the piezo were placed inside the inner conductor. A Position Sensitive Photodiode (PSPD) with integral amplifier (First Sensor QP50-6SD2-500741) was used to monitor the resonance of the cantilever. The AC output signal is obtained by subtraction between the signals obtained from individual photodiodes. Prior to its construction, the modified cavity was modelled with CST Microwave Studio [18] to ensure that the wire probe was in a high-field region of the cavity resonance. An incidental advantage of the optical beam deflection method is that it requires no parts to be placed in proximity to the probe tip (which could cause disturbance to fields) so calculability of complex permittivity should be improved compared to tuning fork methods.

## III. CALCULATION

Complex permittivity  $(\varepsilon^*)$  can be determined from measurements of the Q-factor and resonant frequency of the cavity unperturbed and with the probe tip in proximity to the specimen. For single dielectric-layer specimen of sufficient thickness (specimens were 2-mm thick in the work described) the image charge theory published by Gao and Xiang (GX) [2][4] can be applied. In principle, the permittivity of a specimen could then be determined from measurements in contact mode and at a gap that is sufficient (e.g. ~5 mm) to ensure that it does not perturb the resonant frequency of the cavity. A calibration measurement on a reference specimen that has known complex permittivity is also needed. However observations of approach curves show that, if the frequency is extrapolated to a large gap, the value for the frequency that is obtained is lower than the actual measured frequency at a large gap (Fig. 7). This may be attributed to stray-field effects. To obtain accurate measurements of permittivity, all of the data must apply to the same 'regime' (e.g. gaps  $\leq 10 \mu m$ ), therefore it is necessary to measure approach curves over the small gap range and obtain the unperturbed frequency by fitting the approach-curve data to the GX formula (which gives the extrapolated value). The radius of the sphere is fitted (in practice the fitted value differs significantly from the actual radius). A scaling constant A is also fitted.

 $<sup>^1</sup>$  Expressed by  $\varepsilon^*$  =  $\varepsilon'$  - j  $\varepsilon''$  where  $\varepsilon'$  and  $\varepsilon''$  are both positive.

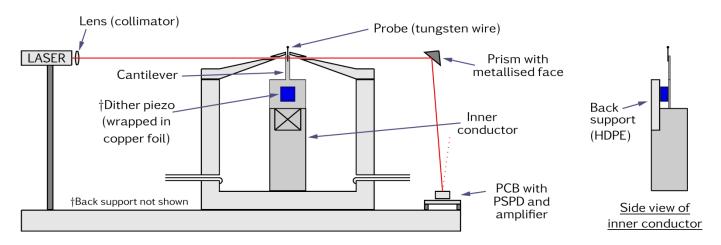


Fig. 6: Optical beam deflection system and modified quarter-wave cavity. The wire probe is attached to the cantilever with conducting paint.

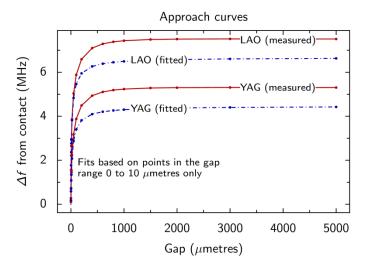


Fig. 7: Approach curves measured using the quarter-wave cavity (resonant frequency 1.37 GHz).

GX provide a method for obtaining dielectric loss using calibration coefficients. According to these authors, this method is suitable only for measurement of the loss of low loss materials. Kimber *et al* [19] study the GX method of determining dielectric loss in some detail. An alternative method that has not, to the authors' knowledge, previously been applied to microwave microscopes is to use the idea that the Q-factor and resonant frequency can be mathematically combined into a Laplacian 'complex frequency',

$$f = f' \left( 1 + \frac{\mathsf{j}}{20} \right),$$

where f' and Q are the measured (real) resonant frequency and Q-factor. Complex frequency as a concept is fairly little known and there are not many publications that make use of it. Reference [20] provides a derivation of complex frequency by applying the Laplace transform to a resonant circuit using parallel RLC components. In the microwave microscope it is applied by replacing the frequency in the GX formulas by the complex frequency, and replacing the permittivity by the complex permittivity. Optionally, the GX constant A may also be changed to a complex type, but in practice this is found to have little effect on calculated results.

Gao, Hu et al (GH) [3] published a method for calculating the frequency shift produced by a two-layer specimen which is also based on image charges. This was required for measurement on liquids contained by a window, but can be applied to the measurement of thin films also. The two-layer theory was also implemented using complex frequency to allow loss to be determined. The calculation requires traversal of a binary tree. GH and the present authors do this with a recursive method. For films with submicron thickness, the number of recursions (using a compiled C program) becomes so large that memory overflow problems can occur; nevertheless recursive solution using a PC is far more practical than it was when GH produced their paper in 2004 because computer hardware has evolved so much. Implementation of a non-recursive method for traversing the binary tree is an aspect which the authors plan to investigate in future. Software implementations of the formulations given by GX and GH were tested against each other for the case of a specimen that has two identical layers. They were in agreement.

TABLE I
CALIBRATION REFERENCE MATERIALS

Material	Formula	Permittivity and loss tangent		Comments	
		at 20 °C ε'	$ an\!\delta$		
Fused silica	SiO <sub>2</sub>	3.78 to 3.80	~ 10 <sup>-4</sup>	Very small variations (+/- 0.02) in permittivity between samples may occur due to differences in water content.	
Undoped Yttrium Aluminium Garnet (YAG) single crystal	$Y_3Al_5O_{12}$	10.59	~ 10 <sup>-5</sup>	Measurement of $\varepsilon'$ made by the authors of this paper using a Split-Post Dielectric Resonator (SPDR) [25].	
Lanthanum aluminate (LAO) single crystal	LaAlO <sub>3</sub>	23.9	~ 10 <sup>-4</sup>	Measurement of $\varepsilon$ made by the authors of this paper using an SPDR [25]. Permittivity can vary between batches as rare earth materials are difficult to separate [26]. May show crystal twinning [27]. Reported to be slightly anisotropic [26].	
Ethanol measured in liquid cell (Fig. 8)	C <sub>2</sub> H <sub>5</sub> OH	10.0	0.92	Complex permittivity data from reference [24]. Interpolated to 1.37 GHz.	
Ethanediol measured in liquid cell (Fig. 8)	$C_2H_6O_2$	20.4	0.83	Complex permittivity data from reference [24]. Interpolated to 1.37 GHz.	
Dimethyl sulfoxide (DMSO) measured in liquid cell	(CH <sub>3</sub> ) <sub>2</sub> SO	45.8	0.16	Complex permittivity data from reference [24]. Interpolated to 1.37 GHz.	

## IV. CALIBRATION AND MEASUREMENT PROCESS

Reference specimens are used for calibrating and also for checking the accuracy of calibrations. Individual specimens must be polished and uniform on the small scale. The materials from which they are made must have known and reproducible properties. Fused silica and single crystals such as Y<sub>3</sub>Al<sub>5</sub>O<sub>12</sub> (YAG) and LaAlO<sub>3</sub> (LAO) are ideal as low-loss reference materials (Table 1). However, suitable materials that have a high loss tangent<sup>2</sup> are much harder to find. Carbonloaded polymers, for example, are lossy but not reproducible or uniform on the small scale. Doped silicon was also considered, but was observed to exhibit interfacial (SiO2:Si) trapped charge effects [21] which greatly affected the measured permittivity. It is also light sensitive. In this work a new strategy has been tried; by using a polar liquid separated by a window (Fig. 8). Polar liquids have a loss peak in the microwave part of the spectrum [22]. To give maximum loss, a polar liquid that has the loss peak of its first-order relaxation close to the cavity resonant frequency can be chosen, e.g. butan-1-ol (relaxation frequency 257 MHz at 20° C), ethanol (829 MHz), ethanediol (962 MHz) dimethyl sulfoxide (7.6 GHz) or water (17 GHz). Dielectric relaxation occurs over a broad frequency range, so it is not necessary that the relaxation frequency should coincide with the cavity resonant frequency exactly. Traceable reference data is available for water [23] and a number of organic liquids [24]. The window material used was PEEK, 0.05 mm thick. The dielectric properties of the PEEK were measured at 1.8 GHz ( $\epsilon$ ′ = 3.28,  $\tan \delta$  = 0.004) with an SPDR [25].

In the experiment described, contact mode was established by using the optical beam deflection system (Fig. 6). Then approach curves for all of the specimens were obtained. Approach curves for YAG and LAO reference specimens were used for calibration by a least-squares approach to improve accuracy. This was possible as there was more data than strictly necessary (i.e. the calibration is over-defined). Approach curve data over a short-range (e.g. up to 10 µm) are used for calibration. A measurement of an unperturbed reading with a large gap (5 mm) is always made to act as a

<sup>&</sup>lt;sup>2</sup> Loss tangent  $\tan \delta = \varepsilon'' / \varepsilon'$ 

reference to allow drift between measurements to be monitored and corrected for. Once the calibration has been completed, permittivity can be measured in two ways: (i) from contact mode measurements of frequency and Q-factor, (ii) by fitting to approach curve measurements of frequency and Q-factor. Contact mode measurements can be applied during image scans. Both methods can be applied to the calibration measurements themselves which, for an over-defined calibration, provides a check on the calibration accuracy.

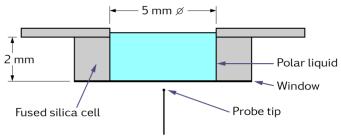


Fig. 8: Cell for measurement of a liquid.

## V. RESULTS AND ANALYSIS

Table 2 shows fitted results following calibration using by fitting to LAO and YAG approach curves for measurements at gaps in the range 0 to 10 µm. These measurements were made using a cavity resonance at 1.37 GHz, with Q-factor ~500. The measured loss tangent of the polar liquids is approximately correct even though the loss of the YAG and LAO calibration specimens is negligible by comparison. This validates the use of 'complex frequency' and also shows that the loss of specimens can be determined even when the calibration specimens are practically lossless. In other tests, it is found that the using a 'complex frequency' gives almost the same result as the unmodified GX theory for low-loss materials, but there is a divergence for high-loss materials.

TABLE 2
MEASUREMENT RESULTS (C.F. DATA IN TABLE 1)

Specimen	Fitted to 0 to 10 µm approach curve		Fitted to contact- mode data only		
	ε΄	$tan\delta$	ε΄	$ an\delta$	
Fused silica	3.2	-0.02	3.3	-0.02	
*YAG	10.6	0.02	10.9	0.00	
*LAO	23.8	0.01	23.4	0.01	
Ethanol	9.5	0.91	9.9	0.93	
Ethanediol	19.7	0.86	20.2	0.88	
DMSO	41.6	0.15	43.9	0.16	

<sup>\*</sup> Approach curves over range of 0 to 10  $\mu$ m for YAG and LAO were used for calibration.

When the cavity was designed it was hoped that it would be usable at several resonant frequencies; corresponding to  $\lambda/4$ ,  $3\lambda/4$  etc. of a simple coaxial resonator. On account of the complicated design of the inner conductor a fairly complicated mode spectrum is observed, which includes higher-order modes which couple little energy out of the cavity via the wire probe. Only the lowest mode (1.37 GHz) was found to be satisfactory for measurement; other modes were found to have poor shape, low Q-factor, or to be in close proximity to higher-order modes. Modifications to the inner conductor would be required to make other modes suitable for measurement available.

The other aspect of the design that will be improved in future work is the choice of material for the window of the liquid cell. A compromise is needed between the requirements for structural strength and minimal thickness (to give best sensitivity). The PEEK window was not sufficiently strong as it tended to bulge when filled with liquid (and Z readings in contact mode showed significant drift). A stiffer window material with suitable thickness ( $\leq 0.05$  mm) should give improved measurements.

## VI. CONCLUSION

In the experiment described two significant advances have been made: An optical beam deflection system has been developed for a microwave microscope with wire probe. A complex-number implementation of the published theories based on image charges (using the 'complex frequency') allows the loss of high-loss specimens to be obtained accurately. This has been demonstrated by measurements on polar liquids.

#### ACKNOWLEDGEMENT

The NSMM was developed under the project "Electromagnetic Materials Measurements for Industrial Applications (EMINDA)". This was a 3-year project under the European Metrology Research Programme (EMRP) under Grant Agreement No. 217257. The EMRP is jointly funded by the EMRP participating countries within EURAMET and the European Union. Additional funding from the IRD programme of the National Measurement Office of the UK Government Department of Business, Innovation and Skills supported the development of tuning fork and beam deflection systems.

The authors thank M. Stewart and A. Yacoot (NPL) for useful discussions on the beam deflection system. The authors also thank D.-Y. Sheu of the National Taipei University of Technology, Taiwan, for supply of EDM probe tips.

## REFERENCES

- [1] A. Imtiaz, T. Wallis and P. Kabos, "Near-field scanning microwave microscopy: An Emerging Research Tool for Nanoscale Metrology," *IEEE Microw. Mag.*, vol. 15, no. 1, pp. 52-64, 2014.
- [2] C. Gao and X.-D. Xiang, "Quantitative microwave near-field microscopy of dielectric properties," *Rev. Sci. Instrum.*, vol 69, no. 11, pp. 3846-3851, 1998.
- [3] C. Gao, B. Hu, P. Zhang, M. Huang, W. Liu, I. Takeuchi, "Quantitative microwave evanescent microscopy of dielectric thin films using a recursive image charge approach," *Appl. Phys. Lett.*, vol. 84, no. 23, pp. 4647-4649, 2004
- [4] H.-F. Cheng, Y.-C. Chen and I.-N. Lin, "Evanescent microwave probe study on dielectric properties of materials," *J. Eur. Cer. Soc.*, vol. 26, pp. 1801-1805, 2006.
- [5] V. Talanov, A. Scherz, R. Moreland and A. Schwartz, "A near-field scanned microwave probe for spatially localized electrical metrology", *Appl. Phys. Lett.*, vol 88, pp. 134106, 2006.
- [6] G. Gramse, M. Kasper, L. Fumagalli, G. Gomila, P. Hinter-dorfer and F. Kienberger, "Calibrated complex impedance and permittivity measurements with scanning microwave microscopy," *Nanotechnology*, vol. 25, no. 14, pp. 145703, 2014.
- [7] N. Okazakia, H. Odagawa, Y. Cho, T. Nagamura, D. Komiyama, T. Koida, H. Minami, P. Ahmet, T. Fukumura, Y. Matsumoto, M. Kawasaki, T. Chikyow, H. Koinuma, T. Hasegawa, "Development of scanning microwave microscope with a lumped-constant resonator probe for high-throughput characterization of combinatorial dielectric materials", *Appl. Surf. Sci.*, vol. 189, no. 3, p222-226, 2002.
- [8] J. Hoffmann, G. Gramse, J. Niegemann, M. Zeier and F. Kienberger, "Measuring low loss dielectric substrates with scanning probe microscopes," *Appl. Phys. Lett.*, vol. 105, pp. 013102, 2014.
- [9] S. Hanham, A. Gregory, S. Maier, N. Klein, "A dielectric probe for near-field millimeter-wave imaging," 37th International Conference on Infrared, Millimeter, and Terahertz Waves (IRMMW-THz), 2012.
- [10] B. Techaumnat and T. Takuma, "Analysis of the electric field and force in an arrangement of a conducting sphere and a plane electrode with a dielectric barrier," *IEEE Trans. Diel. Electr. Insul.*, vol 13, no. 6, pp. 336-344, 2006.
- [11] A. Gregory, "Q-factor measurement using a vector network analyser," NPL Report MAT 58, 2014 (to be published).
- [12] D.-Y. Sheu, "Micro-spherical probes machining by EDM," J. Micromech. Microeng., vol. 15, no. 1, pp. 185-189, 2005.
- [13] A. Yacoot and L. Koenders, "Aspects of scanning force microscope probes and their effects on dimensional measurement," J. Phys. D: Appl. Phys., vol. 41, 103001, 2008.
- [14] L. Beaulieu, M. Godin, O. Laroche, V. Tabard-Cossa, and P. Grütter, "Calibrating laser beam deflection systems for use in atomic force microscopes and cantilever sensors," *Appl. Phys. Lett.*, vol. 88, 83108, 2006.
- [15] A. Putman, B. de Grooth, N. van Hulst, J. Greve, "A detailed analysis of the optical beam deflection technique for use in atomic force microscopy," *J. Appl. Phys.*, vol. 72, no. 1, pp. 6-12, 1992.
- [16] Y. Seo and S. Hong, "Quartz crystal based scanning probe microscopy," *Modern Phys. Lett. B*, vol. 26, No. 26, 2005, pp. 1302-1322.
- [17] J. Morville, J. Liu, A. Callegari and M. Chergui, "Q-factor optimization of a tuning-fork/fiber sensor for shear-force detection,", Appl. Phys. Lett., vol. 86, no. 6, pp. 64103, 2005.
- [18] CST Microwave Studio. http://www.cst.com

- [19] D. Kimber, R. Pullar and N. Alford, "The effects of dielectric loss and tip resistance on resonator Q of the scanning evanescent microwave microscopy (SEMM) probe," *Meas. Sci. Tech.*, pp. 115502, 2008.
- [20] J. Chauveau, N. de Beaucoudrey, and J. Saillard, "Characterization of perfectly conducting targets in resonance domain with their quality of resonance," PIER, vol. 74, pp. 69-84, 2007
- [21] S. Lai, "Interface trap generation in silicon dioxide when electrons are captured by trapped holes," *J. Appl. Phys.* vol 54. no. 5, pp 2540-2546, 1983.
- [22] A. Gregory and R. Clarke, "A review of RF and microwave techniques for dielectric measurements on polar Liquids," *IEEE Trans. Diel. and Elec. Insulation*, vol. 13 no. 4 pp. 727-743 2006.
- [23] U. Kaatze, "Complex permittivity of water as a function of frequency and temperature," *J. Chem. Eng. Data*, vol. 34, no. 4, pp. 371-374, 1989.
- [24] A. Gregory and R. Clarke, "Tables of the complex permittivity of dielectric reference liquids up to 5 GHz," NPL Report MAT 23, 2012.
- [25] J. Krupka, A. Gregory, O. Rochard, R. Clarke, B. Riddle and J. Baker-Jarvis, "Uncertainty of complex permittivity measurements by split-post dielectric resonator technique", *J. Eur. Cer. Soc.*, vol 21, no. 15, pp. 2673-2676, 2001.
- [26] E. Hollmann, O. Vendik, A. Zaitsev and B. Melekh, "Substrates for high-Tc superconductor microwave integrated circuits," *Supercond. Sci. and Technol.*, vol. 7, pp. 609-622, 1994.
- [27] Q. Zhang, and P. McGinn, "Imaging of oxide dielectrics by near-field microwave microscopy," *J. Eur. Ceram. Soc.*, vol. 25, no. 4, pp. 407-416, 2005.

## Measurement Uncertainty in Waveguide VNA calibrated by Offset Short Calibration with Oversized Waveguide Aperture at Sub-millimeter Wave Frequency

## Masahiro Horibe and Ryoko Kishikawa

National Metrology Institute of Japan, National Institute of Advanced Industrial Science and Technology masahiro-horibe@ieee.org, masahiro-horibe@aist.go.jp, ryoko-kishikawa@aist.go.jp

This paper describes a new concept of calibration standards for waveguide Vector Network Analyzer (VNA) measurement in the millimeter and sub-millimeter wave frequency bands. High precision and traceable scattering parameter measurements have been established by using precision design of waveguide interface [1] and optimizing the measurement condition and setup of measurement system [2]. Even if using precision machining to make a precision waveguide, there is non-zero mechanical tolerance providing the degradation of connection repeatability. The National Metrology Institute of Japan (NMIJ) proposes to use the waveguide standard line with oversized aperture compared to aperture size of test-port waveguides. This new concept provides to improve the connection repeatability coming from misalignment. Results of the measurements and uncertainty estimation are described, and then, comparison results between conventional and new concepts are described for measurement uncertainty.

INDEX TERMS — Vector network analyzers, offset short calibration, waveguides, sub-millimeter wave, connection repeatability, oversized aperture.

## I. Introduction

The use of sub-millimeter-wave electronic applications and instruments have used in recent years, and commercial vector network analyzers (VNA) are now operating up to terahertz



Fig. 1 Photograph of test port (WM-864) and Standard line (WM1651)

frequency due to demand of device measurement over the millimeter wave frequency. The NMIJ has achieved the national standard techniques providing a high precision measurement in VNA with traceability to SI-base unit [1, 2]. The paper describes a new concept of measurement standard design for accurate S-parameter measurements over 110 GHz. In the concept of standards, waveguide with oversized aperture, i.e. WM-1651, is used for standards compared to waveguide aperture of test-ports. In this case, reflection characteristics should large value at the waveguide interface. However, the reflection characteristics at interface can be calculated from the

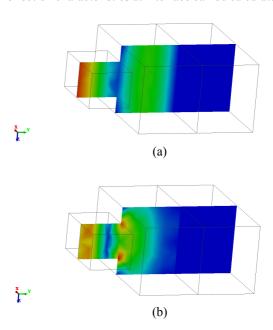


Fig. 2 Structure of oversized offset-short terminations with 0.728 mm offset length and their simulation model. Left end indicate test-port waveguide, mid part is offset prat of short and right end is flush short. Simulation frequencies of both figures (a) and (b) are 220 GHz and 330 GHz, respectively.

Table 1 Waveguide aperture size of offset shorts (unit: um)

	Tuble 1 Waveguide aperture bize of officer shorts (anti: µin)								
NI-	Star	ndard aperture (WM-8	364)	Oversized aperture (WM-1651)					
No.		Length	а	b	Length	а	b		
	Line-1	365	-3.7	-2.1	728	787.4	398		
	Line-2	1000	-4.1	-1.6	1912	790.5	395		
	Line-3	1291	-3.1	-1.0	2191	791.7	395.6		

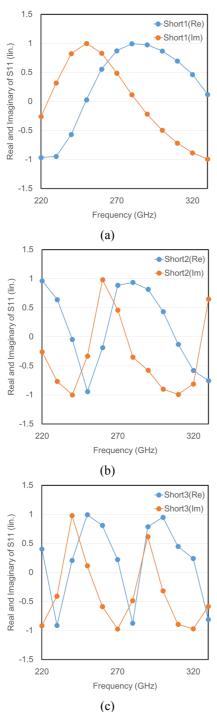


Fig. 3 Calculation results of reflection coefficients for oversized offset short terminations with (a) 0.728 mm, (b) 1.000 mm and (c) 1.291 mm offset lengths.

dimension using simulation and electromagnetic theory or electromagnetic simulation. Then, use of different size aperture can inhibit the misalignment effect providing the deterioration of connection repeatability [3, 4]. We have investigated the repeatability performance of some waveguide connections of

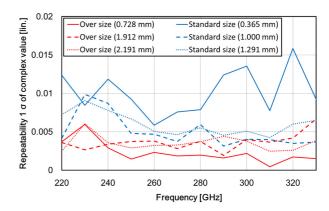


Fig. 4 Results of experimental standard deviation,  $1\sigma$ , (i.e. repeatability) for a series of 10 repeat reconnection/disconnection measurements for offset short terminations with three different length in the WM-864 waveguide frequency band.

offset short standard terminations for the WM-864 [5] (WM-864, WR-3) waveguide band. To validate the performance of connection repeatability performance for design concept of oversized aperture standards, the connection repeatability of offset short with standard aperture size and oversized aperture has be estimated and compared each other by VNA measurements. Then, measurement uncertainty of one-port VNA has been estimated using the both standard aperture size and oversized aperture.

## II. STANDARD DESIGN USING OVERSIZED APERTURE

Precision waveguide flange was adopted as waveguide interface of the VNA test-ports in order to establishing the precise connection. The test port has a precise machined waveguide aperture, i.e. 0.868 mm width and 0.434 mm height of waveguide aperture, fitted to specification of the IEEE P1785 standard [5]. In this study, offset short terminations were formed by combination of waveguide standard line and flush short termination. Three different length lines were used for forming the three different offset short terminations. Then, standard aperture fitted with WR-864 and oversized aperture fitted with WM-1651 were prepared as the offset lines. Table 1 shows the dimensional difference between the both waveguide apertures of test-port and standard lines. Lines with standard aperture have almost the same aperture size of test-port. However, lines with oversized aperture have almost twice large aperture size of test-port (Fig. 1 and 2).

The S-parameter was estimated from the mechanical measurements: width, height and line length of the standard waveguide lines terminated by flush short. It was derived from a series expansion of the field in eigenmodes [6] by a Monte Carlo simulation involving 100,000 trials. Results of reflection coefficient value for offset short terminations with 0.728 mm, 1.000 mm and 1.291 mm offset lengths are shown in Fig. 3.

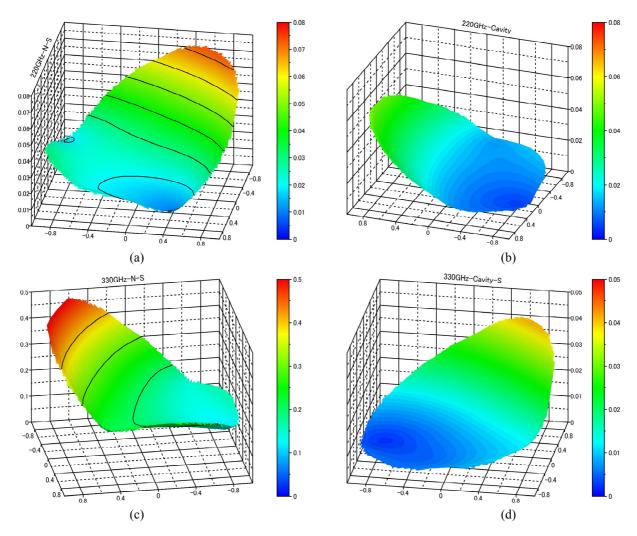


Fig. 5 Measurement uncertainty at 220 GHz in VNA calibrated by three offset short terminations with (a) standard aperture size and (b) oversized aperture waveguide.

## III. ELECTRICAL MEASUREMENT REPEATABILITY

Fig. 4 shows the results of connection repeatability evaluation, i.e. the experimental standard deviation, as a function of frequency for offset short terminations with standard and oversized apertures. The offset short terminations with oversized aperture produced better connection repeatability than that with standard size aperture. The results indicate that the oversized aperture design of standard terminations gives the dramatically improvement of connection repeatability in usage of short terminations.

## IV. UNCERTAINTY ESTIMATION IN VNA MEASUREMENTS

The device characteristic was calculated by correcting the residuals obtained by offset short calibration. The estimation of

the expanded uncertainties,  $u(\Gamma_{\rm dut})$ , was performed by referring the Guides to the expression of uncertainty in measurement (GUM). At both band edges, i.e. 220 GHz and 330 GHz, the measurement uncertainties for VNA calibrated by the both two sets of offset short terminations are shown in Figure 5. Offset short calibration on the basis of oversized aperture standards provides smaller uncertainty of reflection characteristics measurement in VNA. This was because repeatability effect in the VNA measurement uncertainty can be reduced by the terminations with oversized aperture waveguide.

## V. CONCLUSION

This paper has challenged improvement of VNA measurement uncertainty by using new concept of the offset

short terminations as standards. An effect of oversized aperture on connection repeatability in VNA calibration are investigated and provides improving the repeatability contribution to VNA measurement uncertainty.

## REFERENCES

- [1] M. Horibe, et. al., "Modification of Waveguide Flange Design for Millimeter and Sub-millimeter-wave measurements," 77th ARFTG Conf. Digest, pp. 1-7, June. 2011.
- [2] M. Horibe, et. al., "Comparing Accuracy of Waveguide VNA Measurement Calibrated by TRL Calibration Using Different Length of Line Standard in Terahertz Band," 81th ARFTG Conf. Digest, pp. 1-7, June. 2013.
- [3] M. Horibe, et. al., "Investigations of Capability of Connection Repeatability for Waveguide with Different Size Apertures," 82th ARFTG Conf. Digest, pp. 1-7, Nov. 2013.
  [4] M. Horibe, et. al., "Improvement of Offset Short Calibration
- [4] M. Horibe, et. al., "Improvement of Offset Short Calibration Technique in Waveguide VNA Measurement at Millimeter and Sub-millimeter Wave Frequency", CPEM2014 conference digests, Aug. 2014.
- [5] "IEEE Standard for Rectangular Metallic Waveguides and Their Interfaces for Frequencies of 110 GHz and Above," IEEE P1785, <a href="http://grouper.ieee.org/groups/1785">http://grouper.ieee.org/groups/1785</a>.

# Broadband Dielectric Spectroscopy Calibration Using Calibration Liquids with Unknown Permittivity

S. Liu<sup>1</sup>, I. Ocket<sup>2,1</sup>, P. Barmuta<sup>1,3</sup>, T. Markovic<sup>1</sup>, A. Lewandowski<sup>3</sup>, D. Schreurs<sup>1</sup>, and B. Nauwelaers<sup>1</sup>,

<sup>1</sup>University of Leuven, Div. ESAT-TELEMIC, Kasteelpark Arenberg 10, 3001, Leuven (Heverlee), Belgium 
<sup>2</sup>Interuniversity Microelectronics Center, Kapeldreef 75, 3001, Leuven (Heverlee), Belgium 
<sup>3</sup>Warsaw University of Technology, Pl. Politechniki 00-661 Warsaw, Poland

Abstract—This paper presents a calibration method for broadband dielectric spectroscopy of micro-liter samples of biological liquids with transmission line sensors up to 110 GHz. The method uses water and methanol as calibration liquids to perform a probe-tip-to-liquid calibration without prior knowledge of their complex permittivity. Extracted complex permittivities of the calibration liquids show good agreement with literature values. Furthermore, sensors with different first-tier calibrations and geometries show consistent results.

Keywords—on-wafer, calibration, dielectrics, spectroscopy, biology, millimeter wave.

## I. INTRODUCTION

Broadband dielectric spectroscopy reveals valuable information about biological liquids such as cell suspensions and protein solutions. For example, in [1], different microwave signatures are used to distinguish viable and non-viable cells. In [2], based on a bulk measurement technique, the dielectric spectra are used to differentiate different proteins in solutions, independent of their concentration.

Microfluidics is the technology of dealing with, *e.g.*, the generation, mixing, transportation and reaction, etc., of nl-pl volumes of fluid samples. It offers a promising future of high-throughput biological analysis to the scientific community. In recent years, due to the ease of integration with microfluidics, planar microwave sensors, *e.g.*, coplanar waveguide (CPW) transmission lines and interdigitated capacitors, are popular candidates to perform label-free and non-invasive characterization and sensing of biological liquids in microfluidic channels [3][4].

To accurately extract the broadband complex permittivity  $(\epsilon_r = \epsilon' - j\epsilon'')$  of the material under test (MUT) in order to study, for example, cell behavior, cell composition, and protein types, etc., the extra phase shift and loss caused by the microfluidics have to be removed by a de-embedding step. Usually this step requires the fabrication of redundant test structures with the polymer used for the microfluidics on top of transmission line to accurately characterize the characteristics of the polymer [4] or to enable the extraction of just the propagation constant of the MUT-loaded line [3].

In [5], we have proposed a calibration method based on calibration liquids to perform this de-embedding step. It eliminates the need of fabricating redundant structures and instead uses measurements of water and methanol which are generally available in the laboratory. One drawback of the method is that it relies on the permittivity data of water at a certain temperature which itself has some uncertainty. In this paper, we improve the method by allowing the  $\epsilon_r$  of both calibration

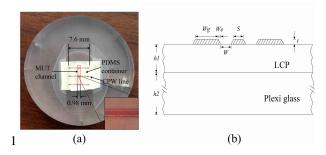


Fig. 1. (a): Picture of the sensor with 0.98 mm long MUT channel. The MUT channel is highlighted in red. (b): cross-section of the CPW transmission line.

liquids to be unknown. By utilizing the redundancies in the equations, their  $\epsilon_r$  are extracted in the calibration procedure. We will show good agreement with literature values, proving the validity of the method. Furthermore, calibrations with sensors with different dimensions exhibit consistent results in terms of extracted  $\epsilon_r$  of the calibration liquids.

This paper is organized as follows: in Section II, the CPW sensor used is introduced, in Section III, the calibration method is described in detail, in Section IV, the validity of the calibration method is checked in different aspects, and in section V, some conclusions are drawn.

## II. CPW SENSOR

The sensor used to verify the calibration method is a CPW transmission line realized on a liquid crystal polymer (LCP, ULTRALAM 3000 from Rogers) substrate with a polydimethylsiloxane (PDMS) container bonded to it as shown in Fig. 1(a). The metalization of the CPW line is copper and has a thickness of 18  $\mu$ m. The PDMS container is fabricated separately from the LCP part with a PVC mold and is bonded to the CPW line on the LCP substrate with PDMS. The LCP substrate is attached to a thick plexiglass sample to suppress the excitation of the unwanted microstrip mode between the CPW conductors and the metal chuck used to hold the sensor during measurement. The cross-section of the CPW line is shown in Fig. 1(b) and its dimensional parameters are listed in Table. I. The temperature of the liquid in the container is monitored constantly with a T-type thermocouple with 1°C tolerance [6]. Although in this work our calibration method is verified with open containers shown in Fig. 1, it can also be applied to other CPW sensors with sealed microfluidic channels.

TABLE I. Cross section of the CPW transmission line

Wg [um]	We [um]	W[um]	S[um]	t [um]	h1 [um]	h2 [mm]
91	10.5	41	38.5	18	100	8.05

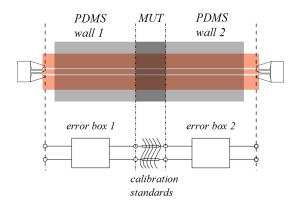


Fig. 2. Schematic of the error boxes and calibration standards. (--) indicates the reference plane of the first-tier calibration (LRRM or multiline TRL) and  $(-\cdot-)$  indicates the reference plane of the second-tier calibration using calibration liquids.

## III. CALIBRATION METHOD

In this section, the calibration method using water and methanol as calibration liquids is described in detail. The schematic of the calibration problem is shown in Fig. 2. The network analyzer is first calibrated with a LRRM or multiline TRL (MTRL) calibration to the probe-tips. In order to extract the  $\epsilon_r$  of the liquid, the reference planes have to be moved from the probe-tip to the liquid by a second-tier calibration as discussed in this paper. The aim of this second-tier calibration is to determine the probe-tip-to-MUT error boxes by using calibration-liquid-loaded transmission lines as calibration standards.

Measurements of the CPW sensor loaded with demineralized water, methanol, and air are used for the calibration method. The S-parameters of the transmission line standards are fully described by their effective permittivity  $\epsilon_{eff}$ , characteristic impedance Zc, and line lengths through transmission line equations. The propagation constant of the plain transmission line is measured by performing a MTRL [7][8] on plain CPW lines of the same cross-section. It uses lines of 641, 1189, 2282, 2885, 4096, 7592, and 20598 um, respectively, and an open standard of 639 um. The cross-section of the CPW line (Fig. 1(b)) is simulated in HFSS v.14 to obtain the DC capacitance per unit length. In the simulation, the permittivity of LCP is set to 3.16 with loss tangent 0.0025 [9] and that of plexiglass is set to 2.5929 with loss tangent 0.0087 [10]. The simulated capacitance per unit length is 58.62 pF/m from which the characteristic impedance of the CPW line is extracted from the propagation constant [11]. From  $\epsilon_{eff}$  and Zc of the plain CPW lines, the inductance and resistance per unit length can be easily derived. They depend primarily on the conductor properties and can be assumed to be independent of the material on top of the CPW lines. So for the air-loaded and liquid-loaded lines, the inductance and resistance per unit length are assumed to be the same which is an assumption

also used by [4]. By combining the following equations

$$\gamma_{liquid} = \sqrt{(j\omega L_{liquid} + R_{liquid})(j\omega C_{liquid} + G_{liquid})}. (1)$$

$$Z_{c,liquid} = \sqrt{\frac{j\omega L_{liquid} + R_{liquid}}{j\omega C_{liquid} + G_{liquid}}}.$$
 (2)

$$\epsilon_{eff,liquid} = -\left(\frac{c\gamma_{liquid}}{\omega}\right)^2,$$
(3)

one can obtain

$$\epsilon_{eff,liquid} Z_{c,liquid}^2 = -\left(\frac{c}{\omega}\right)^2 (j\omega L_{liquid} + R_{liquid})^2.$$
 (4)

In (1)-(3),  $\gamma_{liquid}$ ,  $Z_{c,liquid}$ , and  $\epsilon_{eff,liquid}$  are the propagation constant, characteristic impedance, and effective permittivity of the liquid-loaded transmission line respectively,  $R_{liquid}$ ,  $L_{liquid}$ ,  $G_{liquid}$ , and  $C_{liquid}$  are the resistance, inductance, conductance, and capacitance per unit length of the same line respectively, c and  $\omega$  are the speed of light in vacuum and the angular frequency respectively. The right hand side of (4) is independent of the material loading the transmission line, so the S-parameters of a liquid-loaded line can be modelled by one unknown which is either  $\epsilon_{eff,liquid}$  or  $Z_{c,liquid}$ .

Finally the calibration problem using air-loaded, waterloaded, and methanol-loaded lines as standards can be stated as follows: there are in total nine unknowns to be solved, seven of which are the elements of error box 1 and 2, and two of which are  $\epsilon_{eff,water}$  and  $\epsilon_{eff,methanol}$ . By embedding the S-parameters of the calibration standards in the error boxes, one can model the S-parameters of the calibration standards at the probe-tips. Equations can be formed by equating the measured and modelled probe-tip S-parameters of the calibration standards. Due to the reciprocity of the calibration standards and error boxes, each measurement gives in total three equations for  $S_{11}$ ,  $S_{21}$  and  $S_{22}$ . Also the reciprocity of the probe-tip-to-MUT error boxes gives one extra equation about the error box elements. So in total, there are ten equations to solve a nonlinear system with nine variables. These equations are automatically formulated and solved in Matlab using the algorithm reported in [12]. The algorithm supports symbolic formulation of partially defined standards and computes error boxes using nonlinear least-square fitting. Due to the uncertainty in the MUT channel length, the MUT channel length is swept around its nominal value, which is 1 mm, to further reduce the error in S-parameters. The channel length obtained after optimization is 0.98 mm.

## IV. CALIBRATION VERIFICATION

In this section, the calibration method is tested with actual probe-tip measurements. The measurements are performed with a 67 GHz network analyzer with 110 GHz extension modules and 110 GHz GSG microwave probes with 100 um probe pitch. The frequency sweep is set to be from 0.5 GHz to 110 GHz with 0.5 GHz steps. Off-wafer LRRM calibration on an ISS and on-wafer multiline TRL (MTRL) calibration are performed separately as first-tier calibration for comparison

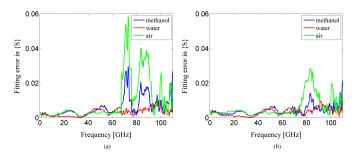


Fig. 3. Fitting error of our calibration procedure after (a) a first-tier LRRM calibration and (b) a first-tier multiline MTRL calibration.

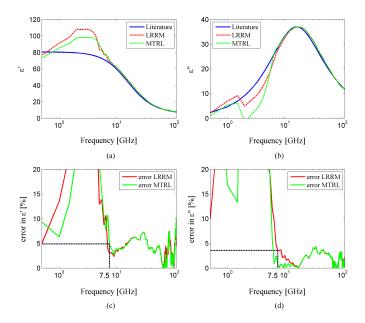


Fig. 4. Extracted  $\epsilon_r$  of water at  $18.8^{\circ}\mathrm{C}$  using the proposed calibration method with LRRM and MTRL as first-tier calibrations in comparison with literature values [13]. (a): $\epsilon'$ . (b):  $\epsilon''$ . Relative error in (c)  $\epsilon'$  and in (d)  $\epsilon''$  with respect to literature values.

purposes

Fig. 3 shows the fitting error in S-parameters which is defined in (5)

$$error = \sqrt{\sum_{i,j=1}^{2} |S_{i,j,meas} - S_{i,j,model}|^2}$$
 (5)

where  $S_{i,j,meas}$  and  $S_{i,j,model}$  represent the measured and modelled probe-tip S-parameters, respectively. The small fitting errors indicate the success of the optimization procedure. Raw data calibrated with the MTRL calibration shows less fitting errors. The reason is still under investigation.

To further verify the calibration method, the measured  $\epsilon_{eff,water}$  and  $\epsilon_{eff,methanol}$  are translated into  $\epsilon_{r,water}$  and  $\epsilon_{r,methanol}$  by iterative simulations of the 2D cross-section of the liquid-loaded CPW line which minimizes the difference in measured and simulated  $C_{liquid}$  and  $G_{liquid}$ . The extracted  $\epsilon_r$  of the calibration liquids are shown in Fig. 4 and Fig. 5 together with literature values [13] [14]. In general, the measured  $\epsilon_r$  of the calibration liquids show good agreement with literature values, especially for water. Like the TRL calibration,  $\epsilon_r$  shows frequency-dependent errors. More specifically, the errors of

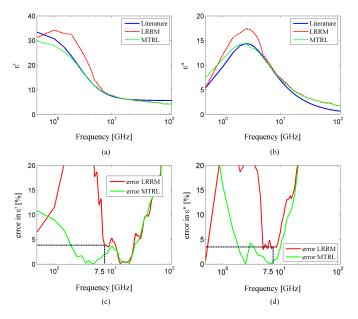


Fig. 5. Extracted  $\epsilon_r$  of methanol at 15.8°C using the proposed calibration method with LRRM and MTRL as first-tier calibrations in comparison with literature values [14]. (a): $\epsilon'$ . (b):  $\epsilon''$ . Relative error in (c)  $\epsilon'$  and in (d)  $\epsilon''$  with respect to literature values.

both extracted  $\epsilon_{r,water}$  and  $\epsilon_{r,methanol}$  are high at low frequencies. The error of  $\epsilon_{r,water}$  drops to a few percent at frequencies above 7.5 GHz. However that of  $\epsilon_{r,methanol}$  first drops but increases again above 10 GHz. The main reason might be that the reference data was only measured up to 5 GHz. Other reasons include limited control of the methanol temperature due to evaporation and the impurity of the methanol sample. Judged from the small difference between  $\epsilon_r$  extracted from the LRRM and MTRL calibrated data, the use of different first-tier calibrations has a marginal effect on the extracted  $\epsilon_r$  of the calibration liquids.

The extracted wave cascading matrix of the probe-tip-to-MUT error boxes are transformed to S-parameters. The result is shown in Fig. 6. The S-parameters of the transitions show physically meaningful behaviour. The large ripples are due to the impedance mismatch of the air-loaded and PDMS-loaded CPW lines.

In addition to the sensor with 0.98 mm MUT channel discussed above, the calibration method is further tested with 1.01 mm and 2.42 mm channels. The extracted  $\epsilon_r$  of the calibration liquids with a MTRL first-tier calibration are plotted in Fig. 7 and Fig. 8. It is clear that sensors with different MUT channel lengths produce consistent results in terms of  $\epsilon_r$  of the calibration liquids. The 2.42 mm MUT channel shows improved extraction of the calibration liquids at low frequencies.

For characterization of biological liquids using the CPW sensor, the obtained error box 1 and 2 can be used directly to de-embed the probe-tip S-parameters measurement. Another way is to replace water with the biological liquid to be measured as one of the calibration liquid because the  $\epsilon_r$  of the calibration liquids are extracted from the calibration method.

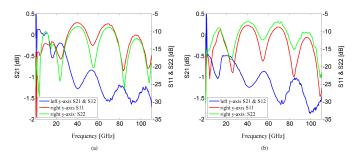


Fig. 6. S-parameters of (a) error box 1 and (b) error box 2 extracted from the calibration procedure with a first-tier LRRM calibration.

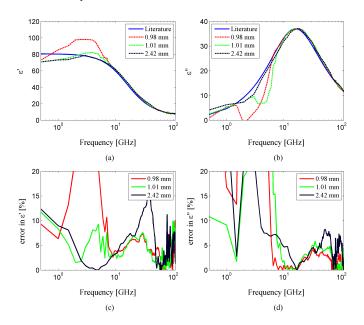


Fig. 7. Extracted  $\epsilon_r$  of water at  $18.8^{\circ}$ C,  $18.9^{\circ}$ C and  $18.3^{\circ}$ C using MUT channels of 0.98 mm, 1.01 mm and 2.42 mm respectively and a first-tier MTRL calibration. Literature values at  $18.7^{\circ}$ C [13] are shown as reference. (a):  $\epsilon'$ . (b):  $\epsilon''$ . Relative error in (c)  $\epsilon'$  and in (d)  $\epsilon''$  with respect to literature values.

## V. CONCLUSION

In this paper, we have presented a calibration method for determining the probe-tip-to-MUT error boxes for the purpose of broadband dielectric spectroscopy of biological liquids up to 110 GHz. Compared to our previous method using calibration liquids [5], the method in this paper doesn't rely on reference data for the  $\epsilon_r$  of water, which is itself limited in accuracy. Instead its  $\epsilon_r$  is extracted from the calibration procedure and shows good agreement with literature values. Comparisons are made for different first-tier calibrations and sensors with different MUT channel lengths and they all have consistent results.

## VI. ACKNOWLEDGMENTS

Arkadiusz Lewandowski was funded by the Polish National Science Center in the framework of project no. DEC-2011/03/D/ST7/01731. Pawel Barmuta was supported by the Research Foundation Flanders (FWO-Vlaanderen). The authors are grateful to ARFTG (the Automatic RF Techniques Group) for granting support to this work through their 2013

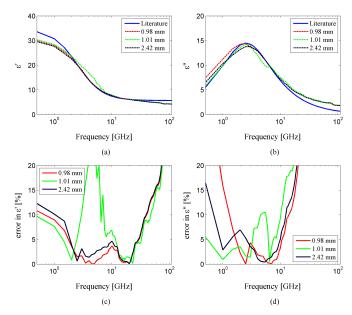


Fig. 8. Extracted  $\epsilon_r$  of methanol at  $15.8^{\circ}\mathrm{C}$ ,  $14.7^{\circ}\mathrm{C}$  and  $14.4^{\circ}\mathrm{C}$  using MUT channels of 0.98 mm, 1.01 mm and 2.42 mm respectively and a first-tier MTRL calibration. Literature values at  $15.0^{\circ}\mathrm{C}$  [14] are shown as reference. (a):  $\epsilon'$ . (b):  $\epsilon''$ . Relative error in (c)  $\epsilon'$  and in (d)  $\epsilon''$  with respect to literature values.

student fellowship. The authors would also like to thank Dr. Dylan Williams and Dr. James Booth for the fruitful discussions.

## REFERENCES

- [1] T. Chen, D. Dubuc, M. Poupot, J.-J. Fournié, and K. Grenier, "Broadband discrimination of living and dead lymphoma cells with a microwave interdigitated capacitor," *IEEE Topic Conference on Biomedical Wireless Technologies, Networks, and Sensing Systems*(BioWirelessSS), pp. 64–66, 2013.
- [2] T. H. Basey-Fisher, S. M. Hanham, H. Andresen, S. A. Maier, and M. M. S. et al., "Microwave debye relaxation analysis of dissolved proteins: towards freesolution biosensing," *Applied Physics Letters*, vol. 99, pp. 233701–1–233703–3, 2011.
- [3] K. Grenier, D. Dubuc, P.-E. Poleni, M. Kumemura, H. Toshiyoshi, T. Fujii, and H. Fujita, "Integrated broadband microwave and microfluidic sensor dedicated to bioengineering," *IEEE Transactions on Microwave Theory and Techniques*, vol. 57, no. 12, pp. 3246–3253, 2009.
- [4] J. C. Booth, N. D. Orloff, J. Mateu, M. Janezic, M. Rinehart, and J. A. Beall, "Quantitative permittivity measurements of nanoliter liquid volumes in microfluidic channels to 40 GHz," *IEEE Transactions on Instrumentation and Measurement*, vol. 59, no. 12, pp. 3279–3288, 2010.
- [5] S. Liu, I. Ocket, P. Barmuta, A. Lewandowski, D. Schreurs, and B. Nauwelaers, "Broadband dielectric spectroscopy calibration for microliter samples of biogenic liquid," *European Microwave Conference*, accepted, 2014.
- [6] T. Markovic, S. Liu, J. Bao, I. Ocket, and B. Nauwelaers, "Temperature controlled permittivity extraction of water on microliter scale up to 40 GHz from 10 to 40°C," *IEEE MTT-S International Microwave Workshop Series on RF and Wireless Technologies for Biomedical and Healthcare Applications (IMWS-Bio)*, accepted, 2014.
- [7] R. B. Marks, "A multiline method of network analyzer calibration," IEEE Transactions on Microwave Theory and Techniques, vol. 39, no. 7, pp. 1205–1215, 1991.
- [8] "MultiCal software package," National Institute of Standards and Technology.

- [9] D. C. Thompson, O. Tantot, H. Jallageas, G. E. Ponchak, M. M. Tentzeris, and J. Papapolymerou, "Characterization of liquid crystal polymer (LCP) material and transmission lines on LCP substrates from 30 to 110 GHz," *IEEE Transaction on Microwave Theory and Techniques*, vol. 52, no. 4, pp. 1343–1352, 2004.
- [10] U. C. Hasar and C. R. Westgate, "A broadband and stable method for unique complex permittivity determination of low-loss materials," *IEEE Transactions on Microwave Theory and Techniques*, vol. 57, no. 2, pp. 471–477, 2009.
- [11] R. B. Marks and D. F. Williams, "Characteristic impedance determination using propagation constant measurement," *IEEE Microwave and Guided Wave Letters*, vol. 1, no. 6, pp. 141–143, 1991.
- [12] P. Barmuta, A. Lewandowski, S. Liu, W. Wiatr, and D. Schreurs, "General method of seven-term statistical calibration with partially defined standards," *International Conference on Microwaves, Radar,* and Wireless Communications, pp. 219–222, June 16-18, 2014.
- [13] W.J.Ellison, "Permittivity of pure water, at standard atmospheric pressure, over the frequency range 0 25 THz and the temperature range 0 100 °C," *Journal of Physical and Chemical Reference Data*, vol. 36, no. 1, 2007.
- [14] A. P. Gregory and R. N. Clarke, "Tables of the complex permittivity of dielectric reference liquids at frequencies up to 5 GHz," *Report of National Physical Laboratory*, UK, 2012.

## Progress Towards a NIST Microwave Brightness Temperature Standard for Remote Sensing\*

Derek A. Houtz<sup>1,2</sup>

Dept. of Aerospace Engineering and Sciences
University of Colorado
Boulder, CO, USA
Derek.Houtz@colorado.edu

Abstract— We discuss work at NIST aimed at developing a passive microwave brightness temperature standard. By reducing uncertainty, we can provide better calibrations for future weather and climate-monitoring radiometers. We discuss the calibration procedure used, measured data, and various theoretical and simulated results that have led to an improved understanding of the various uncertainty contributions in the measurement. We overview a Monte Carlo simulation to determine the uncertainty in target brightness temperature as a function of measurement distance and target size. We also discuss other future improvements including an improved blackbody design. The achievable calibration source brightness temperature uncertainty is expected to be reduced from the current 0.7 to 1.0 K from 18 to 65 GHz to less than 0.3 K.

Keywords—remote sensing; blackbody; passive microwave; calibration; traceability

## I. INTRODUCTION

Passive microwave radiometers are used for remote sensing of the earth's land, atmosphere, and oceans. Microwave measurements are used in satellite-and aircraft-mounted radiometers for numerical weather prediction and in innumerable other climate monitoring projects on both satellites and aircraft. NIST has developed a method to extend our standard waveguide radiometers to free space, allowing us to calibrate flight reference sources or 'blackbodies'. This approach relies on the standard radiometer as the primary reference. We can also calibrate against a primary blackbody reference if available. The combination of both references creates a more robust calibration scheme and may reduce uncertainties.

The currently used hardware and measurement methods can provide a best-case calibration uncertainty of about  $\pm 0.7~\rm K$ . This level of uncertainty would be helpful for studying some environmental variables across different measurement platforms, but many long term climate variables require much smaller uncertainty in order to make significant scientific claims on a global scale. Recent work has involved simulation aimed at fully exploring the sources of uncertainty and identifying areas of potential improvement.

## II. MEASUREMENT PROCEDURE

Free-space radiometric measurements are made in an anechoic chamber with the calibrated waveguide radiometer

David K. Walker<sup>2</sup>, Dazhen Gu<sup>2</sup>

<sup>2</sup>RF Electronics group

National Institute of Standards and Technology

Boulder, CO, USA

flange (the reference plane for the measurements) attached to a horn antenna. The blackbody reference used for past measurements is an array of absorber-coated aluminum square pyramidal structures 40 mm in height with a base of 10 mm. Standard RF absorber is often made from pyramidal structures of carbon-loaded foam, but this target is manufactured with a 1 mm thick coating of high-quality iron loaded epoxy absorber. The absorber is cast onto the aluminum substrate material and an electronic resistance heater is attached to the backside of the aluminum. The target is designed to have a microwave emissivity of close to unity in order to most closely resemble an ideal blackbody. The passive blackbody radiance from the target, often referred to as "brightness temperature" (Tb), is directly related to the temperature of the target by Planck's For a true blackbody, knowledge of the physical temperature is all that is needed to perfectly characterize its Tb. Temperature non-uniformity in the heated target will lead to measurement error because the analysis relies on a constant and uniform temperature distribution. When the horn views the blackbody there are some other considerations such as the target not completely filling the horn's antenna power pattern. We quantify this with the illumination efficiency ratio. The measurement distance must also be carefully chosen to avoid coherence effects at close distances, while maintaining adequate signal strength and avoiding too much spillover from The background temperature must be the background. measured and is also assumed to be uniform. Determining the optimal measurement conditions is not trivial and requires some analytical and experimental investigation.

The relationship expressed in (1) describes how the brightness temperature of the target is calculated from a free-space radiometric measurement:

$$\bar{t}_{tg} = \frac{1}{\alpha \eta_{IE}} T_x - \frac{1}{\eta_{IE}} T_{bg}^{phy} - \frac{1}{\alpha \eta_{IE}} T_{ant}^{phy}, \tag{1}$$

where  $\bar{T}_{tg}$  is the effective target brightness temperature,  $\alpha$  is the antenna efficiency (related to ohmic loss),  $\eta_{IE}$  is the illumination efficiency,  $T_x$  is the brightness temperature measured at the waveguide flange of the radiometer,  $T_{bg}^{phy}$  is the physical temperature of the background, and  $T_{ant}^{phy}$  is the physical temperature of the antenna. The effective target brightness temperature is determined by integrating the product of the target's physical temperature field, angular dependent

emissivity, and the power pattern of the antenna over the solid angle subtended by the target.

Fig. 1 shows the pyramidal array blackbody target mounted in the large NIST anechoic chamber with a standard gain horn mounted and aligned to take measurements of the target. Here, the target is exposed to the chamber environment. We have also made measurements using various types of insulation to reduce temperature gradients on the target surface, but this does slightly reduce the effective emissivity of the target.

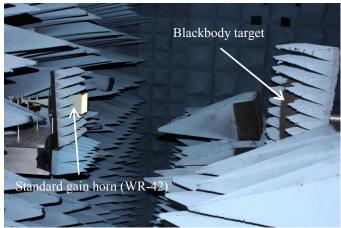


Fig. 1. Measurement setup in the NIST anechoic chamber.

#### III. RESULTS

Fig. 2 presents the results of the calculated target brightness temperature versus measured physical temperature for measurements on the square pyramidal array target at 18 GHz. The error bars show the propagated uncertainty at each measurement distance. The full derivation for the uncertainty can be found in [1]. As the separation distance between the horn and the blackbody increases, the influence of the background increases because the target subtends a smaller solid angle fraction of the antenna pattern. The uncertainty in the background temperature is relatively high for this setup and dominates at larger distances. Research has been focused on reducing uncertainties in these measurements which would allow for a more robust and desirable standard.

The method described in [1] discusses the extraction of the illumination efficiency  $\eta_{IE}$ . The uncertainty in the illumination efficiency is correlated through a non-linear fitting to multiple radiometric data and the other physical temperatures in (1), so the overall calculated target brightness temperature uncertainty is difficult to express or predict analytically. A Monte Carlo simulation was performed to determine the uncertainty of the target brightness temperature as a function of measurement distance and blackbody size. Fig. 3 shows a contour of the Monte Carlo data. The illumination efficiency here is determined from a computer simulation result according to the method described in [2]. The plot shown is for 18 GHz. The plot is bounded at 0.5 K for improved resolution at lower uncertainty: the white area in the lower right is all > 0.5 K. The predicted total uncertainty is highly dependent on the systematic or type B uncertainty within the radiometer system.

An in-depth theoretical electromagnetics model was assembled to understand the effect of coherence on the black-

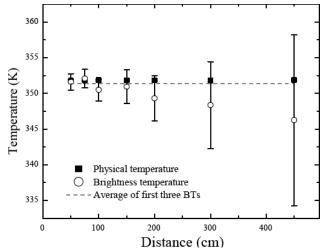


Fig. 2. Radiometrically derived target brightness temperature versus physical temperature at 18 GHz.

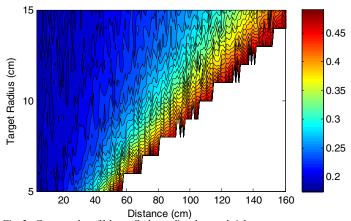


Fig. 3. Contour plot of Monte Carlo predicted target brightness temperature uncertainty (K).

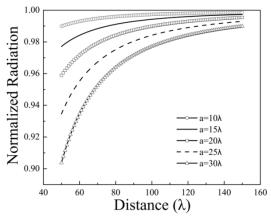


Fig 4. Result of coherence model showing normalized radiation magnitude versus distance for different blackbody radii (a).

body's radiation [3]. Fig. 4 shows the result of the electromagnetic analysis. When the blackbody target is located close to the radiometer front-end, the coherence effect of the blackbody radiation needs to be taken into account. There is a tradeoff between optimal blackbody size and measurement distance due to increased uncertainty at large distances and decreased normalized radiation at close distances resulting from coherence.

Current research at NIST involves the design of a blackbody that will optimize the measurement system and minimize measurement uncertainty. The blackbody will be a NIST primary standard intended for the calibration of customer radiometers. The typical square pyramidal arrays cover a small frequency range of optimal performance due to standing waves created by the pyramid absorbers. Alternative geometries such as single conical and wedge shaped cavities are being examined for use as a broader frequency laboratory standard. The proposed design will also greatly reduce uncertainty due to non-uniformity in the physical temperature distribution of the target.

The effective target brightness temperature is defined by the following integral:

$$\bar{T}_{tg} = \frac{\int_{target} T_{tg}(, \varphi) \varepsilon(, \varphi) F_n(\theta, \varphi) d\Omega}{\int_{target} F_n(\theta, \varphi) d\Omega},$$
 where  $T_{tg}$  is the physical temperature of the target,  $F_n$  is the

where  $T_{tg}$  is the physical temperature of the target,  $F_n$  is the normalized antenna power pattern, and  $\varepsilon$  is the target emissivity. The integral is evaluated in the spherical coordinate frame of the viewing antenna over the solid angle  $\Omega$  subtended by the target. By minimizing the physical temperature gradients in the target and maximizing the emissivity, the angular dependence becomes negligible and the physical temperature can be removed from the integral. The method in [1] can then be used without need for the explicit antenna pattern data. The integral in (2) is evaluated for different blackbody variations and used as a performance metric for the design. The closer the effective brightness temperature is to the set temperature on the heated target, the better the performance of the blackbody.

Evaluation of (2) involves knowledge of the three variables in the integrand of the numerator. All three of these quantities are simulated with commercial software. The temperature field is simulated by means of commercial finite-element-method (FEM) computational fluid dynamics software. anechoic chamber is modeled in the software including the air circulation fans. The blackbody model is placed inside the chamber and the heater surface is defined as a constant temperature boundary condition. The steady-state temperature distribution on the absorber surface is solved for and saved. We determined that use of a 3 mm layer of closed-cell polyethylene foam insulation directly on the absorber surface greatly reduces the temperature gradients, but the effect on the emissivity must also be considered. Fig. 5 shows the conical blackbody temperature model inside the anechoic chamber, and fig. 6 shows an example of the resulting temperature distribution looking into the cone for the non-insulated target.

The emissivity distribution is determined from a commercial electromagnetic FEM software solution. We simulated the bidirectional reflectance distribution function (BRDF) which can be used to calculate the emissivity through reciprocity. Assuming that there is no transmittance through the aluminum-backed blackbody, the emissivity is calculated from,

$$\varepsilon(, \varphi) = 1 - \int_0^{\pi} \int_0^{2\pi} r(, \varphi, \theta_r, r) \sin(\theta_r) d\theta_r d\varphi_r,$$
 (3)

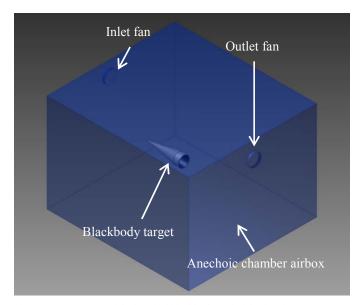


Fig. 5.Temperature model of conical blackbody set inside chamber.

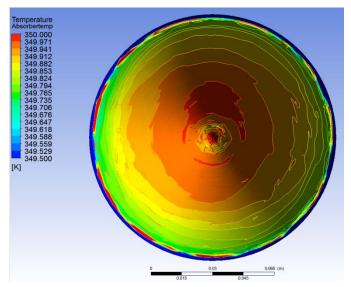


Fig. 6. Resulting temperature distribution of absorber surface.

where r is the reflectance as a function of spherical incidence angles  $\theta$  and  $\varphi$  and spherical reflected angles  $\theta_r$  and  $\varphi_r$ . Fig. 7 shows the reflectance distribution for the insulated conical blackbody at 18 GHz and normal incidence excitation. The cone aperture is oriented downwards in the software so  $\theta$ =180 degrees refers to the view of the conical axis in the blackbody cavity.

The antenna power pattern is also simulated with the same electromagnetic FEM software, and for this case, we simulated a rectangular standard gain horn at 18 GHz.

We calculated the effective target brightness temperature in (2) for the open-air and insulated blackbody design cases. We chose to use an antenna-to-target separation distance of 40 cm for this analysis but this will be further optimized in future studies. The target heater was set to 350 K, as shown in fig. 6. The resulting effective target brightness temperature was 349.84 K and 349.995 K for the open-air and insulated cases,

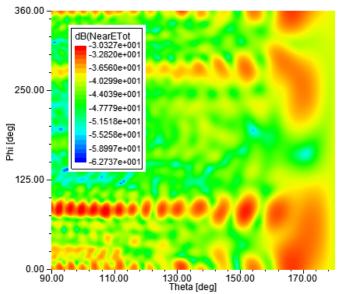


Fig. 7. 18 GHz reflectance distribution for conical blackbody excited at normal incidence and 40 cm distance.

respectively. The application of the insulation layer greatly increases the agreement between the heater setting temperature and the effective target brightness temperature. This considerably reduces uncertainty in calibrations performed with the proposed blackbody.

## IV. CONCLUSION

Through a combination of laboratory measurements, data analysis, theoretical derivation, and computational simulations we have been able to tune our measurement procedure to optimize the available hardware and understand the most beneficial improvements for uncertainty reduction.

Measurement distance is a critical parameter to optimize when measuring a blackbody in an anechoic chamber because of its effect on coherence, illumination efficiency, and emissivity.

A new blackbody design is in progress that will further reduce uncertainty in the calibration by optimizing the physical size of the body, reducing temperature gradients across the absorber, and maximizing the integrated emissivity. The measurements and simulations presented here aim to improve upon the NIST passive microwave brightness temperature standard and reduce uncertainties to levels required for long-term climate variable traceability. The results show that we will be able to reduce uncertainties in the 18 to 65 GHz frequency range from  $\pm 0.7$  K as seen in previous measurements to less than  $\pm 0.3$  K.

In the near future, we hope to calibrate the next-generation, operational, satellite-based microwave radiometer, called the Advanced Technology Microwave Sounder (ATMS) and, thus, begin the era of SI-traceable passive microwave climate data.

#### REFERENCES

- [1] Gu, Dazhen, Derek Houtz, James Randa, David K. Walker. "Extraction of illumination efficiency by solely radiometric measurements for improved brightness-temperature characterization of microwave blackbody targets" Transactions on Geoscience and Remote Sensing, IEEE, vol. 50 no. 11, Nov 2012.
- [2] Houtz, Derek, Dazhen Gu, David K. Walker, James Randa. "An investigation of antenna characterization techniques in microwave remote sensing calibration" Proc. of Int. Geoscience and Remote Sensing Symposium, IEEE, pp. 4660-4663, Munich, 2012.
- [3] Gu, Dazhen, David K. Walker. "Application of coherence theory to modeling of blackbody radiation at close range" Radio Science Meeting (USNC-URSI NRSM), Jan 2014, Boulder, CO.

# Development of an Automated Unintended Radiated Emission (URE) Radio Frequency (RF) Measurement System

Friedel, Joseph Burr, Arnold Nguyen, Van D24 D24 D26

**NSWC Indian Head Explosive Ordnance Disposal Technology Division** 

**EOD Department** 

Indian Head, Maryland

Abstract -- The Naval Surface Warfare Center Indian Head Explosive Ordnance Disposal Technology Division (NSWC IHEODTD) was tasked with the development of an Unintended Radiated Emission (URE) system (Figure 1) for the collection of wideband radio frequency (RF) data. Test facility sharing, large data file sizes (100 GBs), and ambitious production schedules added complexity to the data acquisition assignment. solution would require clever and efficient automatic RF techniques in hardware selection, design, and also in software development. URE is used to identify electronic systems by their RF emissions. At the start of this project in 2012, there was little literature on URE, so the IHEODTD development team had to rely on innovation. Some similarity to the field of electromagnetic compatibility (EMC) provided a starting point for the project. This paper will cover the evolution of the IHEODTD URE system hardware and algorithms, motivated by the need for greater system reliability and data throughput.

Index Terms -- Unintended radiated emission, anechoic chamber, radio frequency measurement.

## I. INTRODUCTION

## NSWC IHEODTD

NSWC IHEODTD is the field activity of the Naval Sea Systems Command (NAVSEA) that provides ordnance, energetics, and Explosive Ordnance Disposal (EOD) solutions. The division focuses on energetics research, development, testing, evaluation, in-service support, and disposal; providing warfighters solutions to detect, locate, access, identify, render safe, recover, exploit and dispose of explosive ordnance threats. The NSWC IHEODTD EOD Department (D) provides engineering and technical services to support Joint Service (Army, Navy, Marines, and Air Force) EOD requirements.

#### The Task

The Sensors and Diagnostic Branch (D24) was tasked with the development of a URE system for the collection of data in the RF bands, from extremely low frequency (ELF) to ultra high frequency (UHF). D24, along with several other government agencies collected data in parallel. Confounding this sizable task, was the need to collect URE data during development; sharing equipment and facilities with other NSWC IHEODTD RF projects during the collection period; and the collection and handling of enormous amounts of data (Terabytes/test object). Efficient automatic RF techniques would be needed to handle the sizable queue of test objects (well over 100); the large amounts of data being generated; and the limited test facility time, while keeping stringent data production schedules.



Chamber Exterior
Fig. 1. Initial Prototype URE System

Chamber Interior

## What Is URE

Processing of URE can assist in the identification of electronic systems by their unintentional electromagnetic radiations. For example, the common simple digital watch has a standard low frequency (LF) oscillator at 32 kHz. RF detection with a spectrum analyzer or frequency counter identifying this common oscillator would be an indication of a watch within the vicinity, even if the watch was not visible. Other common electrical products, such as radios or phones have similar URE characteristics, but with more complexity due to the increased sophistication of the circuitry (i.e., electronics containing multiple oscillators).

## Approach

URE is a less documented field of RF test with few publicly available references to research. This required the

development team to establish innovative methods and unique designs of RF measurements and data acquisition. The parallels of URE to the field of EMC provided some reference and a starting point for the project. EMC equipment, such as antennas and analyzers; and procedures, such as measurement distances, could be considered for adoption into the developing NSWC IHEODTD URE system.

The overarching project specifications for this task were initiated in the Department of Defense (DoD) and followed by the civilian, industry and university team members. While some details of the data collection procedures were specifically spelled out (measurement distances, antenna positions, and data format) other details like particular hardware model numbers and software packages for the system were not specified. These design parameters were left to the decision of the data collection sites (of which Indian Head was one).

## II. INITIAL DESIGN

The simplest URE setup consists of the radiating Device-Under-Test (DUT), a receive antenna, and a measurement instrument like a spectrum analyzer. IHEODTD's original prototype was not much more than this. The design can be improved by using an anechoic chamber for noise reduction, positioners for positioning consistency, and a PC for automation and data collection. The following paragraphs describe EOD's early design decisions.

## Chamber

EOD had one anechoic chamber, and fortunately it was adequate in size and frequency range. It had a 24' by 12' by 12' height interior with a 30 MHz to 18 GHz operating range. The shielding effectiveness is rated at 100 dB attenuation at 18 GHz, with a 1.5 kW per meter squared power rating. It is a semi-anechoic chamber, meaning the floor was not fully ferrite tiled and covered in anechoic materials, while the walls and ceiling were. This design was ideal for development, where the constant test development changes resulted in a steady amount of activity within the chamber. A full anechoic chamber would have suffered more damage to anechoic and ferrite materials due to the more narrow walking paths.

One problem with the chamber was that it was shared by several NSWC IHEODTD projects, one which had higher priority, and used it most days of the week. This could have forced the EOD URE project to seek the use of an anechoic chamber at one of the several nearby military bases, adding logistics complexities to the project. Good cooperation between NSWC IHEODTD departments allowed the URE project to negotiate a chamber sharing arrangement with the priority group. The URE team would get several hours of test time, later in the workday (~3 to 6 p.m.), preventing the need for shift work. The URE project, being initially a development effort, could use the morning hours for needed

system development, which did not require the collection of customer data within the shielded chamber.

Two separate patch panels on different sides of the chamber allowed the projects to have independent non-interfering work areas. Chamber antennas, test stands, and anechoic material positioning within the chamber had to be negotiated. Equipment that was not shared between the projects had to be moved in and out of the chamber; which resulted in the lower-priority URE equipment having to be moved.

## Spectrum Analyzer

Although the NSWC IHEODTD EOD Department had one modest anechoic chamber, it had an abundance of RF test equipment. All the major spectrum analyzer manufacturers were represented, from hand-held units to powerful lab grade models.

Due to the firm project requirement of collecting RF data in the rectangular coordinate (IQ) format, a real-time spectrum analyzer (RSA) with IQ data format (Figure 2) was selected for use. Although NSWC IHEODTD had several IQ analyzers available, we selected one for use which had the best data throughput and the lowest upgrade cost to meet the needs of the project. The large measurement bandwidth of 110 MHz and respectable dynamic range (75 dBc) was found superior to competing models on the base.

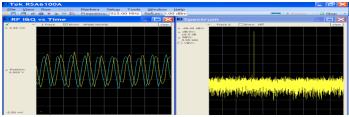


Fig. 2. RSA Display of IQ Format Data

If money was available, a faster spectrum analyzer would have been bought. Due to the large amounts of data that needed to be processed, small improvements in test speed, would result in great improvements in test schedule. The RSA used was several years old, and newer models with more memory and speed (>2x) were available. Additionally, the EOD engineers were aware of spectrum analyzers with larger measurement bandwidths and the availability of high speed memory devices like the redundant array of inexpensive disks (RAID) which could greatly improve data collection speeds (a magnitude or more). However, at the beginning of this program, funding was not available to procure those assets.

## Antenna

Although NSWC IHEODTD had dozens of antennas to work with, the initial URE system utilized a broadband bilogical antenna. The driver in the selection decision was the coverage of project frequency range (ELF to UHF), with linear polarization. The bilogical was a large (~40" x 40" x 20"), but fragile (4.5 pound) antenna. Fortunately the chamber's major project could utilize this same antenna, avoiding the necessity

of daily moving the antenna in and out of the chamber. NSWC IHEODTD also had an adequate antenna stand that allowed the antenna to be located in the center of the chamber. The antenna had a frequency range of 25 to 7000 MHz, with a gain of 6 dBi and a continuous power rating of 1000 Watts.

#### **Positioners**

The test antenna had a mating wood tripod positioner that could be manually adjusted for height. Testing requirements called for vertical and horizontal measurements, so position was changed manually with the use of a bubble-level to keep the antenna straight. A hinge connection between the antenna and stand allowed height to be kept constant when antenna polarity was changed. A twin stand was used to support the DUT, which was typically a small commercial radio device. Since these DUTs were not designed for stand mounting, stability was achieved by low-tech means (tape, ties, etc.). Test requirements, treated all DUTs as a cube, and six measurement positions were required with each of the approximate cube sides of the DUT held perpendicular to the measurement antenna. Height of the two positioners were matched and kept constant to keep the antenna and DUT in the center of the chamber (~6 feet from the floor). The original measurement distance, called out by the test requirements, was 3 meters from test antenna to DUT.

## Computer

The control computer was a Dell Precision M6600 laptop with an Intel Core i7-2960XM processor. The hard drive memory was 685 GB while the RAM size was 32 GB. It had a 64-bit operating system with Windows 7 Professional. It was ordered with a DVD read/write drive.. The highest calculation complexity was expected to be the fast-fourier transform or FFT (Figure 3), which most modern PCs can handle. A laptop was chosen over a cheaper workstation alternative to allow for development work, away from the data collection site. Speed was important to the URE project because IQ data collection involved hours of data processing. A faster processor could shave hours off of the possibly weeks of testing required for each test item. Hard drive memory was not critical, because the memory requirements for the project were so great (Terabytes per test item) that data memory would have to be external. The RAM was maxed on the purchased PC, but that was probably excessive. specification was driven by the potential requirements of the data acquisition and processing software, which was not positively known at the time of the PC purchase. ports maximum number of was desirable, instrumentation control was required and the data processing and storage system details were not yet known, but would be significant. The purchased PC came with four 2.0 USBs and a PCIe interface.

## Network

The plan, from the beginning of the project, was to have computer control of the URE data collection and processing.

The engineers at NSWC IHEODTD were familiar with LAN and General Purpose Interface Bus (GPIB) as choices for network communication between equipment. The choice was made to use LAN, because it was simpler and the interface cables were readily available. (Changed from LAN to GPIB, later in the project, for reasons to be described in the 'Hardware Improvements' section.)

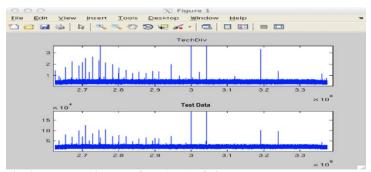


Fig. 3. Fast Fourier Transform (FFT) of IQ Data

## Data Storage

Data storage and the speed of data collection were the driving factors of the project. Less money was spent on speed requirements to keep development costs down, which resulted in using existing equipment that was available. While the system developers could make trade-offs on speed versus equipment money spent, there was no way to reduce the large amounts of data that would be generated. Requirements called for collecting long durations (originally 120 seconds) of IQ data over a wide bandwidth (2.5 GHz), at six DUT positions, at two antenna polarizations, and multiple DUT settings (if the DUT had multiple configurations, such as channels). This resulted in data accumulations of 100's of Gigabytes, even Terabytes, for each test item.

If the needed memory could be built into our spectrum analyzer, this solution would have provided the best data acquisition speeds. The quantity of memory required did not exist as an option for the spectrum analyzer NSWC IHEODTD was working with. Although there were spectrum analyzers with large and fast memories, one was not available for this effort.

If the memory could not be put on the spectrum analyzer, the next choice for location would be on the PC. At the time of procurement, such a PC option was not readily available. Additionally the PC budget was finite (<\$3K). Another consideration was that the collected data had to be transferred to another laboratory for further processing. If the PC or PC drive had to be copied, on or off-site, data acquisition would come to a halt, since at the beginning of the project there was a budget for only one PC.

It was decided to use common, existing hard drives. This was a slow yet inexpensive solution. Unused drives from the base were collected and utilized. Reuse of disk space would have kept the system manageable, but an early decision by EOD management to keep copies of all data acquisitions,

resulted in constant searching for hard drives. This decision turned out to be a good one, since there were several occasions where data was lost or corrupted.

The central processing center for the data collected from the DoD collection sites, periodically sent each site a blank hard drive to transfer the latest collected data. Copying Terabytes of data would take hours on the available PCs. Initially at NSWC IHEODTD, data copying was done unmanned, during the overnight hours. However, shortly into the program, a second older laptop was checked out from base supply and used for this task.

## Software

The project had a choice of software: either using commercially-available instrumentation control and data processing packages or using a development language such as C or Basic. DoD management leaned toward using an instrumentation package and recommended LABVIEW and MATLAB. NSWC IHEODTD bought a license for each. One of the other collection sites developed the first acquisition software program for URE data collection in MATLAB and distributed it to the other sites. Each of the other sites customized this original program for their own use, making MATLAB the primary development software package for the URE data collection project.

## Prototype System

The initial prototyped system is shown in Figure 1: one PC, one RSA, one rectangular-polarized antenna, and one wooden pole to support the DUT. All testing was done in the NSWC IHEODTD Anechoic Chamber. The chamber's RF patch panels allowed for sealed chamber testing, where the receiving antenna would pass the RF data to the out-of-chamber RSA, which would store the recorded large IQ format files on an external multi-Terabyte drive. The control computer directed the RSA in MATLAB. Data requirements called for two polarities of testing (horizontal and vertical), so after testing was completed on one polarity, the antenna was manually rotated and the same test was repeated for the second polarity.

## Initial Data Collection Times

Due to the large IQ times initially required (up to 120 seconds), the broad frequency band coverage (ELF to UHF) and the vast amounts of resultant data (in the hundreds of Gigabytes per test) that had to move from the analyzer to the external drive, test times took 4 to 6 hours per test depending on the speed of the hard drive. Each DUT had to be tested in six positions and two polarizations. Additionally, a background test was taken in both polarizations, where the DUT was removed from the chamber for the duration of the background test. A single DUT would take ([6 positions + 1 background] x 2 polarities x 5 hours) or about 70 hours to test. These hours were multiplied by the test settings (frequency or channels) of the DUT, which were as many as three settings (3 x 70 = 210 hours). This time was multiplied by the number of duplicate items tested (same model, different serial numbers). Typically, two of each model DUT was tested ( $2 \times 210 = 420$  hours). These long test times, coupled with the following additional requirements: a two DUT per month requirement; a 160 hour work month (with no overtime or shift-work); power outages causing test crashes which required repeating tests; periodic bumping from the chamber to make way for higher-priority projects; indicated that the prototype system would have to greatly improve to meet production.

## III. DATA PROCESSING

Raw RF IQ data was captured and sent to another facility for processing. Figure 2 (right side) shows a sample RSA display of collected IQ data. Typically, IQ data was collected using a 1.25 MHz measurement bandwidth for a period of 50 seconds. For quality assurance, a small percentage (~1 to 2%) of collected IQ data files was processed at NSWC IHEODTD to verify that the data is correct. This was done using MATLAB and executing a FFT on the examined data file. Figure 3 shows an example of a frequency spectrum display created after running an IQ file through the FFT.

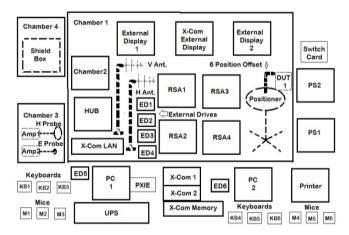


Fig. 4. Block Diagram of Current IHEODTD URE Measurement System [1]

## IV. IMPROVING THE URE MEASUREMENT SYSTEM

Figure 4 shows a block diagram of the current system with four chambers, two PCs, and four RSAs. Figure 5 is a photo of the current control console. The DUTantenna positioning system went from manual to fully-automated. Along with the hardware improvements, the software greatly improved, resulting in reduced test times. Early system test times that were longer than six hours, are now slightly below 4 hours. Software improvements now allow up to four channel-recordings simultaneously, compared to the system's original single channel. The dramatic improvements that occurred over a 1 ½ year period, to make the NSWC IHEODTD URE system successful in its mission are detailed in this section. The RF hardware and instrument evolution are discussed along with the improving software control, automation, and processing algorithms, for greater data acquisition speed and

reliability.

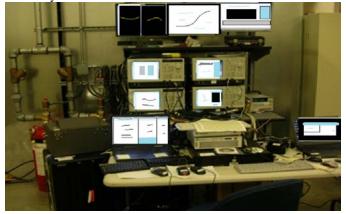


Fig. 5. Current URE Control Station

## Improvement Goals

The improvement goals were threefold:

## 1) Make system more reliable.

With the simple data acquisition system discussed, NSWC IHEODTD was up and running and collecting usable data within 3 month of project start. As with many prototype systems, there were many system crashes. A crash on a 5 hour test could result in the entire test being repeated, causing delays in schedule.

## 2) Make the system faster.

A single test item could take over a month to complete. The DoD customer expected multiple items a month. EOD did not have the resources to do shift work, and lost chamber time to other projects.

## 3) Keep development costs down.

The managers and engineers shared a philosophy of keeping costs down. The priority was to borrow equipment, long-term, instead of buying new. Software was developed in-house, instead of being contracted. System and software improvement ideas were shared between NSWC IHEODTD and their collection partners.

## Hardware Improvements

It was found that GPIB was more reliable than LAN. During the many hours of testing on the LAN setup, system failures were encountered that appeared to be due to communication problems between the PC and RSA. Although the crashes were infrequent, they were a nuisance because a multi-hour test may have to be repeated. Switching to GPIB virtually eliminated such crashes.

The electrical power in the building where the URE data was collected was unreliable. After a heavy rain, it was common to have a power dip or even an extended outage. These power outages interrupted test collection and sometimes resulted in repeating tests. Uninterruptible Power Supplies (UPS) where

installed on all the system equipment and power related test failures ceased to be a problem.

A second measurement channel was added to the URE system, improving reliability through redundancy. It also allowed test collection on two channels sequentially, which did not reduce test time, but allowed for longer continuous, unmanned (automated) testing. An identical antenna to our broadband antenna was bought, which allowed simultaneous collection of vertical and horizontally polarized data. The NSWC IHEODTD anechoic chamber was large enough to accommodate the large, dual antennas, side by side, while maintaining the required 6 foot test height and 3 meter test distance, for each antenna, from the DUT. Effort was saved by not having to stop testing, to reconfigure the antenna and test setup. A second RSA became available from a terminated project and our software was modified to run both spectrum analyzers at the same time.

An elevation/azimuth positioner was programmed and integrated into the URE system. To keep the electrical noise of the positioner motors from interfering with the RF testing, a double power supply and circuit card switch was designed (Figure 6) [2].

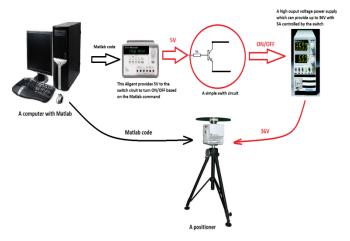


Fig. 6. Antenna Positioning System

An attachment was designed for the positioner to enable it to achieve all six required DUT test positions. Without the attachment, the positioner could only achieve five positions, requiring human intervention to move the DUT into the sixth.

With the capability of longer unmanned test times, and the higher reliability from improvements to the network and power, the URE testing could operate reliably, without personnel, through the overnight hours. This made for a productive coexistence with other NSWC IHEODTD projects, which could use the anechoic chamber during the day.

The chamber characteristics were improved under the URE project. More anechoic and ferrite materials were purchased and placed in the chamber floor areas that were missing these materials, being a semi-anechoic chamber. Just as when the above positioner noise-suppression system was installed, the chamber's interior RF environment was characterized with a

precision spectrum analyzer and the broadband antennas, to verify the reduction to the chamber's interior noise-level [3].

The URE PC had a display failure. The problem was solved by utilizing an external display until it was repaired under warranty. However, these emphasized the need to backup software and, eventually, get a second PC. Duplicate MATLAB licenses were bought for the second PC that mirrored the first PC. All in-house developed software was copied to the secondary PC. The second PC provided further software reliability and also allowed for simultaneous test collection (on one PC) and software development (on the other PC).

URE testing was extended to lower power devices. This enabled testing at closer ranges with EMC probes measuring the E and H fields. The EMC probes worked well with preamps, enabling the measurement of very weak component RF radiations. Smaller RF levels and smaller test distances, enabled the URE project to use smaller shield boxes that were available on the base instead of the large chamber. This freed up the large chamber, further, for sharing by other NSWC IHEODTD RF projects.

Two ~3' cubed, and two ~1' x 1' x 2' shield boxes were added to the EOD URE system, from other projects. One of the small shield boxes was placed inside one of the 3' cubed shield boxes (Figure 7), creating an extremely quiet RF test space and giving the URE system four distinct test chambers to connect to (large, 3' cubed, small, and double-shielded).



Fig. 7. Chamber within a Chamber

Two additional RSAs were made available to the URE project from completed projects. With the two PCs, multiple chambers, and four RSAs, four channels could be collected simultaneously. This meant the URE system could now measure H and V-polarities or E and H-fields on two devices simultaneously, in two distinct chambers, cutting test time in half.

## Software Improvements

Several of the NSWC IHEODTD engineers became knowledgeable MATLAB programmers, continuously automating, improving and speeding up the data processing. Manual operation of the spectrum analyzer, which slowed

down tests and introduced failure points, was automated in the software, increasing reliability and data acquisition speeds. The automated processes included spectrum analyzer calibration, attenuation setting, pre-amp setting, and display setting and scaling.

One of NSWC IHEODTD's first software modifications, to the system code was extending the operation to two channels, enabling simultaneous collection of data on two antenna polarizations. It took more familiarity with the spectrum analyzers to eventually trigger both analyzers simultaneously, with one PC, to cut data collection time in half. Using this technique with two PCs and two chambers (with two DUTs) enabled the quartering of the original test time.

As mentioned, code was written to control a precise azimuth and elevation positioner, and it was integrated into the URE system. This enabled testing the DUT sequentially at each of the required six test positions, while collecting data simultaneously at two antenna polarizations, without the need for operator intervention.

Remaining Test Time algorithms were inserted into the code, with screen displays that enabled the system operator to know when to return for the next test setup. Test run time was counted in the software and displayed on screen to enable the testing of software and hardware speed improvements.

A complex algorithm was coded, as an option, to suppress spectrum analyzer screen updates, which provided a considerable data acquisition speed improvement (~25%).

## V. CONCLUSIONS

This paper details a well-managed and engineered URE measurement development project that succeeded in developing a system that can distinguish the radiated emissions of RF devices from the background noise by using the appropriate configuration of a sensitive receiver, RF chamber, antennas and amplifiers. Following NSWC IHEODTD's example of metered expenditures, a URE development project could use this paper as a template for incrementally building a measurement system. Existing or beginning URE projects can use this paper for ideas on URE techniques and measurement automation.

#### REFERENCES

- TECHDIV URE Measurement System Test Procedure; Friedel, J.; Burr, A.; Nguyen, V.; NSWC IHEODTD; Indian Head, Maryland; 31 July 2014.
- [2] Installation of Positioner and Solution to Noise in Anechoic Chamber; Wilhelm, L.; Nguyen, V.; Friedel, J.; Naval Surface Warfare Center Indian Head Explosive Ordnance Disposal Technology Division (NSWC IHEODTD) 30 September 2013.
- [3] Chamber Characterization after New Positioner Installed; Friedel, J.; Nguyen, V.; NAVEODTECHDIV; Indian Head, Maryland; 22 May 2013.